MSc Thesis: Propeller Slipstream Correction for Wind Tunnel Applications

A panel method approach to model propeller induced rotational flow for aircrafts in mid/high thrust condition
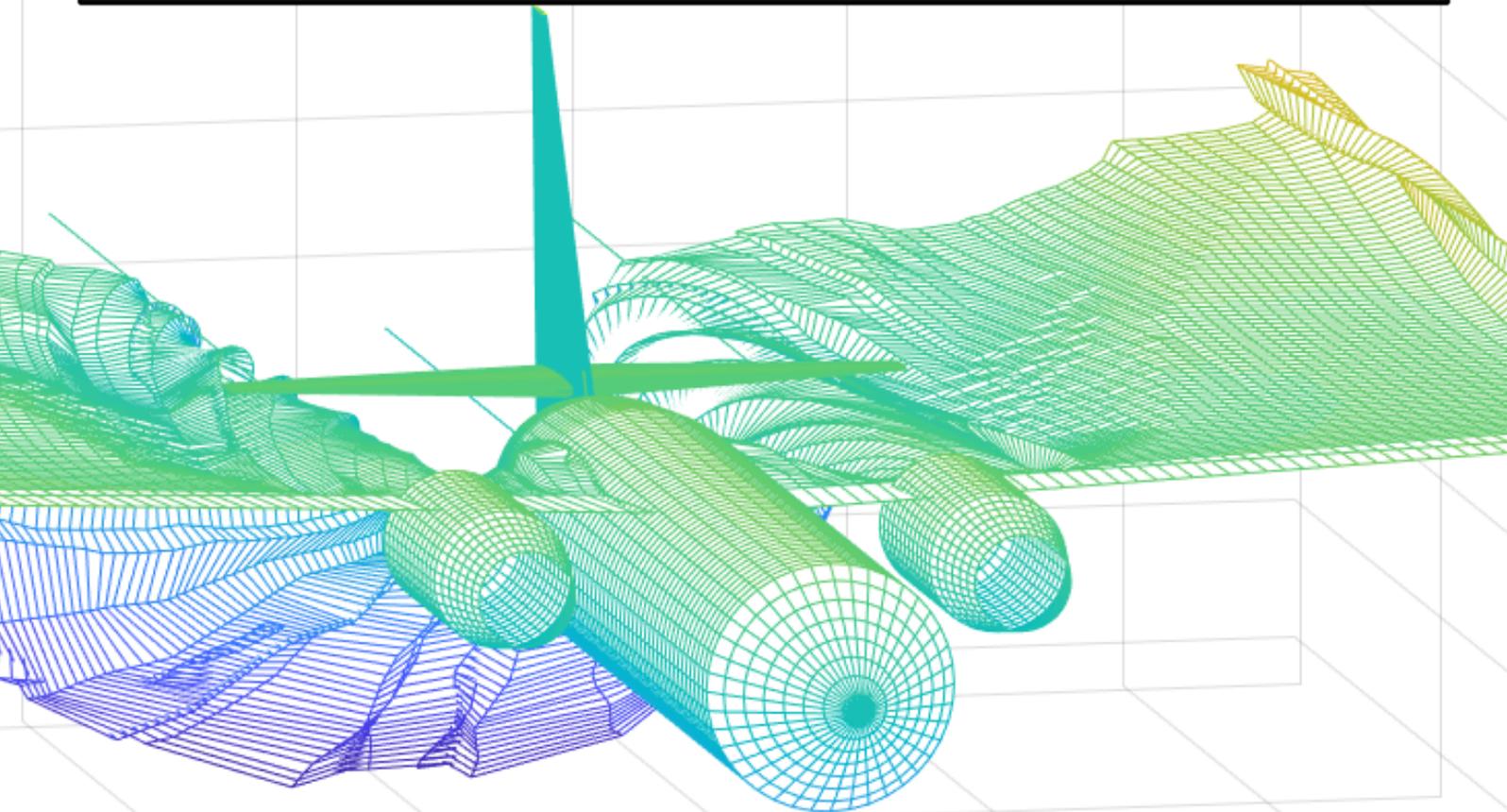
TUDelft

Ekin Orer

MSc Thesis: Propeller Slipstream Correction for Wind Tunnel Applications

TU Delft – Faculty of Aerospace – FPP

By

Ekin Orer

in partial fulfilment of the requirements for the degree of

Master of Science

in Aerospace Engineering

at the Delft University of Technology,

to be defended publicly on Friday September 25th, 2020 at 10:30

Supervisor:	**Prof. Dr. Ing. G. Eitelberg**	**TU Delft, chair and supervisor**
Thesis Committee:	**Dr. Ir. T. Sinnige**	**TU Delft**
	Dr. Ir. S.J. Hulshoff	**TU Delft**
	Ir. S. Hegen	**DNW**

An electronic version of this thesis is available at http://repository.tudelft.nl/

ABSTRACT

In the post processing of acquired wind tunnel force measurements, propeller-driven aircrafts need a preliminary correction of the propeller slipstream. Propeller slipstream effect has two major contributions to the flow field. The first one is the increase in dynamic pressure and the second is the addition of rotation in the flow field. Without a slipstream correction, standard wind tunnel corrections cannot be implemented because powering the propeller violates the underlying assumptions of the standard correction methods according to Eckert. As a result, Eckert has developed a thrust correction formula that only includes the increase of dynamic pressure. This research has been conducted to develop a novel correction to include both the increase in dynamic pressure and the effect of rotation induced by the propeller slipstream. Initially, a non-linear Surface Vorticity Panel Method (SVPM) was chosen in order to have a non-prescribed slipstream strength and shape. However, there were problems with convergence time and slipstream deformation. Therefore, the model was reduced to a linear model first suggested by Schroijen. The propeller was modeled as a mix of BEM and vortex theory. The wing and empennage was modeled by VLM. Fuselage was modeled after Multhopp's vertical slit representation and a forced potential solution was implemented to simulate the wing root effect. The wind tunnel experiments were conducted in various angle of attacks and thrust ranges. Results show that the panel method can simulate the rotational nature of the slipstream accurately and the wing lift distribution is parallel to the literature. The new proposed correction was adequate at approximating the propeller slipstream lift and can produce closer results than the Eckert correction at some instances.

ACKNOWLEDGEMENTS

As I am reaching a very significant milestone in my academic career, I would like to thank first and foremost to Prof. Georg Eitelberg for being understanding and patient during my thesis. I wouldn't be able to complete this research without his guidance. Second, I want to say thank you to Mr. Hegen, who took care of me during my internship days at DNW. He provided me every document that I needed during my research. I appreciate every single person at DNW and NLR; they were all very kind, professional and brilliant people.

To my family and friends: I love each and every one of you! I am very lucky to have a family that has always been supportive of me. My mother, Aslı, is the most loving and open-minded person I know. My father, Altan, always keeps his cool. I always considered him as a dear friend. My grandparents Gülten, Mete, Gülden and Oktay have always been there for me since my first day at elementary school. I know my brothers, Göksu and Lev, will have a great future ahead of them as tennis and hockey players respectively. My cousin Mine is already on her path to become a distinguished judge.

There are four more people that I consider as family: Necmiye brought me up alongside my mother, and I know she loves me as her own. I am forever in your debt. Okan has been my coach, my father and sometimes my older brother when I needed. Yeter and I were housemates for more years than I can count, she is a dear friend. Mehmet is the most compassionate person I have ever met; he always gave great advice and support. I hope you will have blissful and fulfilling lives.

I cannot name every one of my friends, but I know for sure they know who they are. I contact some of them twice a week, some of them once in a decade. You will always have a place close to my heart.

My heart belongs to my partner in crime, Anna-Lotta. She is the kindest, most thoughtful and most intelligent woman I know. We have been on many adventures together in the last 3 years. She was always with me in good times and bad times. I love you.

I had the great privilege of having many pets during my lifetime and they are also family. Their names shall never be forgotten. May Kedişko, Turunç, Şeker, Hamur, Odin and Dippen stay forever young and ever loved. May Kedibey, Kedimo, Badem and Ayva rest in peace.

Finally, I want to acknowledge the ones who will always have a place in our hearts. My grandmother Leyla, who did not get a chance to see me grow. You will always be by my side. My aunt Hülya, who lost her years-long battle with cancer when I was in college. She would be very proud of her daughter and me. My dear friend Tunahan, you are in my thoughts everyday. I wish we had a lifetime together ahead of us. I will always cherish our memories. This is for you.

CONTENTS

LIST OF FIGURES

NOMENCLATURE

Latin Symbols

a_a	Axial velocity factor (v_a/V_∞)	$[-]$
a_t	Tangential velocity factor (v_t/V_∞)	$[-]$
a'	Tangential velocity factor ($v_t/\Omega R$)	$[-]$
a_{ij}	Transformation matrix	$[-]$
A	Surface area, aspect ratio	$[m^2, -]$
AR	Wing aspect ratio	$[-]$
b	Wing span	$[m]$
B	Number of propeller blades	$[-]$
C	Wind tunnel cross-section area	$[m^2]$
$C_{i,j}$	Influence coefficient matrix	$[-]$
C_{N_p}	Propeller Normal	$[-]$
C_T	Propeller thrust force coefficient ($\frac{T}{\rho n^2 D^4}$)	$[-]$
C_d	2D drag coeffcient	$[-]$
C_D	3D drag coefficient	$[-]$
C_l	2D lift coeffcient	$[-]$
C_L	3D lift coefficient	$[-]$
$C_{m,p}$	Pitching moment coefficient	$[-]$
$C_{m,r}$	Rolling moment coefficient	$[-]$
$C_{m,y}$	Yawing moment coefficient	$[-]$
C_Y	Side force coefficient	$[-]$
C_P	Power coefficient	$[-]$
c_p	Pressure coefficient	$[-]$
C_Q	Torque coefficient	$[-]$
c	Chord length	$[m]$
$\bar{c}$	Mean aerodynamic chord	$[m]$
d	Distance	$[m]$
D	Propeller diameter	$[m]$
f	Prandtl tip loss factor	$[-]$
F	Force vector	$[N]$
F	Velocity ratio	$[-]$
F_k	Average vorticity flux through the k-th side face of a panel	$[m/s]$
G_L	Non-dimensional propeller blade circulation $\left(\frac{\Gamma}{2\pi R_p V_\infty}\right)$	$[m]$
h	Helicity, enthalpy	
ΔH	Head pressure jump	$[Pa]$
i, j, k	Unit vectors	$[m]$
J	Advance ratio (V_∞/nD)	$[-]$
$K_{1,3}$	Solid blockage constant	$[-]$
l	length	$[m]$
L	Lift force	$[N]$
m	mass	$[kg]$
$\dot{m}$	Mass flow rate	$[kg/s]$

M	Mach number	$[-]$
M_p	Pitching moment	$[N.m]$
M_r	Rolling moment	$[N.m]$
M_y	Yawing moment	$[N.m]$
n	Unit normal vector from a surface	$[-]$
n_p	Number of propellers	$[-]$
$P(x,y,z)$	Point in space	$[-]$
p	Static pressure	$[Pa]$
p_t	Total pressure	$[Pa]$
q	Dynamic pressure	$[Pa]$
r	Radial coordinate	$[m]$
r_0	Centroid of the panel	$[m]$
r_ε	Infinitessimal core radius of the Rankine vortex filament	$[m]$
R_p	Propeller radius	$[m]$
R_s	Local slipstream radius	$[m]$
Re	Reynolds number	$[-]$
S	Area, Wing area	$[m^2]$
S_{14}, α_4	The slope and slope angle of side 1-4 of a panel	$[-]$
S_{23}, α_2	The slope and slope angle of side 2-3 of a panel	$[-]$
S_p	Propeller disk area	$[m^2]$
ΔS	The area of the surface vorticity panel S_p	$[m^2]$
t	time	$[s]$
T	Thrust	$[N]$
T_c	Thrust coefficient $(\frac{T}{\rho V^2 D^2})$	$[-]$
T_c'	Thrust coefficient $(\frac{T}{q_\infty S_p})$	$[-]$
U_∞	Uniform free stream velocity in the axial direction	$[m/s]$
V_a	Axial Velocity	$[m/s]$
V_t	Tangential Velocity	$[m/s]$
V	Velocity vector	$[m/s]$
V_∞	Undisturbed flow velocity	$[m/s]$
V_A	Advance velocity	$[m/s]$
V_m	Mean velocity vector at the propeller free cortex sheet	$[m/s]$
V_S	Velocity vector induced by a unit strength source panel	$[m/s]$
V_V	Velocity vector induced by a constant vorticity strength density panel	$[m/s]$
$w_{i,j}$	Width of panel $C_{i,j}$	$[m]$
x,y,z	Global axis system	$[-]$

Greek Symbols

α_0	Zero lift angle of attack	$[deg]$
α_p	Propeller angle of attack	$[deg]$
$\tau_{1,2}$	Wing, Tail Correction Coefficient	$[-]$
∇	Gradient	$[-]$
Γ	Line Vortex Strength	$[m^2/s]$
Π	Pitch of the propeller slipstream at free-stream	$[rad]$
Φ	Potential	$[m^2/s]$

Ω	Angular velocity	$[rad/s]$
α	Angle of attack	$[deg]$
β	Yawing angle, local propeller blade angle	$[deg]$
γ	Surface vorticity strength	$[m/s]$
δ	Interference constant	$[-]$
η	Efficiency	$[-]$
θ	Rotation angle about x-axis	$[deg]$
μ	Doublet Strength	$[m^2/s]$
ξ, η, ζ	Local coordinates	$[m]$
σ	Source strength	$[m^2/s]$
τ	Tolerance	$[-]$
φ	Local blade flow angle	$[deg]$
ω	Vorticity	$[1/s]$
ϵ	Blockage constant	$[-]$
ϕ	Panel rotation angle	$[deg]$

Abbreviations

ADM	Actuator Disk Model
ATP	Advanced Turboprop Project
BEM	Blade Element Model
DLR	German Aerospace Laboratories
DNS	Direct Numerical Simulation
DNW	German-Dutch Wind Tunnels
$NASA$	National Aeronautics and Space Administration
NLR	Dutch Aerospace Laboratories
PIV	Particle Image Velocimetry
$STOL$	Short Take-Off Landing
$SVPM$	Surface Vorticity Panel Method
VLM	Vortex Lattice Method
$WFNVH$	Propeller-Off Configuration
$WFNVHP$	Propeller-On Configuration

Subscripts

$3c/4$	Three-quarter chord
∞	Free-stream, infinity
c	Corrected
$c/4$	Quarter-chord
f	Fuselage
g	Geometric
i	Propeller index, induced
m	Model, mean
p	Propeller
uc	Uncorrected
w	Wall, wing

0

SHORT HISTORY OF PROPELLERS & PROPELLER-DRIVEN AIRCRAFT

The development of propeller theory dates back 50 years before when Wright brothers had made their first successful launch of a propeller-powered aircraft. Even though, there were no air-driving propellers before them, they knew that the empirical and experimental knowledge on the marine propellers could support the required thrust for a successful take-off. On December 17 1913, The Wright Flyer III made its debut flight, which would change the history of transportation. Ever since the success of the first flight with the use of an air-screw, propeller driven aircraft and propeller theory became a fundamental topic on aircraft design.

0.1 Early Development

Before Wright Brothers, the marine propeller theory had two main approaches that are still constitutes the basis of current model of propeller flow. The first theory was suggested by Rankine around 1865 and is currently known as simple momentum or more commonly as the Actuator Disk Model Theory (ADM). This simplified approach was a two dimensional model, where the propeller cross-section is modeled as a homogenous disk, which causes a pressure jump at the location of the simplified disk. The discontinuity results in a uniform induced velocity over the uniform velocity, which was caused by the added kinetic energy in the system. This approach does not take into account the blade geometry, which cannot be overlooked for an accurate propeller model. The second approach was first addressed by Froude in 1878. The Blade Element Momentum Theory (BEM) is modeled around the geometry of the propeller. Each blade of the propeller is divided into independent airfoil sections (elements), in which the rotation and translation of the flow for each element is calculated. The main downside of the proposed model was the actual geometrical size properties like aspect ratio of the blades were not taken into account. [1] Therefore, when Wright brother started their research they had a very crude idea of their actual propeller efficiency.

Around 1920s, the research on aircraft and propellers kept rising. The vortex theory (first addressed by Lanchester in 1907), proposed that the induced velocity that is created by each propeller element should be modeled in the trailing vortices. Three prominent scientists made substantial progress for an optimum design of airscrew using vortex theory. Initially, Betz found

the optimum condition where the trailing vortex (consequently induced flow) matches the rigid surface of the blade surfaces (helicoid flow). Then, Prandtl adapted this solution to finite number of blades with an approximated tip loss correction factor. Finally, Goldstein solved for an exact solution using potential flow theory to find the optimum radial distribution for circulation of the trailing vortices in 1929. [2]

On the quest for finding the optimum propeller design, Prandtl had observed in his wind tunnel tests that the propellers have interacted and affected the solid bodies that they were in close proximity. [3] Especially, the trailing surfaces behind the propeller downwash had a mutual interference between each other. He concluded that the wing was influencing the induced velocities on the propeller blades, while the direction of the flow was altering in the slipstream going over the wing.

With the development of the jet engines towards the end of World War II, propeller driven aircraft had two clear disadvantages. The height of service ceiling and the maximum speed of the jets were higher, which gave jets the upper hand in air combat and skirmishes. Propeller driven aircraft before 1945 were largely limited to $M \approx 0.6$. After the war, jet engines were also integrated as a more popular commercial propulsion system for civil air transport. Until the oil crisis of 1973, propellers were losing interest because of the development of the turbofan engine. After '73, engine manufacturers and NASA accelerated their research on propulsive efficiency that had become a priority because of the increasing fuel prices. [4]

NASA launched their advanced turboprop project (ATP), which targeted to decrease fuel consumption in passenger aircraft with a propeller driven engine. In summary, there are two major parameters that contribute to thrust. These are mass flow rate ($\dot{m}$) and change in axial velocity (ΔV). In order to increase the thrust, usually increasing mass flow rate is preferred because the ideal propulsive efficiency drops with larger change of axial velocity. V_∞ is the freestream velocity:

$$T = \dot{m}\Delta V$$

(0.1)

$$\eta_p = \frac{2}{2 + \dfrac{\Delta V}{V_\infty}}$$

(0.2)

Relationship above shows that the change in velocity has an inverse relation with propulsive efficiency. The solution for increasing thrust without efficiency penalty for turbofan engines is usually increasing the bypass ratio. However, by design, propellers have the highest bypass ratio of any engine because of the absence of a fan cowl. As a result, the high mass flow is reached relatively easier without cowl weight and drag penalty compared to a turbofan engine.

The newly named propfan engines were first introduced in 1975. With the new incentive to enter the emerging market Boeing, McDonnel Douglas and later Airbus has developed co- and contra-rotating propfan configurations. [5] During the development of propfans in the subsequent 10 years, complex design of aeroelastic effects, fatigue, early shock formation and propeller slipstream created a harder challenge than industry had expected. Consequently, the market for propfan research has declined over the years until the resurrection of the turbofan research in the new millennia.

0.2 Late and Current Research

Aviation industry has been consistently growing since the 1980's with better fuel economy and increasing market size. The frequency of passenger commute has increased and it brings new opportunities and concerns for the aerospace companies. [6] The limits of turbofan engines were studied by Pratt & Whitney in the 90's that a turbofan cannot reach the ultra-bypass ratio without nacelle drag penalty. Also, they have cooperated with Allison to produce a turboprop engine to enter the market for short-medium length flights. [7] In theory, turboprop engines are 10-30% more efficient than jet engines where cruise speed is less than M=0.7. [4] The slow, low altitude flight of the turboprop engines are suitable for short-haul flights where the extra flight duration compared to turbofan engines are less than half an hour. Turboprops have also other advantages like: high thrust at take-off, wider operational speed range, increased endurance due to efficiency, response advantage at aborted landing and thrust reversal with less weight penalty. As a final point, turboprop engines may lead a drop of CO_2 and NO_X emissions with less fuel consumption and become a climate friendly solution.
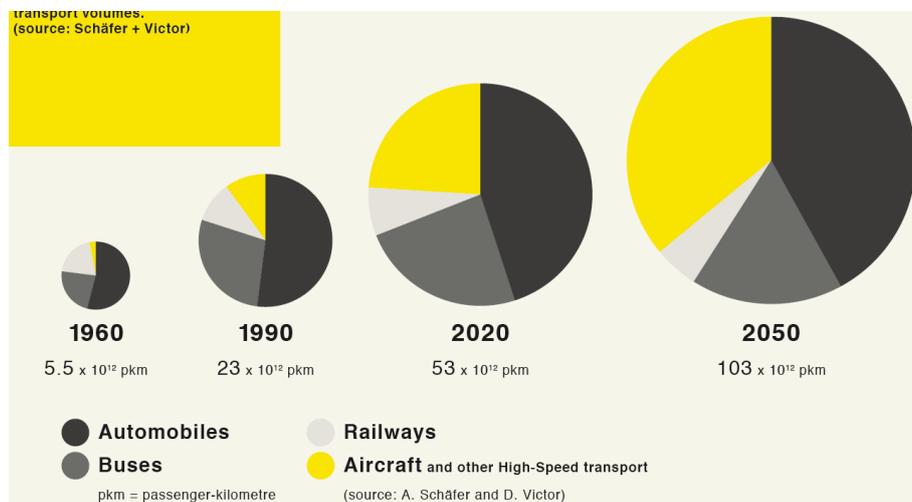
Figure 1: Historical and Expected Growth of Aircraft Transport [8]

On the other hand, the negative effects of conventional propeller engines start around M = 0.6. Air speed cannot be exceeded beyond a certain Mach number because of the compressibility/sonic behavior at the tip of the propeller blades. In history, the first significant progress for the compressibility effect was attained by Hamilton Standards in the 60s and 70s by changing the planform of the propeller blade to compensate shock/tip losses. Moreover, in the 80s counter rotating propellers were developed to decrease the swirl effects, which theoretically can increase the efficiency of the propulsion system by 8%. [9] Lower cruise speed automatically decreases specific fuel consumption, however this is not always an advantage for turboprops in both civil (increasing noise, less-frequent commute etc.) and military (losing speed advantage over foe, detectability) applications. In 2011, before acquired by GKN, Volvo Aero had made a multi-disciplinary feasibility study for a new STOL turboprop aircraft that would be expected to be in the market by 2020. [10] However, the parent company decided not the go further with the development.
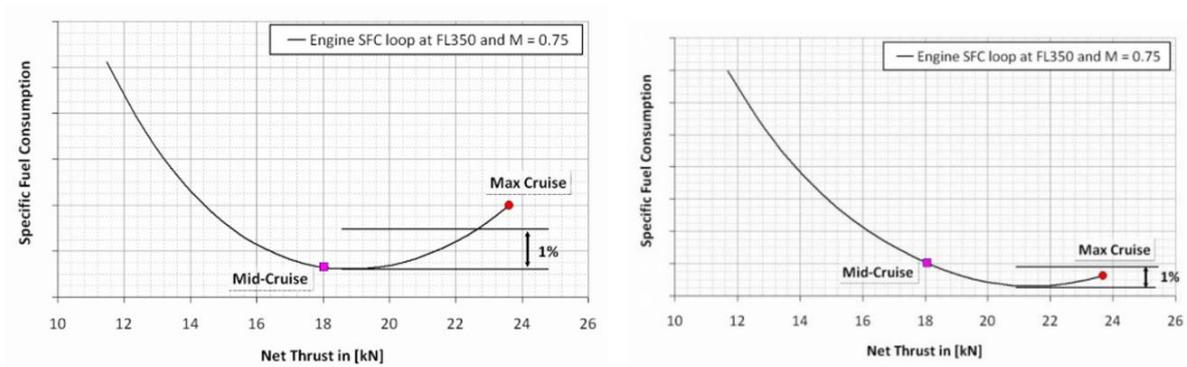
Figure 2: The Operation Range and Corresponding Change of Fuel Consumption for Turbofan (Left) and Turboprop (Right) Propulsion Systems (study made by Volvo Aero) [10]

EU Commission takes propeller research very seriously due to its potential positive environmental impact and funded many projects under FP6, FP7 and Horizon 2020 initiatives over the last 20 years. TU Delft was a pioneer in almost all decades of commercial propeller-driven aircraft research since the inception of Fokker. This thesis strives to continue the grand tradition that has been ongoing for a century.

1

INTRODUCTION & RESEARCH OBJECTIVES

The design and analysis process of propeller-driven aircrafts are dependent on the influence of the propeller slipstream of the flow. The forces and moments around the aircraft change drastically when a propeller is present compared to its absence. Moreover, the level of thrust produced by the propeller is also significant because the propeller slipstream has a potential to become the prime driver of the aerodynamic flow on the wetted surfaces of the aircraft. The solution for these problems are not solved using one method, but multiple disciplines. A multitude of solution methods are used together when the preceding method doesn't cover or accurately fulfill the required territory. Ultimately, aircraft manufacturers consult variety of solutions for an effect as complex as the propeller slipstream interference.

In the iterative design process, the architecture of the plane changes with the input from main influencers. The propeller slipstream changes the lift distribution on the wing unevenly, and lift is considered one of the main aerodynamic influencers for an aircraft configuration. With the use of empirical and numerical methods at the disposal of an engineer, it is his/her job to use these towards an accurate preliminary analysis of the desired solution.

1.1 Introduction

In conventional design of propeller-driven aircraft, the propellers stand right in front of the wing. The aerodynamic flow around individual parts are not just exclusive but also interfering. These components cannot be taken by their individual performance in the operation. One of the most prevalent interference effects is known as the propeller slipstream effect. [4] The wing section behind the propeller does not experience irrotational flow along the propeller downflow; in contrast, the vorticity causes a rotational non-uniform distribution along slipstream-wetted wing surface. [1]

The improvement on the slipstream effect (wing-propeller interference) can increase the propulsive efficiency in the preliminary design phase and improve the induced drag on the aerodynamic surfaces. [4] [5] [11] Moreover, in the further downstream, problems like instability at the tail, friction drag on the fuselage can also be ameliorated. [12] To improve the maneuverability and propulsive efficiency, an optimization has to be performed. [13] [14] The solution for this optimization is to use a non-prescribed vortex system, where the shape and the strength of the vortex is iteratively solved. [15] [16]

In both maritime and aeronautical flow research, the slipstream is defined as a high energy region where the axial and tangential velocities are induced by the propeller action. Even though there are two-dimensional models that further simplify the rotational nature, the circulation continues downstream with a varying radius. [17] [18] [2] In the case of vortices that are created by propellers, the experimental studies show that the flow is rotating while causing a non-uniform incoming flow. [19] [20] [21] Moreover, the slipstream is sheared at the onset flow when it encounters another lifting surface like wings. [4] The most common linear models assume that the vortices trailing the propeller have continuous geometry and strength. However, this also suggests that the vortex can transparently flow in and out of the solid body, which is not possible in the real world. There are two shortcomings of a linear approach: First, the local changes on the wing surface and the shape of the propeller slipstream is not taken into account. Accounting the local changes in the lift distribution along the wing gives a reliable correction for the lift coefficient compared to the unaccounted case. Second, the kinematic boundary conditions at the wing surface contradicts, in a linear system, particle carryover due to the vortex can penetrate inside the solid wing surface. [22] [23]

The interference effects are not only observed in the propeller wetted surfaces. It has been proven repeatedly that slipstream imposes various changes in lift and stability coefficients for a wide range of different aircraft configurations. [24] [14] [12] [25] Therefore, it is crucial to test a full aircraft model for a real comparison. Wind tunnel tests are the closest experimental scenarios, in which the real fluid flow can be simulated. With the right scaling of the flight conditions, the forces and moments imposed by the aircraft model can be observed in laboratory setting. There is a monetary cost and a physics cost for these experiments. The physics cost is known as the wall interference, where the bounded flow around the model is not similar to the free-flow conditions. [26]

Research centers like NLR, TU Delft, NASA, DNW and many others use on-line processing (computerized corrections) for primary corrections. [27] [28] [29] [30] The method for wall interference corrections usually derive from potential flow solutions and empirical data. [31] A combination of two is used to calculate the wall corrections in this research.

The wind tunnel corrections presented in the documents like Barlow, AGARDograph 109, AGARDograph 336 are all appropriate to lift generated by unpowered aircraft. [32] [26] [31] Propeller input contradicts the potential flow solution. It directly increases the momentum going over the wing. There is no way to add the circulation and induced dynamic pressure in the wake or in the lift interference corrections. The increasing lift along the wingspan should be "cleaned" for propeller slipstream before applying standard wind tunnel corrections.

There are two contemporary methods of thrust cleaning presented in this thesis. DNW uses the Eckert method, which has been proven useful for commercial tests like AIRBUS A400M. However, it doesn't account for the rotational nature of propeller slipstream. [27] Another correction can be found in the article by Patterson and German, where the lift increase in tip-mounted (multi)propellers is estimated to optimize the propeller performance. [33]

The main goal of this research is to introduce a model where both axial flow and rotational flow caused by the propeller slipstream is represented. Then, this model will be investigated to find if the wind tunnel correction is an improvement compared to other thrust cleaning corrections.

The propeller slipstream model proposed by this research is to create a non-linear system based on Li's panel method. [23] Li's method has been proven to show the change in

circulation and induced axial/tangential velocities behind the propeller flow field. [15] As a consequence, the lift distribution behind the propeller can be accurately simulated. A non-linear system will take into account the change in vorticity strength density. The objective of this non-linear system is to show the variance of the shape and strength of the vortex and further influence on the flow field behind the propeller plane. Before formulating the necessary equations, it is mandatory to have underlying assumptions to decrease CPU usage and calculation time. These assumptions should not be contradicting the major flow properties.

The wind tunnel model selected for experimentation is Fokker F27 model in the Low Turbulence Tunnel inside TU Delft. The setup for F27 is used in Experimental Simulations class by Prof. Georg Eitelberg. The balance and pressure measurements have become standard over the years. Therefore, the data is presumed to be precise and accurate for post-processing. The F27 test cases consist of propeller-off and on configurations with variation in thrust and angle-of-attack. One of the goals of using the wind tunnel experiment is to evaluate different thrust corrections under propeller slipstream.

1.2 Research Objectives
The research objectives were established in the literature study:

1) Improvement by accounting for the angular orientation of the incoming propeller flow.
2) Improvement by accounting for the angular momentum in the slipstream of the propeller flow.
3) Identification of the forces and moments on the aircraft.
4) Identification of standard wind tunnel correction methods and possibility of implementation of a new slipstream correction.
5) Improvement on evaluation of the slipstream interference in the on-line processing.

1.3 Research Questions
To achieve these goals, the following questions are constructed. These are intended to improve our understanding of propeller slipstream corrections.

Main Research Question: <u>Is there a method, which accounts for the rotation in the slipstream, that can improve the wind tunnel correction?</u>

Questions on background information and concepts:

- What is wall interference effect for closed wind tunnels? What kind of corrections are used for propeller driven aircraft inside the wind tunnel?
- What are the observed effects of propeller slipstream? How was it investigated in previous research?
- Which methods are the contemporary thrust (slipstream) cleaning methods? What are their strengths and shortcomings?

Questions on method and propeller-driven aircraft:

- Which solution method can accurately model the slipstream rotation in order to achieve a reliable correction?
- How is the flow solution formulated (assumptions, method, implementation) for propeller slipstream? Is there a way to verify the accuracy of the flow solver?
- What are the main aircraft components that directly influence overall aircraft lift?

- What is the influence of bodies (fuselage, nacelle) inside the close proximity of propeller slipstream area? Are they directly or indirectly altering the lift distribution?
- How important is the flow behind the trailing edge? Is the wing+propeller downwash effect the lift at the empennage?

Questions on experimentation and implementation:

- Which propeller driven aircraft is selected for experimentation? Are there sufficient data and reliable sources dedicated on the selected aircraft?
- What is the range of flow conditions achieved in the wind tunnel? Are there precautions that need to be considered to guarantee the reliability of the data for post-processing?

The first section of the questions address the correction and numerical tools to improve on the standard models. If the questions in the first section lead to a new design approach, then the models and numerical tools to predict slipstream has to be developed.

The second section of the questions are aimed to comprehend and implement a solution that are presented in this report. The diagnosis of the aerodynamic properties will accommodate quantifying the resolution for our first research target. Critical analysis of the concepts in the current approach is essential to identify insufficient and improvable solutions. Initially, the assumptions and the hypothesis has to evaluated. Also, the boundaries and the limitations with the current approach has to be identified.

The third section of the questions should bring reasoning to implemented solution methods and experiments.

1.4 Research Framework
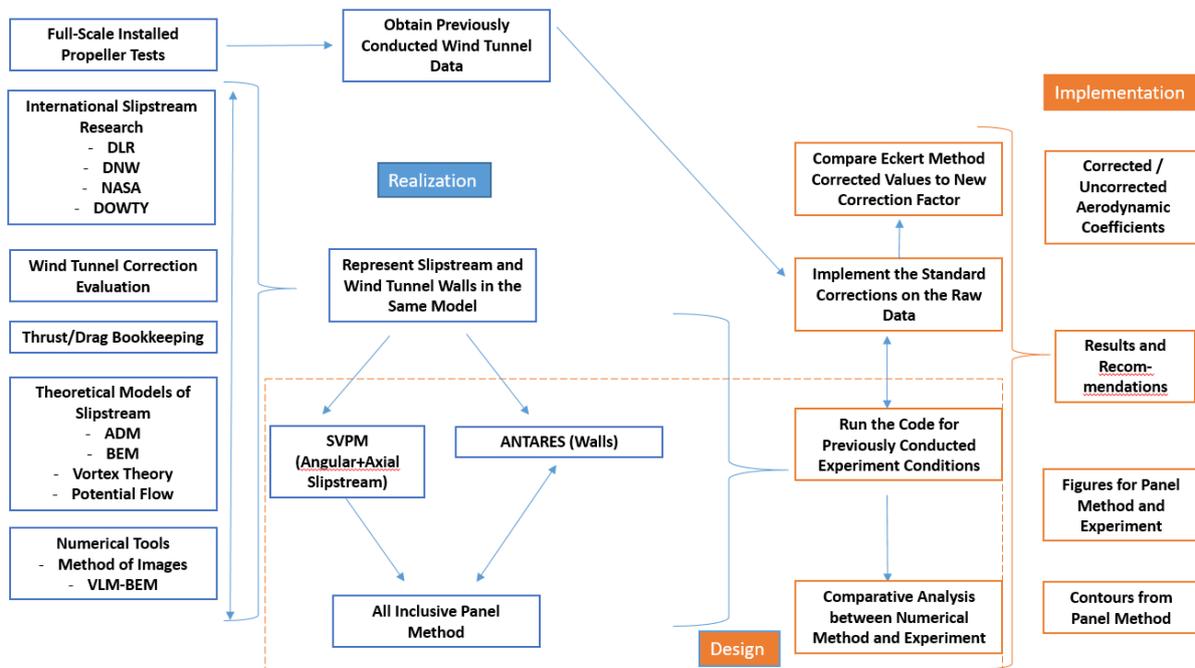
Figure 3: Research Framework Foreseen in Literature Study

I

FUNDAMENTAL CONCEPTS AND FOCUS OF RESEARCH

The first part presents the basic theory on propeller aircraft in wind tunnels. The standard correction techniques used in wind tunnels while testing a propeller-installed aircraft is introduced in Chapter 2. The propeller effect (slipstream) is investigated from previous research in Chapter 3. The contemporary correction techniques and new proposed slipstream correction technique is described in Chapter 4. Chapter 5 presents the aircraft and flow solver that will be utilized in the analysis.

2

PROPELLER AIRCRAFT EXPERIMENTS INSIDE CLOSED WALL WIND TUNNEL

The wind tunnel experimental setup has its roots since late 1800s. It is mostly based on the principle of hydrodynamics when it was first used for maritime experiments. [1] These experiments had included ship propellers in some shape or form, so it is safe to say that the propeller aircraft wind tunnel experiments are some of the oldest research in fluid dynamics. The objective of the wind tunnel is to simulate the airflow over a moving body in a controlled environment. The best way to ensure the real life versus controlled setup comparability comes from two important parameters. These are similarities and scaling. Similarities in flight tests are usually dependent on Reynolds and Mach numbers, while for propellers Strouhal number can be included if frequency is an important parameter (i.e. noise). [34] For more basic information on propeller modelling and testing refer to Appendix A-F.

There are various wind tunnel configurations used for different flow characteristics. For this research, subsonic/closed test section/closed return configuration will be discussed. Subsonic wind tunnels operate below $M < 0.3$ and they are usually used to test take-off and landing scenarios for commercial aircrafts. Closed test section means that model is surrounded by solid walls. This is the most common configuration for wind tunnel design test section. The main drawback is the unrealistic constraint of having solid walls around the aircraft, which can disturb the airflow boundary layer close to the wind tunnel walls. Moreover, it can cause a change in the mass flow rate due to the constrained area. However, it also keeps the high circulation/high lift flow in order so the advantage of data accuracy outweigh the disadvantages of post experiment corrections for aeronautical applications. Finally, closed return wind tunnels have a high initial cost of construction and maintenance but it ensures airflow quality and efficient energy use.
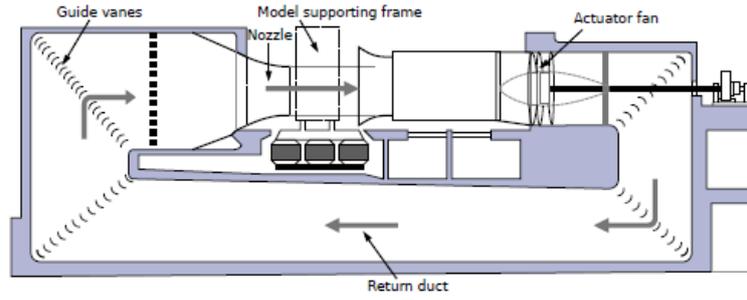
Figure 4: Closed Return Wind Tunnel Plan [34]

2.1 Potential Flow Approach in Wind Tunnel Tests

For closed wind tunnels, the majority of corrections are based on the existence of wall boundary interference. Compared to infinite upstream and downstream of air in real life conditions, wind tunnel conditions are limited by the geometry of the wind tunnel. There are a few assumptions made while calculating the wind tunnel wall corrections. [35] These are applicable to the classical corrections, however these assumptions might be wrong or incomplete depending on the experiment. First, the flow has a linear potential flow. Second, the wall boundary perturbs the airflow. Third, the model is relatively small compared to the wall distance and the wakes in the downstream extend straight through the tunnel. Fourth, the wind tunnel dimensions are constant in the height and width direction and doesn't change along the downstream line. As a result, the boundary condition on the walls is no flow normal or a constant pressure on the wall.

In incompressible flow, the wall boundary conditions can be expressed by the perturbation velocity potential ϕ of the closed wind tunnel. The simplified version for a closed wind tunnel is as follows:

$$\frac{\partial \phi}{\partial n} = 0$$

(2.3)

Where n is the normal to the wall of the wind tunnel. The total perturbation velocity is expressed as the sum of the potential by the wall interference boundary ϕ_w and the model potential in exposed to the free stream in the wind tunnel ϕ_m.

$$\phi = \phi_m + \phi_w$$

(2.4)

Because of the compressibility effects rising with increasing Mach number, the subsonic potential has to be corrected using Prandtl-Glauert compressibility coefficient. For the subsonic region, the potential equation is given by [36]:

$$\frac{\sqrt{(1 - M_\infty^2)}\partial^2 \phi}{\partial x^2} + \frac{\partial^2 \phi}{\partial y^2} + \frac{\partial^2 \phi}{\partial z^2} = 0$$

(2.5)

The coordinates are given in Cartesian coordinates where x denotes the flow direction. For a planar closed wall wind tunnel which extends far downstream the potential is denoted in $\phi(x, y, z)$. For the solution of uneven lift distribution along the propeller wetted wing span, the

method of images solution may be used to simulate the propeller. Depending on the propeller thrust, the propeller wake can be modeled as a point sink (powered condition) or point source (windmilling condition). The symmetry condition can be used to take advantage of to simplify the analysis and decouple the model interference from wake characteristics. Moreover, point wakes can be used to simulate lifting surfaces. The solution for extensive methods will be touched upon at further chapters.

Using a single singularity as a reference, symmetrical images can be used to satisfy the boundary condition given above Eq (2.3). If the derivative of potential to the wall is an odd function, an image of same magnitude and strength should be placed symmetrically at the other side of the wall. If the function is even (i.e. vortex), the potential is cancelled out by same magnitude and opposite strength.
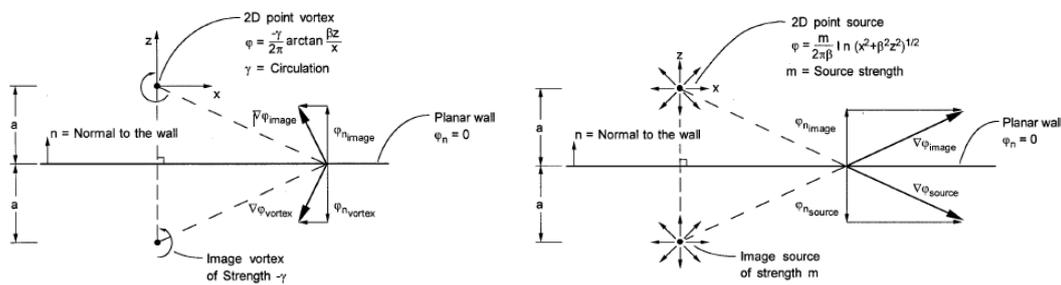
Figure 5: Mirror Images on 2D Plane for a Vortex (Left) and for a Source (right) [31]

The 2D simplified image representation is shown above. The reason for an image is to introduce a zero streamline at the solid boundary (walls). However, an additional image has to be used to counteract the first image at twice the distance, which violates parallel flow boundary condition. This process goes naturally to infinity; therefore, the number of images should be selected based on tolerance and computation power. When represented correctly, the dynamic pressure from pressure taps of the wind tunnel model matches the velocity perturbation by the potentials by solid bodies and wakes (represented as sources, doublets etc.).

For a 3D testing simulation, the images should be placed diagonally to represent walls in y, z direction. The images double as the summation of the potentials as well.
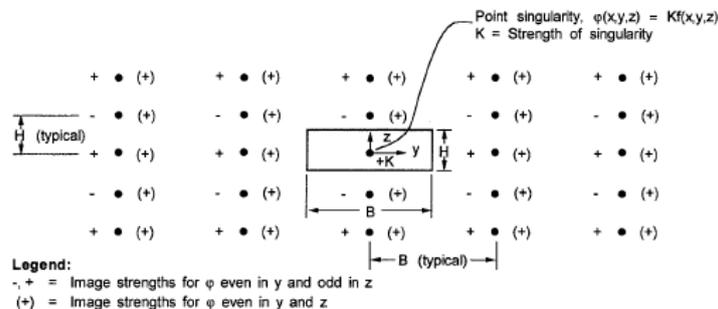
Figure 6: Example of System of Images for a Singularity [31]

Since the single singularity solutions have their limitations, a multiple-singularity and/or line-doublet solution may be used for extensive models. The blockage and interference corrections are based on these solutions at DNW and slipstream model requires a technique where the vortices caused by the lifting wing and blade element can be modeled in one superpositioned image system.

2.2 General Overview of Classical Corrections

There are three main effects that are directly related corrections for propeller-powered aircraft in a wind tunnel. These are blockage, lift interference and thrust effects. In essence, classical corrections are non-dimensionalized coefficients that are used to factor the unrealistic effects in a closed test section (usually alteration of the axial velocity vector). These unrealistic effects are the total factors of the difference between free stream flight and bounded flight conditions.

The most intuitive correction is called the blockage correction. The existence of solid bodies (and additional aerodynamic phenomena) inside a constrained volume causes a contraction of the cross-sectional area, where the flow is passing through. Therefore, by decreasing the area, the velocity of the flow is increased. If the blockage is caused by the existence of solid geometric bodies, then it is called a solid blockage. So solid blockage is mainly a function of volume, thickness of the model and cross-section of the wind tunnel. For solid blockage Herriot's empirical solid blockage value may be used. [32]

$$U_c = U_\infty(1 + \epsilon)$$

(2.6)

$$\epsilon_{sb} = \frac{K_1\tau_1 Vol_{wing} + K_3\tau_1 Vol_{fus}}{C^{\frac{3}{2}}}$$

(2.7)

The second type of blockage is called a wake blockage. Wake blockage is caused by the flow behind the model being slowed down compared to the free stream. Because of principle of continuity, this effect is enhanced to ensure the same mass flow. The acute difference between two speed regions create an unwanted wake, hence the wake blockage. The wake blockage has different solutions for separated and unseparated flow. However, because of the low Reynolds number and high thrust setting, the separation behavior is frequently encountered. Maskell's method of wake blockage correction is a standard method to account for the separated flow in the wake. [32] For the unseparated flow, the wake blockage formula is a direct relationship between uncorrected drag and induced drag. It can be written as:

$$\epsilon_{wb,us} = \frac{S}{4C}\left(C_{D,wing,uc} - \frac{C_L^2}{\pi A}\right)$$

(2.8)

Notice, how the wake blockage is dependent on the square of the lift coefficent. Maskell has added the effects of momentum outside of the wing wake.

$$\epsilon_{wb,s} = \frac{S}{4C}C_{D_0} + \frac{5S}{4C}(C_{D_{wing,uc}} - C_{D_i} - C_{D_0})$$

(2.9)

The final blockage is called the slipstream blockage and it is a result of the increased velocity vector behind the propeller. This effect is first corrected by Glauert but simple potential flow theory can be used for most applications. [18] The propeller defined as a sink at the propeller location gives comparable and robust results compared to the Glauert method. For windmilling (like wind turbines), no/negative thrust applications, Mikkelsen and Sorensen method also exists but the trade-off for the positive thrust case is not sufficient. [37] [28]

$$\epsilon_{pb} = -\frac{1}{4}\frac{S_p}{C}(T_C/\sqrt{1+T_c})$$
(2.10)
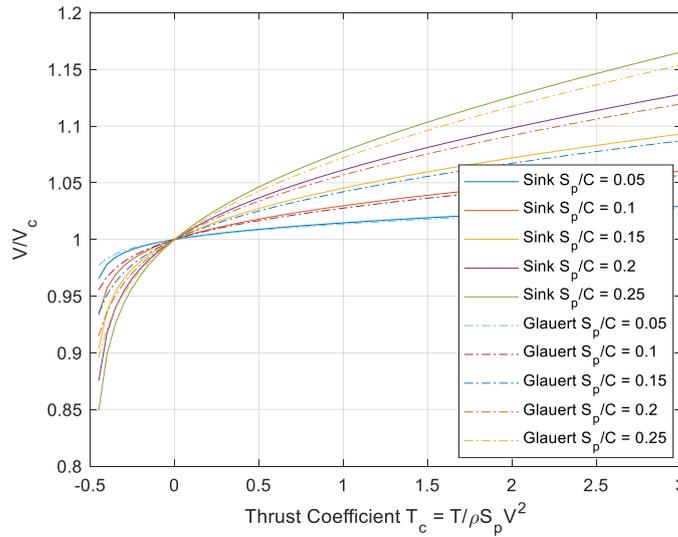
Figure 7: Comparison of Glauert and Sink Method for Slipstream Blockage

$$\epsilon = \epsilon_{sb} + \epsilon_{wb} + \epsilon_{pb}$$
(2.11)

Blockage is mainly a factor on the axial velocity; axial velocity is directly related to the dynamic pressure. As a result, the numbers where lift force is used are directly dependent on the axial velocity and blockage correction. Remarkably, the lift is not only effected by the axial velocity but also by the upwash (and circulation) effects due to the wind tunnel walls. The presence of the closed test section also effects the downwash behind the lifting bodies. In return, the upwash changes the effective angle of attack experienced by the lifting surfaces. The procedure to remedy this effect is called lift interference correction. Heyson's lift interference correction allows for a model configuration with a propeller. [31] [38] The equations below are a simplified version based on the empirical data gathered over the years. The change is directly a correction for the change in angle of attack.

$$\alpha = \alpha_{uc} + \Delta\alpha$$
(2.12)

$$\Delta\alpha = \delta\, C_{l,uc,w}\left(\frac{S_w}{C}\right)\frac{180}{\pi}$$
(2.13)

The same change can also be implemented for the tail. It only requires a downwash correction factor.

$$\Delta\alpha_{tail} = \delta\tau_2 C_{l,uc,w}\left(\frac{S_w}{C}\right)\frac{180}{\pi}$$

(2.14)

The formulas above are based on potential flow theory. Refer to AGARDograph 109 and 336 for more basis of these corrections. [26] [31] There exists a thrust correction addition to powered propeller aircraft, which is the prime focus of this research. This correction can be called thrust cleaning for the sake of further discussion on the subject. The thrust cleaning correction is directly dependent on the propeller slipstream effect. Propeller slipstream is a complicated topic with multiple implications on the lift distribution of the aircraft. Hence, a concise but exploratory treatment on propeller slipstream has to be undertaken. Next chapter focuses on propellers and its interference with the aircraft.

3

SLIPSTREAM PHENOMENON

Propellers generate thrust for the aircraft by increasing momentum in the airflow. [4] There are two major outcomes of the propeller-generated thrust, in other words, propeller slipstream. First outcome is the stability issues caused by the vortices and the swirl created by the rotation of the propeller, where the flow behind the propeller has significant helicoid behavior. This helicoid also interferes with the wetted aerodynamic bodies on it its way through the downstream. Therefore, depending on the location, the forces and moments favor one direction to another in the downstream. This causes directional, longitudinal, lateral instabilities over the aircraft and usually leads to significant losses. Contra-rotating propellers and swirl recovery vanes are some of the technologies that propose a solution to this problem. The second outcome of the propeller is the increase in kinetic energy and dynamic pressure over the lifting surfaces. The increase in dynamic pressure has upsides (i.e. short-take off) and downsides (i.e. increased drag).

3.1 Overview of Slipstream Effect

The propeller blade is a special type of wing that deflects the incoming stream to create resulting force in the desired direction by rotation in a co-axial circle. The deflection of the flow creates a vortex behind the propeller and is considered a loss in terms of stability disadvantage. The ongoing flow is not a homogenous flow and the streamlines are not parallel once it is in the propeller slipstream. The change in the local angle of attack alters pressure distribution on the wing. Corresponding lift, drag and moments along the span are also non-homogenous because of the change in local angle of attack. On the other hand, the presence of a wing also has an adverse effect on the propeller. The effect of the wing on the propeller can be presented as a change in incidence angle at non-zero angle of attack. Because the streamlines going through the propeller are directly influenced by the upwash of the wing. Each blade generates a different load depending on the position of the blade. Therefore, the up-going blade experiences relief by the increase in lift and dynamic pressure due to the presence of the wing. On the other hand, the heavy load shifts to the down-going blade, which experiences a larger load than the up-going blade.
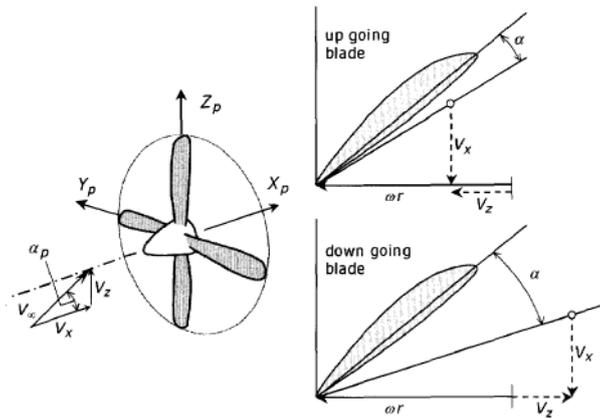
Figure 8: Change in Incoming Flow Angle for Propeller Blades [4]

Overall, propeller slipstream effect is the summation of all the aerodynamic effects that is observed as forces on the wing due to the swirl, axial velocity component and the pressure jump. The normal lift distribution on the wing and the induced velocities on the lifting surfaces are highly affected proportional to the thrust and advance ratio of the propeller. As a rule of thumb, the existence of a solid body always decreases the circulation experienced by the wing, unless if it was designed to do so. [39] [40] Without the kinetic energy that is introduced by the propeller, the blockage of the nacelle/propeller is expected to increase the lift throughout the span. However, this is not the case for propeller slipstream. The swirl of the slipstream creates a non-uniform pressure distribution over the wing because of the local angle of attack change; additionally, the axial velocity increases the dynamic pressure locally in the wetted lifting surface area. For the axial velocity, the distribution of the local lift and drag coefficients are axi-symmetrical. For the swirl velocity, the up-going blade introduces an increase in local angle of attack and the down-going blade induces decrease in the angle of attack. As a result, the overall lift increases, but the distribution of the local coefficients become anti-symmetrical. The slipstream dominates the shape of the lift coefficient because of the rotation of the flow.
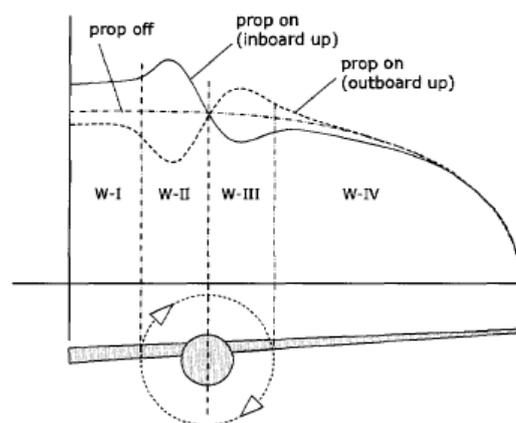
Figure 9: Lift Distribution under Propeller Slipstream [4]

3.2 Summary of Findings on Propeller Slipstream Effect

Fokker, NASA, DLR and TU Delft mostly conducted previous studies on the effects on propeller slipstream. In the design of Fokker 50, researchers had realized that the propeller created

dynamic instabilities depending on the thrust. [12] A numerical simulation was made to predict the effect of the slipstream, which they accurately predicted the low thrust case (high-speed) at cruise unlike the high thrust case (low speed) at lift-off. High thrust configuration showed that the slipstream not only creates superlift on the inboard part of the wing, but also the inboard down propeller had $\approx 80\%$ of the lift predicted by the numerical simulation. This was attributed to the "miscalculated upper section suction level." The interference with the fuselage also affected the slipstream behavior on the aircraft and created a large side-slip angle that had to be accounted for. It was concluded that the aerodynamic modelling of the installed propeller had to take into account the blockage from the fuselage depending on the rotation of the flow.
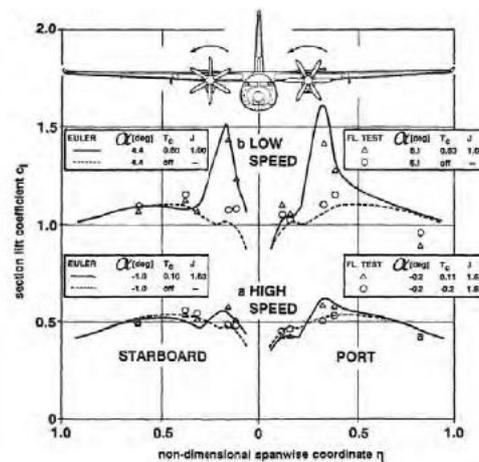
Figure 10: The Experimental and Computed Section Lift Distribution for Fokker 50 [12]

Figure 11 shows a study made by NASA for their turboprop design. [19] This experiment does not include the fuselage and it can be observed that the lift generated at the up-going blade is negated by the down-going blade. There is strong evidence that slipstream wing interference have opposite behavior in terms of local angle of attack and therefore the previous corrections for thrust related effects can be exaggerated along the overall span of the wing. The same case can be made for Figure 13. The section lift coefficient gain at the inboard and the loss of section lift coefficient in the outboard part of the wing have the same absolute change.
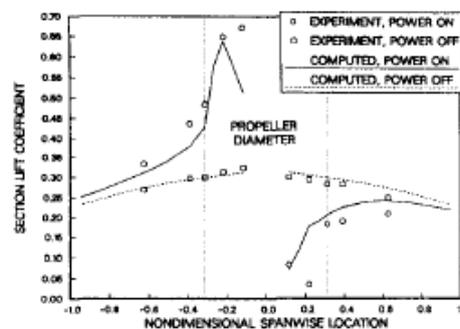
Fig. 5. Computed and Experimental Lift Distribution for Power on Conditions.
(J = 2.0, Alpha = 0 degrees, Mach = 0.5).

Figure 11: Computed and Experimental Lift Distribution for Tractor Propellers [19]

The thrust correction suggested by Takallu [41] and Li [11] suggest that the drag induced by the propeller is negligible after the thrust corrections are made. Li observes that the propeller induced drag only accounts for the 4% all induced drag.
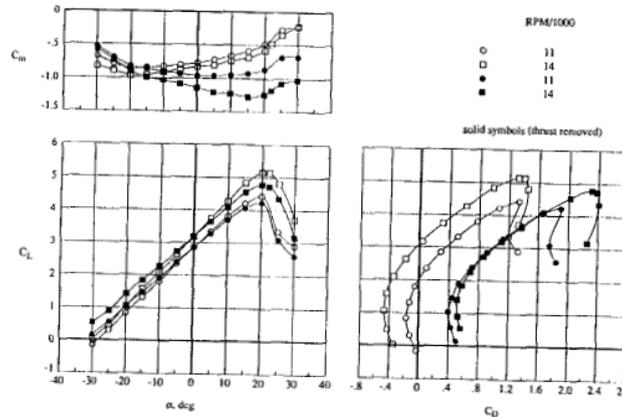
Fig. 6 Effect of Slipstream on Different Wing Configurations
q=15 psf, x/c=.6, z/c=.3, i_{nac}=0°, and 11,000 rpm

Figure 12: Thrust Removed Aerodynamic Coefficients for Propeller Installed Wing [41]
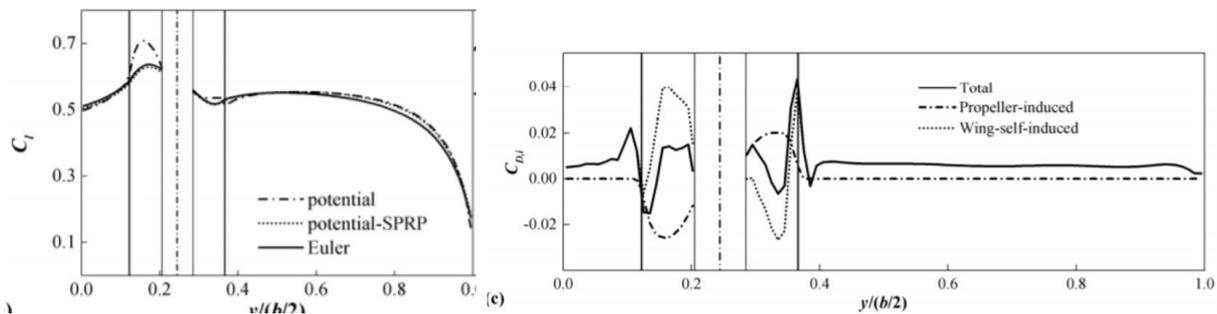
Figure 13: Lift Coefficient and Induced Drag for Potential and Euler Solutions [11]

The propeller slipstream can be visualized in the laboratory using Particle Image Velocimetry (PIV) technologies in the wind tunnel measurement. The additional advantage of visual methods is that the investigated phenomena can be observed real-time (unsteady). The change in angle of attack does not seem to be constant in the propeller downwash. The angle of attack changes continuously because of the vorticity caused by the propeller. Roosenboom [42] has conducted research on particle image velocimetry technique (PIV) at DLR, in which the flow behind the radius of the propeller blade is visualized in 43.000 instantaneous velocity vectors.

High swirl velocities usually dictate the velocity profile along the wing. [4] These changes are unsteady and methods like PIV can show the flow propagation at the propeller wake. The experiments compare the no thrust case with propeller-on and a thrust case where $c_T = 0.1$. The axial velocity component is as expected. The tip vortices do not change between thrust

and no-thrust cases. There is no significant separation due to slipstream. On the other hand, vorticity dominates the flow in the thrust case.
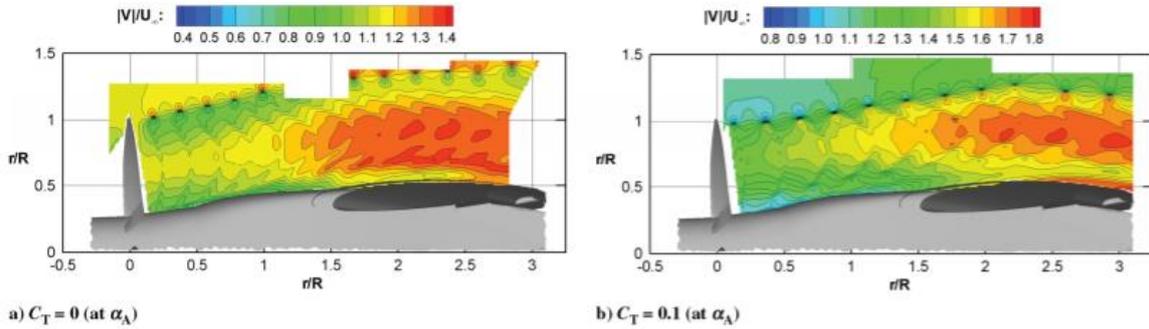
Figure 14: Magnitude of Instantaneous Velocities at the Slipstream for Different Thrust Cases [42]
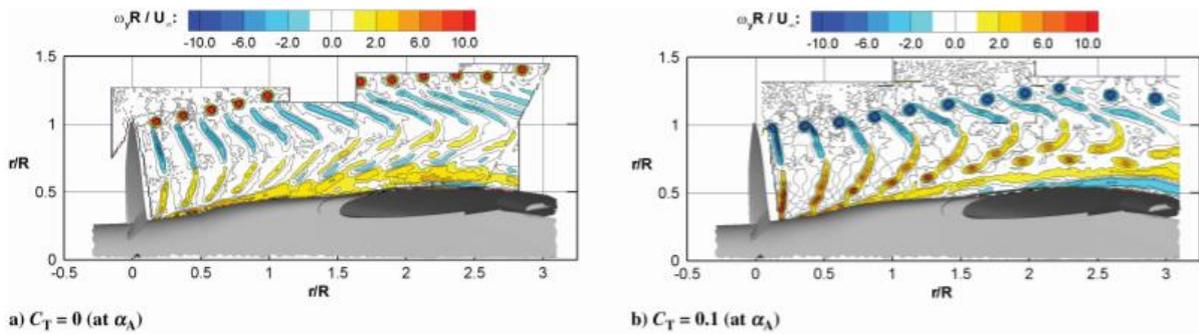
Figure 15: Vorticity Profile at the Slipstream for Different Thrust Cases [42]

The tip vortices in the no-thrust case follow along the boundary layer, however with the additional vorticity induced by the propeller rotation adds secondary vortices in the flow. The thrust case has very strong swirl at certain points of the helical flow. These are due to the higher effective angle of attack when the thrust is higher. The vertical component of the velocity w has strong gradients at the tip on both thrust cases. In contrast, the vorticity causes additional swirl along the blade radius in the trailing helicoid.
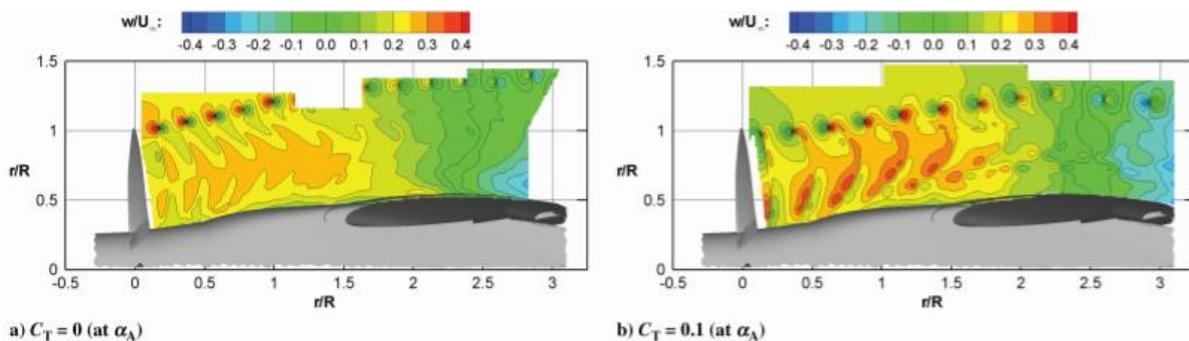
Figure 16: Vertical Velocity Component at the Slipstream for Different Thrust Cases [42]

The vortices cause a phase change between turbulent and laminar flow. This issue was first addressed by Howard et al. [25] as an intermittent change between laminar-to-turbulent then turbulent-to-laminar flow. Therefore, the boundary layer thickness is changing unsteadily with increasing thrust. Finally, it can be observed by the tip vortices that, the slipstream boundary can be traced with the tip vortices.

These visual representations investigated by PIV shows the three main points with slipstream:

- Slipstream is unsteady, unpredictable (laminar/turbulent) and three-dimensional.
- The majority of pressure distribution difference along the span is caused by the change in effective angle of attack.
- The irregular propagation of the flow along the chord displays the same irregular distribution pattern like the spanwise distribution.

As a final note, numerical slipstream modelling can range between a simple two-dimensional potential flow problem or it can extend all the way to a Direct Numerical Simulation (DNS). The first can be solved in a matter of seconds by an ordinary computer or the second may take multiple days on an advanced computer with multiple processors. There is a trade-off between these two extremes. In the ideal scenario, the slipstream shape and strength can be solved in a three-dimensional flow field without any prescribed parameters while satisfying all the boundary conditions.

Ultimately, the experiments presented in this chapter helped to deduct these final remarks:

1) Slipstream effect is well researched and documented. However, the complexity of the analysis is high and there is plenty of room for improvement.
2) Slipstream has two important effects on other solid bodies. First, the dynamic pressure increases with increasing propeller thrust. Second, the local angle of attack changes depending on the position and movement of the propeller blade.
3) The numerical analysis methods usually do not cover the whole thrust range. Separate or combination of methods have to be utilized to properly measure accurate results.
4) The wind tunnel experiments on slipstream already have methods to account for negative blockage and the increase in dynamic pressure on lifting surfaces. However, the change in local angle of attack is not included in these corrections.
5) The results for isolated propeller tests and wing/nacelle/propeller systems have drastically different results because of the interference effect between them. Therefore, an accurate representation cannot be made without accounting the wing and the nacelle in the analysis method.
6) The unusual nature of propeller flow is caused by the vortices that are created in the wake of the propeller. The vorticityl vector achieves a larger magnitude with increasing thrust. The resulting swirl may double or negate the effect of the induced axial velocity.

The contemporary methods for correcting the slipstream lift will be introduced in the next chapter.

4

THRUST CLEANING METHODS AND PROPOSED CORRECTION

The method for thrust cleaning was not included in the wind tunnel correction discussion in Chapter 2. Thrust cleaning is directly related to propeller slipstream and the core of this research. Without the background information on basic wind tunnel corrections and propeller interference, the ideas behind the current thrust cleaning methods and the new proposed method cannot be clearly justified.

A clarification has to be made on the propeller generated thrust before explaining the thrust cleaning corrections. The methods presented here are all developed for positive generated thrust, where the propeller thrust force is higher than the sum of aircraft drag forces. Windmilling and negative thrust conditions are not in the scope of this research. The thrust cleaning procedures explained in this chapter are based on tractor propellers where the wing is wetted by the propeller flow.

Unlike the most turbofan and turbojet engines, propeller aircraft directly increases the momentum going over the wing. Therefore, the lift coefficient changes drastically due to this special region, which was established as the propeller slipstream region. The lift coefficient due to the powered circulation from propeller input should not be contributing blockage and lift interference corrections because the corrections are overestimated. DNW has addressed this issue in the article by Eckert for wind tunnel corrections. [27] Another correction can be found in the article by Patterson and German, where the lift increase in tip-mounted (multi)propellers is estimated to optimize the propeller performance. [33]

4.1 Accounting Propeller Thrust in the Correction Method

There are two contemporary methods of thrust cleaning presented in this thesis. Before explaining in detail how each method works, it is critical to establish the main problem. The wind tunnel corrections presented in Chapter 2 and in the documents like Barlow, AGARDograph 109, AGARDograph 336 are all appropriate to lift generated by the wing and only the wing. [32] [26] [31] There is no way to add the circulation and induced dynamic pressure in the wake or lift interference corrections. The increasing lift along the wingspan should be cleaned for propeller thrust, thus the term thrust cleaning.

The correction factors are affected severely with the uncorrected slipstream effect. Likewise, the calculated drag is also subject to a major change.

$$\alpha \propto C_l, \qquad C_d \propto C_l^2 \qquad\qquad (4.15)$$

It can be observed from the relations above that the change in angle of attack and drag are directly proportional to the lift coefficient. [43] Drag increases with the square of C_l, so the error is much more drastic. Eckert has addressed this issue in his paper, in which he reported two times larger correction for the angle of attack and four times larger correction for the drag coefficient. [27]

The repercussions for overestimating the propeller lift behavior is also undesired for propeller optimization. Patterson and German have also developed a correction for their multi-rotor experimental aircraft. [33] Since the size and usage of propellers differ over different phases in the flight envelope, it is crucial to interpret the wing lift at different configurations.

The corrections and the assumptions behind those ideas with their potential shortcomings and advantages will be broken down starting with the Eckert method. [27] As explained, Eckert method has been developed because the thrust contribution and additional propeller forces need to be accounted before making other wall corrections. DNW investigated this effect for the AIRBUS A400M where the discrepancy in the lift coefficient between the propeller-on and off cases have been significantly different. Also, addition of the extra momentum in the system violates the wall corrections which are based on the potential flow theory.

Figure 17: AIRBUS A400M Model in Wind Tunnel (Left) [27]
Actual (Right) ©Wikimedia Commons

The advantage of the Eckert method lies in the usage of a simple thrust coefficient C_T value. This is a big advantage for the on-line systems because it is robust and requires little computational resource.

$$C_T = \frac{T}{S_p q_\infty} \qquad\qquad (4.16)$$

The values for the equation is very easy to acquire so it makes the implementation of the correction much easier. Eckert method also makes few assumptions before constructing the lift equation.

1) *The jet speed over the one-quarter chord has an overspeed ratio of 2*. This assumption comes from the actuator disk model. [39] According to Ting, this is an overestimation. [44] The lift generated inside a slipstream is less than what it would be if it was only the

under the effect of jet speed, which is what is assumed here inside the propeller diameter.

2) *The contraction of the slipstream is also not taken into account while it passes over the wing surface.* The slipstream contraction for an installed propeller with the nacelles is hard to predict, but it is far away from full slipstream contraction at this point. [4]

3) *A shape factor k has been designated to include the local angle of attack change behind the propeller. Shape factor k is derived from experimental data.* Therefore the swirl is not added in the derivation of the final formula, but it is also a correction to include the overall effect of local change of attack.

The lift equation is constructed as the addition of the lift from areas affected by slipstream and not affected by slipstream.
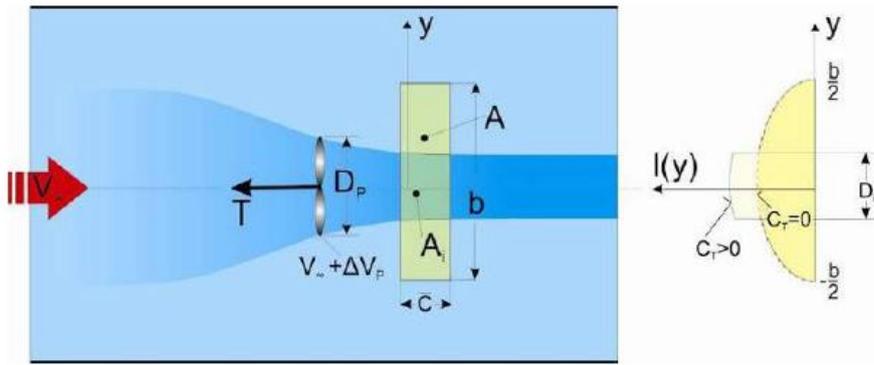
Figure 18: Single Propeller Effect on the Lift Distribution according to Eckert Method [27]

$$L = \int_{-b/2}^{b/2} c C_l q_\infty dy + \sum_{i=1}^{n} \int_{Y_i}^{Y_i+D_i} c_i C_{l,i}(q_i - q_\infty)dy \tag{4.17}$$

The subscript i symbolizes the specific propeller, while c_i is the thrust wetted wing chord and q_i is the dynamic pressure induced by the specific propeller. The values for thrust wetted geometry and velocity are also derived from the relation:

$$\Delta V_{c/4} = \left(\sqrt{1 + C_T} - 1\right)V_\infty \tag{4.18}$$

$$q_i = \left(1 + C_{T,i}\right)q_\infty, \qquad D_{i,c/4} = D_p\left(\frac{\left(\sqrt{1 + C_T} + 1\right)}{2\sqrt{1 + C_T}}\right)^{\frac{1}{2}}, \qquad A_i \approx A\frac{D_{i,c/4}\,c_i}{bc} \tag{4.19}$$

The lift coefficient C_L is defined as: $C_L = \frac{L}{q_\infty A}$ and the final solution can be achieved with the formula below:

$$C_{L,CT} = C_{L,CT=0}\left[1 + \sum_{i=1}^{n} \frac{A_i C_{l,i}}{C_{L,CT=0}}\left(\frac{q_i}{q_\infty} - 1\right)\right] \tag{4.20}$$

With addition of the swirl shape factor k and assuming that the lift coefficient is the same in the wetted section with and without thrust on the wing $C_{l,i} \approx C_{L,CT=0}$, final correction is achieved.

$$C_{L,CT,0} = \frac{C_{L,CT}}{1 + \frac{kD_p}{b}\sum_{i=1}^{n}\frac{c_i}{c}\left(\left(\frac{\sqrt{1+C_{T,i}}+1}{2\sqrt{1+C_{T,i}}}\right)^{\frac{1}{2}} C_{T,i}\right)} \tag{4.21}$$

The shape factor k is found to be 0.6 for AIRBUS A400M and Fokker F27. [27] [45] The largest shortcoming of the theory is that the lift is directly proportional to increase in dynamic pressure. From the previous chapter it was established that the change in axial velocity is only one part of the slipstream effect. The vorticity inside the slipstream tube should not be ignored. Furthermore, Eckert method depends on having an isolated measurement of the propeller (to correctly predict $C_{T,i}$), which is not possible to obtain for every experimental rig. Lastly, the shape factor k must be approximated from the experimental data, which assumes that the experimental set-up is close to perfect and there must be data from other experiments, which are akin for such deduction.

In Eckert correction, lift generated by a propeller-installed aircraft is directly proportional to the equivalent dynamic pressure q_e (a combination of induced dynamic pressure and free-stream dynamic pressure).

$$\frac{L_\infty}{q_\infty} = \frac{L_e}{q_e} \tag{4.22}$$

The second contemporary thrust cleaning correction is proposed by Patterson and German. [33] The propeller blade is reduced to a two-dimensional section, which is the basis of BEM theory. The blade airfoil is assumed to be thin and in incompressible flow. The airfoil flow properties are calculated in the propeller blade local coordinates, where the two velocities acting are free-stream velocity V_∞ and induced propeller velocity V_p. This correction was introduced to optimize the propeller installation angle, which changes the local geometric angle of attack of the propeller substantially.
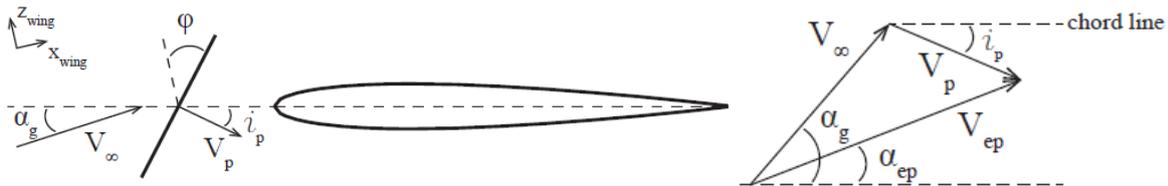
Figure 19: Diagram of the Propeller Incoming Flow in 2D Wing Airfoil Section [33]

The local geometric angle of attack is α_g and slipstream incoming angle i_p are defined instead of using propeller installation angle φ and wing angle of attack α.

$$\alpha_g = \alpha + \alpha_{twist}, \qquad i_p = \varphi - \alpha_{twist} \qquad (4.23)$$

The wing is modeled as a point vortex using Kutta-Joukowski where lift per unit span is defined as:

$$L' = \rho V \Gamma, \qquad where \qquad \Gamma = \pi c w_\infty \qquad (4.24)$$

The induced velocity by only the point vortex w_∞ (2D wing section) and with the addition of the propeller induced velocity w_{new}. is given in the figure below. More detailed discussion on Kutta-Joukowski lift and Vortex Lattice Method (three-dimensional flow) can be found in Appendix M.
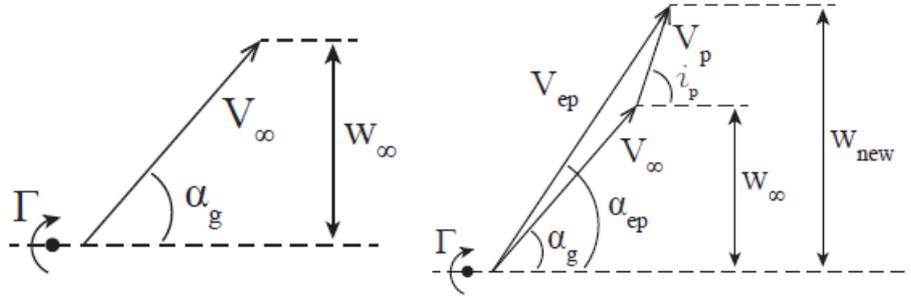
Figure 20: Velocity Diagram for a Single Wing (Left) and Wing+Propeller (Right) [33]

The propeller induced lift is defined as follows (V_{ep} is presented in the figure):

$$\Delta L' = \rho V_{ep} \Gamma_{new} - \rho V_\infty \Gamma_\infty \qquad (4.25)$$

There are important assumptions made to construct a three-dimensional lift correction in Patterson method, which needs to be investigated:

1) *The swirl is negligible or the effect of swirl cancels out due to symmetry.* This assumption might be an oversimplification of the swirl effect. Papers by Lenfers, Yang and Stokkermans suggest that symmetry in high lift applications is not always the case. [21] [46] [20]
2) *The slipstream velocity is assumed to be constant behind the propeller.* As suggested in Patterson and German's paper, the axial and radial velocity changes along the propeller blade. A more accurate solution would be using discreet points to signify the sections of the propeller blade. [47] [48]
3) *The wing is only subject to unseparated flow and far from stall angles.* Lenfers suggest that, for high lift application with flaps, separation may occur at unexpected angles of attack (where the lift curve is linear). [21] There is no clear source if separation occurs on wings without flaps (not including low Reynolds number effects, $Re < 0.2 \times 10^6$). [49] [29]
4) *Propellers are not located at the wing tips.* This assumption is valid for all conventional propeller aircraft where the propellers are located in the near vicinity of the fuselage.

Wing-tip propellers have distinct features that are not applicable to common actuator disk assumption. [5]
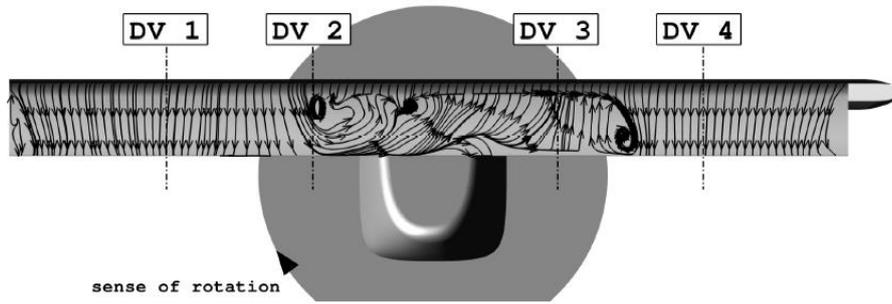
Figure 12. *full-thrust*, $v_\infty = 51.0\,\text{m/s}$, $c_\mu = c_{\mu,crit}, \alpha = 0.0°$

Figure 21: Separation Observed at the Upper Surface of the Wing with Flaps [21]

The wing is divided again into slipstream wetted section and unwetted section similarly to Eckert method. The change of lift along the wing span due to the propeller is summarized as:

$$\frac{\Delta C_L}{C_{L,\infty}} = \sum_{i=1}^{n} \left(\frac{\Delta L'}{L'_\infty}\right)_i \left(\frac{b_{wetted}}{b}\right)_i \qquad (4.26)$$

The final equation is derived from the velocity diagram with a correcting velocity multiplier β. The factor β was included in the derivation to simulate the finiteness of the slipstream diameter.

$$\frac{\Delta L'}{L'_\infty} = \left(1 - \frac{\beta V_p \sin(i_p)}{V_\infty \sin(\alpha_g)}\right) \frac{\sqrt{V_\infty^2 + 2V_\infty \beta V_p \cos(\alpha_g + i_p) + (\beta V_p)^2}}{V_\infty} - 1 \qquad (4.27)$$

The value for β is derived in a later paper where it can be deduced from the graph below:
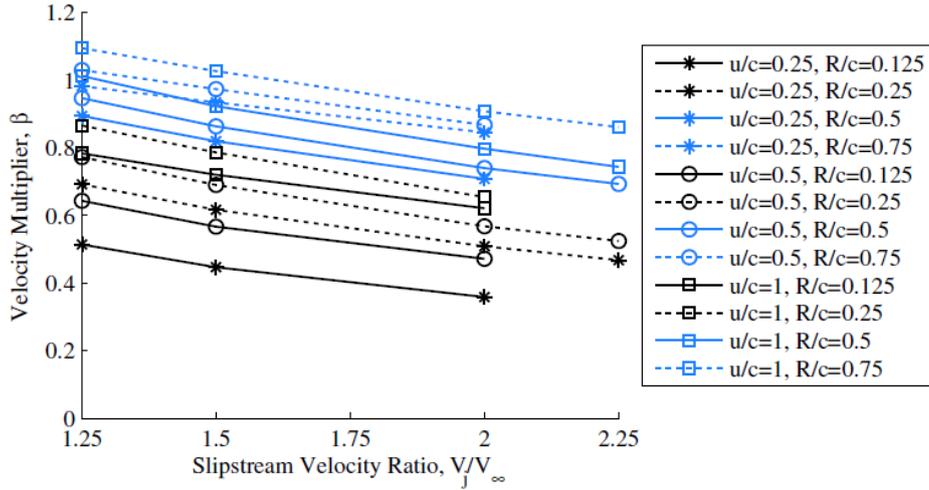
Figure 22: β Values for Various Propeller/Wing Configurations [50]

The value u/c in the figure above corresponds to the ratio between the propeller distance from leading edge u to chord length c. R/c corresponds to propeller radius R to chord length c ratio. The advantage of this correction method is that the propeller angle and slipstream geometry are both considered so a relative improvement for the local change of angle of attack exists. Moreover, it allows predicting the effect of a wide range of propeller installation angles.

Finally, the desired functions intended for a new lift correction method can be listed:

1) Increase in dynamic pressure (subsequently axial velocity) effect must be included.
2) Rotation of the flow should not be ignored. The incoming local angle of attack should be specifically calculated.
3) Both the slipstream shape and strength must be resolved to avoid overspeeding and incorrect/premature slipstream contraction.
4) The slipstream velocity is not constant and it should differ along the radial positions of the blade.
5) The influence of major aircraft components should be included in the analysis.
6) The geometry/dimensions of the aircraft should be appropriately represented in the solution.

The proposed correction method and later the flow solution method is created keeping these six criteria in mind.

4.2 Proposed Correction Method
The proposed correction method is inspired by both the Eckert method and Patterson method. The lift is defined similar to the Eckert method as:

$$L = \int_{-\frac{b}{2}}^{\frac{b}{2}} c C_l q \, dy$$

(4.28)

It is known that lift coefficient C_l is a function of α and the dynamic pressure q is a function of axial velocity.

$$C_l = f(\alpha), \qquad q = f(V) \tag{4.29}$$

The contribution of angle of attack comes from two sources. These are the wing angle of attack α and propeller induced angle of attack α_p. The dynamic pressure on the wing is mainly affected by three bodies. These are free-stream velocity V_∞, propeller induced velocity $V_{i,p}$ and fuselage induced velocity $V_{i,f}$.

$$C_l = f(\alpha, \alpha_p), \qquad q = f(V_\infty, V_{i,p}, V_{i,f}) \tag{4.30}$$

So the final equation becomes:

$$L = \int_{-\frac{b}{2}}^{\frac{b}{2}} cC_l\{f(\alpha, \alpha_p)\} q\{f(V_\infty, V_{i,p}, V_{i,f})\} dy \tag{4.31}$$

Moreover, since these are induced velocities, they can be separated by addition and subtraction. A vital distinction has to be made here. The induced velocities are modular in a handful of methods. Thus, the flow solver should be compatible with modular solution. Potential flow based solvers are usually compatible with modular solutions, so they can be implemented for this correction method. [51] [35]

The correction for the lift is the subtraction of slipstream related induced velocities and angle of attack

$$\Delta C_L = \frac{\Delta L}{q_\infty S_w} = \frac{1}{q_\infty S_w} \left[\int_{-\frac{b}{2}}^{\frac{b}{2}} cC_l\{f(\alpha, \alpha_p)\} q\{f(V_\infty, V_{i,p}, V_{i,f})\} dy - \int_{-\frac{b}{2}}^{\frac{b}{2}} cC_l\{f(\alpha)\} q\{f(V_\infty)\} dy \right] \tag{4.32}$$

The value for ΔC_L is recalculated for each flight condition.

5

SELECTION OF AIRCRAFT AND FLOW SOLVER

Pure potential flow solutions usually provide fast and practical solutions, however panel methods offer the opportunity to numerically calculate the slipstream with varying strength and shape. [16] [23] It enables a wider range of large-scale models to be implemented in a single solution. [52] Maybe the most important of them all is to be able to model the geometric shapes that cannot be defined by simple potential flow solutions. [53] [31] The flow and slipstream conditions can be varied between different location and planes. If desired, the trailing vortex flow field and empennage can be modeled in addition to other aircraft section. The shortcomings of panel methods also exists because the complexity and inputs in the system increase substantially. Using iterative methods and recursive relations can cause a computational overload for the computer processor. Moreover, for each setting/configuration/property the problem formulation needs to be changed (i.e. compressibility effects, varying sonic regions, altitude). There is no way to say a solution is correct without verification by comparable methods and/or experiments.

5.1 Reason for Selection of Panel Method as the Flow Solver

The panel method for slipstream in this research doesn't deviate much from the previous slipstream panel methods. [4] [16] [14] In the bounds of the boundary conditions, the potential at a certain location can be calculated by the total of all panel singularities. Since the computation power has increased exponentially in the last 50 years, the computational potential has also allowed for complex potentials. [31] For example, the fuselage upwash can be calculated by the method of Multhopp and the slipstream effect close the wing root can be calculated by Giesing solution. A finite wing can be represented by several horseshoe vortices in VLM. [43]

The three most important decisions for slipstream panel method design is:

i) Satisfying the unique simulation requirements by correct formulation of the problem (flight conditions, boundary conditions etc.).

ii) Collection of singularities to represent an accurate model of the test subject (in this case aircraft model).

iii) Deciding the amount and distribution of the slipstream panels, while linearly or non-linearly updating the shape and/or strength of the propeller slipstream.

Consequently, the SVPM panel method was selected for the following reasons.

1) The computation takes place in the low subsonic region.
2) All the necessary boundary conditions are included in the problem formulation.
3) Clear and complete procedure is available to public.
4) Propeller slipstream + wing lift can be calculated.in one model.
5) All of the derivations related to numeric calculations are given in the Li's report.
6) Panel shape and density are adjustable.
7) Computation is manageable by a cheap personal computer.

5.2 Aircraft Selection

The model aircraft chosen further into the research is Fokker F27 "Friendship". TU Delft has extensive research on the aircraft and owns a wind tunnel model at Low Turbulence Tunnel in Low Speed Laboratory. Fokker F27 is a commercial, high wing, two-prop aircraft with a conventional tail. Further examples and results presented in this paper will be based on F27 dimensions and parameters.
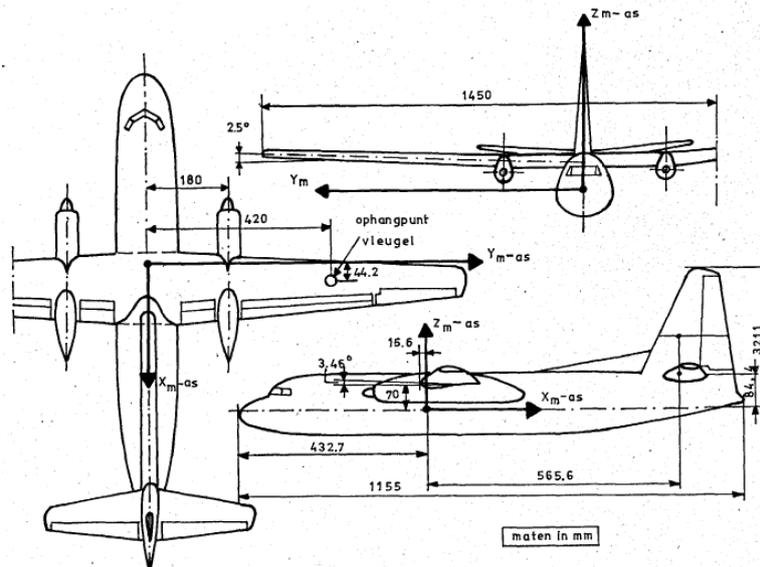
Figure 23: Dimensions of Fokker F27 1:20 Scale Model [54]

The propeller diameter D_p for the model is 183 mm and the number of propeller blades B is 4. The aircraft can be installed in two different aircraft configurations.

1) Wing-Fuselage-Nacelle-Vertical Tail
2) Wing-Fuselage-Nacelle-Vertical Tail-Horizontal Tail
3) Wing-Fuselage-Nacelle-Vertical Tail-Horizontal Tail-Propeller

These the wing configurations will be used with their acronyms: $WFNVH$, $WFNVHP$ respectively. $WFNV$ is used to show /fuselage/nacelle lift forces and may be used to show directional stability characteristics like side force and yaw moment. $WFNVH$ is used to measure the effect of horizontal tail on pitching moment and overall increase in lift. It is also used to get measurements for the "prop-off" condition so that it can be compared with the $WFNVHP$

configuration. $WFNVHP$ configuration is measured to see the effects on powered models. These are usually power, thrust and drag related. It should be acknowledged that the lift of the model is taken as a total, therefore it is not possible to measure the lift distribution along the span or the chord neither the propagation of the slipstream effect along the downstream. Nevertheless, it is crucial to be able to interpret propeller thrust and induced velocity vectors in order to correct for the thrust.
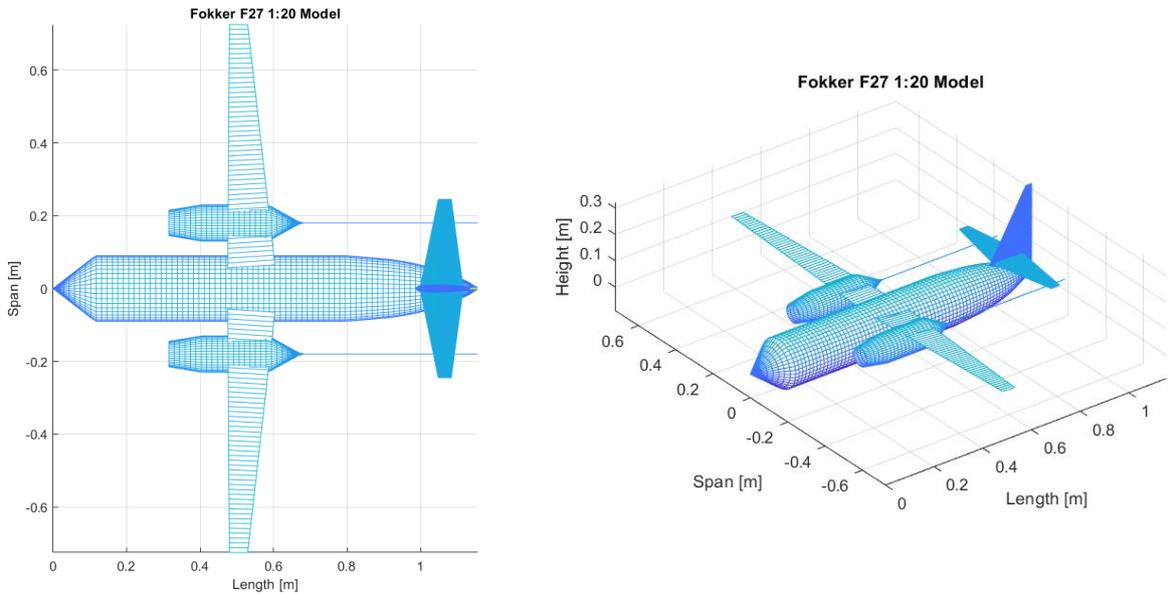
Figure 24: Fokker F27 Model Top View (Left) and Isometric View (Right)

To achieve a high accuracy of the test model, all of the major components (and their forces and moments) acting on the aircraft will be examined. These are: Propeller, wing, nacelle, fuselage and the empennage (vertical and horizontal tail).

II

METHOD AND FORMULATION OF PROPELLER AIRCRAFT

Assumptions, theory and implementation behind slipstream panel method are established in Chapter 6. The solution algorithm and performance of Surface Vorticity Panel Method (SVPM) are presented in Chapter 7. How to model each major aircraft component to find forces and moments exerted on to the aircraft is described in Chapter 8.

6

FORMULATION OF SLIPSTREAM PANEL METHOD

The root of the slipstream panel method lies in basic potential flow theory. [22] Hence, it is important to identify the assumptions, laws and boundary conditions in the formulation of the problem. This section is based on the method of Kerwin and Li. [22] [15] [23]

6.1 Assumptions

The problem is simplified using the assumptions stated below for different parts of the simulation components:

The propeller is modeled as a hub vortex and a propeller vortex sheet. The number of blades on the propeller can be selected. Instead of an unsteady or a time-averaged method, a steady method has been chosen. Because of the last assumption, time-dependent velocities or azimuthal velocities do not exist. In addition, the helicoid surrounding the slipstream is named as slipstream surface because the circulation is always in the boundary of slipstream. The slipstream surface divides the freestream with propeller-wetted stream. The wake behind the propeller is defined as a free vortex sheet. [15]

The wing is modeled after the lifting line model described by Katz and Plotkin. [35] The velocities induced on the wing is divided into different components and the vectors are added in its local reference frame to find the overall velocity.

The flow field is generally inviscid and incompressible for the potential flow theory; however, exceptions apply at important stations. For example, the propeller has constant circulation and the vorticity behind the propeller, which are modelled as two different kinds of vortices. The slipstream boundary (where the blade tip is tangent at the propeller plane) is modeled as a thin vortex sheet continuing far downstream. At the center, the effect of blade root is modeled as a vortex filament. These effects are defined as singularities, which will be explained further in the document.

6.2 Preparation of the Problem

There are two ways considered to solve the problem at hand. The first one is to iteratively solve the boundary conditions for different flow fields for different bodies until a convergence criteria is reached. The second method is to solve all the boundary conditions at once, however this creates too many unknowns and equations to be solved at once. Since it is not feasible to

solve very large non-linear algebraic equations that complies with all the boundary conditions at one go; the first method is chosen.

The iterative method uses a loop of recursive functions within an arbitrary flow field. The main bodies that affect the slipstream are separately considered. The alteration of the flow field starts with the application of the propeller related forces. In the second step, the effect of the wing on the altered flow field is considered. This loop is then repeated until a certain tolerance is achieved. With this approach, the boundary conditions imposed by multiple bodies will be reduced to one set of boundary conditions with the initial values are taken from the previous iteration. [13] [15]

One of the most crucial reasons to use an iterative method with independent bodies is to be able to formulate the problem as a potential flow calculation. The advantage of this approach is that the solid boundary and the wake boundary conditions can be solved in one integral equation. Other bodies are not needed to be considered at the rest of the flow field, which is faster and computationally cheaper. The disadvantage of this approach is that the interaction between different lifting bodies is not immediately solved. Therefore, it requires many iterations with well-defined convergence and/or tolerance criteria for an accurate solution.

The integral resulting by the boundary conditions is solved using a panel method, specifically Surface Vorticity Panel Method; in which the singularities from potential flow theory is assumed instead of the solid bodies and/or wakes. When the boundary conditions are satisfied, the strengths of the singularities can be known.

The Surface Vorticity Panel Method (SVPM) is a unique case of a panel method, where the propeller slipstream is defined as a vortex sheet, this assumption is also called surface vorticity singularity. For the wing, a Vortex Lattice Method (VLM) is used to determine the singularities on the wing.

6.3 Potential Flow Theory and Boundary Conditions

The propeller-wing interaction is defined as two different three-dimensional bodies in an infinite domain. This domain Ω is subject to a free-stream flow U_∞, and it is assumed that the wake of the lifting body results in a 2D-sheet. This is because the thickness of the wake is assumed to approach infinitesimally thin. Another assumption is that the outflow does not extend to infinity, but the effect is so small that the infinite domain Ω can be limited with a finite boundary S_∞, in which the downflow outside of S_∞ doesn't practically have an effect on the upflow. The inner boundaries inside the outer boundary S_∞ can be defined as the boundary of the solid body inside the domain S_B and the wake surface S_w. n is defined as a normal pointing out of the surface of the body. For an incompressible and irrotational fluid, the Laplace equation is simplified into:

$$\nabla^2\phi = 0 \tag{6.33}$$
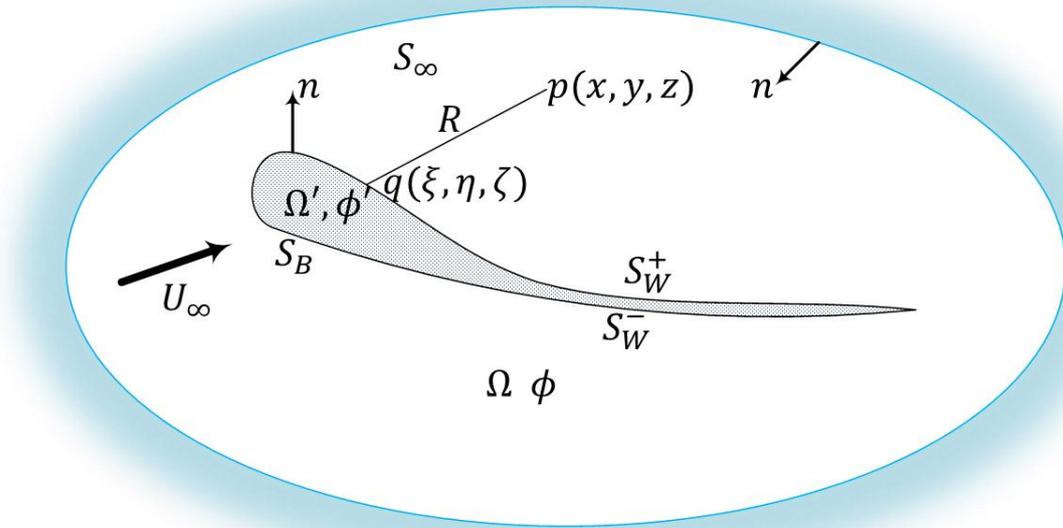
Figure 25: Notations Used in A General Body with Closed Domain [22]

The boundary conditions for the propeller system is defined as:

The trailing edge velocity (Kutta Condition) at the wing is not infinite, and can be represented by a number.

$$|\nabla \phi| < \infty \tag{6.34}$$

The kinematic boundary condition is satisfied on the solid body surface S_B:

$$\frac{\partial \phi}{\partial n} = -U_\infty . n \tag{6.35}$$

The circulation is conserved inside the flow. Kelvin's Circulation Theorem states: there exists no rate of change of a circulation around a closed curve involving same fluid elements.

$$\frac{D\Gamma}{Dt} = -\oint_C d\left(\frac{p}{\rho}\right) + \oint_C f . dl = 0 \tag{6.36}$$

One such system can be represented for an airfoil and a wake.

Figure 26: Airfoil Wake [35]

$$\frac{D\Gamma}{Dt} = \frac{1}{\Delta t}(\Gamma_{\text{airfoil}} + \Gamma_{wake}) = 0 \tag{6.37}$$

Parallel to circulation conservation, Helmholtz's vortex quantities complete the boundary conditions on rotational flow. These vortices consist of stream surfaces, tubes and lines in this paper.

1) A vortex filament has constant strength along its path.
2) The element that creates a vortex tube (i.e. propeller) forms a continuous vortex tube with constant strength where the streamtube is located.
3) The vortex quantities (filaments, surfaces, tubes) cannot end in the fluid domain. It has to extend at the boundary domain or to infinity.

The pressure and normal velocity jump at the wake S_W are zero.

$$p_{S_W} = 0 \qquad \text{and} \qquad \frac{\partial \phi}{\partial n_{S_W}} = 0 \tag{6.38}$$

Finally, the perturbation velocity approaches zero at the borders of S_∞

6.4 Integral Representation of the Flow Field

The equations governing the potential flow in the Ω domain and perturbation velocity ϕ can be formed as a Boundary Value Problem in integral form by including pseudo fluid domain Ω' and pseudo velocity potential ϕ' inside surface body S_B. The derivation is made by Kerwin and it is largely based on Lamb's work. [22] [55]

$$\begin{aligned} 4\pi\phi(p) = &\iint_{S_B} \left[(\phi(q) - \phi'(q)) \frac{\partial}{\partial n_q} \frac{1}{R(p;q)} - \left(\frac{\partial\phi(q)}{\partial n_q} - \frac{\partial\phi'(q)}{\partial n_q} \right) \frac{1}{R(p;q)} \right] dS \\ &+ \iint_{S_W} \Delta\phi(q) \frac{\partial}{\partial n_q} \frac{1}{R(p;q)} dS \end{aligned} \tag{6.39}$$

The expressions above are defined as following:

1) ϕ perturbation velocity potential in domain Ω
2) $p(x, y, z)$ induced potential is calculated at this point inside the flow field

3) $q(\xi, \eta, \zeta)$ singularity is defined at source point
4) ϕ' pseudo perturbation velocity potential in pseudo domain Ω'
5) $\dfrac{\partial}{\partial n_q}$ derivative of normal respective to source point q
6) $R(p; q)$ the distance between p and q

There are three distributions of strength in the velocity potential described above. There is a normal dipole distribution strength $\phi - \phi'$ and a source distribution strength $\frac{\partial \phi}{\partial n_q} - \frac{\partial \phi'}{\partial n_q}$ acting upon S_B, at the wake surface S_W a normal dipole distribution of strength $\Delta\phi = \phi^+ - \phi^-$ (defined as potential jump across the wake field) is acting. The velocity at any point p can be expressed as taking the gradient of velocity potential ϕ.

In the equation below, the strengths are defined as $\mu = \phi - \phi'$ and $\sigma = \frac{\partial \phi}{\partial n_q} - \frac{\partial \phi'}{\partial n_q}$, also the velocity vector at point p is defined as $v = \nabla\phi(p)$.

$$
\begin{aligned}
4\pi v &= 4\pi\nabla\phi(p) \\
&= \iint_{S_B}\left[(\mu(q))\nabla\left(\frac{\partial}{\partial n_q}\frac{1}{R(p;q)}\right)dS - \iint_{S_B}\sigma(q)\nabla\left(\frac{\partial}{\partial n_q}\left(-\frac{1}{R(p;q)}\right)\right)\right]dS \\
&\quad + \iint_{S_W}\Delta\phi(q)\,\nabla\left(\frac{\partial}{\partial n_q}\left(\frac{1}{R(p;q)}\right)\right)dS
\end{aligned}
\tag{6.40}
$$

Since ϕ' and Ω' do not physically exist inside S_B, to reduce the equation $\frac{\partial \phi}{\partial n_q} = \frac{\partial \phi'}{\partial n_q}$ can be chosen and the source distribution strength is eliminated because $\sigma = 0$. The equation can be reduced to:

$$
\begin{aligned}
4\pi v &= 4\pi\nabla\phi(p) \\
&= \iint_{S_B}\left[(\mu(q))\left(\frac{\partial}{\partial n_q}\frac{1}{R(p;q)}\right)dS\right] \\
&\quad + \iint_{S_W}\Delta\phi(q)\left(\frac{\partial}{\partial n_q}\left(\frac{1}{R(p;q)}\right)\right)dS
\end{aligned}
\tag{6.41}
$$

The surface vorticity panel method can be created by the relation that the velocity field induced by dipole distribution is equal to the surface vorticity distribution for the same surface. The vorticity strength density $\vec{\gamma}$ is defined as:

$$
\vec{\gamma} = \nabla\mu \times n = \nabla(\phi - \phi') \times n
\tag{6.42}
$$

After replacing vorticity strength density $\vec{\gamma}$, the equation becomes:

$$
4\pi v = 4\pi\nabla\phi(p) = \iint_{S_B}\left[\vec{\gamma}(q)\nabla\left(-\frac{1}{R}\right)dS\right] + \iint_{S_W}\vec{\gamma}(q) \times \nabla\left(-\frac{1}{R}\right)dS
\tag{6.43}
$$

Since the wake and body have the same expression (also $S = S_B + S_W$) the relation can be further reduced to:

$$4\pi v = \iint_S \vec{\gamma}(q) \times \nabla\left(-\frac{1}{R}\right) dS \tag{6.44}$$

It can be observed that the equation above is a form of the Biot-Savart's Law. This can be proven if the surface is reduced into a filament with l length and δ width where the circulation is defined as:

$$\Gamma = \vec{\gamma}\delta \tag{6.45}$$

Through this relation, Biot-Savart's law for a single vortex filament can be achieved:

$$v = -\frac{\Gamma}{4\pi} \int_l \frac{R \times dl}{|R|^3} \tag{6.46}$$

Remember that $\vec{\gamma}dS = \vec{\gamma}\delta dl = \vec{\Gamma}dl = \Gamma dl$ and R in the final equation is the distance between center and the calculated point on the integral of vortex filament length l.

The circulation Γ or the vorticity strength $\vec{\gamma}$ can be evaluated using the law of circulation conservation and the boundary conditions. Using the Biot-Savart's Law, the flowfield can be solved for in the domain Ω, once Γ or $\vec{\gamma}$ is known. The overall potential flow problem, requires forming a discrete set of equations, setting up the singularities and geometric properties of the bodies inside the flowfield.

6.5 Panel Creation and Global Coordinates

The coordinate system is set up with point O in the center of the reference plane. Coordinate system is in Cartesian for ease of use and the slipstream is assumed to be a cylindrical shape for panel setup. The cylinder extends in longitudinal x-direction and circumferential yz-plane. The cylindirical surface is sliced into $MP \times NP$ stations, where MP represents each division in x-direction and NP represents the sections of the circle in yz-plane. The length and shape of the slipstream is defined by the propeller and flight conditions. The number of elements can be determined by the user.

The corners of a single element can be defined as $Q_{1,2,3,4}$ in the three-dimensional Cartesian system. The trapezoidal elements with Q corners are enlisted as single elements. The position of the corner points are denoted as $\vec{Q}$ in the O-centered Cartesian reference system. The first investigation is done on the surface point, whether four of them create a trapezoid.

Define: $R_{12} = \overrightarrow{Q_1} - \overrightarrow{Q_2}$ and $R_{34} = \overrightarrow{Q_4} - \overrightarrow{Q_3}$ to see if vertices R_{12} and R_{34} are parallel to each other. The condition for parallel sides is:

$$R_{12} \times R_{34} = 0 \tag{6.47}$$

If the condition is satisfied, then the Q_j can be defined as the four vertices P_j of the panel. If the condition is not satisfied then the weighted average factor Y^* is calculated:

$$Y^* = \frac{R_{12} + R_{34}}{||R_{12} + R_{34}||} \tag{6.48}$$

Afterwards, the vectors R_{12} and R_{34} are re-adjusted with respect to their midpoints X_F and X_S to become parallel with the weighted average.

$$X_F = \frac{1}{2}(\overrightarrow{Q_1} + \overrightarrow{Q_2}) \tag{6.49}$$

$$X_S = \frac{1}{2}(\overrightarrow{Q_3} + \overrightarrow{Q_4}) \tag{6.50}$$
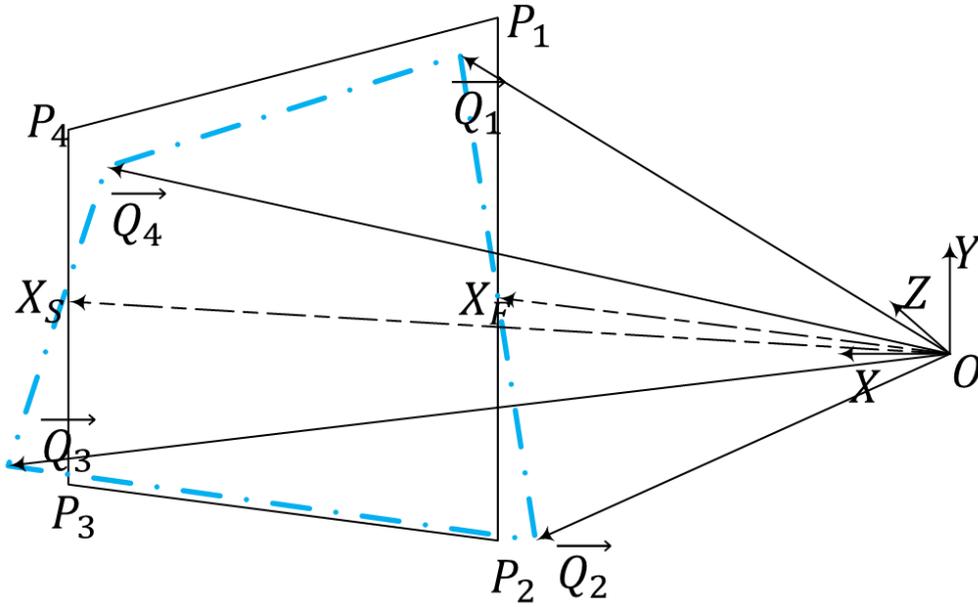
Figure 27: Definition of Corners and Vertices [15]

The four vertices P_j can be used as their rotated updated coordinates.

$$R_1 = \vec{P}1 = X_F + \frac{1}{2}||R_{21}||Y^* \quad R_3 = \vec{P}3 = X_S - \frac{1}{2}||R_{34}||Y^*$$

$$\tag{6.51}$$

$$R_2 = \vec{P}2 = X_F - \frac{1}{2}||R_{21}||Y^* \quad R_4 = \vec{P}4 = X_S + \frac{1}{2}||R_{34}||Y^*$$

This method is chosen to make sure that the parallel sides correspond to same midpoint and it has the same side length. As a result the updated side vectors are handled as:

$$R_{12} = R_2 - R_1 \quad R_{34} = R_4 - R_3 \tag{6.52}$$
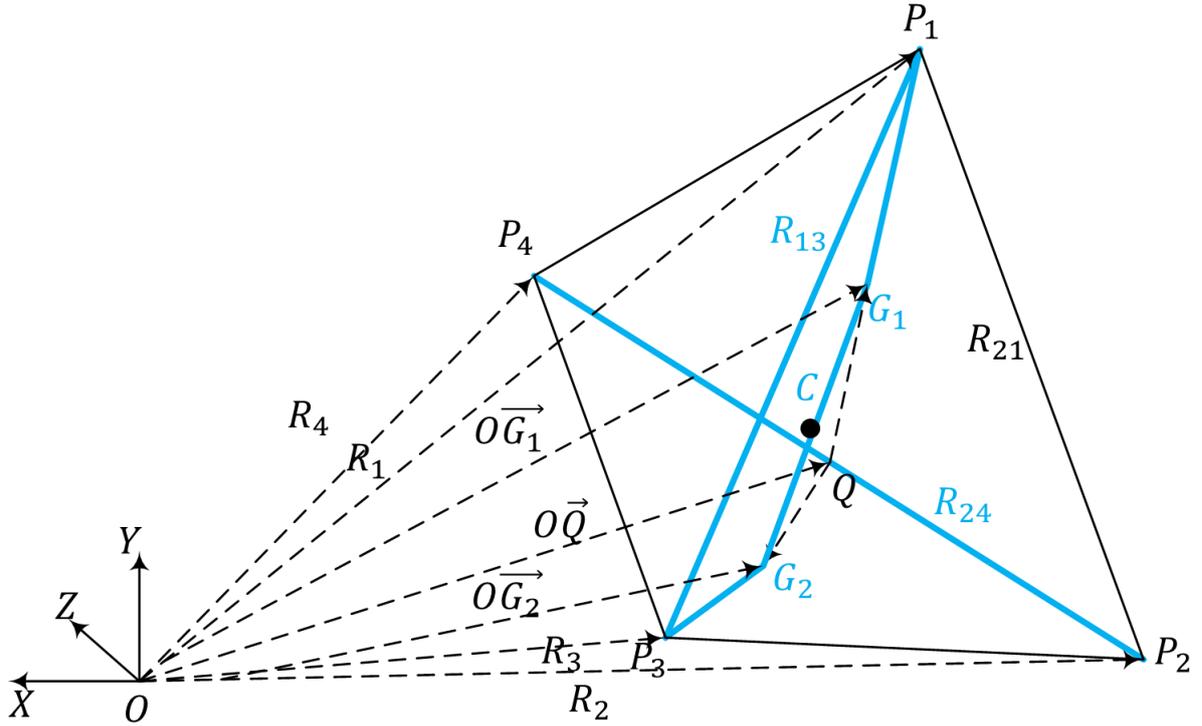
Figure 28: Location of Centroid [15]

The centroid is defined as the control point of the panel and the location of the centroid is $C(x_0, y_0, z_0)$. The centroids are determined by dividing the trapezoid into two triangles at location $\overrightarrow{G_1}$ and $\overrightarrow{G_2}$, which are the centroids for the two triangles. From Euclidian geometry, we know that the location of the centroids of the two triangles as:

$$\overrightarrow{G_1} = \frac{1}{2}(R_4 + R_2) + \frac{1}{3}\left(R_1 - \frac{1}{2}(R_4 + R_2)\right) = \frac{1}{3}(R_4 + R_2 + R_1) \tag{6.53}$$

$$\overrightarrow{G_2} = \frac{1}{2}(R_4 + R_2) + \frac{1}{3}\left(R_3 - \frac{1}{2}(R_4 + R_2)\right) = \frac{1}{3}(R_4 + R_2 + R_3) \tag{6.54}$$

Since the vertices of the triangles are also known, the total area for the trapezoid is:

$$S = \frac{1}{2}\left(||R_{24} \times R_{21}|| + ||R_{24} \times R_{23}||\right) \tag{6.55}$$

Now, the centroid can be finally achieved:

$$C(x_0, y_0, z_0) = \frac{||R_{24} \times R_{21}||(R_4 + R_2 + R_1) + ||R_{24} \times R_{23}||(R_4 + R_2 + R_3)}{6S} \tag{6.56}$$

Propeller Slipstream Correction for Wind Tunnel Applications

6.6 Local Coordinate System and Transformation between Coordinate Systems

The centroid $C(x_0, y_0, z_0)$ can be used as the new reference for the local coordinates (ξ, η, ζ). The unit vectors can be computed as follows:

- j_E is the normal out of the panel surface and defined by $R_{24} \times R_{13}$
- k_E is equal to the weighted average factor Y^*
- i_E is defined as $j_E \times k_E$

Creating a 3x3 linear system allows for a transformation between two coordinate systems:

$$i_E = a_{11}i + a_{12}j + a_{13}k$$
$$j_E = a_{21}i + a_{22}j + a_{23}k$$
$$k_E = a_{31}i + a_{32}j + a_{33}k$$
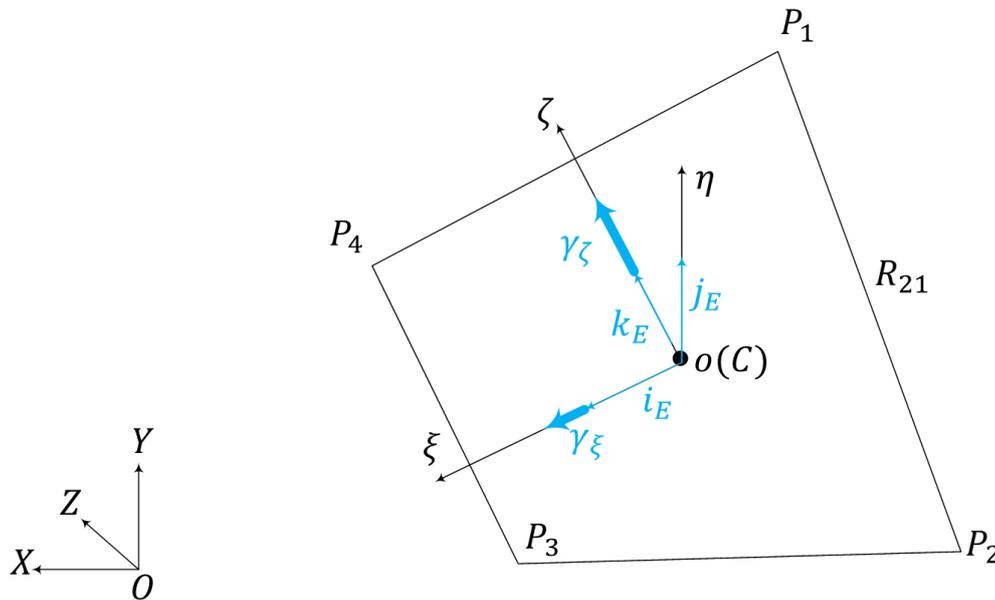
Figure 29: Local Coordinate System for a Panel [15]

It can also be shown as below where $\overline{\overline{a_{ij}}}$ is the transformation matrix.

$$\begin{bmatrix} i_E \\ j_E \\ k_E \end{bmatrix} = \overline{\overline{a_{ij}}} \begin{bmatrix} i \\ j \\ k \end{bmatrix} \tag{6.57}$$

Now define $r = r_o + r_E$, as a random distance from the global reference point O. The relation can be written as:

$$[x \ y \ z] \begin{bmatrix} i \\ j \\ k \end{bmatrix} = [x_0 \ y_0 \ z_0] \begin{bmatrix} i \\ j \\ k \end{bmatrix} + [\xi, \eta, \zeta] \begin{bmatrix} i_E \\ j_E \\ k_E \end{bmatrix} \tag{6.58}$$
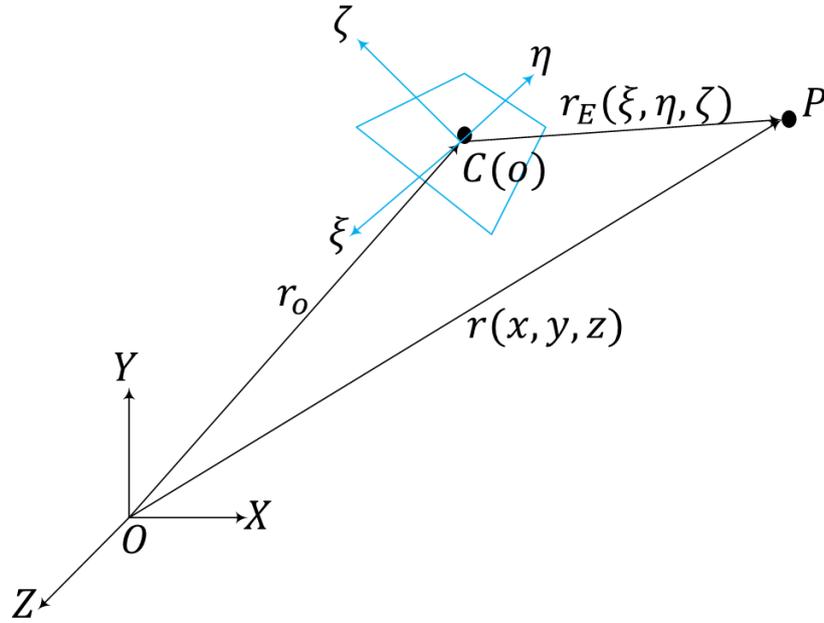
Figure 30: Distance from Local and Global Reference Points [15]

This relation can be reduced by the transformation matrix relation we found earlier:

$$[x\ y\ z] = [x_0\ y_0\ z_0] + [\xi, \eta, \zeta]\,\overline{\overline{a_{\iota J}}} \quad or \quad [\xi, \eta, \zeta] = [(x - x_0)\ (y - y_0)\ (z - z_0)]\,\overline{\overline{a_{\iota J}}}^{-1} \quad (6.59)$$

The global and local velocity vectors are straight forward for transformation:

$$[V_x\ V_y\ V_z] = [V_\xi\ V_\eta\ V_\zeta]\,\overline{\overline{a_{\iota J}}} \tag{6.60}$$

The correctness of the local transformation can be checked by recalculating the area of the trapezoid in the local coordinates. The location of P_j in (ξ, η, ζ) has to be correct, therefore recalculating the area:

$$S^* = \iint_{S_p} d\xi d\eta = \frac{1}{2}(\zeta_3 - \zeta_2)[(\zeta_1 + \zeta_4) - (\zeta_2 + \zeta_3)] \tag{6.61}$$

Propeller Slipstream Correction for Wind Tunnel Applications

7

CONFIGURATION OF SLIPSTREAM CONDITIONS IN SVPM

The slipstream for the case of propeller-only model and propeller-wing model are not regarded the same. The vorticity strength calculated for the propeller-only slipstream condition does not yield the same vortex sheet as the case with the wing. Therefore, the vorticity strength $\vec{\gamma}$ and the induced flow by the vortex sheet has to be recalculated to get an accurate propeller-wing interference. There are three ways to take into account strength density and propeller geometry:

a) Linear: The slipstream and the wing vortices have prescribed geometry and the shape is unaffected by the interaction between them.

b) Non-linear: The influence of the wing on the shape and strength of the slipstream is taken into account in the calculation.

c) Semi-nonlinear: The geometry of the slipstream shape is kept prescribed while the strength of the slipstream vortex system is influenced by the wing.

The method explained below strives to create a non-linear method, where both the strength and the shape of the slipstream is influenced by the wing

In order to establish the slipstream conditions, some assumptions have to be made. The fundamental assumption is that the propeller is steady and consists of infinite number of blades. The slipstream contraction has been taken into account, however it is impossible to have a full contraction of the slipstream on a propeller airplane over the wing and nacelle. Therefore, the inclusion of the contracted slipstream is dependent on the near bodies because the complexity of the slipstream radius variation is far too complex. [4]
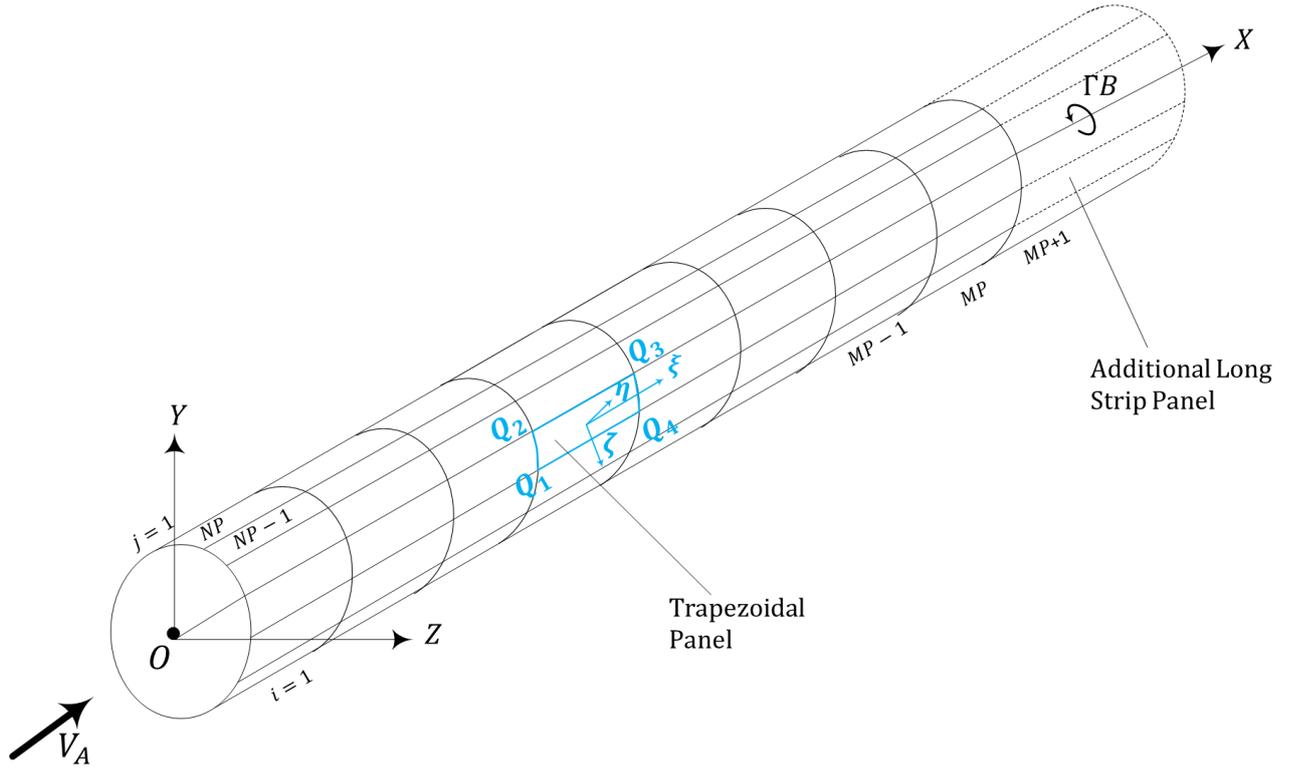
Figure 31: Slipstream Panel Representation with Mapping [15]

7.1 First Iteration

The first iteration of the computation could be calculated by knowing the advance ratio J, the advance velocity V_A, and hub vortex ΓN_b. This allows for the uniform inflow at the actuator disk to be computed to find constant vorticity strength density γ_0.

$$\gamma_0 = \gamma_{\xi_0} i_E + \gamma_{\zeta_0} k_E \tag{7.62}$$

The hub vortex filament in Biot-Savart law is similar to the presented earlier. It includes the effect of the number of blades on the propeller. It is the foundation of the concentrated vorticity at the center.

$$v = -\frac{\Gamma B}{4\pi} \int_l \frac{R \times dl}{|R|^3} \tag{7.63}$$

The vortex behind the propeller is separated into two parts using the local vector system. There are two main vortices. The first one is an infinite number of bound horseshoe vortices that simulates the circulation at the hub as bound vortices streamlining along the axial direction at the slipstream radius. This is denoted by constant strength density γ_ξ. The second is a semi-infinite slipstream tube with infinite ring vortices with strength γ_ζ along the circumferential direction.
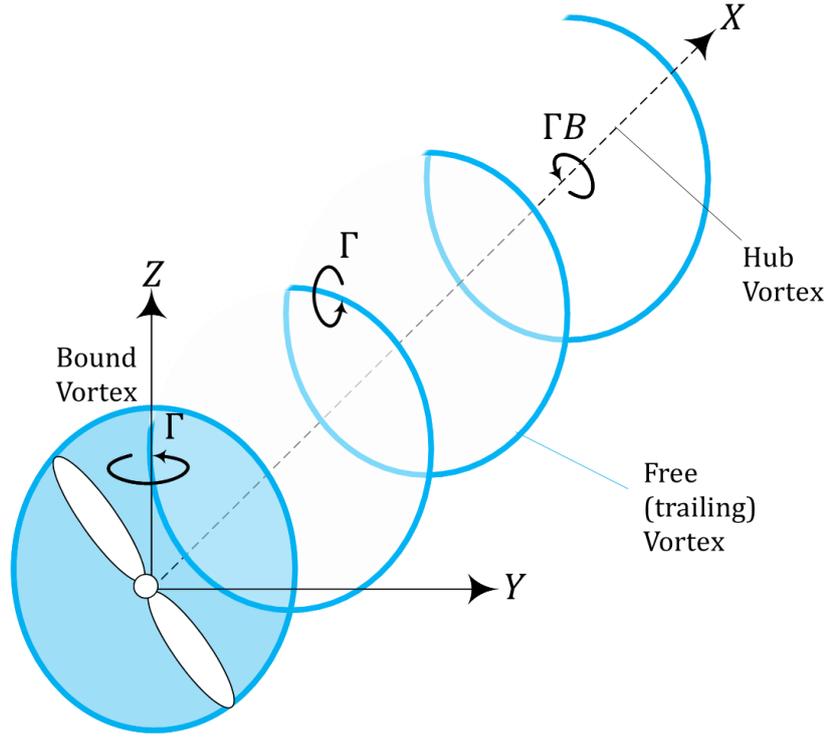
Figure 32: Definition of the Vortices in the Slipstream [15]

$$\gamma_{\xi_0} = \frac{\Gamma B}{2\pi R_s} \tag{7.64}$$

The slipstream radius is denoted as R_s,

$$\gamma_{\zeta_0} = -\frac{\Gamma B}{\Pi} \qquad \Pi = \frac{2R_p\pi\left[1 + \sqrt{1 + \frac{2\pi}{J}\left(\frac{\gamma_{\xi_0}}{V_\infty}\right) - \left(\frac{\gamma_{\xi_0}}{V_\infty}\right)^2}\right]}{\frac{2\pi}{J} - \left(\frac{\gamma_{\xi_0}}{V_\infty}\right)} \tag{7.65}$$

Finally for the initial conditions, the helical vortex sheet pitch Π is evaluated by the average velocity of neighboring outside and inside velocities. These numbers are directly related to local vorticity strengths γ_{ξ_0} and γ_{ζ_0}. The only step required to reach the solution for the initial conditions is the calculation of concentrated vorticity using the vortex theory.

In slipstream model, when incoming flow passes the propeller plane there is a rise in static pressure p_{static} and a jump in total pressure p_t. [4] The change between these pressures is attributed to the torque of the propeller. At the inflow, the total pressure is defined as p_{t_∞}.

$$p_{t_\infty} = p_\infty + \frac{1}{2}\rho V_\infty^2 = p + \frac{1}{2}\rho((V_\infty + v_a)^2 + v_t^2) \tag{7.66}$$

The axial and tangential velocities (v_a and v_t respectively) are both represented in the model. In the downflow, the components are denoted with an s subscript. The Bernoulli equilibrium in the downflow is:

$$p_{t_s} = p + \Delta p + \frac{1}{2}\rho\left((V_\infty + v_a)^2 + v_t^2\right) = p_s + \frac{1}{2}\rho\left(\left(V_\infty + v_{a_s}\right)^2 + v_{t_s}^2\right) \tag{7.67}$$

As a result:

$$p_{t_s} - p_{t\infty} = \Delta p + \frac{1}{2}\rho v_t^2 \tag{7.68}$$

So, the increase in total pressure is larger than change in static pressure Δp. There is a contribution by the increasing dynamic pressure by the tangential velocity component. Moreover, this relation can be extended to find the vortex strength.

$$\frac{1}{S_p}\iint_{S_p}\Delta p_t\,dS = \frac{1}{S_p}\iint_{S_p}\left(\Delta p + \frac{1}{2}\rho v_t^2\right)dS \tag{7.69}$$

It is known that, $T = \iint_{S_p}\Delta p\,dS$. Also to be able to differentiate the total pressure jump from the static pressure easily, the change will be called total head jump where: $\Delta p_t = \Delta H$.

$$\frac{1}{S_p}\iint_{S_p}\Delta H\,dS = \frac{T}{S_p} + \frac{1}{S_p}\iint_{S_p}\left(\frac{1}{2}\rho v_t^2\right) = \frac{T}{S_p} + \frac{2}{S_p}\iint_{S_p}(\Omega a' r)^2 dS \tag{7.70}$$

Finally, the vortex theory gives out the concentrated vorticity strength (hub vortex).

$$\Gamma B = \frac{2\pi}{\Omega\rho}\left(\frac{R_s}{R_p}\right)\Delta\bar{H} \tag{7.71}$$

Notice that this formula is also required to find initial conditions of the first iteration. $\Delta\bar{H}$ is the average of the pressure change in the integrals for ease of computation.

7.2 Velocity Induced by a Single Panel

The Biot-Savart law is used to find the induced velocity from a surface vorticity sheet. For a constant strength vorticity panel, there is a direct relation between a source of unit strength and constant strength vorticity for the same panel. This relation can be written as:

$$V_V = \frac{\vec{\gamma}}{4\pi}\times\iint_{S_p}\nabla\left(-\frac{1}{R}\right)dS = \frac{\vec{\gamma}}{4\pi}\times V_S \tag{7.72}$$

The vorticity panel velocity V_V and unit strength source velocity V_S can also be written in its orthogonal panel form for clarity:

$$V_V = V_V^\xi i_E + V_V^\eta j_E + V_V^\zeta k_E \tag{7.73}$$

$$V_S = V_S^\xi i_E + V_S^\eta j_E + V_S^\zeta k_E \tag{7.74}$$

The velocity due to source distribution (of panel S_p) is given by Johnson in the Appendix G. [53] After acquiring V_S, there are different ways to compute the velocity depending on the distance between centroid of panel C and field point $P(\xi, \eta, \zeta)$.

If the distance $\overline{PC}$ is greater than the selected criteria (i.e. $\frac{\overline{PC}}{t} > 11$) , then the Biot-Savart Law can be used instead of using exact velocity induced by the point vorticity, while not jeopardizing the accuracy of the solution. Then the formula becomes:

$$V_V = \frac{\vec{\gamma}}{4\pi} \times \iint_{S_p} \frac{\vec{\gamma} \times R}{||R||^3} dS = \frac{1}{4\pi} \frac{\vec{\gamma} \times R}{||R||^3} \Delta S \tag{7.75}$$

ΔS denotes the area of the source panel and $||R|| = \overline{PC} = \left\| \begin{bmatrix} \xi - \xi_p \\ \eta - \eta_p \\ \zeta - \zeta_p \end{bmatrix} \right\|$

There are also some cases where $\eta \to 0$ because point P can be in the same plane with the panel that needs to be evaluated. This usually causes singular results for the velocity found by the version of Biot-Savart Law that is introduced earlier. To ease the numerical difficuties when calculating the velocity factors, the Cauchy principle values are used. Therefore, if point P is located in the mean plane of the panel $\left(|\eta| \le \frac{\bar{R}}{2}\right)$, then:

$$V_V = \frac{\vec{\gamma}}{4\pi} \times V_S \quad where \quad V_S^\eta = 0 \tag{7.76}$$

Moreover, there are cases where the point P is located in the upper or lower surface of the panel $\left(|\eta| = \frac{\bar{R}}{2}\right)$:

$$V_V = \frac{\vec{\gamma}}{4\pi} \times V_S \quad where \quad V_S^\eta = \frac{\eta}{|\eta|} 2\pi \tag{7.77}$$

Finally, if none of the above conditions are valid, then the formula is directly used for the near field conditions.

$$V_V = \frac{\vec{\gamma}}{4\pi} \times V_S \tag{7.78}$$

7.3 Induced Velocity on the Propeller and Rankine Vortices

There are three main sources of velocities on the propeller. These can be summarized as: the free-stream flow, the vorticity effects and the self-induced slipstream velocity. The vorticity effect is taken separately by the wing and the hub of the propeller blade, so it can be further divided into two sections.

1. Free-stream flow: the complete system of panels is assumed to be exposed to free-stream flow. For each panel, it is defined in the local coordinate system that it corresponds to.
2. Vorticity-induced flow: the vortices in these system are modeled as Rankine vortices with a radius of r. The usage of Rankine vortices differ as follows:
   a. Wing-induced vorticity: the wing was modeled by the lifting line theory. Then the vortex strength distribution is found using Rankine vortices.
   b. Propeller hub vorticity: two semi-infinite Rankine vortex filaments are created for upper and lower slipstream sections. These vortices are have its core radius defined as the hub radius r_h. The location of the hub vortices are taken as the mean of the first and last panels of the slipstream section.
3. Slipstream induced flow: the slipstream surface induces velocity on itself. It is explained in the SVPM methodology.

The Biot-Savart law has a common numerical problem of singular results at certain situations. It is imperative to have another assumption to model the vortex filaments (which can result in singular answers) other than Cauchy principle assumptions for panel distance related calculations, The Rankine Vortex Model has a core tube with vorticity $\vec{\omega}$, in which the radius r_ε is infinitesimally small. For the numerical model it is assumed to be a very small finite constant otherwise the collocation points near to the vortex can cause in infinite results. The Rankine vortex is only valid in the core region, where Biot-Savart Law causes singular answers.
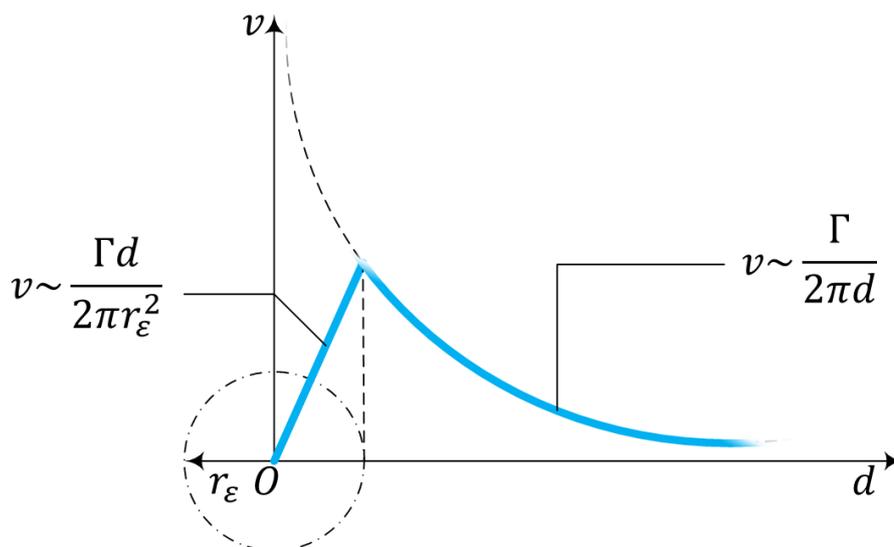
Figure 33: Induced Velocity by Rankine Vortex with Varying Distance [15]

For a 2D model, the Rankine vortex model can be divided into two areas. Inside the core region, vortex induced tangential velocity is proportional to distance d. The velocity inside the

Propeller Slipstream Correction for Wind Tunnel Applications   Ekin Orer

core region rises linearly; while outside the core region, there is non-linear drop with increasing distance.

$$
v = \begin{cases}
\dfrac{\Gamma d}{2\pi r_\varepsilon^2}, & d \leq r_\varepsilon \\[2ex]
\dfrac{\Gamma}{2\pi d}, & d > r_\varepsilon
\end{cases}
\tag{7.79}
$$

It can be seen that without a Rankine condition, the value for v is infinitely large corresponding an infinitesimal distance of d. For a straight vortex element AB and evaluation point P the velocity due to the vortex element can be written as:

$$
v_{AB} = \begin{cases}
\dfrac{\Gamma d}{2\pi r_\varepsilon^2}(\cos(\phi_1) - \cos(\phi_2)), & d \leq r_\varepsilon \\[2ex]
\dfrac{\Gamma}{2\pi d}(\cos(\phi_1) - \cos(\phi_2)), & d > r_\varepsilon
\end{cases}
\tag{7.80}
$$

Where ϕ ($0 \leq \phi \leq \pi$) is defined as the angle between r (the vector distance between the center of element vortex filament dl and point P) and vortex filament dl. The function uses limiting core radius r_ε. Instead of the reciprocal relationship $v \sim \frac{1}{d}$, the linear distribution inside the vortex is used.
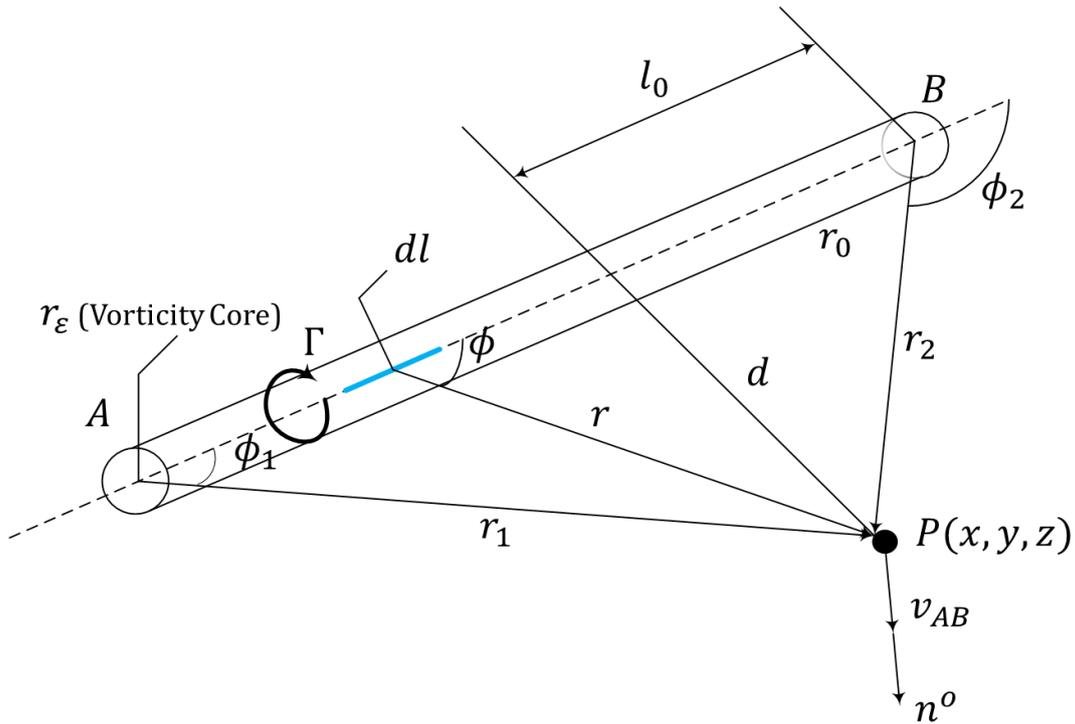
Figure 34: Vortex Filament Geometry [15]

The magnitude of the v_{AB} can be found by the various ways to compute d, $\cos(\phi_1)$, $\cos(\phi_2)$:

$$d = \frac{||\vec{r_1} \times \vec{r_2}||}{||\vec{r_0}||} = \frac{||\vec{r_0} \times \vec{r_1}||}{||\vec{r_0}||} = \frac{||\vec{r_0} \times \vec{r_2}||}{||\vec{r_0}||} \tag{7.81}$$

$$\begin{cases} \cos(\phi_1) = \dfrac{\vec{r_0} * \vec{r_1}}{||\vec{r_0}|| ||\vec{r_1}||} \\ \cos(\phi_2) = \dfrac{\vec{r_0} * \vec{r_2}}{||\vec{r_0}|| ||\vec{r_2}||} \end{cases} \tag{7.82}$$

The length vectors $\vec{r_0}$, $\vec{r_1}$, $\vec{r_2}$ are lengths AB, AP, BP respectively. Finally the vector can be computed by the inclusion of the direction vector $\vec{n}^o$.

$$\vec{n}^o = \frac{\vec{r_1} \times \vec{r_2}}{||\vec{r_1} \times \vec{r_2}||} = \frac{\vec{r_0} \times \vec{r_1}}{||\vec{r_0} \times \vec{r_1}||} = \frac{\vec{r_0} \times \vec{r_2}}{||\vec{r_0} \times \vec{r_2}||} \tag{7.83}$$

$$\vec{v}_{AB} = v_{AB}\vec{n}^o \tag{7.84}$$

7.4 Boundary Conditions at Slipstream Surface

There are two boundary conditions on the slipstream surface. The first one is the kinematic boundary condition: the normal velocity jump at the surface is zero at the slipstream wake, plus the normal velocities are also zero. This was addressed on Chapter 3 as: $\frac{\partial \phi}{\partial n}_{S_W} = 0$. Furthermore, the average velocity between inside and outside slipstream surface has a zero normal velocity.

$$V_m . n = 0 \tag{7.85}$$

It means that the transporting speed of vorticity in the normal direction is always zero. For prescribed slipstream shapes, this condition is not always satisfied numerically; so very small tolerance numbers can be used instead.

The second boundary condition on the slipstream boundary is that the pressure jump across wake boundary is 0. Both the first and second boundary conditions are tested for every control point and $\vec{\gamma}$.

7.5 Fundamental Equations Governing Vortices on the Slipstream Surface

It was explained in the previous chapters that when the strength of the vortex and shape of the slipstream is known, the SVPM code can solve for the induced velocity behind the propeller. The vorticity is carried within the free vortex sheet, which separates the flow inside and outside of the free vortex sheet. These two different zones have different potentials. Normally, inside the slipstream, the induced velocity is carried by the local mean velocity however when it passes through the wing, the flow is disturbed. The disturbance is assumed to be steady in the global coordinate system and the vorticity changes while passing the wing surface. Therefore, there are some fundamental laws that includes vorticity to determine the alteration process.

The first equation is the Bernoulli equation, giving a relation in total pressure. The second equation is the continuity equation of vorticity, which is used to define the vorticity field.

The second equation, that needs to be solved for is the continuity equation of vorticity, where vorticity $\vec{\omega}$ is defined by:

$$\vec{\omega} = \nabla \times V \tag{7.86}$$

The divergent of the vorticity is 0, which means the vorticity is inside the slipstream tube boundary just like the velocity vector.

$$\nabla . \vec{\omega} = 0 \tag{7.87}$$

If it is assumed that a constant very small thickness ($0 < \varepsilon \ll 1$) for the vortex sheet thickness. By the definition of the vorticity strength density inside a vortex sheet:

$$\vec{\gamma} = \varepsilon \vec{\omega} \tag{7.88}$$

The continuity equation can be written in terms of $\vec{\gamma}$ in the local coordinate system. Therefore:

$$\nabla . \vec{\gamma} = 0, \qquad \frac{\partial \gamma_\xi}{\partial \xi} + \frac{\partial \gamma_\zeta}{\partial \zeta} = 0 \tag{7.89}$$

Bernoulli Equation was used to obtain an initial circulation for the first iteration. It will be also used to find the γ_ζ using the zero-jump condition at the slipstream boundary. Assume two points A and B, where the first one is located at the inflow and the second one is located at the outflow of the propeller on the slipstream boundary. There are also categorization between the in and out of the boundary locations, $-$ and $+$ respectively.
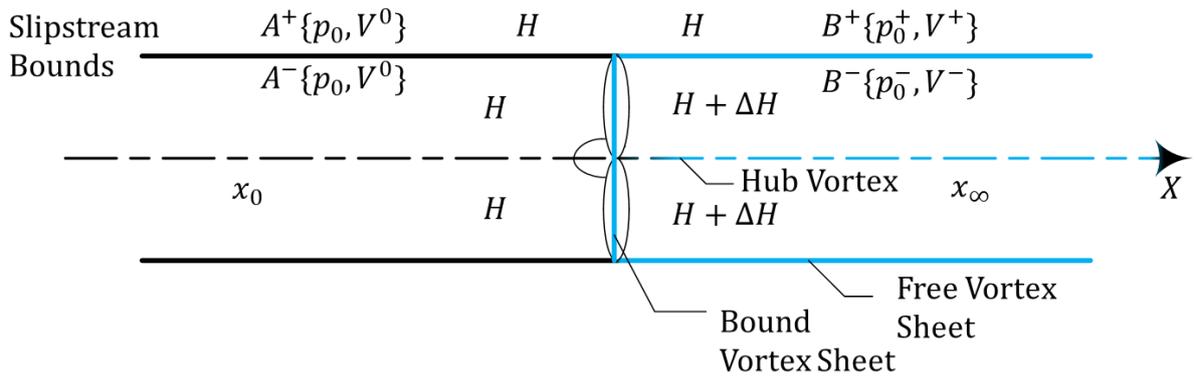
Figure 35: Different Pressures Inside and Outside Slipstream Boundary [15]

Outside of the slipstream, at $A^+ B^+$ the equation gives:

$$p_0 + \frac{1}{2}\rho \left(V_\xi^{0^2} + V_\eta^{0^2} + V_\zeta^{0^2} \right) = p_\infty^+ + \frac{1}{2}\rho \left(V_\xi^{+^2} + V_\eta^{+^2} + V_\zeta^{+^2} \right) \tag{7.90}$$

Inside of the slipstream, at A^-B^+ the equation gives:

$$p_0 + \frac{1}{2}\rho\left(V_\xi^{0\,2} + V_\eta^{0\,2} + V_\zeta^{0\,2}\right) + \Delta H = p_\infty^- + \frac{1}{2}\rho(V_\xi^{-\,2} + V_\eta^{-\,2} + V_\zeta^{-\,2}) \tag{7.91}$$

ΔH is the total head jump and p is the static pressure in the equation above. The resulting equation results in:

$$\Delta H = \overline{p_\infty} + \frac{1}{2}\rho\left[(V_\xi^{-\,2} - V_\xi^{+\,2}) + (V_\eta^{-\,2} - V_\eta^{+\,2}) + (V_\zeta^{-\,2} - V_\zeta^{+\,2})\right] \tag{7.92}$$

$\overline{p_\infty}$ in the equation above symbolizes the differences between pressures at the inside and outside of the slipstream boundary. However, the zero jump condition dictates that there is no pressure change, therefore $\overline{p_\infty} = 0$

Moreover, because of the shape of the propeller wake ($V_\eta^- = V_\eta^+ = 0$). This velocity is tangent to the slipstream tube.

$$\Delta H = \frac{1}{2}\rho\left[(V_\xi^{-\,2} - V_\xi^{+\,2}) + (V_\zeta^{-\,2} - V_\zeta^{+\,2})\right] \tag{7.93}$$

The vorticity strength density $\vec{\gamma}$ can be defined by the velocity jump at the slipstream boundary ΔV. It is defined by: $\Delta V = V^- - V^+$.

$$\vec{\gamma} = -n^+ \times \Delta V \tag{7.94}$$

The normal vector n^+ points outwards of the vorticity surface panel. If the velocities are divided to their local panel coordinates, then the resulting vector is:

$$\begin{bmatrix} \gamma_\xi = -\Delta V_\zeta \\ \gamma_\eta = 0 \\ \gamma_\zeta = \Delta V_\xi \end{bmatrix} \tag{7.95}$$

The change is defined similarly with other velocity definitions:

$$\begin{aligned} \Delta V_\xi = V_\xi^- - V_\xi^+ \\ \Delta V_\zeta = V_\zeta^- - V_\zeta^+ \end{aligned} \tag{7.96}$$

At the slipstream, the mean velocity V_m is assumed to transport the vorticity. As a general expression:

$$V_m = \frac{1}{2}(V^+ + V^-) \tag{7.97}$$

The mean velocities can be divided into the local coordinate components as well:

$$\Delta V_{\xi_m} = \frac{1}{2}\left(V_\xi^- - V_\xi^+\right)$$
$$\Delta V_{\zeta_m} = \frac{1}{2}\left(V_\zeta^- - V_\zeta^+\right)$$

(7.98)

Modifying the equation that was obtained by the Bernoulli equation, a non-linear equation for the vorticity strength density can be computed. The reason for the non-linearity is caused by the relationship between the constant interaction of unknown neighboring and distant vorticities from other panels.

$$-\gamma_\xi V_{\zeta_m} + \gamma_\zeta V_{\xi_m} = \frac{1}{\rho}\Delta H$$

(7.99)

7.6 Calculation of the Vorticity Strength Density γ_ξ, γ_ζ

The vorticity strength density $\vec{\gamma}$ can be solved using the two equations that were calculated in the previous two sections. The component γ_ξ is solved using the continuity equation using a Finite Volume Method approach. The component γ_ζ is solved by the iterative procedure on the Bernoulli equation to give an algebraic equation. γ_η is considered 0 for the solution.

The complexity of the problem at hand comes from the second order terms and coupling terms while calculating γ_ξ and γ_ζ. The mean velocity V_m is found using the results from each panel in the computation and it is impossible to solve in a direct manner. Since the interaction problem is using the results from the previous computation, if the mean velocity is assumed to be the same with the previous computation, the problem becomes linear.

Each iteration is called k for further applications. The linear iterative formula can be written as:

$$-\gamma_\xi^{(k)} V_{\zeta_m}^{(k-1)} + \gamma_\zeta^{(k)} V_{\xi_m}^{(k-1)} = \frac{1}{\rho}\Delta H$$

(7.100)

Leaving only $\gamma_\zeta^{(k)}$, it becomes:

$$\gamma_\zeta^{(k)} = \frac{\frac{1}{\rho}\Delta H + \gamma_\xi^{(k)} V_{\zeta_m}^{(k-1)}}{V_{\xi_m}^{(k-1)}}$$

(7.101)

It can be figured that the value for $V_{\xi_m}^{(k-1)}$ is a large positive number because the velocity in the axial direction is always a large positive. Therefore, except the point where the wing and propeller vortex sheet stagnation point intersect, the denominator value is always a large positive.

The continuity equation is solved to find the γ_ξ value. The vorticity continuity equation is written in in a finite control volume Ω_p. Using a Finite Volume Method approach the volume is assumed to be filled by vorticity $\vec{\omega}$. Using the gauss theorem and defining surface as S_p yields:

$$\iiint_{\Omega_p} \nabla . \vec{\omega} d\Omega = \iint_{S_p} n . \vec{\omega} dS = 0 \qquad (7.102)$$

So the total vorticity flux inside surface S_p is 0, which shows that the vorticity is conserved inside the closed surface.
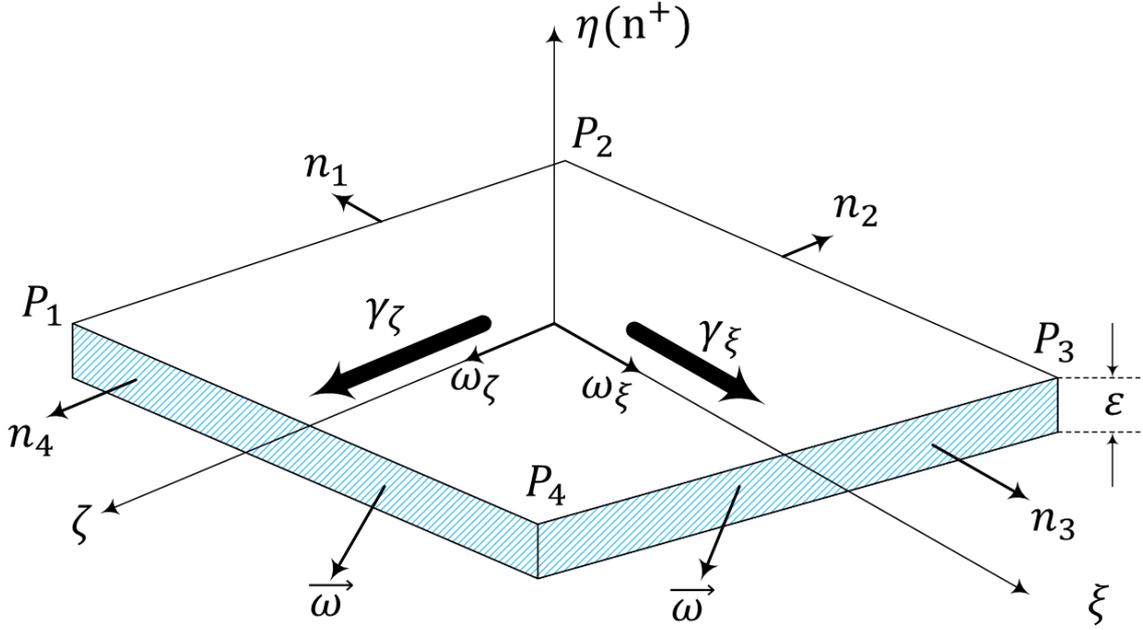
Figure 36: Vorticity Flux on a Panel Element [15]

For the vortex sheet panel, the four sides of the panel with thickness ε and vorticity ω can be represented as the summation of four integrals.

$$\int_S n_1 . \vec{\omega}_1 dS + \int_S n_2 . \vec{\omega}_2 dS + \int_S n_3 . \vec{\omega}_3 dS + \int_S n_4 . \vec{\omega}_4 dS = 0 \qquad (7.103)$$

Moreover, the vorticity fluxes for each four sided can be called F_k.

$$\sum_{k=1}^{4} F_k = 0 \qquad (7.104)$$

As a result, the general formula for the vorticity fluxes on each side face S_k is:

$$F_k = n_k . \vec{\omega}_k S_k = n_k . \vec{\omega}_k (\varepsilon . l_k) = n_k . \vec{\gamma}_k l_k, \qquad k = 1,2,3,4 \qquad (7.105)$$

Define the following:

1) F_k Vorticity flux average on the side k
2) n_k Normal unit on the side k

3) $\vec{\omega}_k$ Vorticity vector average on the side k

4) S_k Geometric area on the side k, $S_k = \varepsilon l_k$

5) $\vec{\gamma}_k$ Vorticity strength density vector average on the side k, $\vec{\gamma}_k = \vec{\omega}_k(\varepsilon)$

6) l_k Length of the side k

7) $\vec{\gamma}_{ij}$ Vorticity strength density vector at the panel $C_{i,j}$

The values for calculating the fluxes is represented in the table below.

Table 1: Overview of Vorticity Flux Solutions

Normal Vector n_k	Local Coordinate System (ξ, η, ζ)	Vorticity Strength Density $\vec{\gamma}$	Component Form $\gamma_{(\xi,\eta,\zeta)}$
n_1	$(-1,0,0)$	$\vec{\gamma}_1$	$(\gamma_{\xi_{ij}}, 0, \gamma_{\zeta_{ij}})$
n_2	$(\sin(\alpha_2),0,-\cos(\alpha_2))$	$\vec{\gamma}_2$	$\left(\frac{1}{2}\left(\gamma_{\xi_{ij}} + \gamma_{\xi_{ij+1}}\right), 0, \frac{1}{2}\left(\gamma_{\zeta_{ij}} + \gamma_{\zeta_{ij+1}}\right)\right)$
n_3	$(-1,0,0)$	$\vec{\gamma}_3$	$(\gamma_{\xi_{i+1j}}, 0, \gamma_{\zeta_{ij}})$
n_4	$(-\sin(\alpha_4),0,-\cos(\alpha_4))$	$\vec{\gamma}_4$	$\left(\frac{1}{2}\left(\gamma_{\xi_{ij}} + \gamma_{\xi_{ij-1}}\right), 0, \frac{1}{2}\left(\gamma_{\zeta_{ij}} + \gamma_{\zeta_{ij-1}}\right)\right)$
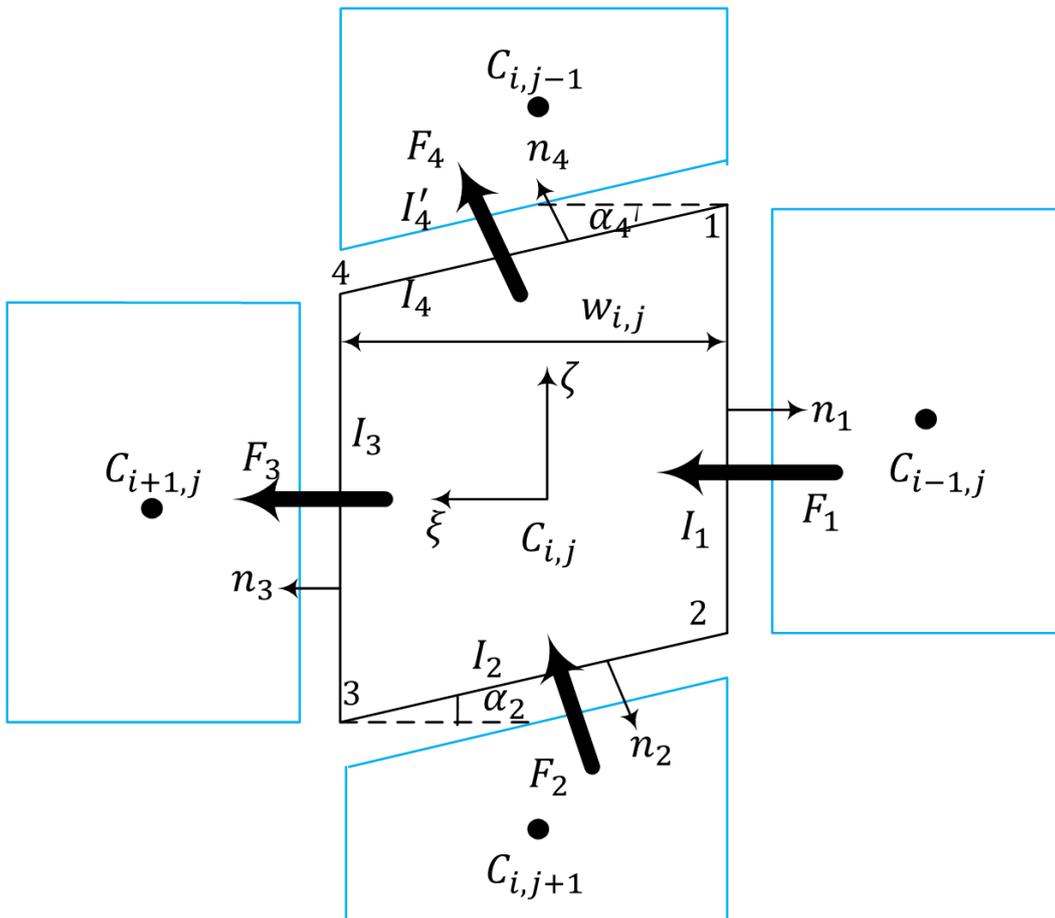
Figure 37: Panel Notation on a Control Volume with Vorticity Fluxes [15]

From the conservation of vorticity flux and the relationship given below, the relation for the vorticity strength density value for the next panel $\gamma_{\xi_{i+1,j}}$ can be achieved.

$$\gamma_{\xi\,i+1,j} = \frac{I_1}{I_3}\gamma_{\xi i,j} - \frac{w_{i,j}}{2I_3}\left(\gamma_{\zeta i,j-1} - \gamma_{\zeta i,j+1}\right) + \frac{w_{ij}}{2I_3}\left[S_{14}\left(\gamma_{\xi ij} + \gamma_{\xi ij-1}\right) - S_{23}\left(\gamma_{\xi ij} + \gamma_{\xi ij+1}\right)\right] \quad (7.106)$$

For an extended step-by-step explanation for the steps taken above, refer to the Appendix H.

The equation above is valid everywhere except at the point where the wing panels intersect the slipstream panels.

7.7 Modification of Panels to Resolve Unsatisfied Conditions

To achieve a full non-linear model, there are two apparent concerns that needs to be dealt with during the application of the SVPM. The first one is satisfying the kinematic boundary condition, when the mean velocity $V_{\eta m}$ (the normal vector component of V_m) is not 0. The second one is the unique stagnation point where the wing-slipstream intersection takes place. In this case $V_{\xi m}$ and $V_{\zeta m}$ are 0, which fails the equations that are used to calculate $\vec{\gamma}$. A method of slipstream deformation and an exception to the vorticity flux calculation for the panels at the wind-slipstream intersection is established in Appendix I.
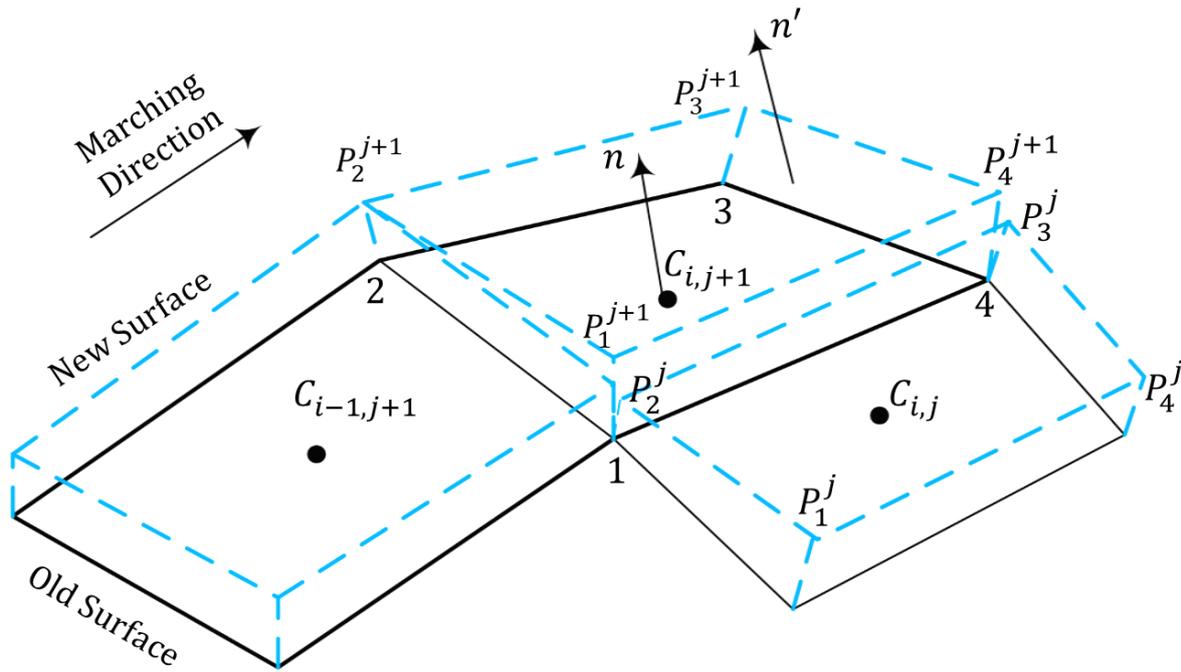
Figure 38: Deformed Slipstream Panel [15]

7.8 Performance of SVPM in MATLAB

SVPM was coded using MATLAB® for a wing and propeller (wing and rudder for Da-Qing Li's case). The first case is given for CPU intensive comparison of choosing different panel numbers. For the circumferential direction, a symmetry has to be achieved in xy plane and $x = y$ plane. The rule for the distribution is:

$$n_p = 2^{2+n_{p,circ}} \quad (7.107)$$

Four numbers were chosen for $n_p = 1,2,3,4$. Unfortunately, MATLAB is a single-threaded application. It has parallel computing abilities using "parfor" construct but it doesn't guarantee a faster solution for single convergence solutions. Therefore all CPU hours presented here are computed in single core processor.

The wing (or in this case rudder) forces were calculated using lifting line method. Appendix M explains the basis of VLM for wings.

$$F_r = \rho V_\infty \Gamma \times I \tag{7.108}$$

$$F_r = F_x i + F_y j + F_z k \tag{7.109}$$

The sum of all elements in the axial direction gives the rudder thrust C_r, which can be non-dimensionalized using the free stream conditions and the area of the rudder.

$$C_r = \frac{\sum_{j=1}^{MN} F_x}{\frac{1}{2} \rho V_A^2 S} \tag{7.110}$$

This value is then used as a convergence factor:

$$|\tau_{C_r}| = \left| \frac{C_r^k - C_r^{k-1}}{C_r^k} \right| \leq 10^{-3} \tag{7.111}$$
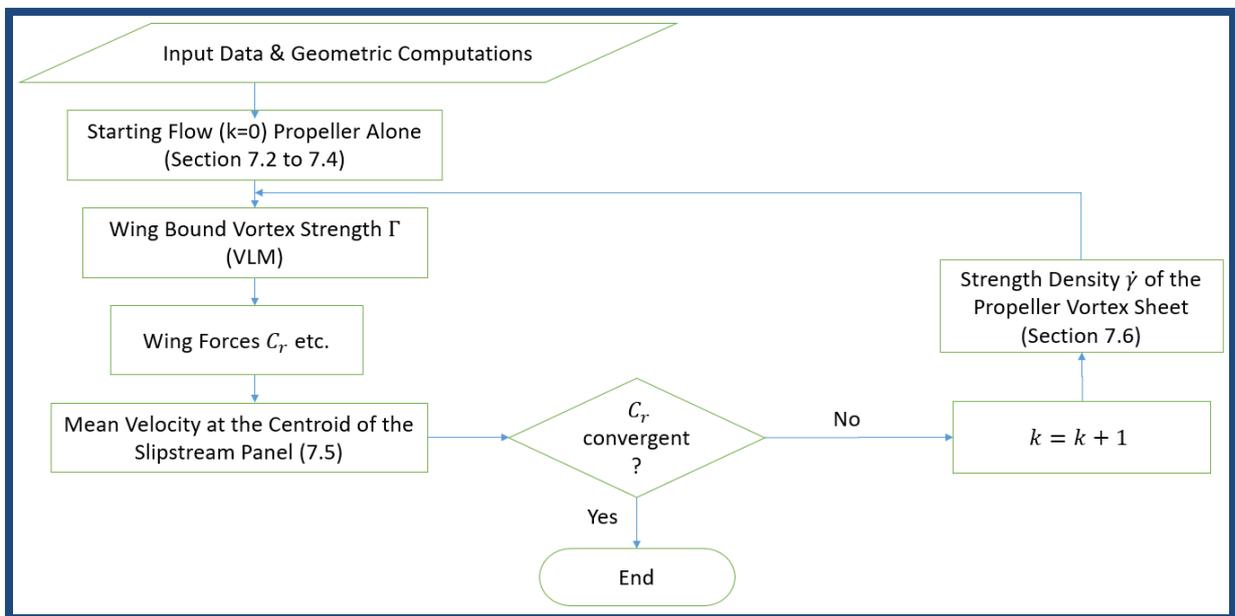
Figure 39: Flowchart Used to Test the SVPM Algorithm

The results are represented below. It should be noted that this preliminary study doesn't include deformation procedure explained in previous section. Deformation adds other

convergence criteria $(i.e. V_{\eta m} = 0)$. The procedure is kept simple to predict required computational resources for an accurate solution.

Table 2: Computational Performance and Accuracy of SVPM

$n_{p,circ}$	n_p	$CPUh$	Iterations	$|\tau_{C_r}| \leq 10^{-3}$
1	8	18	27	No
2	16	32.8	16	Yes
3	32	50.5	25	Yes
4	64	> 95	19	n/a

The first issue with the panel selection is the obvious fact that the number of panels increase in the power of 2, which limits the number of choices substantially. Second, the convergence time is unexpectedly large for each choice of n_p.
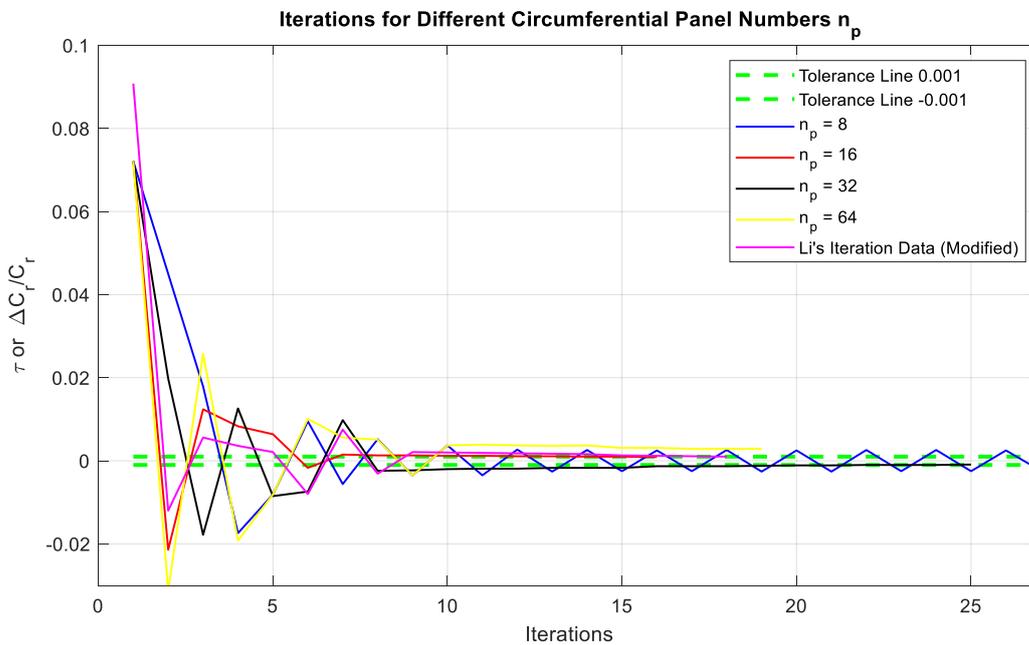
Figure 40: Convergence vs. Iterations for Various Panel Numbers Including Li's Data [23]

The problem with large number of panels is that the iterations take much larger time. The program had to be terminated because of the time constraint. For a low number of panels, convergence criteria $|\tau| \leq 10^{-3}$ cannot be achieved. Unfortunately, Li does not specify how many panels have been used in his model.

The choice for n_p lies either for 16 or 32 circumferential panels. 16 panels achieve faster convergence, so it has a clear advantage. Then next step is to compare the flow field behind the wing that best represents the slipstream effect.

Propeller Slipstream Correction for Wind Tunnel Applications
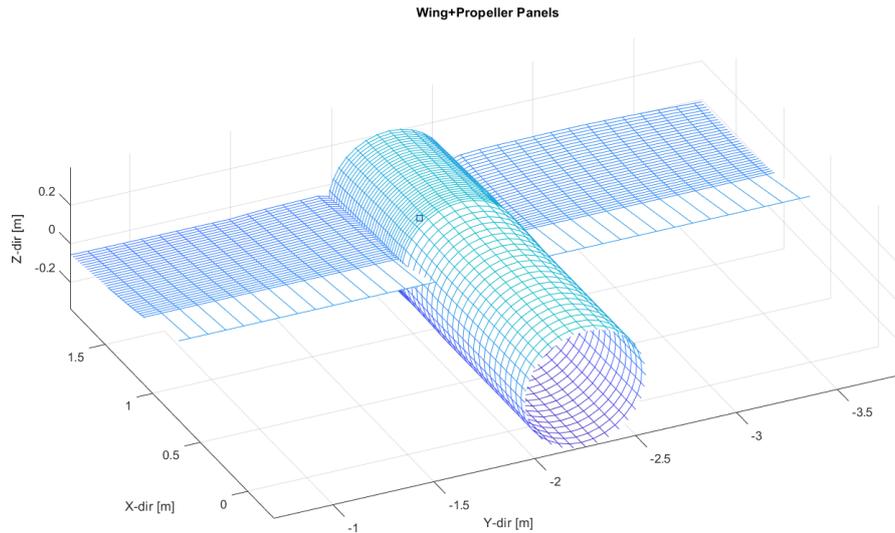
Figure 41: Example Wing and Propeller Configuration

An example panel representation for a wing-propeller setup is shown in the figure above. Li's numerical experiments were done for ship rudders. However, the example model setup for this research holds up well in comparison. The trend for the value γ_ξ is quite similar to the setup created by Li's panel method. The difference mainly comes from the different calculation of induced velocity by each panel. Li uses his method while this model uses Johnson's method. It should be noted that for this calculation neither Li nor the MATLAB code uses any slipstream deformation scheme.
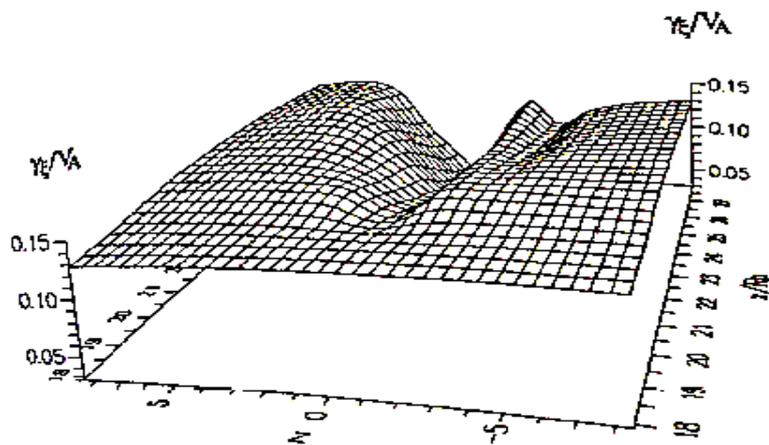
Figure 42: Surface Vorticity Component γ_ξ in Non-Linear Method by Li [23]
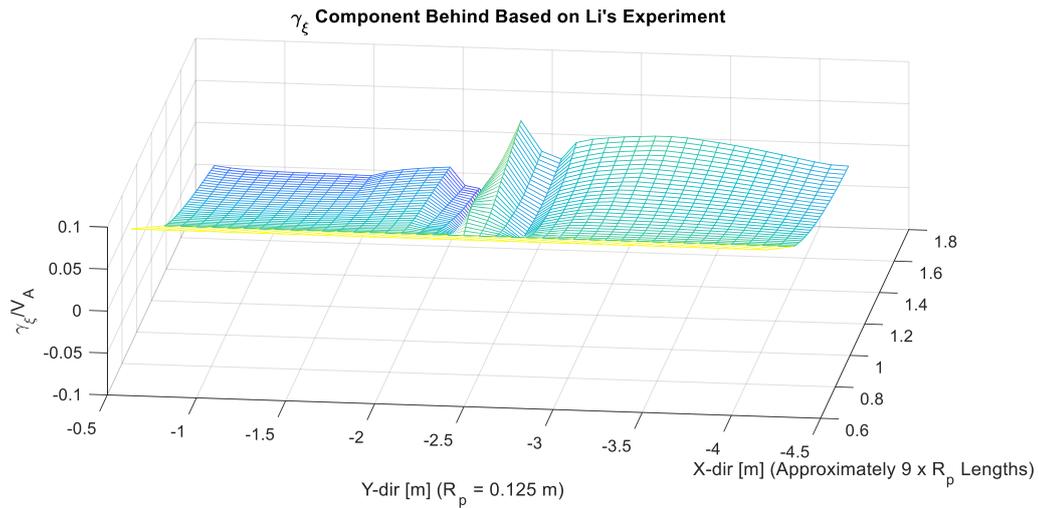
Figure 43: Surface Vorticity Component γ_ξ Calculated

The last step to conclude how many number of circumferential panels n_p needed is testing the deformation of slipstream panels. The deformation condition is $V_{\eta m} = 0$. So the convergence is based on:

$$\tau_{V_{\eta m}} = \max \left| \frac{V_{\eta m}}{V_A} \right| \leq 0.05 \tag{7.112}$$
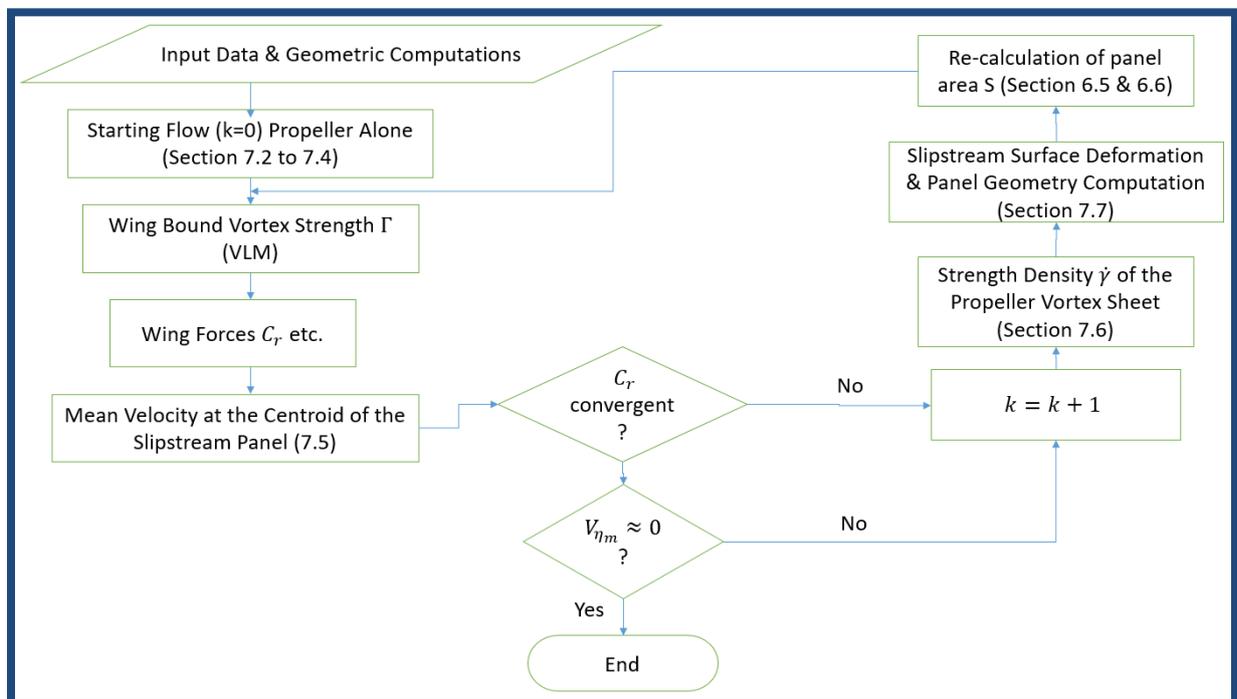
Figure 44: Flowchart for the SVPM Case with Slipstream Deformation

According to Li, the tolerance level should be between $\tau_{V_{\eta m}} \leq 0.01$ to 0.05, however the closest value reached in any configuration is around 0.04. So the higher value is chosen for the given range. Unfortunately for both $n_p = 16$ and 32, there is substantial shear once the slipstream hub vorticity meets the vortex lattice circulation at the wing. The effect is severely increased with the increasing number of blades B. The figure below has 4 blades on the propeller.
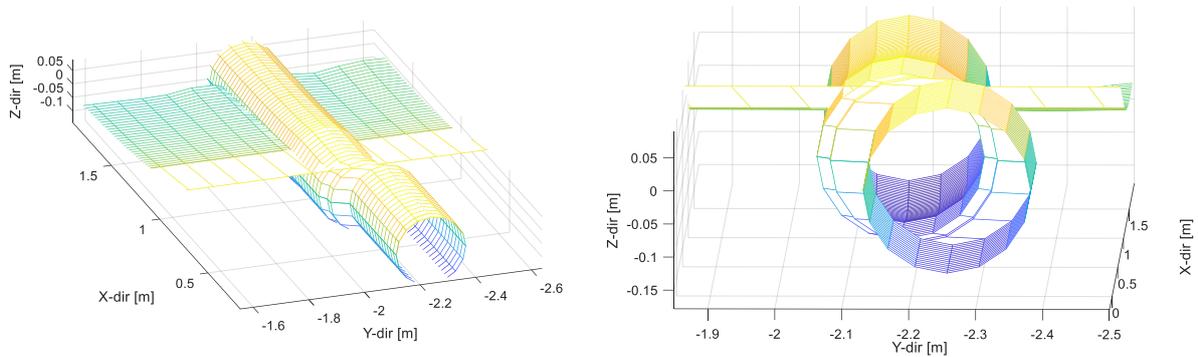
Figure 45: Deformation Due to Extreme Shearing

A similar phenomenon was observed by Veldhuis in his PROWIM experiment and Navier-Stokes solution. Even though the effect observed in SVPM is not unnatural, it does not allow for a fully converged solution within the desired tolerances.
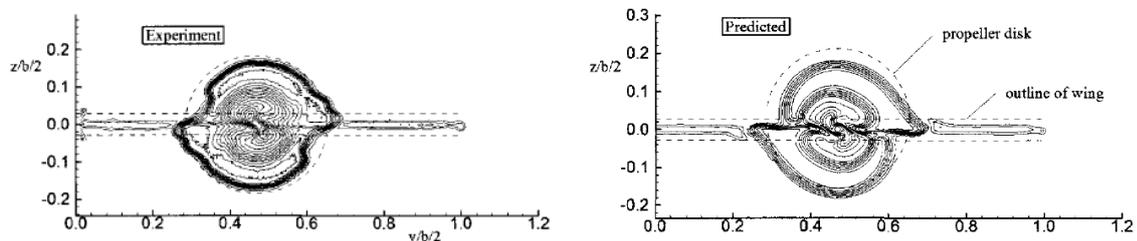
Figure 46: Slipstream Shearing Observed by Veldhuis in PROWIM [4]

Setting the tolerance to $\tau_{V_{\eta m}} \leq 0.1$ is not acceptable for a precise measurement in each run. Assuming an average advance velocity $V_A = 50 \, m/s$, the value for $V_{\eta m}$ would have to be around $5 \, m/s$. This is a very large value for any induced velocity, furthermore it is a crucial boundary condition that is left unsatisfied. Li also notes that the he had had uncoverged solutions for $V_{\eta m}$ in the deformation procedure.

An extensive overhauling approach regarding vorticity panel method will be explained in the next chapter.

8

PROPELLER AIRCRAFT COMPONENTS

One of the key research objectives indicated on Chapter 1 is to find the moments and forces acting on the aircraft. The aircraft is divided into several parts: fuselage, wing, propeller, nacelle, vertical tail and horizontal tail. Some parts are considered with their interference effect. The most prominent are the propeller-wing and propeller-fuselage contribution. For other parts, for example empennage, the effect is a linear increase or decrease on the overall forces and moments on the aircraft.

This chapter will explain each major aircraft component and how they are modeled in the panel code

8.1 Refinements on Propeller Slipstream Model

The vorticity panel method described in Chapter 7 did not give results in the desired tolerances. The results for SVPM were inconclusive because of the extreme shearing and unsatisfactory deformation of the panels at the wing intersection. Therefore, a new model needs to be re-introduced:

1) The model is changed from a non-linear model to a linear model. Therefore, the geometry of the slipstream and vorticity strength of the slipstream panels are not affected by the wing.
2) The propeller forces and moments are calculated using a mix of blade element and vortex theory. (Section 8.2)
3) The main criteria for a new model is to have a vorticity tube at the propeller in order to model the circulation at the slipstream.

There were two problems with Li's SVPM non-linear approach. First was the convergence time due to the calculation of each vorticity at every single panel. In the non-linear model, almost every panel had an effect on each panel present in the global system. Second was the uncovergence of the multiple boundary conditions. Schroijen created a new method called PSSM (Propeller Slipstream Shearing Model) to reduce the calculation time and reach similar results with SVPM. [56] There are three major changes with this approach.

1) Velocities induced at a certain point in the flow field are only evaluated from neighboring panels.

2) The model is now linear and the effect of "$i + 1$" $- th$ panel does not induce velocities on the panel i.
3) The slipstream model is a two-dimensional version of SVPM. dX-steps are used for each panel to simulate the third-dimension.
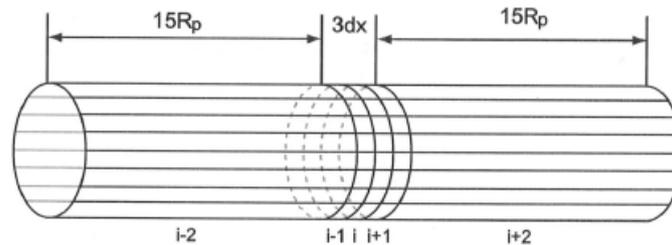
Figure 47: Prescribed Shape of the Two-Dimensional Slipstream Element [56]

The development of slipstream along the axial direction is calculated with Runge-Kutta time-stepping method, where the panels $i - 2, i - 1$ are known and $i, i + 1, i + 2$ are calculated. So, the far field has no effect on the panel i. The values for γ_ξ and γ_ζ are still calculated from the equation presented in Chapter 5. The values for $i - 2$ and $i + 2$ are used to simulate infinity and they have a length of $15R_p$.
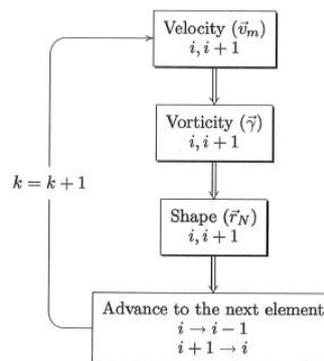
Figure 48: New Iteration Scheme for the Vorticity Panel Method [56]

According to Schroijen, the results between Li's model and his are minimal and the computation time has improved 36 times.

8.2 Propeller Interference Model

McCormick developed the first significant propeller interference model using the principals of vortex theory and blade element method by Glauert. [57] [58] These were then improved upon by Miranda and Metcalfe and compiled by Veldhuis. [47] [48] [4]The chosen propeller interference model was developed under the supervision of late TU Delft professor R. Slingerland. [59] [60] [61] [56] It is originally developed to compute the OEI condition for a propeller aircraft with the focus on the vertical tail. The propeller interference model accounts for the rotational flow behind the propeller and establishes a vortex flow field. Consequently, it has been decided to continue with this model.

In order to calculate propeller forces and moments, it is crucial to establish a diagram of induced velocities on the propeller blade element. Rauhut has developed a propeller induced velocity scheme using vortex theory and Prandtl tip correction. [62] [60] The induced velocities on the propeller can be calculated at many discrete points.
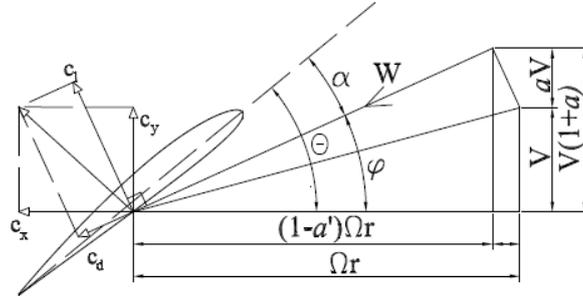
Figure 49: Blade Element Diagram with Relative Induced Velocities [62]

For reference, θ is β in McCormick's diagram, aV corresponds to w_a and $\varphi = \alpha_i + \phi$. [58]

$$\tan(\varphi) = \frac{V}{\Omega r} \left[\frac{1 + \frac{\sigma\left((\theta - \varphi)C_{l_\alpha}\sin(\varphi) + C_d\cos(\phi)\right)}{4\sin(\varphi)\cos(\varphi)\,F}}{1 - \frac{\sigma\left((\theta - \varphi)C_{l_\alpha}\cos(\varphi) - C_d\sin(\phi)\right)}{4\sin^2(\varphi)\,F}} \right] \tag{8.113}$$

The equation for solidity σ and the Prandtl tip correction F are denoted as:

$$\sigma = \frac{Bc}{2\pi r} \tag{8.114}$$

$$F = \frac{2}{\pi}\cos^{-1}\left(e^{\left(\frac{B(R_p - r)(1+\lambda)^{\frac{1}{2}}}{2R_p\lambda} \right)} \right) \tag{8.115}$$

There are many advantages to this approach. First, the implicit function is easy to resolve using computer power. Second, after acquiring the value φ, all the induced velocities at any tangential or radial direction on the blade element can be calculated. Third, the torque and thrust behind the propeller can be assessed by integrating the dQ and dT for each discrete point. Fourth, the streamline following the propeller disc can be altered by the pitching moment since the induced velocities can be re-assessed for a given angle-of-attack.

Propeller Slipstream Correction for Wind Tunnel Applications

Circumferential and Radial Stations F27 Propeller [deg x m] (32x7)
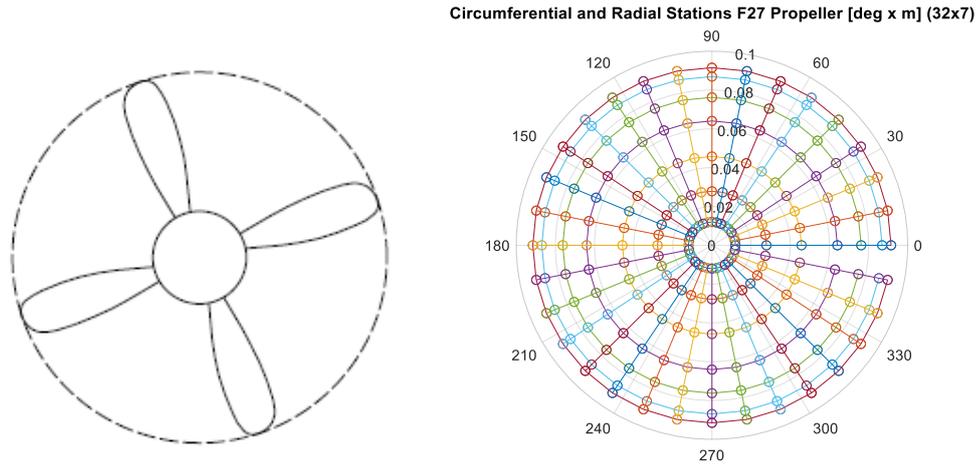
Figure 50: F27 Propeller Divided into Stations of Discrete Points

The propeller blade is divided into discrete points. A representation is given above. The propeller tube is divided into 32x7 stations for calculation.
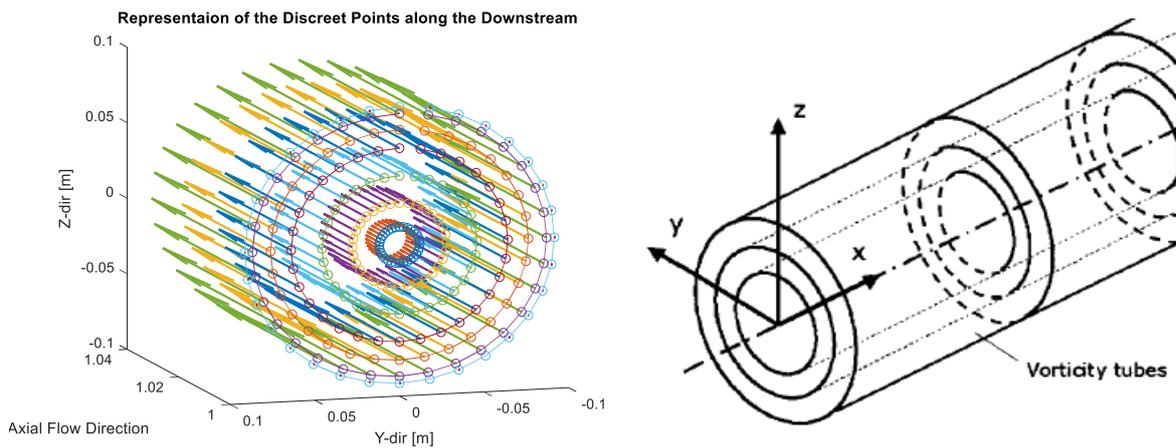
Figure 51: Representation of F27 Propeller Along Downstream (Left) and Vorticity Tube Representation (Right) [4]

Propeller forces are calculated at sea level conditions $U_\infty = 50\ m/s$, $\alpha = 0$, $rps = 270$ and $\beta_{.75R} = 25°$. The diameter of the propeller D_p is 0.183. The advance ratio J is 1.0119. The axial velocities with the tip loss are calculated by the equation below. It should be noted that quantity a is dimensionless relative induced velocity.

$$V_a = V(1 + a)F \tag{8.116}$$
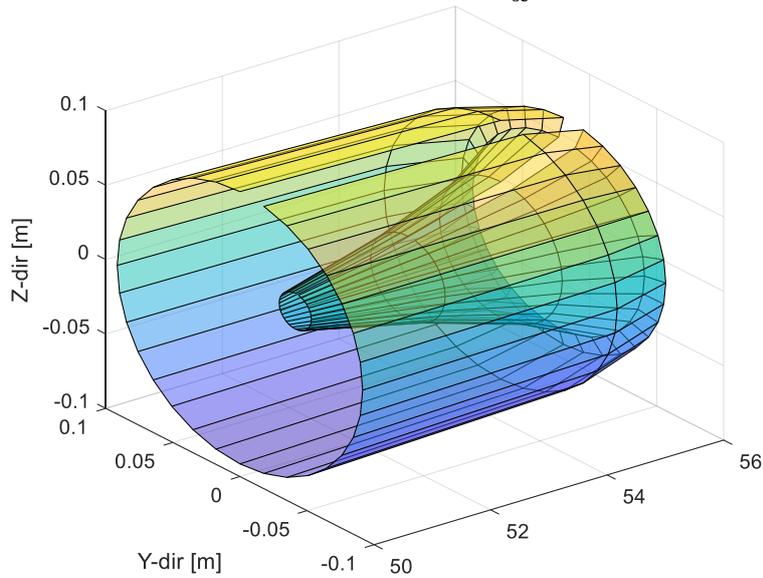
Figure 52: 3D Visualization of Axial Velocity at the Propeller Plane V_a $[m/s]$
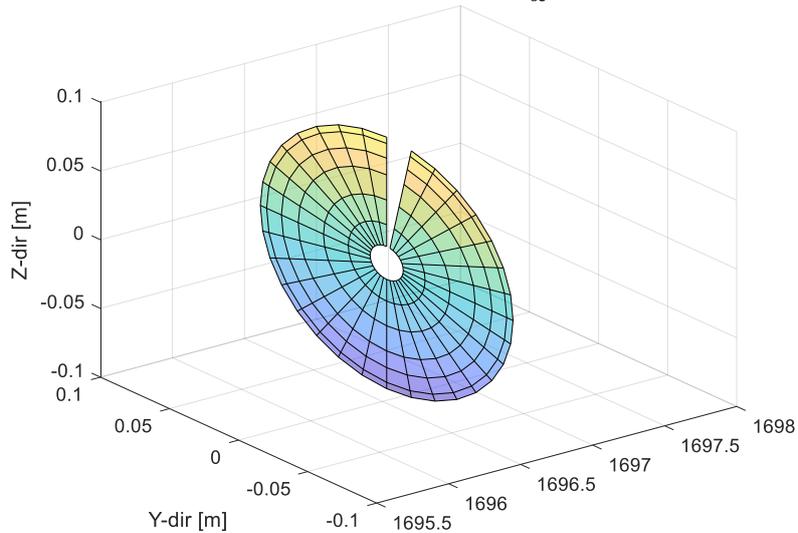
Figure 53: 3D Visualization of Angular Velocity at the Propeller Plane ω $[rad/s]$

The angular velocity is also represented to show that the angular velocity is kept unchanged during the calculation. The change in thrust dT at every station can also be computed. The thrust is the sum of all dT between every station $T = \sum_\theta [\sum_r dT]$. $\sim$ is used to denote the average value between two radial stations.

$$dT = d\dot{m} \cdot dV = \rho \tilde{V}(1 + \tilde{a})\tilde{r}drd\theta \cdot \tilde{V}(2a)F \qquad (8.117)$$
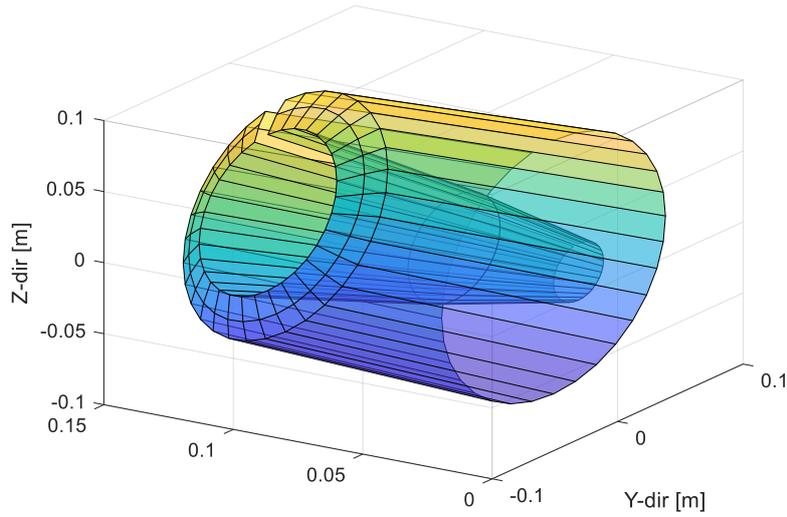
Figure 54: 3D Visualization of Thrust at the Propeller Plane $dT\ [N]$

Change in Pitch Force between Propeller Stations dP U$_\infty$ = 50 m/s α=0 rps = 270
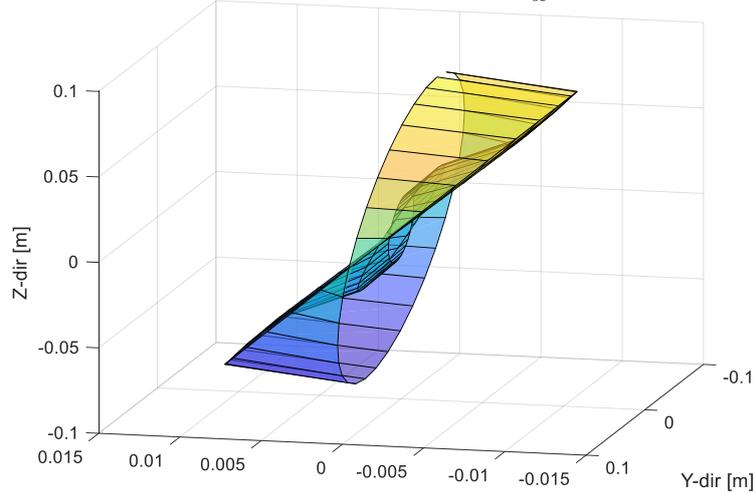
Figure 55: 3D Visualization of Pitch at the Propeller Plane $dP\ [N.m]$

The pitch due to the propeller is acquired similarly $P = \sum_\theta [\sum_r dP]$. It can be seen that the propeller pitch graph is symmetrical. Therefore at $\alpha = 0$, the propeller pitch P is 0. Finally the air going through between each section $d\dot{m}_{air}$ is presented. Also, because of the law of integrals, the total values are the volumes of the graphs.
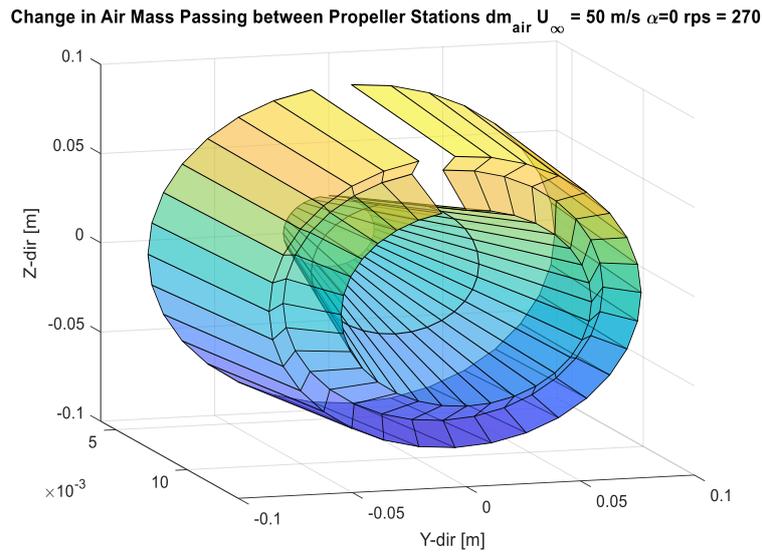
Figure 56: 3D Visualization Air Mass Passing between Propeller Stations dm_{air} $[kg]$

It can be seen that the air flow drops between the last radial stations. This is due to the fact that the stations are very close to each other. Hence, the air going through between them is less than the previous two stations.

The propeller-only thrust coefficient $T_c = T/\rho V^2 D^2$ is found to be 0.1554. Finally, the swirl behind each radial station can be calculated. [4]

$$\theta_{sw} = \tan^{-1}\left(\frac{V_t}{V_a}\right) \tag{8.118}$$

The swirl is constant behind the propeller for each azimuth angle, if it is in the same radial position.

Table 3: Tangent Velocity V_t and Swirl θ_{sw} for Different Radial Stations

Radial Station $r\ [m]$	0.0120	0.0278	0.0457	0.0640	0.0762	0.0869	0.0915
$V_t [m/s]$	5.8872	7.2496	6.8790	6.1808	5.4632	4.1338	0
$\theta_{sw}\ [rad]$	0.1150	0.1362	0.1256	0.1110	0.0980	0.0757	0

8.3 Wing, Fuselage and Nacelle Propeller Interaction

The wing is modeled in Vortex Lattice Method. [35] At quarter chord ¼c, desired number of N amount of horseshoe vortices are placed to represent the wing circulation. The induced velocities created are measured at collocation points (half a chord distance from each horseshoe vortex). The wing is immersed under free-stream velocity U_∞, unless it is under the propeller influence. Then the propeller induced velocities are also added.
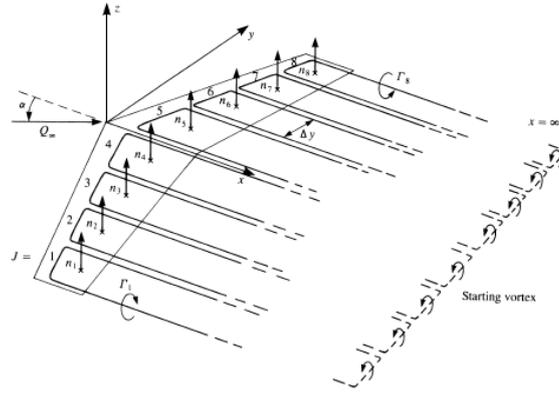
Figure 57: Horseshoe Vortex System for VLM [35]

To resolve the VLM, zero normal velocity at wing surface boundary condition was used. The sum of the induced velocities by the vortex strength and free stream velocity should be equal to 0.

$$\bar{\bar{A}}\bar{\Gamma} + \overrightarrow{V_\infty}.\vec{n} = 0 \tag{8.119}$$

This equation can be rearranged to solve for $\bar{\Gamma}$.

$$\bar{\Gamma} = \bar{\bar{A}}^{-1}\left[\overrightarrow{V_\infty}.\vec{n}\right] \tag{8.120}$$

The wing lift is calculated using Kutta-Joukowski lift equation.

$$L' = \rho V_\infty \Gamma \tag{8.121}$$

The profile drag is calculated by contributing the effect of the local lift coefficients at every panel.

$$C_d = c_{d_0} + k c_l^2 = c_{d_0} + k\left(\frac{2\Gamma}{V_\infty c}\right)^2 \tag{8.122}$$

The effect of the change in local induced velocities are also taken into account while calculating the induced drag. For each section the induced drag is calculated by

$$C_{d,i} = -l \cdot sin(\alpha_{eff}) + d \cdot cos(\alpha_{eff}), \quad \text{where} \quad \alpha_{eff} = \alpha_i + \alpha_p \tag{8.123}$$
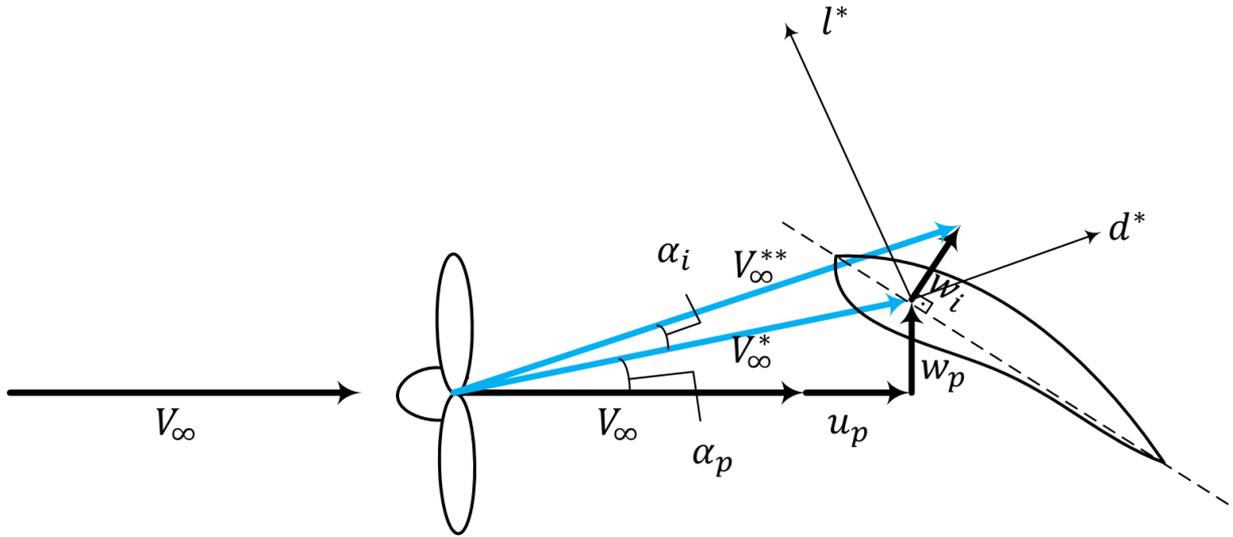
Figure 58: Velocity Diagram for a Wing Profile in Slipstream [56]

The values for the velocities and induced angle of attack are given by the relations below. [56]

$$V_\infty^* = \sqrt{\left(V_\infty^* + u_p\right)^2 + w_p^2} \tag{8.124}$$

$$V_\infty^{**} = \begin{bmatrix} V_\infty^* + w_i \sin\left(\alpha_w + \alpha_p\right) \\ w_i \cos\left(\alpha_w + \alpha_p\right) \end{bmatrix} \tag{8.125}$$

$$\alpha_i = \tan^{-1}(V_{\infty,y}^{**} / V_{\infty,x}^{**}) \tag{8.126}$$

More discussion on Vortex Lattice Method and variations of implementation can be found in Appendices N,O and P.

The effects of fuselage under slipstream is twofold. The slipstream may wash near the fuselage, effectively direct contribution in the change of pressure distribution. It also produces a different magnitude of lift as a solid surface. The fuselage effects are explained by Renooij. [61] [63]

First effect of fuselage is the lift-carry-over because of the wing-fuselage interaction. Inside the fuselage, the vortex lattices are mirrored by

$$Y_{mir} = Y \frac{R_{fus}}{Y^2 + Z^2} \quad \text{and} \quad Z_{mir} = Z \frac{R_{fus}}{Y^2 + Z^2} \tag{8.127}$$

Each element of lattices have the location y and z. According to Renooij, a second mirror is not needed because the vortex location at the fuselage cross-section is zero.
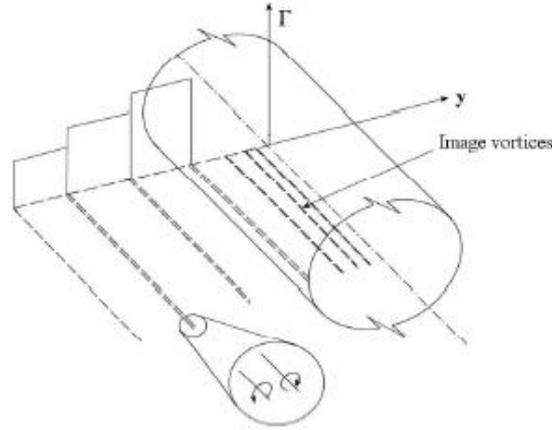
Figure 59: Horseshoe Vortices and Their Image in the Fuselage [63]

The second effect is the alteration of the local flow when the fuselage is flying in $\alpha_{fus} \neq 0$. This method is based on Multhopp and also explained by Renooij. [40] [63] The fuselage under goes a Joukowski transformation and becomes a vertical slit. The upwash induced by the fuselage can be obtained by

$$R\left\{\frac{\bar{u}}{u}\right\} = R\left\{1 - \frac{R_{fus}^2}{u}\right\} \tag{8.128}$$

R corresponds to the real part of the solution where $u = Z + iY$. This equation is two-dimensional. The change in radius of the fuselage can also be added by:

$$\frac{dr}{dX} \approx \frac{R_{fus}}{r}\frac{dR_{fus}}{dX} \tag{8.129}$$

The distance is $r = Y^2 + Z^2$. In three dimensional form it becomes:

$$\begin{bmatrix} dY \\ dZ \end{bmatrix} = \frac{R_{fus}}{Y^2 + Z^2}\frac{dR_{fus}}{dx} = \begin{bmatrix} Y \\ Z \end{bmatrix} \tag{8.130}$$

The lift of the fuselage along the span is calculated spanwise by accounting the specified strength vortex distribution at a specific position with its mirror image inside the fuselage. The distribution of the potential φ is presented by Renooij from Giesing's solution. [64] [63]

At a complex point $u = Z + iY$, the potential φ by a certain vortex at position ζ can be written as:

$$\varphi = R\left\{\frac{i}{2\pi}\ln(u - \zeta)\right\} \tag{8.131}$$

Again, R here is the real part of the solution. The total of all the potentials due to the wing and image system inside the fuselage does not give the correct lift distribution along the span

of the fuselage. To achieve the correct values, the potential increase caused by the vortices and mirror images ζ_I compelled to arise at the wing root ζ_k. Thus, the equation is rewritten:

$$\varphi = R\left\{\frac{i}{2\pi}\ln\left(\frac{(u-\zeta)}{(u-\zeta_k)}\right) + \ln\left(\frac{(u-\zeta_k)}{(u-\zeta_I)}\right)\right\} \tag{8.132}$$

Finally the lift can be written as the difference between upper and lower fuselage surface using the lift circulation formula.

The nacelle is computed in the same manner with the fuselage. The wing vortex lattice is mirrored in the nacelle as well as the fuselage. The effect of mirrored vortices were shown by Durand, and it is a decrease in circulation and lift experienced along the span of the wing. [39]
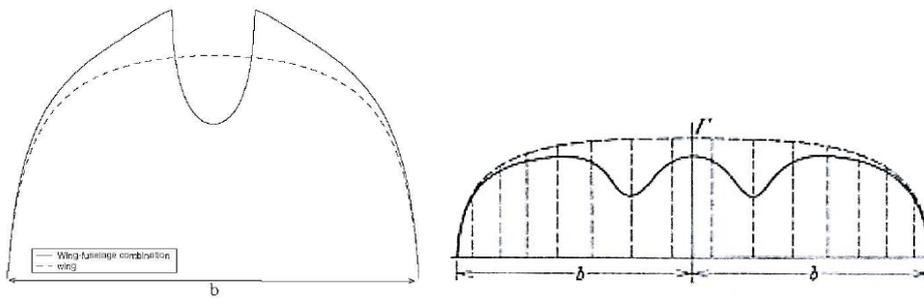
Figure 60: Fuselage Influence on Lift (Multhopp) (Left) [63] and Nacelle Influence on Lift (Durand) [39]
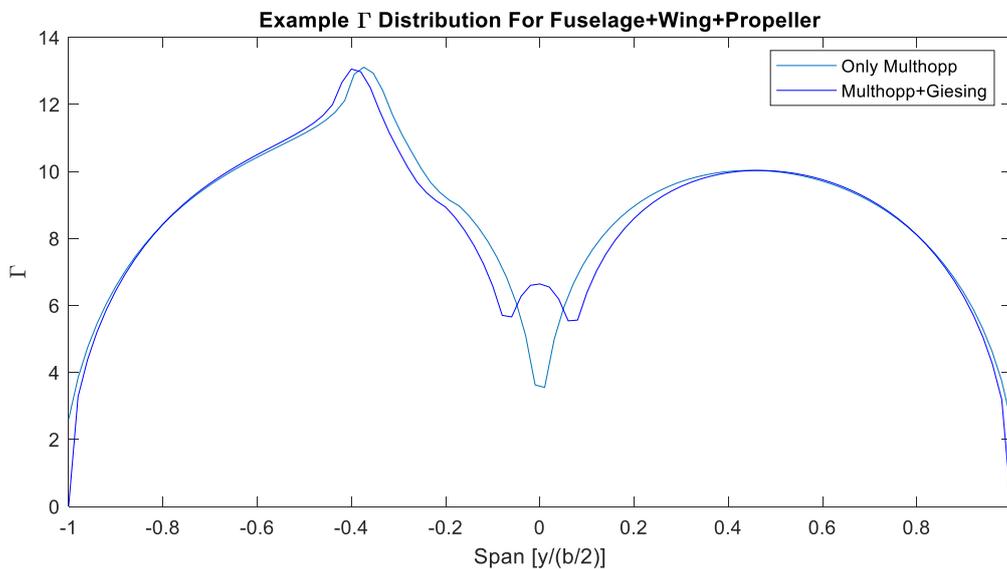
Figure 61: Gamma Distribution along the Wing Chord with Fuselage Effects

8.4 Two Dimensional Wing Trailing Vortices and Empennage
The Fokker F27 model is tested with an empennage at TU Delft LLT. Therefore the effect of the circulation (consequently vortex) has to be reasoned for the flow about the empennage.

Since the flow propagates in the axial direction, it is imperative to be able to observe the flow characteristics along the fuselage and the tail. The observation is crucial because the location of each vortex changes as it moves. Hence, the vortex flow field is modeled by taking into account the flow at the wing trailing edge at its first iteration and the effect of fuselage is kept as an influence while it moves parallel to the fuselage axis.

The two-dimensional vortex flow field is created by Rogers for delta wings with slender bodies. [65] The method is a time stepping method commencing at the wing root trailing edge, in which the flow about ΔX distance is solved iteratively. The induced velocities at the wing trailing edge is calculated by:

$$V_i = \frac{\Gamma_j}{2\pi r} \qquad (8.133)$$

It should be noted that this equation is only true for two-dimensional approach where $r = Y^2 + Z^2$ (distance between two trailing vortices). The iteration is resolved on each change in axial location.

$$\begin{bmatrix} X \\ Y \\ Z \end{bmatrix} = \begin{bmatrix} X + dX \\ Y + \dfrac{V_Y}{V_X} dX \\ Z + \dfrac{V_Z}{V_X} dX \end{bmatrix} \qquad (8.134)$$

The change in induced velocity dV_i can be written for a trailing vortex in two-dimensions where $d\Gamma$ is the vortex strength of the trailing vortex.

$$\begin{bmatrix} -dV_{i,Z} \\ dV_{i,Y} \end{bmatrix} = \frac{d\Gamma}{2\pi r} \begin{bmatrix} -Z \\ Y \end{bmatrix} \qquad (8.135)$$

The position of the slipstream hub and surrounding vortex sheet is also needed to be calculated for each position of $X + dX$. The only three-dimensional effect included in the model is the change of fuselage radius along the axial direction. (8.130)

The empennage is modeled the same way as the wing. The wing trailing vortices, fuselage and slipstream are all taken into account.
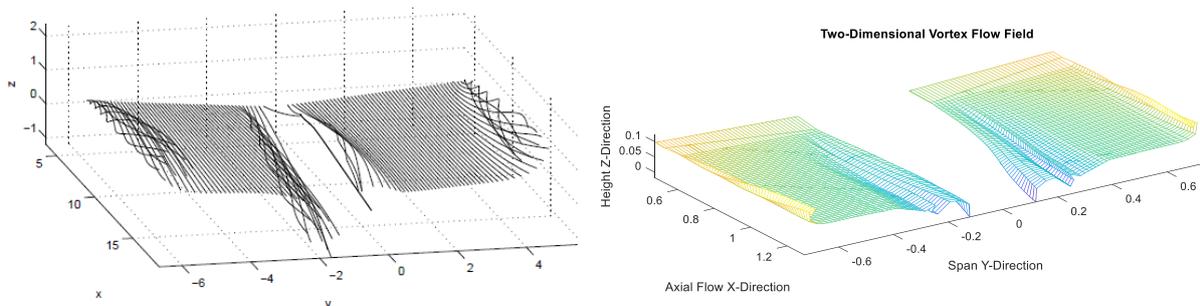
Figure 62: Two-Dimensional Vortex Flow Field with Side-Slip (Renooij) (Left) [63] without Side-Slip (Right)

Propeller slipstream is assumed to fully-contract when it reaches the tail. Influence of the nacelle does not allow for a fully-contracted slipstream assumption at the wing trailing edge. [4]

$$R_\infty = R_p \sqrt{\frac{1+a}{1+2a}} \tag{8.136}$$

These conclude the overview of the slipstream panel method solution. In the next section, the implementation of panel method for Fokker F27 will be discussed.

III

EXPERIMENTATION AND IMPLEMENTATION

The wind tunnel and aircraft model characteristics are presented in Chapter 9. A list of the corrections and test setups are also shown in the same chapter. Chapter 10 presents a preliminary study of the flow solution with new modifications and identifies the limits of the flow solver.

<div style="text-align: right; font-size: 3em;">9</div>

FOKKER F27 INSIDE WIND TUNNEL

9.1 Short Description of the Wind Tunnel and F27 Model

The Fokker F27 model is tested in Delft Low Turbulence Tunnel (LTT) inside Low Speed Laboratory.

1	Fan and straighteners
2	Motor
3	Corner vanes
4	Settling chamber
5	Expansion screen
6	7 Anti-turbulence screens
7	Screen store room
8	Contraction
9	Exchangeable test section
10	Diffuser
11	Security screen
12	Spider web
13	Screen
14	Six-component balance
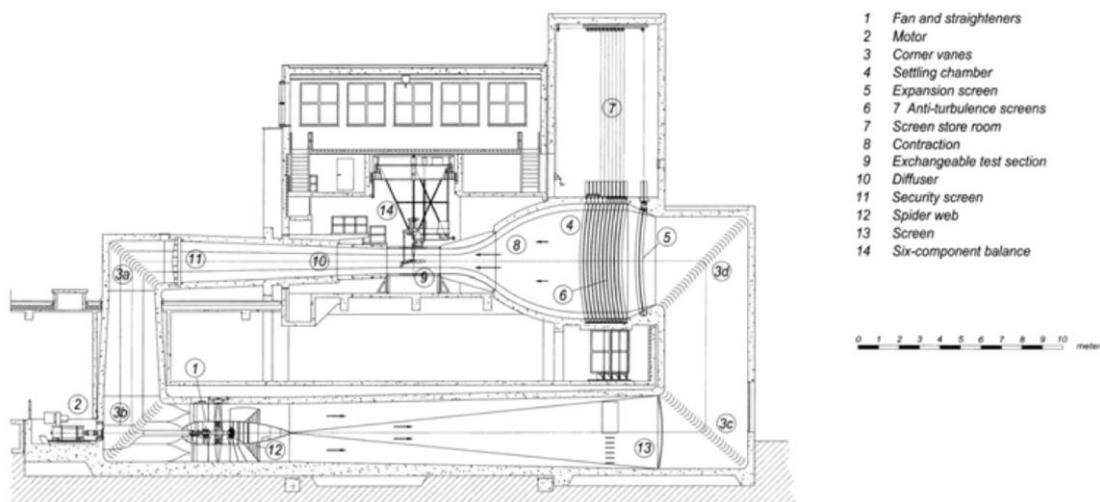
Figure 63: Diagram of Delft LTT [66]

It is a closed return wind tunnel with a maximum achievable speed of approximately 120 m/s. It is driven by a 525 kW DC motor and is built on two floors. The maximum Reynolds number achievable is around $3.5 \cdot 10^6$. [66] The test section area is given below:
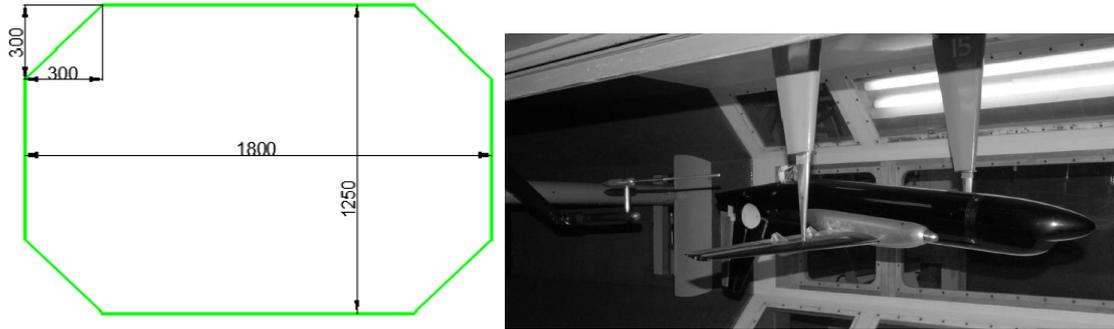
Figure 64: Test Cross-Section of the Wind Tunnel (Left) and Fokker F27 Installed in the Test Section (Right) [34]

Table 4: Basic Parameters for F27 Model

BASIC PARAMETERS OF FOKKER F27 1:20 SCALE MODEL	
Wing	
SPAN	$1.450\ [m]$
AREA	$0.175\ [m^2]$
MEAN AERODYNAMIC CHORD	$0.1282\ [m]$
TAPER RATIO	0.4225
ASPECT RATIO	12
Fuselage	
LENGTH	$1.155\ [m]$
HEIGHT (CYLINDRICAL PART)	$0.1385\ [m]$
WIDTH (CYLINDRICAL PART)	$0.135\ [m]$
Horizontal tail	
SPAN	$0.490\ [m]$
AREA	$0.0402\ [m^2]$
MEAN AERODYNAMIC CHORD	$0.0877\ [m]$
ASPECT RATIO	5.95
Propeller	
DIAMETER	$0.183\ [m]$
NUMBER OF BLADES	4
Engines	
POWER	$3.6\ kW\ +\ 3.6\ kW$
MAXIMUM RPM	$30000\ rpm$
NUMBER	2

9.2 Experiment Setup and Data Processing

The experiment is divided into 3 sections. The first one is the F27 model without the effect of propeller thrust. Therefore, this setup may be called the gliding version. It will be used to differentiate the effect of thrust on the aircraft. In this section, only flow velocity V_∞ and angle-of-attack α is varied.

Table 5: Test Setup 1

	WFNVH	
Free-stream Flow Velocity, V_∞	$50\ m/s$	$80\ m/s$
Angle-of-attack Range, α	$-6°\ to\ 16°$	$-6°\ to\ 12°$

The second setup is where the propeller is added in the configuration. The effects of angle-of-attack α with various advance ratios J are observed. $V_\infty = 50\ m/s$.

Table 6: Test Setup 2

	WFNVHP		
Revolutions-per-sec, rps	$220\ rps$	$270\ rps$	$320\ rps$
Angle-of-attack Range, α	$-6°\ to\ 7°$	$-6°\ to\ 7°$	$-6°\ to\ 7°$

The final setup is called rps sweep. The variance of advance ratio J and its effect on the thrust coefficient T_c is observed. $V_\infty = 50\frac{m}{s}$, $\alpha = 0°$. Measurement taken for every $20\ rps$ increase.

Table 7: Test Setup 3

RPS Sweep	
Revolutions-per-sec, rps	$220\ rps\ to\ 340\ rps$

Barlow's step-by-step approach was implemented for the wind tunnel interference corrections. [32] The support interference for the balance measurements is already calibrated. $WFNVH$ values are taken as zero measurements for the $WFNVHP$ configuration. The difference between the forces of the two were deducted to find net thrust generated by the installed propellers.

The net thrust coefficient according to Philipsen is: [38]

$$T_c = \frac{S_w}{S_{p,1} + S_{p,2}}(C_{D,WFNVHP} - C_{D,WFNVH})$$

(9.137)
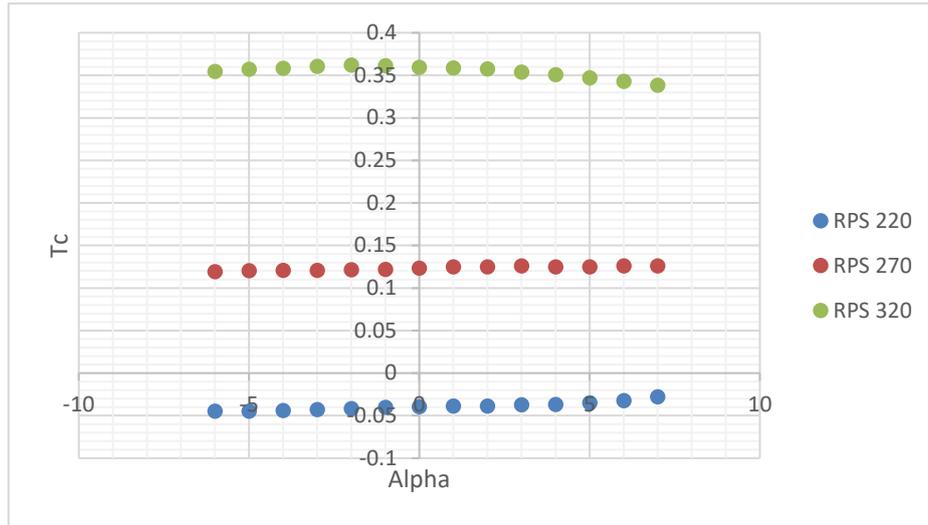
Figure 65: Uncorrected T_c $vs.$ α at Three Different rps Values, $Re = 0.41 \cdot 10^6$

From the figure above, the change in thrust coefficient T_c can be observed. The Reynolds number is $0.41 \cdot 10^6$. It is important to note that these are based on uncorrected values. They are for observing which α to base the thrust measurements from. It looks like the induced drag is lowest around $-2°$ to $-1°$. So the thrust curve should be based on these angles-of-attack. The compressibility effects are not considered in the majority part of the wind tunnel tests since $M \approx 0.15$.

The values for lift interference and blockage corrections were first considered in NASA's ANTARES method. However in the preliminary study, there was no clear advantage of using a wind tunnel panel method to obtain the blockage and lift interference results. (Appendix L) It was decided that the work and computation effort is high, even though the results are similar with empirical methods. Therefore, user-friendly standard corrections were considered.

The standard corrections used in the calculation are described in Eckert and Barlow. [27] [32]

1) Body correction factor for the nacelle. Finding the effective advance ratio J_E (if propeller is installed):

$$J_E = \left(1 - 0.254 \frac{S_n}{S_p}\right) \frac{V_\infty}{nD} \tag{9.138}$$

2) Thrust cleaning using Eckert's method, Patterson method or the proposed correction method (if propeller is installed). Drag is also corrected for induced drag caused by the propeller thrust. The equation is modified from Eckert:

$$C_{D,CT=0} = C_{D,CT} + \frac{C_{L,CT}^2}{\pi A}\left(\left(\frac{C_{L,CT}}{C_{L,CT=0}}\right)^2 - 1\right) \tag{9.139}$$

3) Calculating solid blockage from AGARDograph 109 and Barlow

$$\epsilon_{sb} = T \left(\frac{1}{C}\right)^{\frac{3}{2}} \frac{V}{\beta^3} \left[1 + 1.2\beta\left(\frac{t}{c}\right)\right] + \frac{K_3 \tau_1 Vol_{fus}}{C^{\frac{3}{2}}} \tag{9.140}$$

4) Calculating the wake blockage from Maskell-Veyssaire unseparated flow.

$$\epsilon_{wb} = \frac{S}{4C}\left(C_{D,uc} - \frac{C_L^2}{\pi A}\right) \tag{9.141}$$

5) The slipstream blockage is calculated from sink method (if propeller is installed):

$$\epsilon_{pb} = -\frac{1}{4}\frac{S_p}{C}(T_C/\sqrt{1+T_c}) \tag{9.142}$$

6) Change in angle of attack due to streamline curvature is calculated from Heyson's method.

$$\alpha = \alpha_{uc} + \Delta\alpha + \Delta\alpha_h, \qquad \Delta\alpha = \left(\delta_0 + \frac{c\delta_1}{2\beta h}\right)C_{L,uc}\left(\frac{S}{C}\right)\left(\frac{180}{\pi}\right) \tag{9.143}$$

7) Change in angle of attack at the tail is also Heyson's method

$$\Delta\alpha_h = \tau_2 \delta_0 C_{L,uc}\left(\frac{S}{C}\right)\left(\frac{180}{\pi}\right) \tag{9.144}$$

$$\Delta C_L = -a\Delta\alpha \tag{9.145}$$

8) Drag due to lift interference

$$C_{D,w} = C_{D,u,w} + \delta_0 C_{L,uc}^2 \left(\frac{S}{C}\right) \tag{9.146}$$

The coefficients are listed in the table below:

Table 8: Coefficients and Uncorrected Values Used in F27 Calculations at TU Delft LTT

D_p	0.183	b	1.45	S_p	0.0263
n_p	2	c	0.1282	S	0.1750
k	0.6	c_i	0.1464	A	12
ρ	1.178	T	0.75	δ_0	0.13
V	49.86	β	0.9247	δ_1	0.21
q	1470.5	t/c	0.15	τ_2	0.7
C	2.07	V_{fus}	0.0174		

The results for the corrections are presented in Chapter 11.

10

FOKKER F27 INSIDE PANEL METHOD

10.1 Computational Preferences on Panel Method

There are a number of modifications implemented by Schroijen and kept as a preference in the panel method. [67] [56] These are summarized below:

1) Slipstream shape is limited as a circle with concentric core vortex. This measure is taken because at the wing root trailing edge, the induced velocities are large and slipstream shear is unstable.
2) To keep the model simple, propeller slipstream shears through the center for all angles of attack.
3) The slipstream position is re-calculated in the trailing vortex flow field. Therefore the Z and Y component are updated to show sideward and downward flow after each iteration.
4) To implement different rotation direction, the local reference frame is changed when the sign of the rotation changes (-1 and 1) for IU and (1 and -1) for OU conditions. The pressure jump ΔH between slipstream boundary changes sign when -1 is selected.
5) The vortex is assumed to be finite instead of infinite. To ensure higher angles of attack, $d\Gamma$ value should be corrected for smaller displacements at wing trailing edge.

$$\vec{V} = \Gamma(\cos(\phi_1) - \cos(\phi))\vec{n} \qquad (10.147)$$

$$\vec{V} = \frac{\Gamma}{2\pi r^2}\begin{bmatrix} -\Delta Z \\ \Delta Y \end{bmatrix} C, \quad where \quad C = \frac{\cos(\phi_1) + 1}{2} \qquad (10.148)$$

6) The tip vortices are not force-free. Thus, it does not reel in a smaller radius as it moves in the axial direction.

There are more considerations taken into account by the author. These are related to computational efficiency and accuracy.

The effect of the wing/fuselage influence on the propeller can be taken into account. This is done by using the results of the propeller/wing/fuselage calculations in the previous iteration $k - 1$ and using it in k to estimate $i + 1$ and $i + 2$. The results are given below,
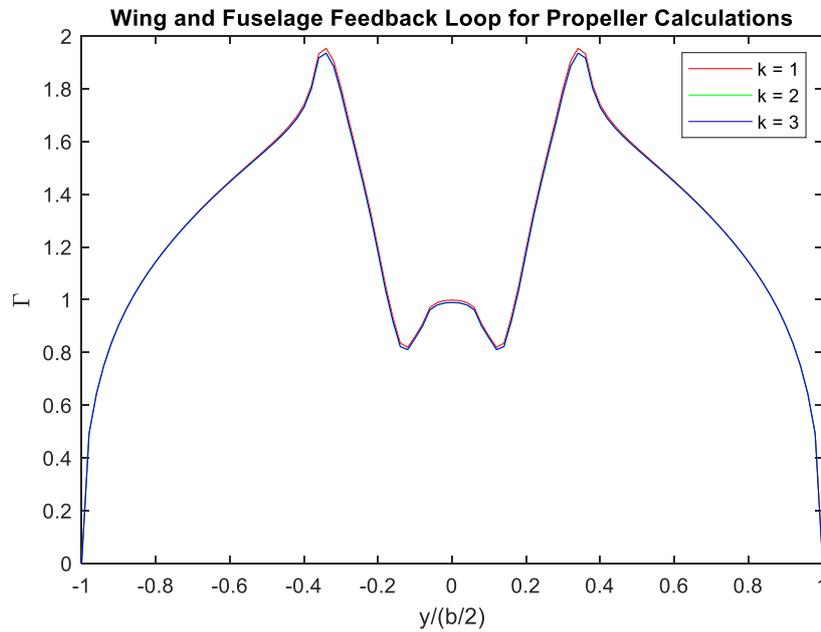
Figure 66: Spanwise Circulation for k Number of Iterations

It can be observed from the graph that the feedback loop is not very effective. After the second iteration, it is not realistically observable between two iterations. The change is less than 0.5%, so $k = 1$ (no feedback) in the various runs to save computational time.

Another possible addition to the propeller slipstream tube is the changing the rotation of the panels with swirl angle. Modifying (8.118)

$$\theta_{sw} = \frac{V_{m,\zeta}}{V_{m,\xi}} \frac{\Delta X}{R_p}$$

(10.149)
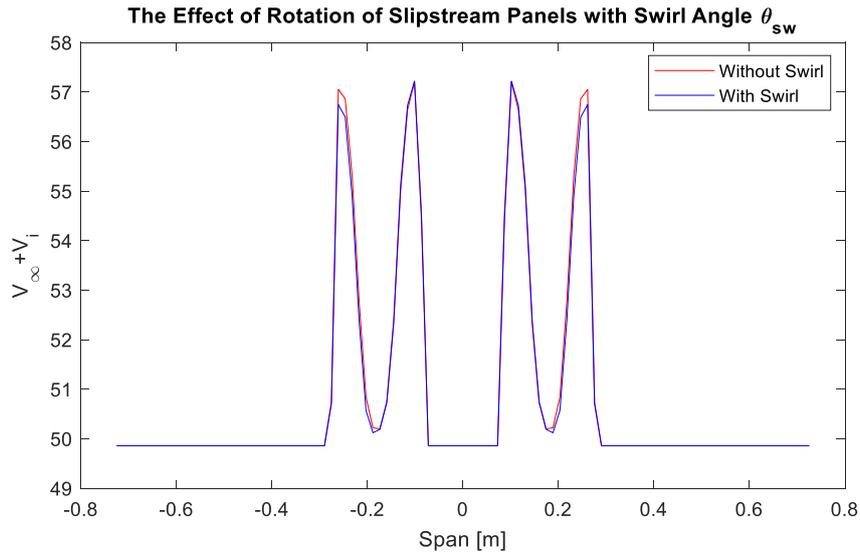
Figure 67: Effect of Swirl on the Axial Velocity Flowing Through the Propeller

The swirl effect is similar to the feedback effect, is also not strong, and increases the calculation time drastically. There is no clear indication in the vortex flow field that it has a substantial impact. Swirl is not implemented because there is no real trade-off.

The number of panels chosen for the calculation was based on less than $\frac{\Delta C}{C} < 0.01$ for coefficients and velocities. Another criterion was: one run for a single configuration should be $t \leq 10\ min$.

Table 9: Number of Panels Used for each Aircraft Component

Number of Circumferential Propeller Stations	N_p	32
Number of Horseshoe Vortices Wing	N_{Hw}	100
Number of Panels on Fuselage In Front of the Wing Trailing Edge	N_{ff}	40
Number of Panels on Fuselage Behind the Wing Trailing Edge	N_{fb}	40
Number of Steps Vortex Flow Field	$N_{\Delta X}$	75
Number of Total Horseshoe Vortices Empennage	N_{He}	100

Only the number of propellers stations were chosen manually in order to achieve precision of the modeled slipstream effect. The panel numbers for horseshoe vortices are rounded up to 100. Average single run takes between 4 to 6.5 minutes depending on the configuration. Vortex flow field is found to be the main source of time consumption.

The co-rotational propellers (propellers spinning in the same direction) are found to have exaggerated rolling vortex flow field. In first glance, it doesn't affect the lift distribution along the span out of the ordinary. However, the vortex flow field shows significant rolling. It is not apparent, if it has a significant impact for this study. From a stability point of view, the effect is too big to overlook.
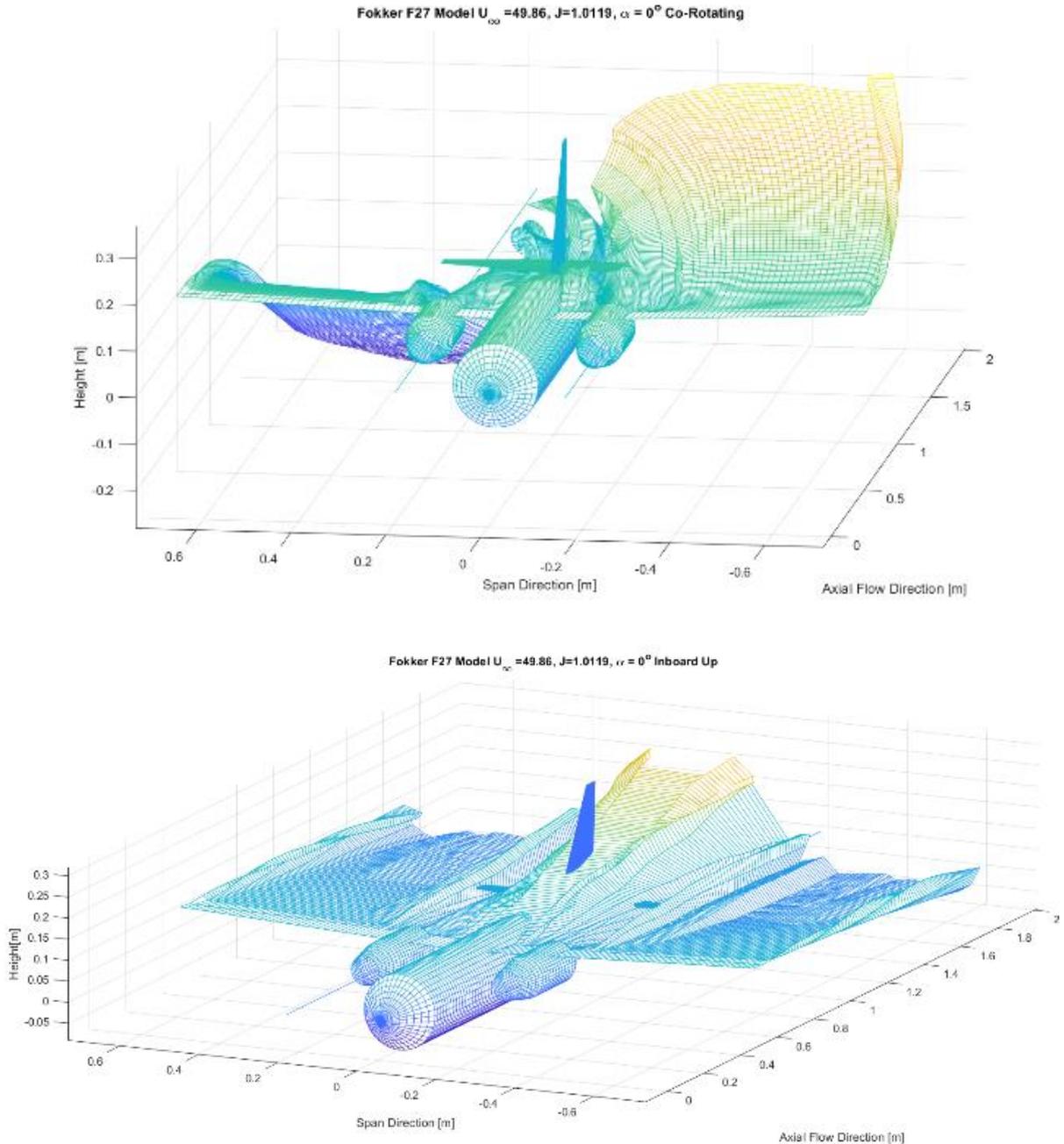
Figure 68: The Excessive Rolling by the Co-Rotating Propeller in the Vortex Flow Field

In the figure above, two configurations were chosen for the propeller rotation direction. While the Co-Rotating Propeller [Figure 68 (Up)] has excessive rolling trailing vortices, the trailing vortices at the Inboard Up configuration [Figure 68 (Down)] are balanced due to opposite propeller rotation.

Another remark has to be added here about the empennage. The correct modelling of vortex flow field once at the empennage is to include the empennage impact in the calculations. However, there are some obstacles:

i)   The vortex flow field is a two-dimensional construct. It has to be decided if the effect of the empennage can be added directly or another two-dimensional vortex field has to start at trailing edge of the horizontal stabilizer.

ii) The addition of empennage in the vortex field arises more complexity on how to include the empennage since they are in a feedback loop once they have a back-on-forth impact in the code.

iii) In low angles-of-attack, the slipstream tube and the vortex field does not wash over but flows under the horizontal tail. In theory, these would create significant pressure gradients around the empennage. It is a convoluted relationship and exceeds the method used in this research.
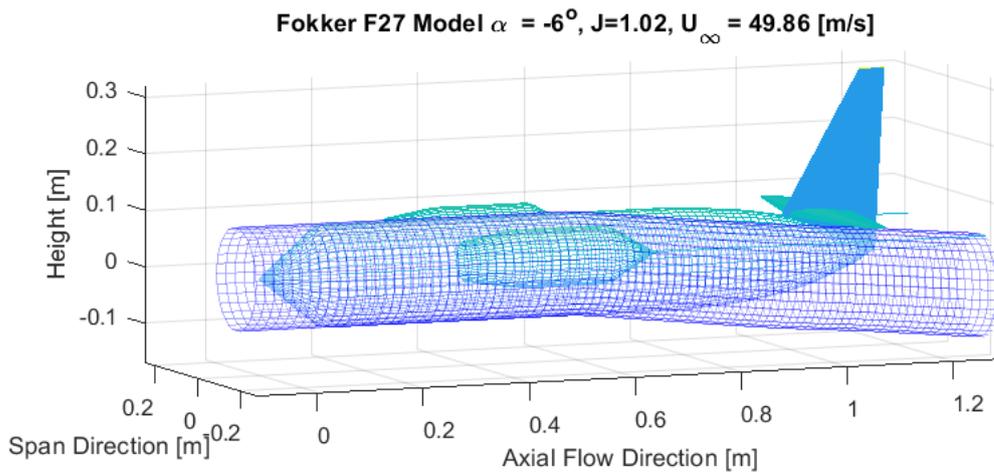
Figure 69: Slipstream Tube Going under the Horizontal tail

As a consequence, the empennage modelling is kept as simple as possible for this research.

Lastly, the limits of the model start around $\alpha = 6°$ at high-thrust configuration. The induced velocities at the empennage root are very large. It can be observed that the vortex field has very steep unrealistic vectors. [Figure 70] The deformation is unstable and the results are untrustworthy.
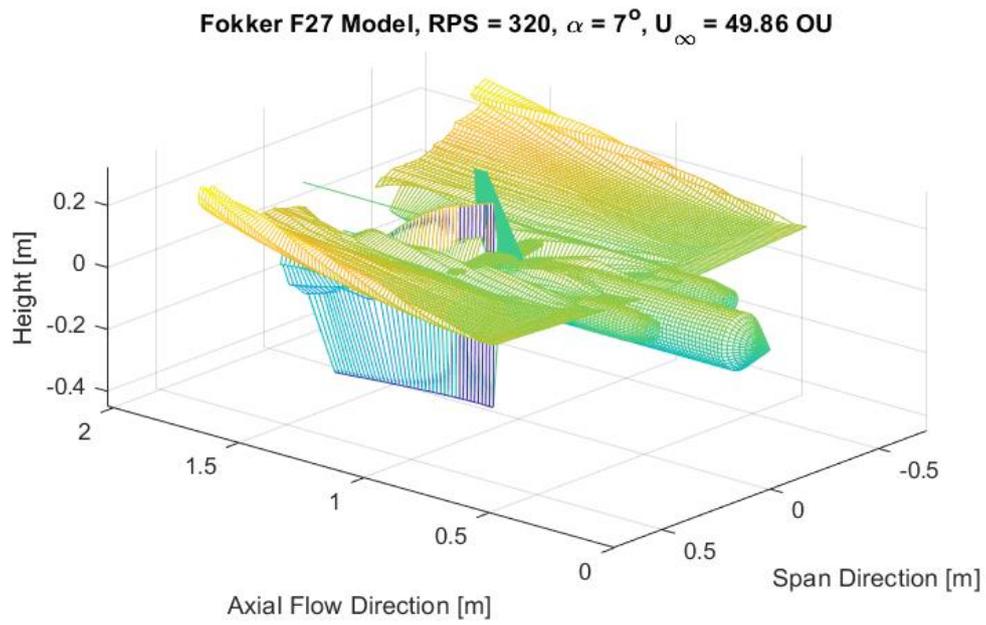
Figure 70: Excessive Panel Deformation at the Starboard Side Horizontal Tail Root

IV

RESULTS AND DISCUSSION

Chapter 11 presents the wind tunnel and panel method results as well as the comparison between proposed thrust corrections. Chapter 12 discussed the research questions formulated in Chapter 1.

11

RESULTS

The $WFNVH$ model is the base wind tunnel configuration, in which the wind tunnel corrections mentioned in Chapter 2 are suitable for direct implementation. Since there is no energy input to the system, potential flow solutions hold well. These potential flow solutions are also the basis of the many corrections that are stated in Chapter 2 and Chapter 9. Because the circulation is caused by the wing (and tail) only and there is no special flow (slipstream region) inside the wind tunnel test section, the data presented in this section is assumed to be an ideal version of the aftermath of thrust cleaning in a propeller installed configuration. Still, this assumption should be taken with a grain of salt. The values for the $WFNVH$ configuration and thrust corrected $WFNVHP$ are expected to be different. There are a handful reasons why this is the case:

1) *Uncertainties in measurement*. These errors may vary because of the measurement equipment and calibration.
2) *Rounding numbers and assuming constants.* There are many numbers that are assumed to vary little or the precision is assumed to be sufficient.
3) *Human error in experiments.* From installing the aircraft rig inside the wind tunnel to gathering data through the software, human error is generally the main reason for discrepancies.
4) *Disregarding supposedly minor effects.* There are many effects that are assumed minor for the F27 test. For this specific test, wall friction is assumed to be minor. There are also effects like compressibility and low Reynolds number effects, which are also assumed to be minor, but have much more relative impact than wall friction. With the wrong reasoning, a simplifying assumption can become the main source of error.
5) *Approximation of fluid domain*. From basic corrections to thrust cleaning, the flow is approximated into a certain model in one way or another. Therefore, the solution will always differ from one system to another. The main reasoning behind this thesis is also establishing an improvement on the previous methods of approximating thrust induced lift.

With these precautions in mind, the results for the wind tunnel experiments and panel method are presented in this chapter.

11.1 Propeller-off (Unpowered) F27 Configuration

F27 propeller uninstalled aircraft characteristics can be determined from the $WFNVH$ configuration. It can also be used as a zero reading to determine installed propeller effects. At a first glance, the major change is with the lift coefficient. Both lift curve and the maximum lift coefficient are exaggerated by the blockage and lift interference. This has serious impact at determining the mission capabilities and maneuverability. The tail sizing will be also severely affected because the moments are not where they are expected to be. Lift-to-drag ratio suffers from a similar problem. Quantities like optimal cruise velocity and fuel consumption are based on C_L/C_D curves.

The decline in lift-curve slope starts at $\alpha_c = 7.1562°$. It is usually an important criteria for the design of high-lift devices. This value is crucial because it is an indicator of mild separation. Small wind tunnels with smaller models are more prone to this problem because of the Reynolds number effect and early laminar separation bubble. It should be also noted that the velocity of the desired jet flow U_∞ is $0.14 \, m/s$ less than the one that is measure in the wind tunnel.
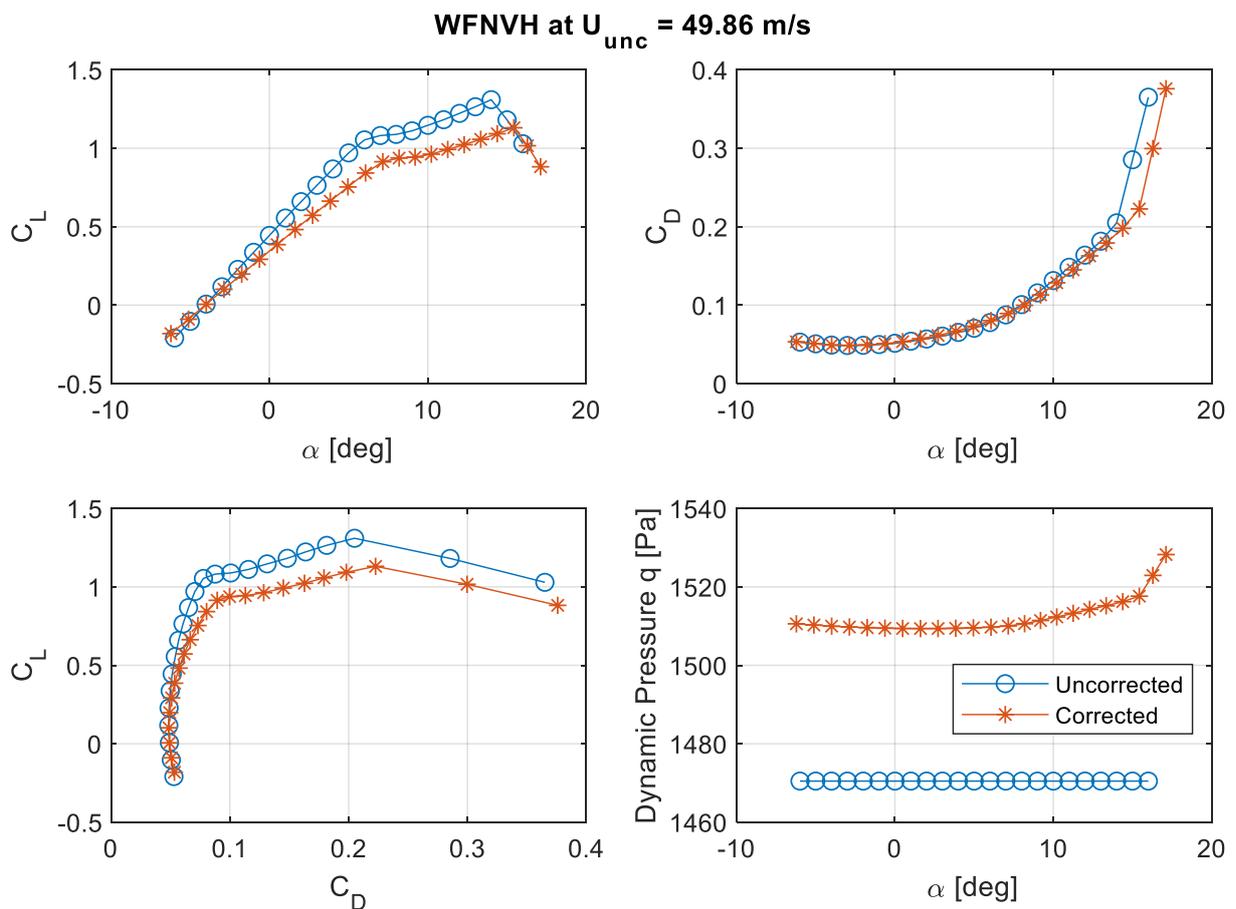
Figure 71: $WNFVH$ Aerodynamic Parameters Values at $U_\infty = 50 \, m/s$, $Re = 0.41 \cdot 10^6$, $M = 0.145$

The only blockage quantity that varies with a change of angle is the wake blockage in the assumed model. The overall change from total blockage is presented in the figure below. The solid blockage is a scalar quantity so it is constant with the change of α. Wake blockage is severe at the stall. An improvement here would be adding the wake blockage for unseparated flow using a least squares method after $\alpha_c = 8.186°$.
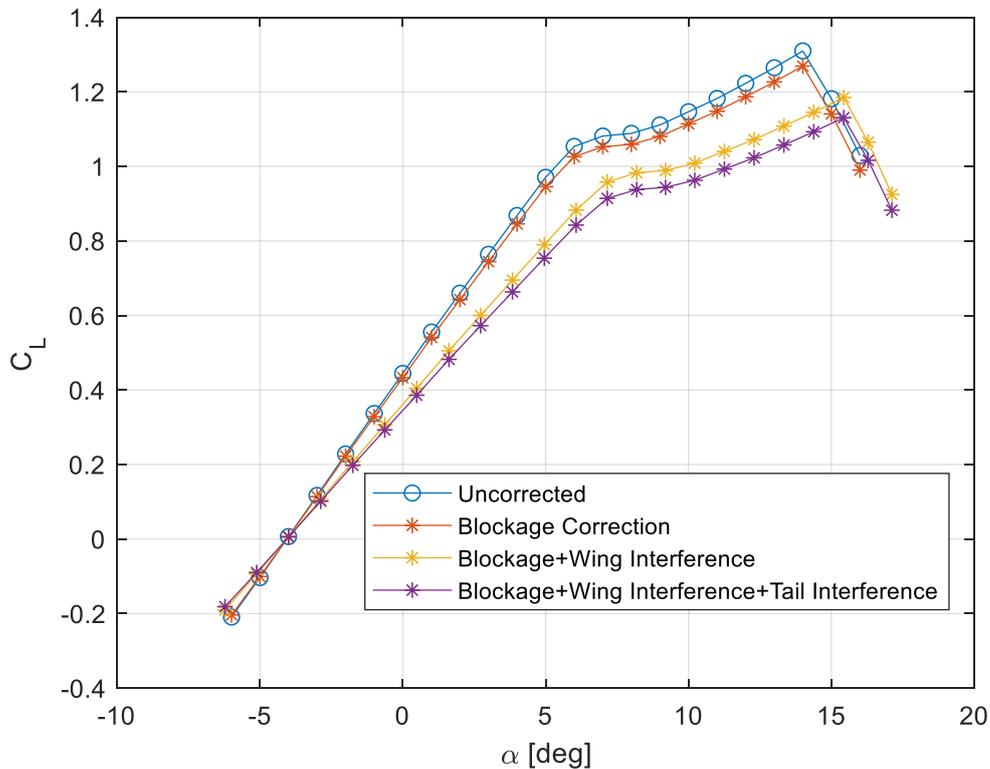
Figure 72: Visualized Impact of Each Correction Method, $WFNVH$ at $U_\infty = 50\ m/s$, $Re = 0.41 \cdot 10^6$, $M = 0.145$

A step-by-step observation is presented in the figure above. The impact of the corrections can be defined as follows, for the F27 model. Wing lift interference is the primary cause of change in lift. The secondary is the tail interference; third is the total blockage. The effect of a wall correction can be interpreted by the impact it has on the lift curve. Blockage is directly related to how blunt an object is and its cross-section. For a glider, blockage is not predominantly caused by lifting effects. Thus, the impact of blockage on the lift-alpha slope is virtually none. It is only a drop on the C_L values at a given angle α. The lift interference is mainly caused by the largest lifting surface, which is the wing. Both of the lifting surfaces play an essential role on determining the lift interference wall corrections.

The results for the WFNVH configuration can be compared with Binkhorst's results. Flow conditions of the wind tunnel tests are not given but the Reynolds number is declared as $Re = 0.7 \cdot 10^6$. From this number, it can be assumed that the flow velocity was around $U_\infty \approx 85\ m/s$.
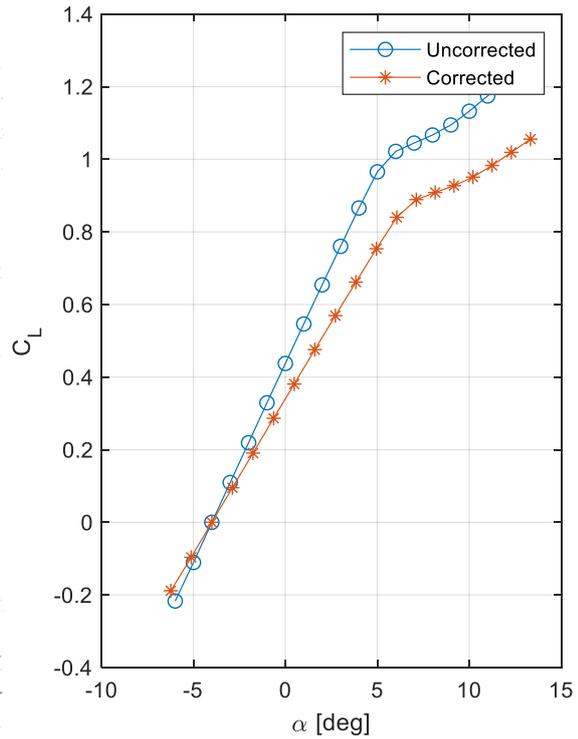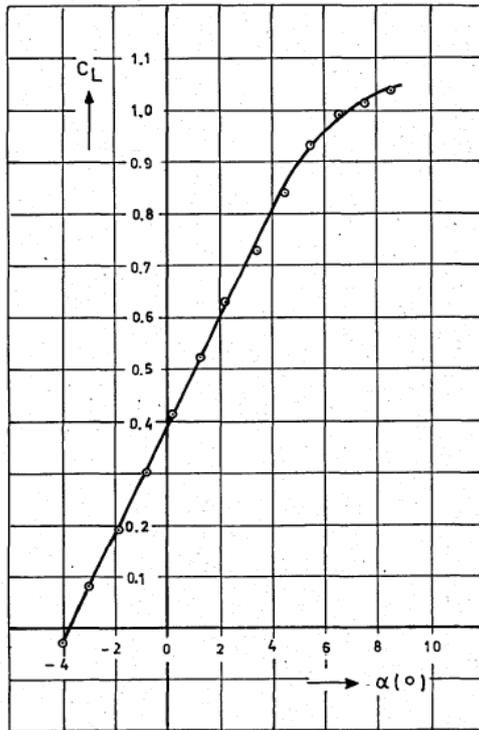
Figure 73: F27 C_L $vs.\,\alpha$, Binkhorst's Lift Curve at $U_\infty \approx 85\,m/s$, $Re = 0.7 \cdot 10^6$, $M = 0.247$ (Left), $WFNVH$ at $U_\infty = 80\,m/s$, $Re = 0.66 \cdot 10^6$, $M = 0.232$ (Right) [54]

The values are very different between the experiment and Binkhorst's data. Lift coefficient at $\alpha \approx 5^o$ is approximately 0.1 higher than the $WFNVH$ corrected data. Unfortunately, there is not much detail given in Binkhorst's correction method. It seems like the values are corrected because they are much less than the uncorrected values, however there is not much to say. Both the lift curve and lift coefficient values are significantly different.

11.1 Propeller-on (Powered) F27 Configuration (Eckert Method)

The $WFNVHP$ configuration is where the propeller thrust is present in the flow. Consequently, there are three more corrections that need to be included in the wall correction. These are trust cleaning, effective advance ratio J_E, and the slipstream blockage factor ϵ_{pb}. For positive thrust conditions, the propeller flow starts to take-over the overall flow characteristics. The expectation is that, these values will get larger with increasing thrust coefficient T_c.

First step is to evaluate the thrust coefficient $C_{T,i}$ in Eckert's method using the $WFNVH$ (zero condition, $J = 0$) data. [Eq. (4.21)] It is also very important to write the definition of T_c for each example because many engineers use different ways of non-dimesionilization.

$$C_T = \frac{T}{S_p q_\infty}$$

(11.150)

There is no isolated propeller to directly implement this formula, however an approximation is possible. Net thrust by the installed propeller can be found using Veldhuis' formula. [4] [68]

$$T_c = \frac{S_w}{S_p}\big(C_D(\alpha, J = 0) - C_D(\alpha, J)\big)$$ (11.151)

Thrust cleaning is supposed to be implemented before blockage corrections, however a compromise has to be made. The corrected value for $C_{D,prop-on}$ cannot be found without a $C_{T,i}$ value. Since there are two propellers in effect, the net thrust by a single propeller $C_{T,i}$ should also be divided by two:

$$T_c = \frac{S_w}{2S_p}\big(C_D(\alpha, J = 0) - C_D(\alpha, J)\big)$$ (11.152)
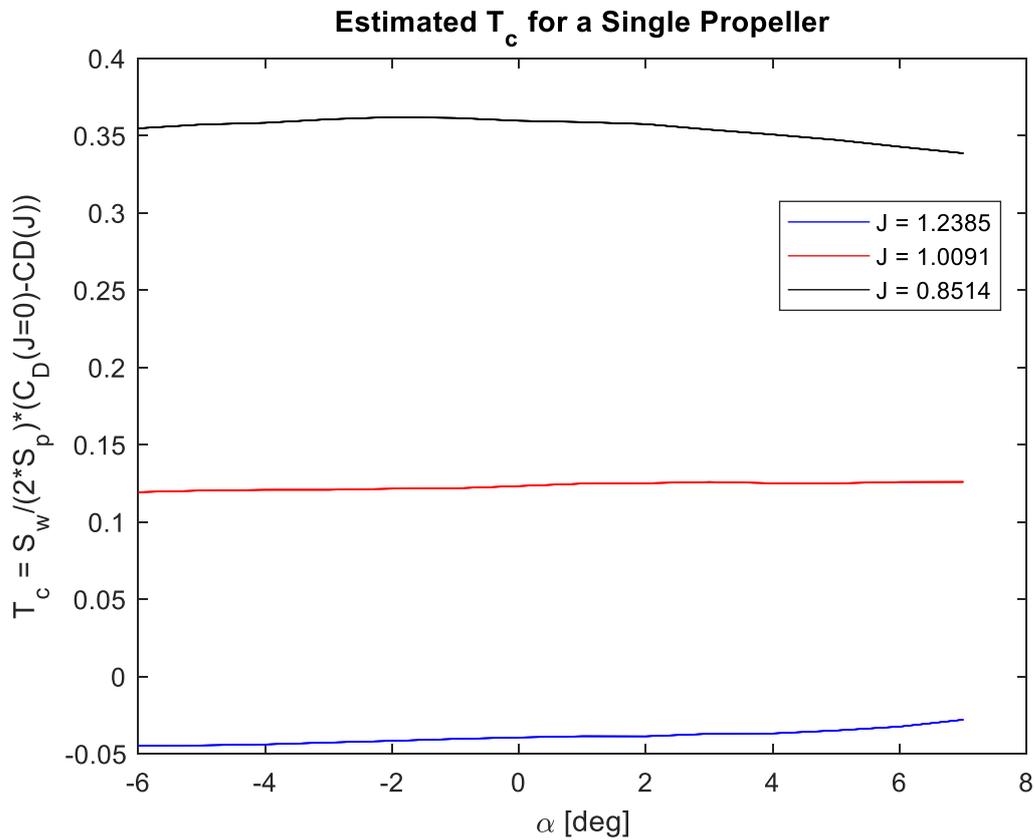
Figure 74: Distribution of Thrust Coefficients at Different α and Different Advance Ratio J

The values chosen for $rps = 220, 270, 320$ are $C_{T,i} = -0.0403, 0.1216, 0.3620$. It is important to observe that $rps = 220$ is not a positive thrust condition, therefore it cannot be used in Eckert's method. [27] The scope of this study is based on positive thrust, so $rps = 220$ won't be a major focus in the analysis. The effective advance ratio was found to be $J_E = 0.9771, 0.8244$ for $rps = 270$ and 320 respectively.

Propeller Slipstream Correction for Wind Tunnel Applications

The measurements were taken at a maximum angle of attack $\alpha = 7°$ because flow separation under propeller thrust is erratic and hard to predict. [21]
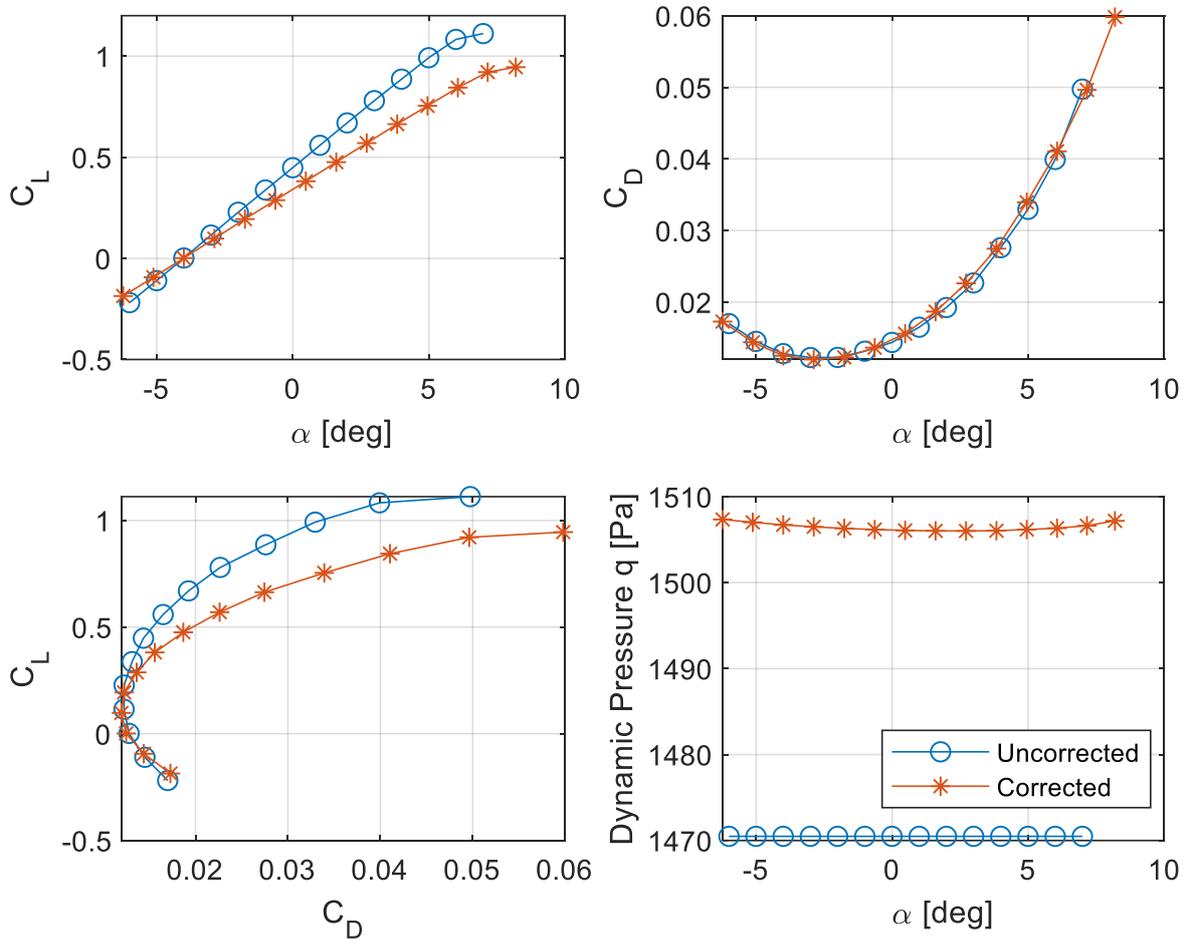
Figure 75: $WFNVHP$ Aerodynamic Parameters at $270\ rps,\ U_\infty = 50\ m/s,\ Re = 0.41 \cdot 10^6, M = 0.145$

For the mid thrust case ($rps = 270$), the change in drag is larger than the high-thrust case. It is also apparent that the drag is negative for the high thrust case. Somewhere between 270 and 320 rps, the drag coefficent of the F27 turns negative. The maximum lift achievable is higher for the mid-thrust case. Comparing the drag curve of the two, the drag correction is larger drag coefficient is negative. This does not mean lower drag has a higher correction value however higher discrepancies are expected between the corrected and uncorrected flow at higher thrust. One of the main reasons for an overall small drag correction factor might be that the Eckert correction does not present a thrust dependent drag coefficient correction. (It is only corrected for induced drag.) Coming up with a drag coefficient correction for thrust effects may be a future work. However, lift coefficient is usually the main focus when it comes to propeller slipstream effect.
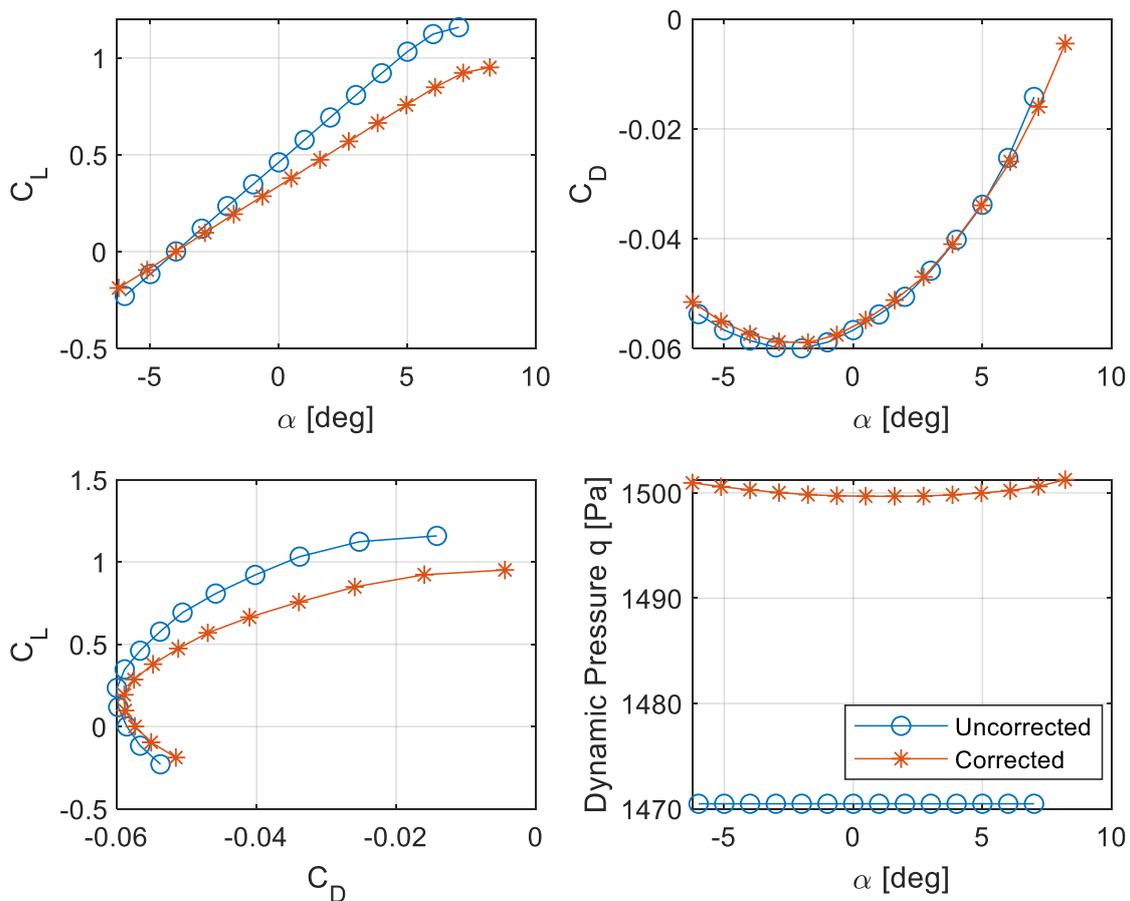
Figure 76: $WFNVHP$ at $320\ rps,\ U_\infty = 50\ m/s,\ Re = 0.41 \cdot 10^6, M = 0.145$

The figures presented below show the impact of each correction for a propeller installed aircraft. Lift interference by the wing is still the primary effect, though the second effect differs greatly depending on the advance ratio. Tail interference has slightly more impact on the mid-thrust configuration. However, Eckert method takes over at high thrust configuration. This shows the eminence of the Eckert method for propeller-driven aircraft. For very high thrust configurations (i.e. lift-off) Eckert correction may be the primary correction factor among other wall interference effects. Lastly, slipstream blockage should be mentioned. Slipstream blockage is a negative blockage, so it has an adverse effect compared to all other blockage corrections. From the figures, the blockage correction is significantly reduced. It can be said that the slipstream effect has a balancing effect for the confined mass flow in a constrained flow.
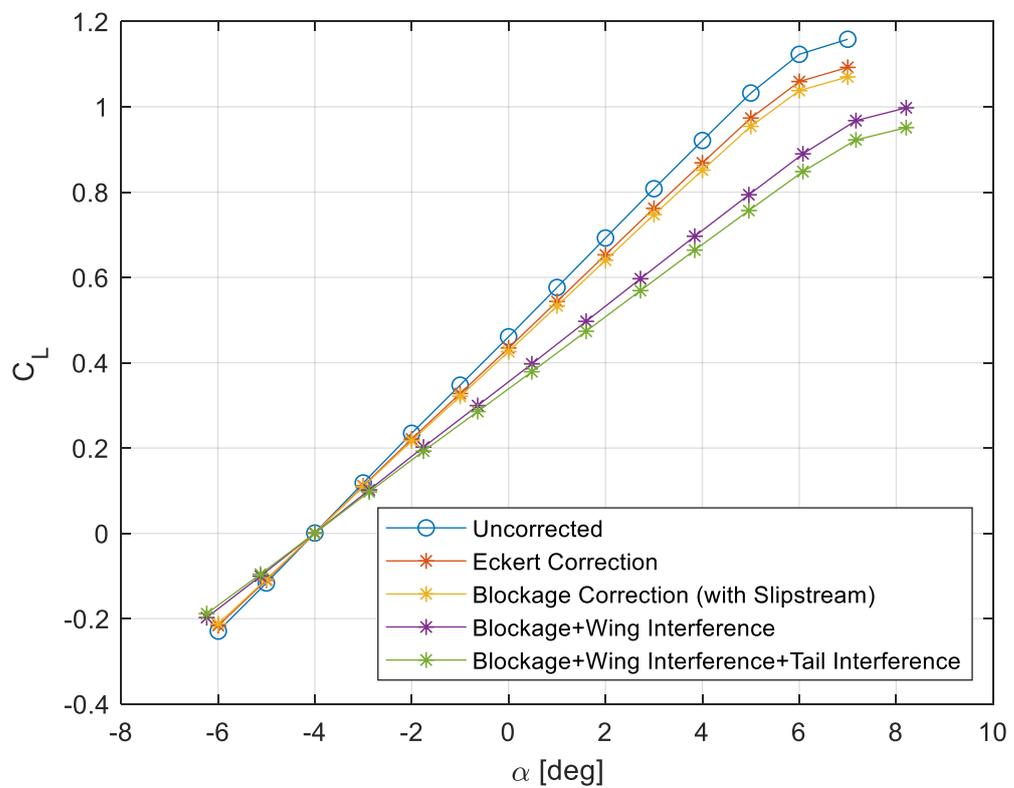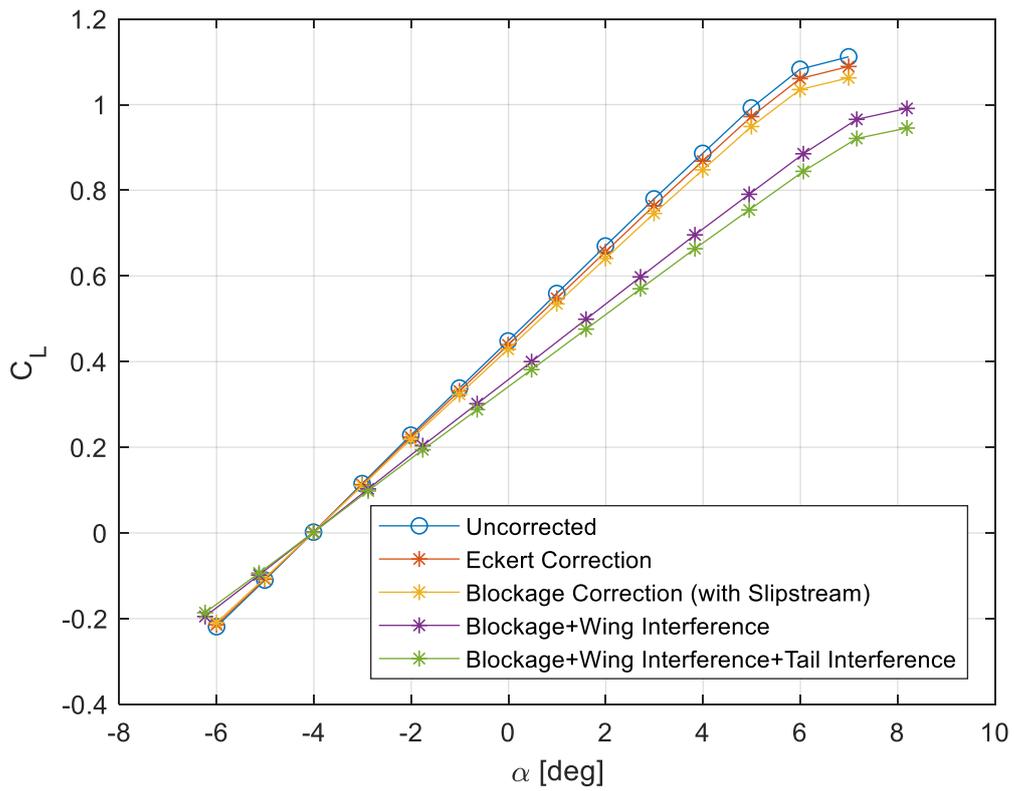
Figure 77: Visualized Impact of Correction Methods including Eckert $rps = 320$ (Down), $rps = 270$ (Up), $U_\infty = 50\,m/s$, $Re = 0.41 \cdot 10^6, M = 0.145$

The body correction is based on the presence of the nacelle behind the propeller. It is a simple correction, yet it shows a non-dismissible shift in the advance ratio. It cannot be determined if this correction is similar to reality, but it is significant enough to be presented.
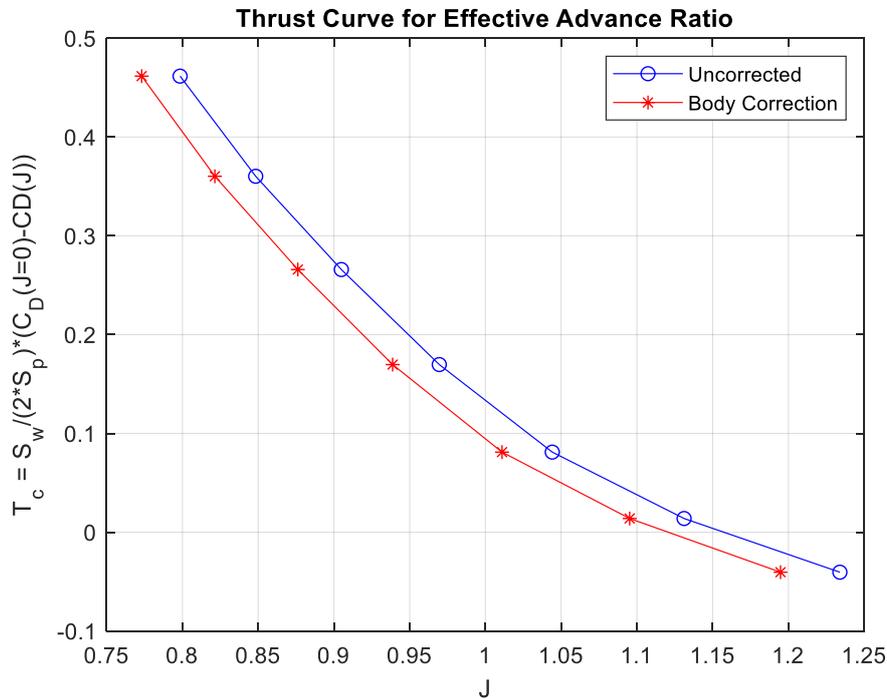
Figure 78: Body Correction J_E for RPS Sweep, $U_\infty = 50\ m/s$, $Re = 0.41 \cdot 10^6$, $M = 0.145$

11.3 Lift Distribution along the Wing and Total Lift in Vorticity Panel Method

The vorticity panel method was prepared to be a comparable model with the wind tunnel tests. Moreover, it allows to visualize the lift distribution along the span. Before comparing the lift correction of different methods, the lift distribution along the span will be examined. These results are important because they are the most crucial indicators of a correct slipstream model.

There are three major factors that effect the lift distribution along the span for the same flow velocity U_∞. The first one is the change of angle of attack α. The second is the propeller rotation direction and the third is the advance ratio.

Both the circulation Γ and section lift coefficient $c_l c$ change with increasing angle of attack. The figures given below are the outboard up propeller direction. It can be seen that circulation graph is very smooth. The peaks represent the propeller-up direction and the fuselage. The fuselage peak is caused by the Giesing solution. It is expected to have a decline in circulation with the classic fuselage modelling by Multhopp. By forcing the potential jump to happen at the wing root, the wing root is clearly shown as a nadir(bottom).
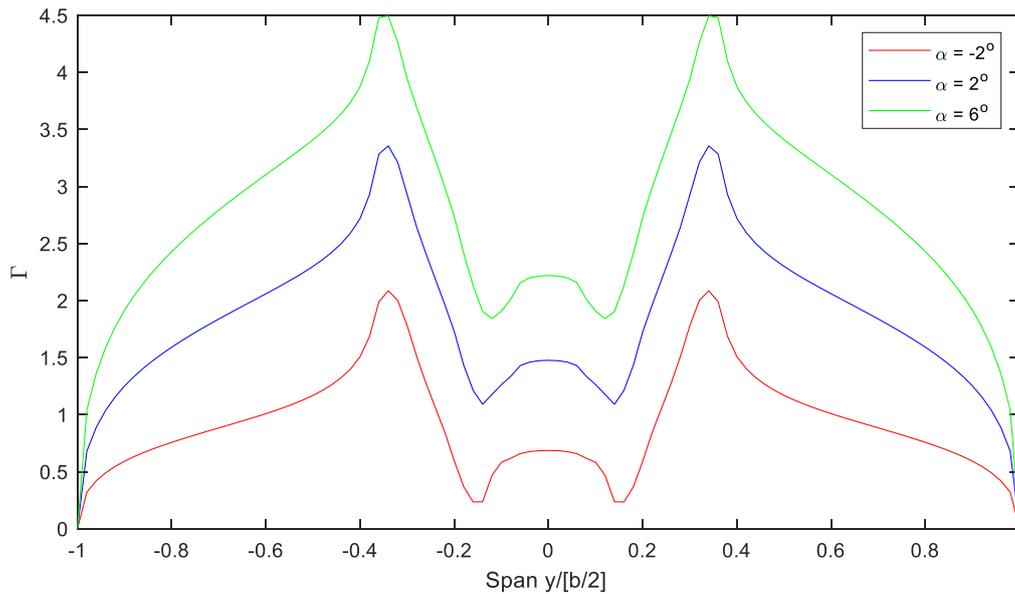
Figure 79: Circulation Distribution along the F27 Wing Span, $U_\infty = 50\ m/s$, $Re = 0.41 \cdot 10^6$, $M = 0.145$, $J = 0.801$, OU

The section lift coefficient gives more detail about what is going along the wing. The effects of the propeller rotation are clearly identifiable. The overall increase in lift is also observed with increasing angle of attack. This distribution is parallel with what was observed in previous research that was explained in Chapter 3.
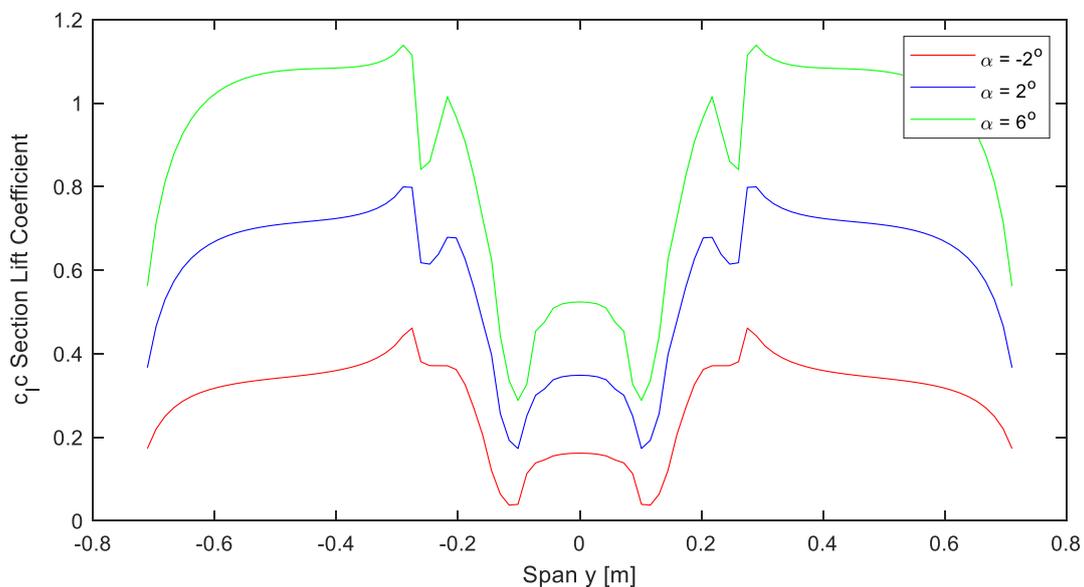
Figure 80: Section Lift Distribution along the F27 Wing Span $U_\infty = 50\ m/s$, $Re = 0.41 \cdot 10^6$, $M = 0.145$, $J = 0.801$, OU

Another major parameter that alter the lift distribution along the wing is the rotation direction of the propellers. There are three directions considered for this thesis. These are Inboard Up (IU),

Propeller Slipstream Correction for Wind Tunnel Applications

Outboard Up (OU) and Co-Rotating (CO). Co-rotating means that the propeller spin in the same clockwise direction. Even though the distribution is asymmetrical, it is usually easier to manufacture and maintain co-rotating propellers. [69]

In the overall circulation distribution co-rotating propellers change the fuselage lift drastically. It is also predicted that it changes the rolling characteristics of the aircraft drasrically, but it is outside the scope of this thesis. Other than the change of fuselage lift, co-rotating propeller is similar to a mix of both IU and OU conditions.
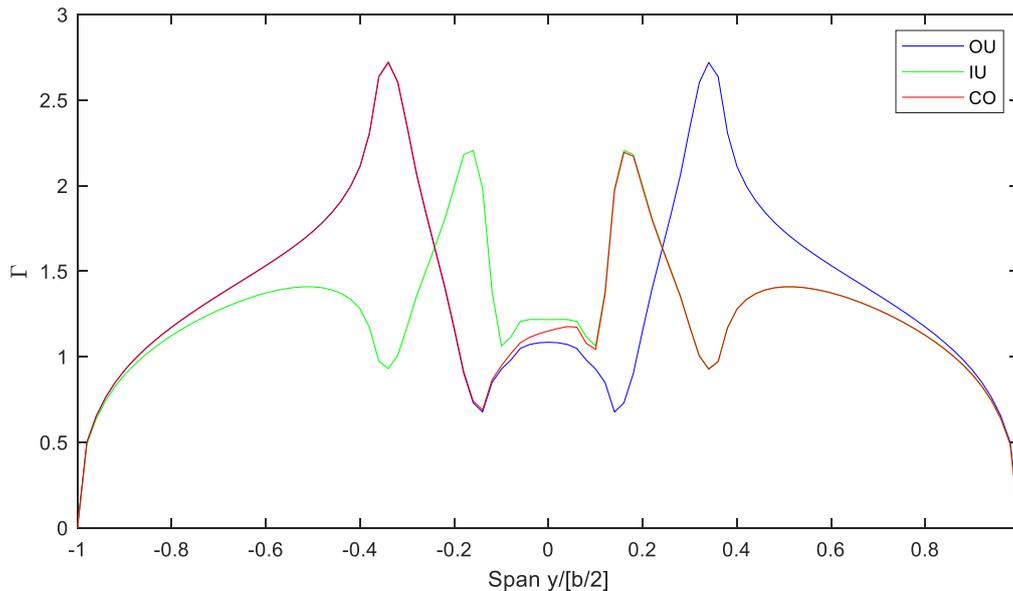
Figure 81: Circulation Distribution along the F27 Wing Span, $U_\infty = 50\ m/s$, $Re = 0.41 \cdot 10^6$, $M = 0.145$, $J = 0.801$, $\alpha = 0^o$

More can be said about the difference between inboard-up and outboard-up directions. It was observed in the Fokker 50 experiments that the panel method overestimated the inboard up lift generation. [14] With the Giesing solution, it seems that the overshoot is ameliorated. The only way to truly see if the IU condition is realistic is to look at the overall lift generation, which will be explored further in the chapter.
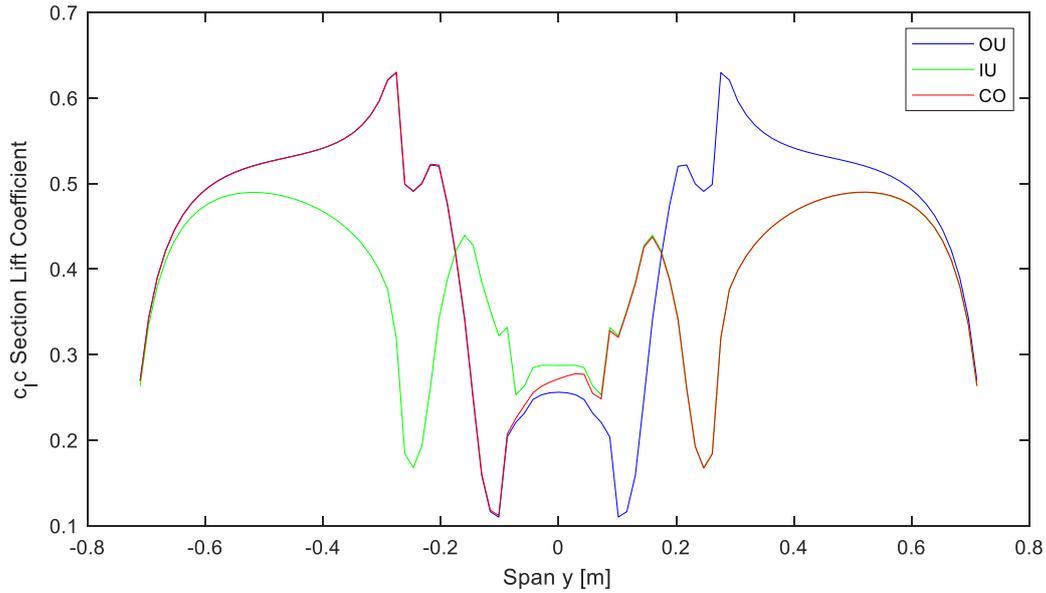
Figure 82: Section Lift Distribution along the F27 Wing Span $U_\infty = 50\ m/s$, $Re = 0.41 \cdot 10^6$, $M = 0.145$, $J = 0.801$,, $\alpha = 0^o$

The final important parameter is the change in lift distribution with varying thrust. Two values for advance ratios J are chosen for the comparison. $RPS = 270$ and 320 are the conditions comparable to wind tunnel results, so it can give an impression on what is happening with increasing thrust.

The immediate observation is that the lift and circulation increases with increasing thrust. Unlike what the Eckert method and Patterson method suggest, the circulation increase is not in the slipstream tube but on the bodies in close proximity. The fuselage lift induced by the slipstream is clearly visible, which should be taken account in the correction method.
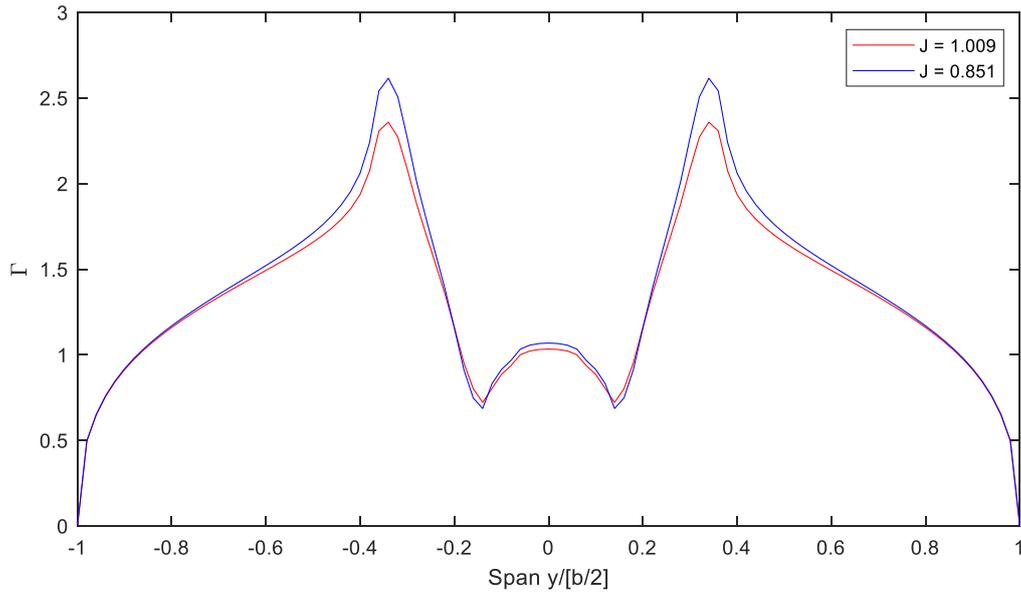
Figure 83: Circulation Distribution along the F27 Wing Span, $U_\infty = 50\ m/s$, $Re = 0.41 \cdot 10^6$, $M = 0.145$, $\alpha = 0^o$, OU

The rotational feature of the propeller slipstream is stronger with higher thrust; hence, the negative local angle of attack at the downward going blade is augmented with higher thrust condition. Furthermore, from the section lift coefficient, it can be deducted that the rotation of the blade is not a purely symmetrical behavior.
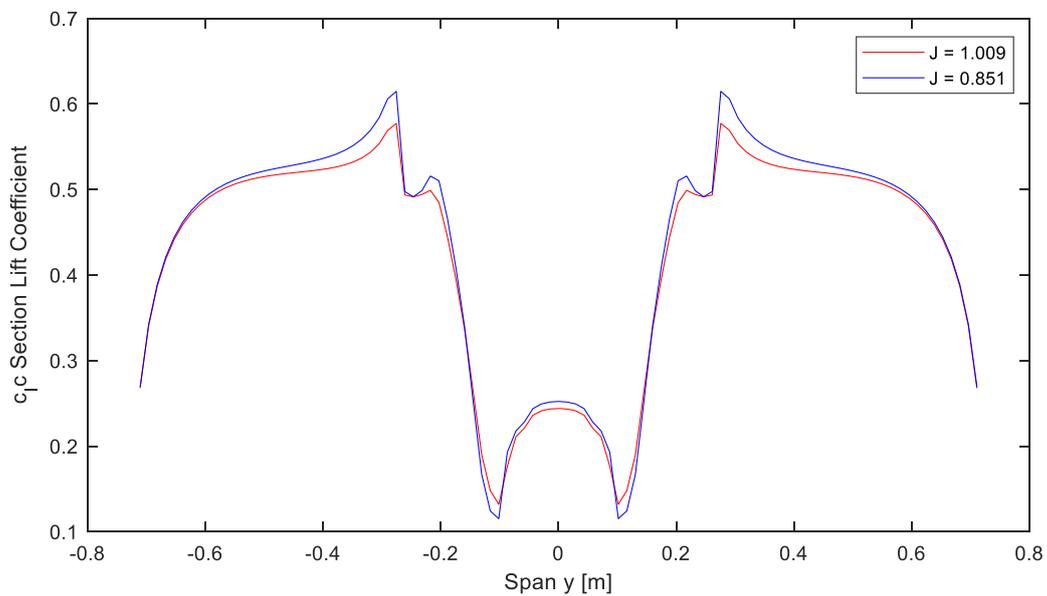
Figure 84: Section Lift Distribution along the F27 Wing Span $U_\infty = 50\ m/s$, $Re = 0.41 \cdot 10^6$, $M = 0.145$, $\alpha = 0^o$, OU

There are no sources for the F27 wing lift distribution but Veldhuis is a major source for the F27 model aircraft characteristics. [4] The values represented below are corrected for thrust and wind tunnel wall interference.
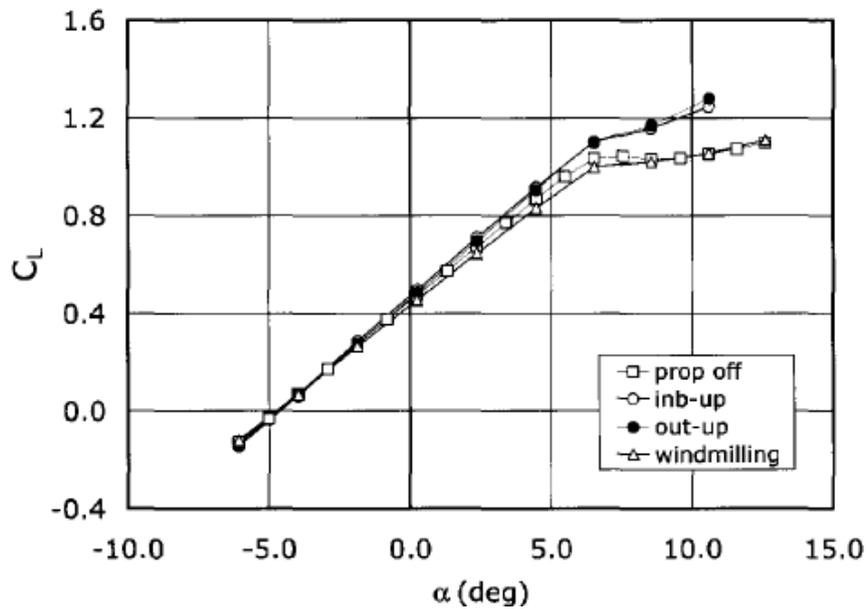
Figure 85: F27 Propeller Installed Wind Tunnel C_L $vs.$ α, $U_\infty \approx 50\ m/s$, $Re = 0.41 \cdot 10^6$ [4]

The measurements in the panel method were taken for advance ratio $J \approx 0.81$, Veldhuis operates around $0.8 < J < 0.825$. From the figures, the lift curves are in a close range. Both of them have approximately the same curve slope. The linear range is captured well. The change in lift curves are deducted to come from the changing wing chord length c behind the up-going propeller blade. Fokker F27 wings are tapered from root to tip therefore more lift force is generated. Additionally, the propeller rotation does not cause a symmetrical lift increase/decrease ($\Delta L_{rot} \neq 0$).
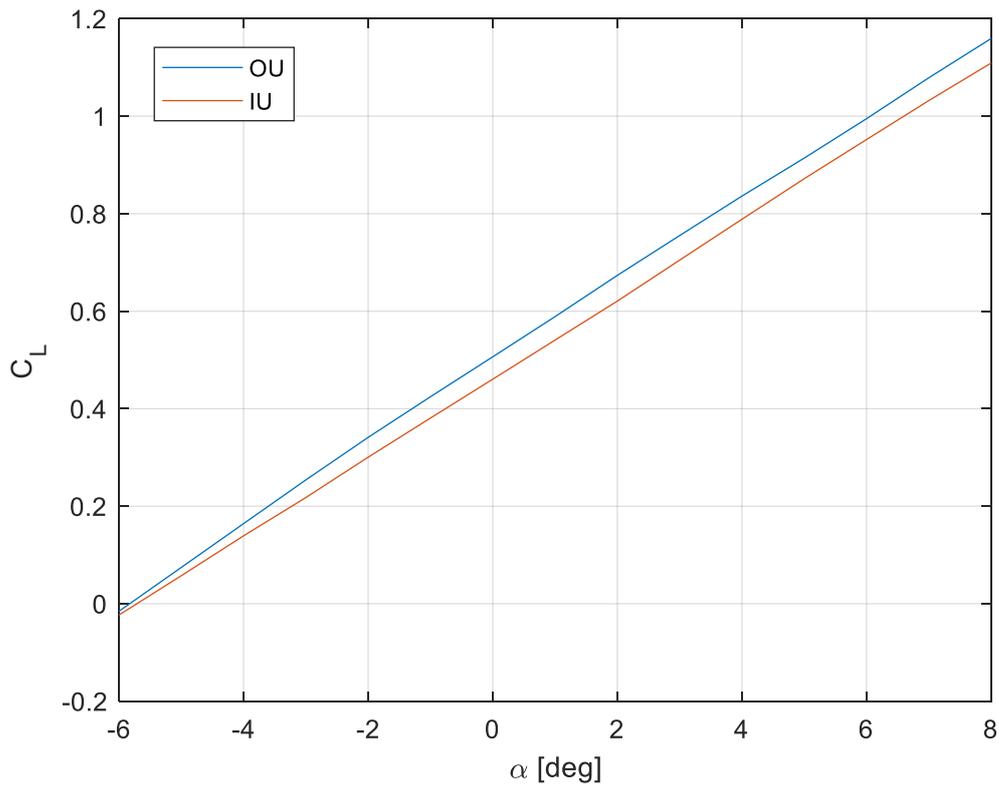
Figure 86: F27 Panel Method C_L $vs.\,\alpha$, $U_\infty = 50\,m/s$, $Re = 0.41 \cdot 10^6$, $M = 0.145$, $J \approx 0.81$

The variation of lift coefficient with varying advance ratio can also be observed from Veldhuis' paper. The change in lift from low thrust to high thrust condition ($J \approx 1.05\ to\ 0.75$) is between 0.03 to 0.04.
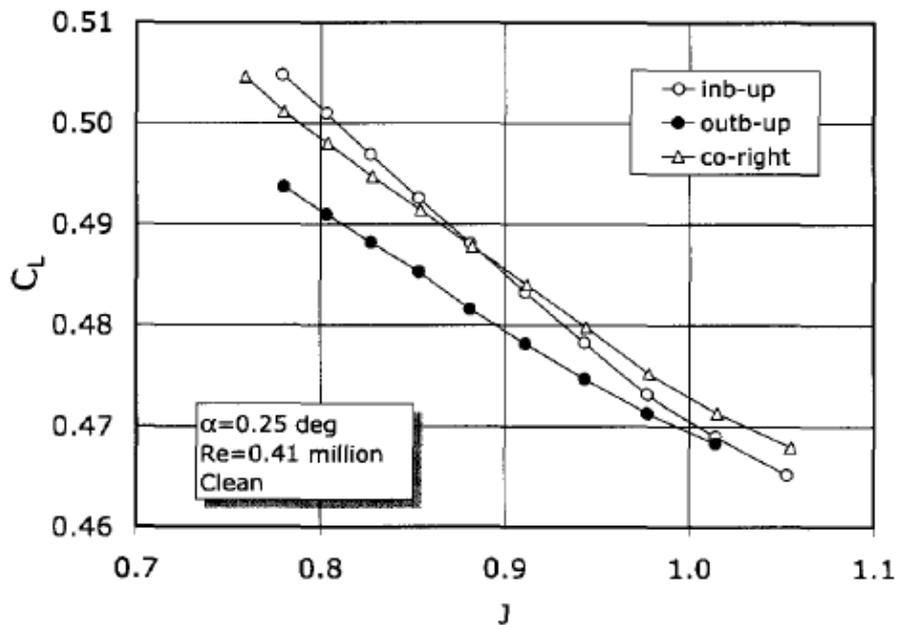
Figure 87: F27 Propeller Installed Wind Tunnel C_L $vs.\,J$, $U_\infty \approx 50\,m/s$, $Re = 0.41 \cdot 10^6$ [4]

The effects of propeller rotation direction are reversed according to Veldhuis' experiments. The lift carry over effect due to slipstream over the fuselage is modeled correctly. The rankings between different propeller rotation configurations are different than Veldhuis' results. The OU and CO conditions are closer to the experimental magnitudes at the given advance ratio. The IU condition seems like an outlier in magnitude but the change of lift is the most similar to Veldhuis' results. The change in lift between low to high thrust condition ($J \approx 1.1 \; to \; 0.8$) is approximately between 0.025 and 0.045.
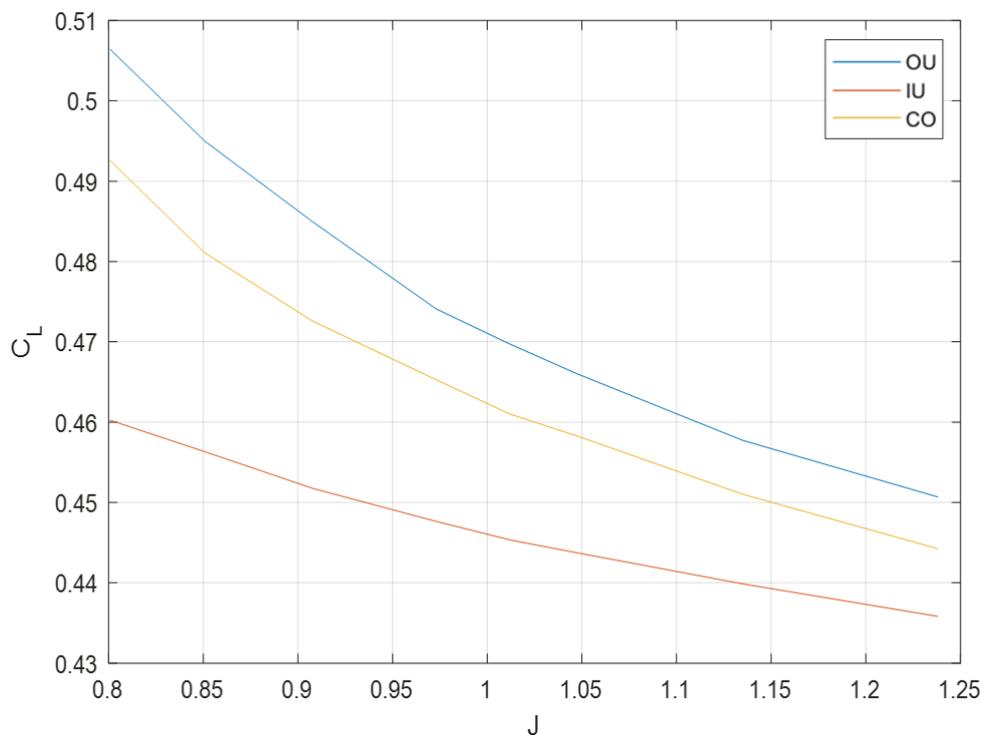
Figure 88: F27 Panel Method $C_L \; vs. \; J, \; U_\infty = 50 \; m/s, \; Re = 0.41 \cdot 10^6, M = 0.145$

Ultimately, lift results from the vorticity panel method seem reliable for correction. The values are within the range of previous empirical studies and the slipstream effect is properly modeled with proof in wing lift distribution.

11.4 Comparison of Thrust Cleaning Methods

There are three thrust cleaning methods that are going to be compared in this section. The first one is Eckert. The computation for Eckert can be observed evidently in Section 11.2, so it won't be repeated again. The second correction is the Patterson method. Since it has not been shown how the calculation for Patterson is achieved, it will be described here.

The formula for Patterson is described in Chapter 4. [Eq. (4.27)] The important values in the equation are i_p, α_g, V_∞, V_p and β. It is important to note that these values are at the wing local reference frame. The value for slipstream angle i_p comes from the propeller installation angle, which is approximately $\approx 3^o$. The geometric angle of attack is the addition of dihedral angle and angle of attack. The flow velocity V_∞ is pre-determined and the propeller velocity V_p is obtained from the panel method. Finally, the slipstream diameter factor β is obtained from the graph given below.
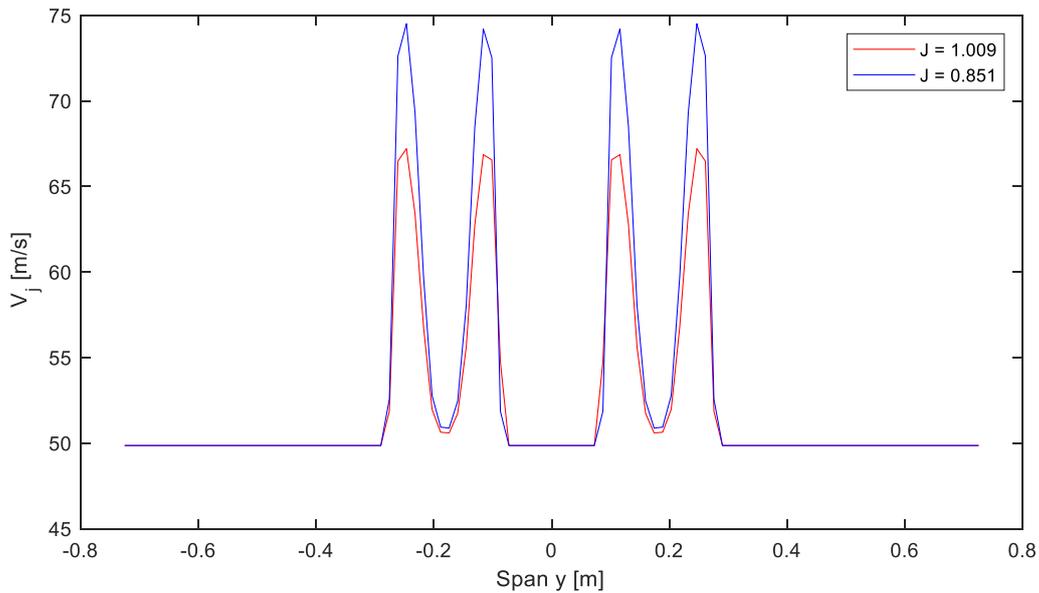
Figure 89: Jet Velocity V_j [m/s] Along the F27 Wing (Peak Velocity is Used for Patterson)

The values for u/c and R/c are found from the blueprint and they are 1.09 and 0.625 respectively. The slipstream velocity ratio V_j/V_∞ for $J = 1.009$ is 1.34 and for $J = 0.851$ is 1.48. The values chosen for β are 0.98 and 0.95 for $J = 1.009$ and 0.851 respectively.
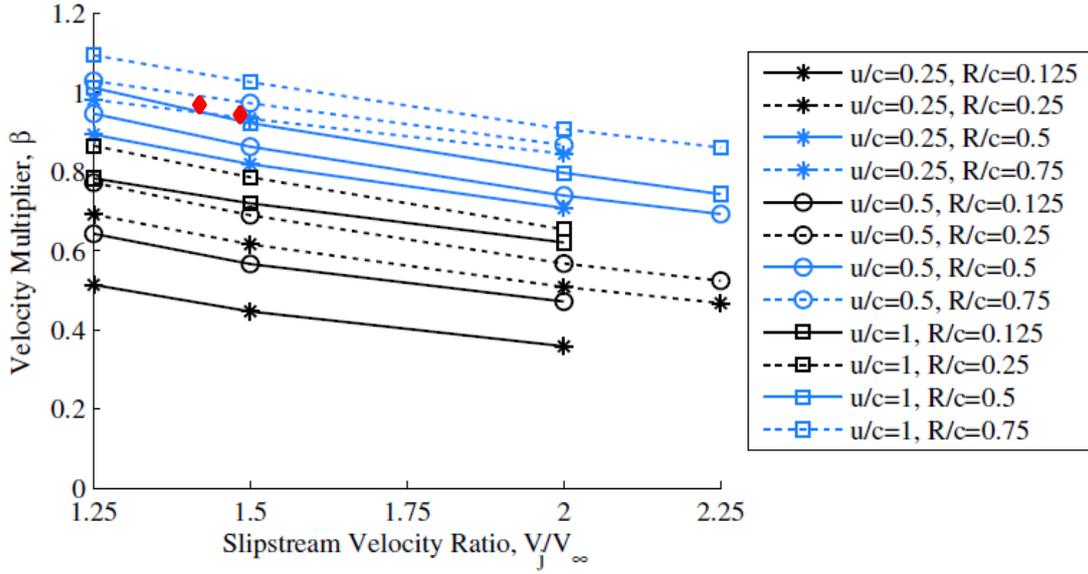
Figure 90: β Values for Various Propeller/Wing Configurations [50] (Red Dots are the Corresponding Points to the Experiment)

There is one final issue with the Patterson correction. The value for $\sin(\alpha_g)$ can become 0 and the solution is undefined. It is assumed that:

$$\frac{\sin(i_p)}{\sin(\alpha_g)} \sim 1$$

This is done because the solution is unattainable otherwise. The new formula can be re-written as:

$$\frac{\Delta L'}{L'_\infty} = \left(1 - \frac{\beta V_p}{V_\infty}\right) \frac{\sqrt{V_\infty^2 + 2V_\infty \beta V_p \cos(\alpha_g + i_p) + \left(\beta V_p\right)^2}}{V_\infty} - 1 \qquad (11.153)$$

The final thrust cleaning method is the new proposed lift correction. Concisely, it was acquired using the forces that each aircraft component produced.

$$\Delta L = \sum F_{z,prop-on} - \sum F_{z,prop-off} \qquad (11.154)$$

More detailed description for the components that are included in the force calculation:

$$\sum F_{z,prop-off} = F_{z,wing} + F_{z,fuselage} + F_{z,horizontal\,tail} + F_{z,vertical\,tail}$$
$$(11.155)$$

$$\sum F_{z,prop-on} = F_{z,propeller} + F_{z,wing+slipstream} + F_{z,fuselage} + F_{z,horizontal\ tail}$$
$$+ F_{z,vertical\ tail}$$

(11.156)

Finally the change in lift coefficient is:

$$\Delta C_L = \frac{\Delta L}{q_\infty S_w}$$

(11.157)

The results for the thrust cleaning corrections are presented in two different thrust levels. These are $J = 1.009$ and $J = 0.851$. Since the difference is hard to observe with naked eye, the results are divided into four sections, in which all the values can be seen. The thrust uncorrected lift coefficient and propeller-off data are also represented to show the significance of thrust cleaning. Each figure can be observed in the following description:

1) $RPS = 270$
   a. $\alpha = -6^o\ to - 3.5^o$ [Figure 91]
   b. $\alpha = -2^o\ to\ 0.5^o$ [Figure 92]
   c. $\alpha = 1^o\ to\ 3.5^o$ [Figure 93]
   d. $\alpha = 4^o\ to\ 6.5^o$ [Figure 94]
2) $RPS = 320$
   a. $\alpha = -6^o\ to - 3.5^o$ [Figure 95]
   b. $\alpha = -2^o\ to\ 0.5^o$ [Figure 96]
   c. $\alpha = 1^o\ to\ 3.5^o$ [Figure 97]
   d. $\alpha = 4^o\ to\ 6.5^o$ [Figure 98]

Figure 91: C_L $vs.$ α for Uncorrected and Corrected Values, $U_\infty = 50\ m/s$, $Re = 0.41 \cdot 10^6$, $M = 0.145$, $J = 1.009$, $\alpha = -6^o\ to - 3.5^o$

Figure 92: C_L $vs.$ α for Uncorrected and Corrected Values, $U_\infty = 50 \, m/s$, $Re = 0.41 \cdot 10^6$, $M = 0.145$, $J = 1.009$, $\alpha = -2^o$ to 0.5^o

Propeller Slipstream Correction for Wind Tunnel Applications

Figure 93: C_L $vs.$ α for Uncorrected and Corrected Values, $U_\infty = 50\ m/s$, $Re = 0.41 \cdot 10^6$, $M = 0.145$, $J = 1.009$, $\alpha = 1^o\ to\ 3.5^o$

Figure 94: C_L $vs.$ α for Uncorrected and Corrected Values, $U_\infty = 50\ m/s$, $Re = 0.41 \cdot 10^6$, $M = 0.145$, $J = 1.009$, $\alpha = 4^o\ to\ 6.5^o$

Figure 95: C_L $vs.$ α for Uncorrected and Corrected Values, $U_\infty = 50\ m/s$, $Re = 0.41 \cdot 10^6$, $M = 0.145$, $J = 0.851$, $\alpha = -6^o\ to -3.5^o$

Figure 96: C_L $vs.$ α for Uncorrected and Corrected Values, $U_\infty = 50\ m/s$, $Re = 0.41 \cdot 10^6$, $M = 0.145$, $J = 0.851$, $\alpha = -2^o\ to\ 0.5^o$

Propeller Slipstream Correction for Wind Tunnel Applications
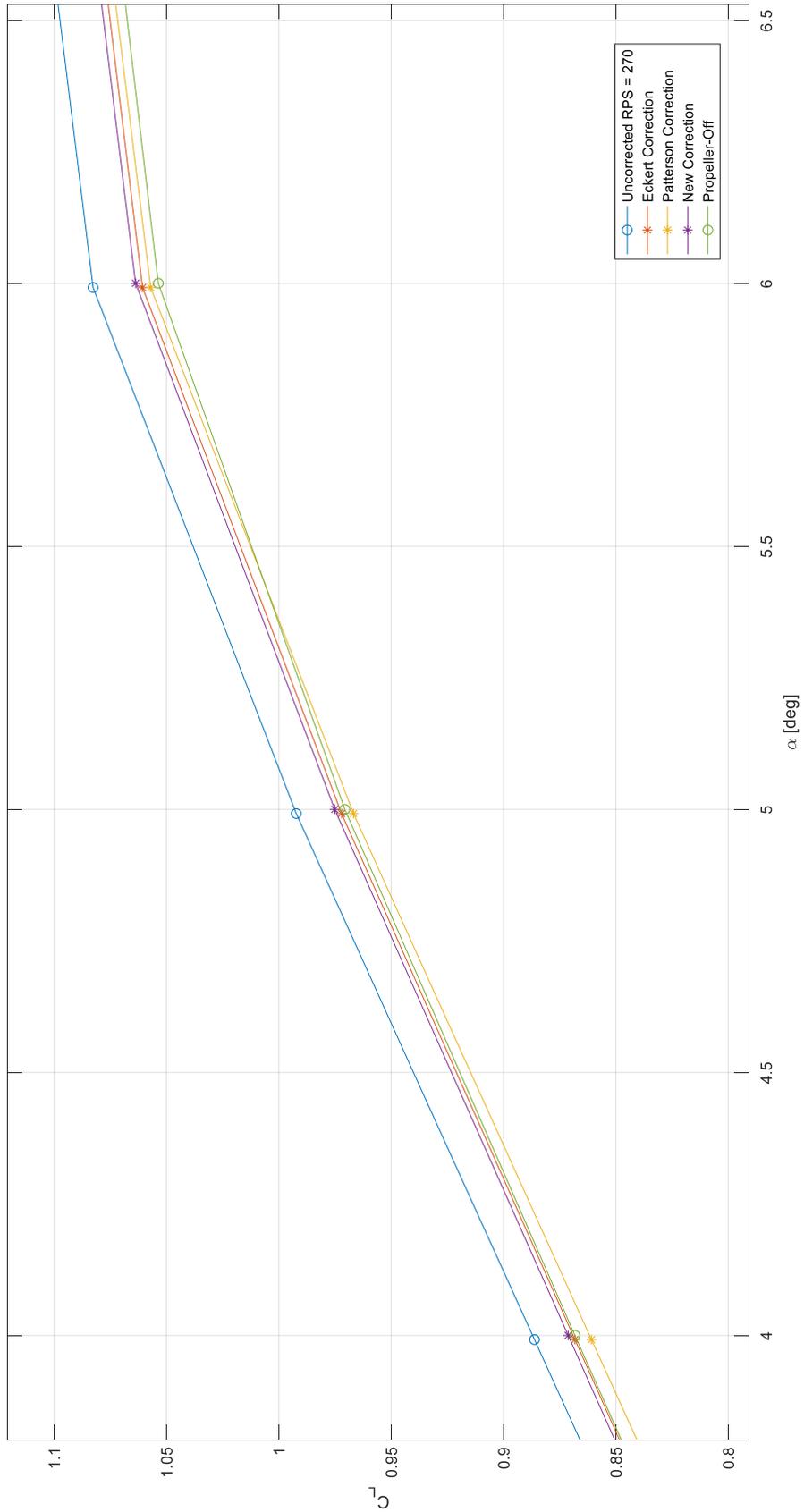
Figure 97: $C_L \ vs. \ \alpha$ for Uncorrected and Corrected Values, $U_\infty = 50 \ m/s$, $Re = 0.41 \cdot 10^6$, $M = 0.145$, $J = 0.851$, $\alpha = 1^o \ to \ 3.5^o$
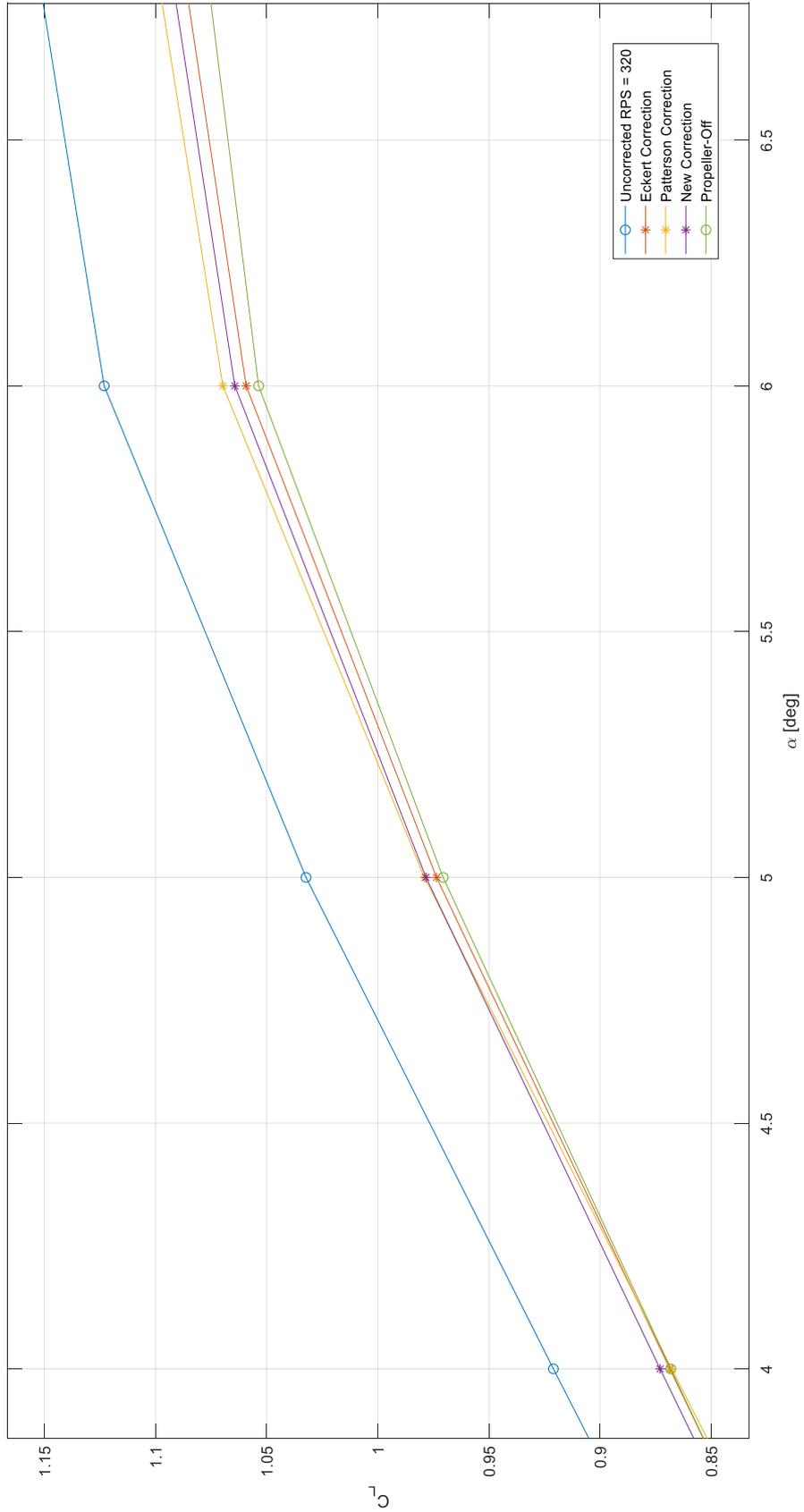
Figure 98: C_L $vs.$ α for Uncorrected and Corrected Values, $U_\infty = 50\ m/s$, $Re = 0.41 \cdot 10^6$, $M = 0.145$, $J = 0.851$, $\alpha = 4^o$ to 6.5^o

From an overall perspective, it can be observed that the Patterson method is the least accurate correction among the three correction. If $WFNVH$ (propeller-off) data is taken as the reference point, then a comparison between the Eckert method and the new proposed method can be made. In the low angle of attack region (between -6° to 2°), the new thrust cleaning method is closer to the propeller-off data, in the high angle of attack region (between 2° to 7°) Eckert method is significantly closer to $WFNVH$ configuration. The accuracy of the new proposed method declines with increasing angle of attack.

Patterson correction deviates from the desired value at low angles of attack, however in a small region between 3° to 5°, it gives values closer to propeller-off data. Both the slope and the magnitude of the lift coefficient with the Patterson correction is not similar to the expected lift curve. Therefore, it is safe to say that it is a coincidence that Patterson correction gives close results in 3° to 5° range. It is safe to say that the Patterson correction is an overestimation of the slipstream effect.

The Eckert method solution is simple and robust as it can be seen in the figures above. The accuracy of the correction increases with increasing angle of attack α. The panel method is the opposite way. New correction based on the panel method is much more accurate in the area of low angle of attacks. The accuracy is lost with the increasing angle of attack after $\alpha > 6^o$. However, Eckert method is also underestimating, even if it is relatively smaller than the panel method correction.

The change in thrust from mid-thrust ($rps = 270$) to high-thrust ($rps = 320$) condition also gives some idea about, which correction may be better than the other. In the mid-thrust condition, new correction and Eckert correction are hard to separate from each other. Since slipstream effect is less in lower thrust conditions, the thrust corrections are also small. Eckert correction seems like overall the most accurate in mid-thrust condition. The panel method correction has an edge only at high-thrust low angle of attack condition.

As a result, Eckert method would be the overall selection for a simple robust correction. The panel method can be used for correction as well, however it requires much more resource. The advantage of the panel method is to be able to observe the flow at a specific location on the aircraft. It can be concluded that, it is important to include the slipstream rotation in the correction method to investigate the flow at a chosen section. However from an overall perspective, if the effect of dynamic pressure increase is calibrated with thrust and corrected with an empirical scaling factor, a precise correction can be achieved.

12

DISCUSSION

This chapter answers the research questions and discusses the results obtained in the previous chapter. The first three section discusses the questions that are formulated in Chapter 1. The fourth section answers questions related to the results that are presented in Chapter 11.

12.1 Discussion on Background Information and Concepts

1) What is wall interference effect for closed wind tunnels? What kind of corrections are used for propeller driven aircraft inside the wind tunnel?

The wall interference effect is the constrained flow conditions due to the geometry of the wind tunnel. The bounded flow inside the closed wind tunnel is not the same with free-flow conditions. Therefore, there are some standard effects that needed to be considered that wouldn't exist in unbounded flow. The first correction is called blockage and it is basically the change in cross-sectional area due to solid bodies and wakes inside the constrained flow. The second correction is called lift interference due to the circulation of the wing inside closed test section. For propeller driven aircraft, there is a third correction which is called thrust cleaning. Thrust cleaning is based on slipstream effect caused by the propeller and violates the assumptions of the previous two corrections. Therefore, it is essential to correct for thrust.

2) What are the observed effects of propeller slipstream? How was it investigated in previous research?

Propeller slipstream effect is the change in flow properties behind the rotational propeller flow and its close proximity. In reality slipstream is an unsteady, three-dimensional effect. However steady methods are also known to approximate the overall slipstream effect.

Slipstream increases dynamic pressure while generating thrust and it also changes the incoming flow angle with substantial variation along the span of the wing. Usually the latter effect is assumed to be ineffective or symmetrical. However, it has been shown that it may be an over simplification.

Usually the numerical methods used for slipstream modelling are concentrated in specific flow regions. As slipstream is a three-dimensional and unsteady effect, the specific solution method should be built around the desired flow conditions. Moreover, the propeller cannot

be designed as a purely separate body because the interference between propeller/wing/fuselage/nacelle have additional implications on the lift distribution.

In the past, slipstream was investigated using a visual aid like Particle Image Velocimetry and pressure readings from wind tunnel experiments. For computer modelling, potential flow solutions, panel methods, Reynolds Averaged Navier-Stokes solutions and some commercial CFD solvers have been used. There advantages and disadvantages of these methods mostly rely on simplicity vs. available computational resources.

3) Which methods are the contemporary thrust (slipstream) cleaning methods? What are their strengths and shortcomings?

Slipstream cleaning is specifically used for propeller-installed aircraft where the wing is in the downwash of the propeller flow. The main problem with uncorrected propeller data is that the primary corrections like blockage and lift interference are incorrectly estimated. The potential flow assumptions are violated with increasing momentum in the system, so it is crucial to get rid of propeller generated lift.

The industry standard method for thrust correction is the Eckert method. Eckert method assumes that slipstream only increases the dynamic pressure in the propeller-wetted wing section and the flow is uniform. The rotation of the flow is added in the equation as a constant. The advantage of this equation is that it uses already known aircraft geometric parameters and thrust. It is robust and easy to implement. Still, it does not include slipstream rotation in its assumption.

The second correction method is the Patterson method. Patterson method was developed to measure the slipstream for multi-rotor and tip-mounted propeller experimental aircraft. The slipstream velocity is also assumed to be uniform but the effect of propeller installation angles is present. The local change of attack is assumed to be symmetrical so it is not accounted.

The proposed correction method involves both dynamic pressure increase and change of angle of attack. Also, the interference between different aircraft components are also included in the solution.

12.2 Discussion on Method and Propeller-Driven Aircraft

1) Which solution method can accurately model the slipstream rotation in order to achieve a reliable correction?

There were three main criteria for the flow solver. These were satisfying the unique flight condition and boundary conditions, collection of singularities to represent an accurate model and the variable slipstream shape and panel distribution. Surface Voritcity Panel Method was chosen as the initial method, however there were problems encountered with the implementation.

The panel method SVPM was a non-linear method. The initial aim in using a non-linear surface vorticity method was the opportunity to model the slipstream with a non-prescribed slipstream shape and strength. However, due to computational complexities (time constraint & low tolerance) another solution was sought after. It was later decided to utilize a linear vorticity panel method with proven similarity and precision of the SVPM model. The

new model is user-friendly and faster. However, it doesn't allow calculations at high angles-of-attack. There is still room for improvement in the vorticity panel method to expand.

2) How is the flow solution formulated (assumptions, method, implementation) for propeller slipstream? Is there a way to verify the accuracy of the flow solver?

The first major alteration for the SVPM panel code was to change it from a non-linear model to a time-stepping linear model. The new model has been proven by Schroijen to be closely similar in its results. The computation time was drastically improved with the assumption of strong influence of only neighboring panels.

It is important to use a vortex theory based method for the modelling of vorticity. The model improves with the core vortex assumption with a slipstream vortex sheet at the circumference of the slipstream boundary. Blade Element Method implementation into vortex theory is particularly helpful because it establishes an initial condition that can be used as an input. Dividing the propeller into discreet points with radial and circumferential stations ensures the magnitude and direction of the induced velocity vector at a higher precision. In return, the extra lift occurs at a well-defined location with a low-discrepancy result.

The influence of the wing on the propeller was found to be dismissible. The design of the empennage was kept as simple as possible because it was not the main focus of this study.

3) What are the main aircraft components that directly influence overall aircraft lift?

The aircraft components are divided into 4. These are propeller, wing, fuselage and empennage. Also, the slipstream is defined as an additional component but it is considered an effect and it is included with the wing. This was necessary in order to have a complete comparison with the wind tunnel results.

4) What is the influence of bodies (fuselage, nacelle) inside the close proximity of propeller slipstream area? Are they directly or indirectly altering the lift distribution?

Interference of the fuselage was modeled in two ways. First was Multhopp's approach, which results in a dip in the circulation. It changes the lift evaluated at the quarter chord considerably. The second was Giesing's potential distribution approach where the perturbation potential was forced to resolve at the wing root trailing edge. It creates an additional step-like response in the overall circulation. Since the vortex flow field always measured the propeller vorticity and images inside the fuselage, the interference of the fuselage along with its varying shape was properly included in the model.

5) How important is the flow behind the trailing edge? Is the wing+propeller downwash effect the lift at the empennage?

The correct modelling of flow field at the empennage is to include the empennage impact in the slipstream calculations. However, this was not done due to several complications. First is the two-dimensional vortex flow field after the trailing edge. It cannot be decided if a secondary trailing vortex field has to be initiated or the empennage influence should be somehow included in the existing vortex flow field. Second is that horizontal tail creates a significant lift and it would have an effect on the flow field, which would create a feedback

loop. The last complexity was the location of the slipstream tube at low angles-of-attack. The slipstream tube flows under the empennage, which would create an adverse pressure gradient that the panel method solver cannot include at this point. It was a design decision to keep it as simple as possible.

12.3 Discussion on Experimentation and Implementation

1) Which propeller driven aircraft is selected for experimentation? Are there sufficient data and reliable sources dedicated on the selected aircraft?

The model aircraft chosen further into the research is Fokker F27 "Friendship". TU Delft has extensive research on the aircraft and owns a wind tunnel model at Low Turbulence Tunnel in Low Speed Laboratory. Fokker F27 is a commercial, high wing, two-prop aircraft with a conventional tail.

The aircraft model allows for (un)installing propellers and horizontal tail for observing the effects of different aircraft components. There are two main sources on F27 experiments in the past available to the public. These are Binkhorst's stability calculations from 70's and Veldhuis' experiments from 90's and 2000's. The wind tunnel and panel method results are compared to these previous findings.

2) What are the ways of optimizing the computer algorithm? Is there an optimal number of resources and parameters without a substantial loss of accuracy and precision?

The first non-linear code for the SVPM was unexpectedly suboptimal for use of this research. Expected tolerances were not achieved and convergence time was too large. Parallel computing resources were experimented but gave no clear sign of decrease in computation time. At the end, a semi-linear approach was implemented. This semi-linear approach was proven to be both optimal and accurate.

For the final implementation, the criterion was to take less than 10 minutes for a converged solution in a single configuration. Moreover, some preliminary tests were conducted to ensure solution accuracy. In the end, <1% solution error achieved. The propeller circumferential stations were determined to be $2^5 = 32$. Number of horseshoe vortices on the wing was chosen to be 100. The fuselage is divided into 80 sections and vortex flow field was 75 steps.

3) What is the range of flow conditions achieved in the wind tunnel? Are there precautions that need to be considered to guarantee the reliability of the data for post-processing?

There were many configurations that can be changed in the wind tunnel experiment. The aircraft components can be installed and uninstalled. Flow velocity can be raised up to $100\ m/s$. The thrust can be varied from $rps = 220$ to 340. The angle of attack of the aircraft can be varied from $\alpha = -10^o$ to 25°. Overall, almost any kind of configuration can be conducted in the wind tunnel rig.

There were five sources of errors assumed for the experiment results. These were: Uncertainties in measurement, rounding numbers and assuming constants, human error in experiments, disregarding supposedly minor effects and approximation of fluid domain.

12.4 Discussion on Results

1) What are the major differences between powered and unpowered test results?

The powered and unpowered configurations were tested with propeller on and off cases respectively at $50 \, m/s$. To be able to compare the two, the powered model had to be corrected for propeller slipstream (thrust cleaning). So, the comparison were done after implementing the Eckert correction. Ideally, after the thrust cleaning, both of the graphs should have similar values and trends.

For the powered test, an approximation of the thrust coefficient had to be done in order to apply the Eckert correction. These values were obtained from the axial force balance readings. The low thrust condition ($rps = 220$) was determined to be not generating positive thrust, so it was not eligible for thrust cleaning. The mid and high thrust conditions ($rps = 270 \text{ and } 320$) supplied positive thrust and a meaningful thrust correction.

Between the mid-thrust and high-thrust conditions, the most obvious difference was the lift generated after applying the Eckert correction. The mid-thrust configuration has a lower lift coefficient than the high-thrust configuration. These are both higher than the lift generated in unpowered configurations.

Drag values tend to drop as the propeller thrust increases. The main reason behind this is the was the force measurement works. The balance in the axial direction is affected by drag and thrust. As the thrust increases, the drag value decreases. Moreover, the drag correction is larger due to the propeller slipstream drag correction.

As a historical reference for the unpowered case, Binkhorst's values were used. The experimental rig was set up to $80 \, m/s$ for a close comparison. Unfortunately, there is no documentation for what kind of corrections Binkhorst has used. This is important because the disagreement between his values and the experimental values were large. It is hard to say which data represents the reality.

2) What are the respective effects of classical corrections' on the graphs?

The classical corrections are divided in two major groups. These are blockage corrections and lift interference corrections. The initial one is divided into two sub groups, which are solid blockage and wake blockage. If there is a propeller in operation, slipstream blockage is also added. The latter sub-group is divided into two for wing and tail lift interference.

The primary influencer for the change in lift coefficient was observed to be the wing lift interference correction. The circulation and change in streamline curvature by the wing is exaggerated by the closed walls. The secondary influencer is the tail lift interference. Even though the tail is significantly smaller than the wing, the circulation created by it is more significant than the blockage.

The blockage correction changes the effective dynamic pressure. Solid blockage is constant between different angles of attack because it is only dependent on the flow velocity and aircraft geometry. On the other hand, wake blockage is dependent on the uncorrected drag and lift. Therefore, it increases drastically when the aircraft stalls. For $WFNVHP$, the correction for slipstream blockage was also included. Unlike all other corrections, slipstream blockage acts

as a negative blockage. Hence, the overall blockage is lower for the propeller-on case than the propeller-off case.

3) What can be deduced from the panel method results?

The panel method results show many aerodynamic properties that cannot be observed in a wind tunnel experiment. The most significant feature of the panel method is to be able to observe the spanwise lift distribution. With the spanwise lift distribution, the influence of the slipstream effect can be observed.

It can be seen that increasing angle of attack increases the circulation and section lift coefficient. The circulation on the wing transitions smoothly, while the section lift coefficient has sharp zeniths and nadirs. Because of the nacelles and fuselage the effective chord length changes suddenly. As a result, the section lift coefficient is not the lowest where the circulation is lowest.

Moreover, the effect of fuselage on the wing root can be observed. The circulation drops swiftly at the root. This is because of the Giesing solution at the wing root. Another effect is the change in propeller rotation direction. There are three different possible configurations. Inboard up, Outboard up and Co-rotating. Co-rotating propellers definitely adds positive rolling moment, which impacts the control characteristics of the aircraft. Outboard up direction generates more overall lift than the inboard up direction.

The change in propeller thrust has a direct impact on the lift generated by the wing. Both the overall circulation and section lift coefficient increases with increasing thrust. At the up going blade, the maximum lift increases with the increasing thrust. In contrast, at the down going blade, the minimum lift at the down going blade stays approximately the same. This shows that the local change of angle of attack is not just a symmetrical behavior.

Finally, the values obtained from the panel method results were compared the Veldhuis' results. The lift slopes were compared at a similar advance ratio. In the linear range, the lift coefficient for outboard up and inboard up were similar in trend and magnitude. The lift changing with advance ratio was also taken into consideration. Unfortunately, the effect of propeller direction was ranked among themselves incorrectly. The outboard up and co-rotating values are very close to Veldhuis' results while inboard-up condition is slightly lower than expected. Yet it is safe to say that the panel method results compare well with Veldhuis' wind tunnel experiments.

4) What can be said about the three corrections (including the proposed correction) after the final results?

Three corrections were evaluated in the last section of the results chapter. These were the proposed correction, Eckert correction and Patterson correction. Overall, Patterson method was the most inaccurate of the three. The formulation for the Patterson method had an inherent problem, so an approximation had to be made In addition, the values for the slipstream jet velocity was taken from the panel method results. These are probably the reason for the major divergence.

All three of the corrections were compared to the uncorrected $WFNVH$ values (propeller-off) because hypothetically it is the value that the correction is trying to achieve. From the results,

it can be emphasized that the Patterson correction overestimates the slipstream effect. It is only similar to reality in a small range of angle of attack.

Even though the Eckert solution does not include the rotational nature of the propeller flow in its approximation, it proves to be very robust. In the mid-thrust condition Eckert solution seems like the overall most accurate correction tool. The results change for the high-thrust condition however. In the low angle of attack region, the proposed correction is closer to the propeller-off values than the Eckert correction. In the high angle of attack region, Eckert method and proposed correction are practically interchangeable.

Ultimately, it can be said that the new proposed correction method is a close contender to the industry standard Eckert correction. It is proven to be a better correction than the Patterson method and it can be used in comparison with the Eckert method. The advantage of the Eckert method comes from the simplicity of the implementation while the new proposed correction needs a well defined aircraft geometry before conducting the wind tunnel experiment.

13

CONCLUSION

13.1 Conclusion

Wind tunnel experiments introduce unrealistic boundaries, which has to be accounted and corrected for. These corrections are standardized for unpowered aircraft. Most of the corrections are based on potential flow and conservation of energy and momentum. However, the existence of a powered propeller violates the assumptions made by the potential flow solutions. [27] Therefore, there is a correction for the propeller thrust that needs to be implemented before other classical corrections.

The first step taken by the thesis was to define the effect of propeller slipstream. The propeller slipstream effect has two main components. The first one is the increase in dynamic pressure due to increasing thrust. The second one is the local change of attack of the incoming flow due to the rotational nature of the propeller induced flow. In reality, propeller slipstream is an unsteady and three-dimensional phenomenon. Moreover, its interference with other aerodynamic bodies makes it impossible to consider as an isolated case. Although there are many models that accurately simplify the propeller slipstream interference, there is no single model that accurately covers the entire thrust range.

There were three slipstream correction methods introduced in the research. The first one was the Eckert method, which is the industry standard slipstream correction. It only requires the thrust coefficient value and aircraft geometry. The second method was the Patterson method. This method is an experimental approach for multiple propellers on a single wing. The main problem with both of these approaches was the dismissal of local angle of attack change under propeller slipstream. So, the research was done to come up with a way that includes the local change of attack. The main research question was to come up with a new correction that includes the change in angle of attack and if it can be used for future wind tunnel tests.

A panel method approach was selected to simulate an aircraft under propeller slipstream. Surface Vorticity Panel Method was implemented because it satisfied the simulation requirements. Moreover, it allowed for the implementation of an entire aircraft design with varying geometry. Some of the criteria for the selection of SVPM were: subsonic region, right boundary conditions, clear instructions and being open to the public. In the experimental side, Fokker F27 "Friendship" 1:20 scale model was chosen. It is a high wing, two-prop aircraft available at TU Delft laboratories. The model also allowed for removal of certain aircraft parts which was vital to see the differences between propeller-on and off cases.

SVPM is based on potential flow theory. The flow was assumed to be steady, incompressible and inviscid. The propeller was divided into two sections. The hub of the propeller was defined as vortex filament and the bounds of the slipstream was defined as a vortex sheet. The wing was modeled after the lifting line theory. SVPM is an iterative method in which the solution is reached by recursive functions until a convergence is reached. The arbitrary flow field is first resolved by the propeller related forces, then these forces are calculated with the effect of the wing. The effect is in a feedback loop until a convergence is reached. For clarity, the boundary conditions and panel creation for the non-linear SYPM were presented. Last of all, slipstream conditions were defined with a step-by-step solution how the convergence criteria was reached.

The performance of the non-linear SVPM solver was measured using Li's trial case. Four different numbers of circumferential panels were chosen to optimize the computation time without sacrificing the accuracy. The first trial was conducted without the slipstream deformation. The convergence criteria was achieved at 16 and 32 slipstream panels in the circumferential direction in the first trial. Unexpectedly, the computation time was larger than 24 hours for both configurations. The second trial included the slipstream deformation. The deformation showed extreme shearing at the point where the wing is positioned. Required tolerance was never achieved for the case with deformation, alas major changes were implemented in the panel method

The propeller slipstream model was changed to a linear model so the strength and shape of the slipstream were not affected by the presence of the wing. The propeller forces were calculated with a mixture of Blade Element Model and Vortex Theory. The slipstream envelope was approximated into a vorticity tube. The slipstream was reduced into a two-dimensional construct where the third dimension was added as a stepping method. Moreover the influence of panels were limited only to the neighboring panels.The wing and tail were modeled as vortex lattices. The fuselage was modeled as a vertical slit from Multhopp method and the wing root is modeled after a forced potential increase at the root by Giesing method. Moreover, the wing trailing vortex flow field was added into the calculations to visualize the propagation behind the wing trailing edge.

The wind tunnel experiments were conducted in the TU Delft LTT. Fokker F27 1:20 model was tested in propeller-on and off configurations, in different flow speeds and a range of different angle of attacks. The classical corrections used for the post-processing were acquired from Eckert and Barlow's articles. For the lift interference model, another panel method called ANTARES (by NASA Ames) was implemented. ANTARES is a panel method developed to find lift interference for a complex geometry, however the results were not different than the empirical tables. Therefore, it was not used in the final results.

Extra considerations were taken in the panel method configuration. The swirl effect was simulated by rotating the slipstream panel. The calculation took considerably more time and had a minor effect, therefore it was deemed to be ineffective. The effect of wing on the propeller was also tested by feeding the values of the wing forces in a second iteration to calculate propeller forces. This was also found to be a minor effect. Since the new model is a linear one, the effect of the wing induced forces don't have much effect on the propeller induced forces. The number of panels were chosen with a time constraint in mind and necessary precision at each run. Lastly, the incoming empennage flow was kept as simple as possible because it was

outside of the scope of the research. The limits of the panel method for varying angle of attacks were also determined in this stage.

The results were presented with precautions in mind due to human error and approximations. In the wind tunnel, flow velocity was approximately $50\ m/s$. The angle of attack of the aircraft was altered between $\alpha = -6^o$ to 8° for the thrust cases. In the panel method, the propeller circumferential stations were determined to be $2^5 = 32$. 100 horseshoe vortices on the wing was selected. The fuselage was divided into 80 sections and vortex flow field had 75 steps.

The wind tunnel experiment was divided into two main configurations. The propeller-off configuration was used to show the effects of standard corrections. The primary influencer for the change in lift coefficient was detected to be the wing lift interference correction. The closed walls of the wind tunnel increased the circulation and exaggerated the streamline curvature due to the wing. The tail lift was a secondary influencer. Interestingly, the tail was significantly smaller than the wing, still the circulation created by the tail was more substantial than the blockage effect on the lift curve. In order to verify propeller-off findings, Binkhorst's Fokker F27 at $80\ m/s$ experiments were utilized. However, the results did not match. It was left as inconclusive because Binkhorst's paper did not specify the correction methods used in his experiments

In the propeller-on cases, only the mid and high thrust conditions ($rps = 270$ and 320) provided positive thrust and a significant thrust correction. The low thrust condition ($rps = 220$) was concluded to be not generating positive thrust, so it was not qualified for thrust cleaning. Between the different positive thrust conditions, the most noticeable difference was the lift generated after applying the Eckert correction. The high-thrust configuration has a higher lift coefficient than the mid-thrust configuration. Still, these coefficients are higher than the propeller-off configurations. As a result, it was believed that the slipstream effect is undermined with the Eckert correction.

In the post processing of panel method results, it was deduced that that increasing local angle of attack increased the circulation and section lift coefficient. Moreover, it was observed that section lift coefficient was not the lowest where the circulation is lowest. The effect of fuselage on the wing root was shown, where the circulation is steeply reduced around the fuselage. This was a clear indication that the Giesing solution worked in the panel method. Therefore the slipstream fuselage interaction was achieved as expected.

The change in propeller thrust had a direct impact on the lift generated by the wing. The main objective of this research was to simulate both the increased rotation due to increasing thrust. This objective was successful. At the up going blade, the lift increased with the increasing thrust. In contrast, at the down going blade, the lift increase due to increasing dynamic pressure was negated by the decrease in local angle of attack. It is clearly shown that the local change of angle of attack did not have a symmetrical behavior as suggested by Patterson.

For a meaningful comparison, propeller-on cases were compared with Veldhuis' experiments. Even though the lift slope and magnitude was similar, unfortunately the effect of the propeller direction was contrary. The reason is not clear, but the direction algorithm be further investigated for future work.

All three of the corrections were measured up to the uncorrected $WFNVH$ (propeller-off) values because it was considered the ideal value. From the results, it was underlined that the Patterson correction overestimates the slipstream effect. It was similar to reality in a small range of angle of attack. Two reasons were presented for the large discrepancy in Patterson method. First was the denominator term that had to be removed from the equation; second was the jet velocity that was gathered using the panel method.

Finally, the proposed correction was presented. The new correction had the slipstream rotation and consequently the local angle of attack change. On the other hand, it did not show a clear advantage compared to Eckert method in the overall results. In the mid-thrust condition Eckert solution proved to be the overall most accurate correction tool. The outcomes for the high-thrust condition suggested that the proposed method could supply accurate slipstream correction. In the low angle of attack region, the proposed correction was closer to the propeller-off values than the Eckert correction. In the high angle of attack region, Eckert method and proposed correction were practically interchangeable. Ultimately, it can be said that the new proposed correction method introduced the rotational effects in its methodology, which were overlooked in other corrections. It has proven to be a reliable substitute to Eckert correction, however it is not a clear improvement. In the future, it can be a foundation for a correction method, which can exactly predict the thrust effect on a propeller aircraft.

13.2 Contributions to Literature

- A new method of propeller slipstream correction (thrust cleaning correction) is introduced. It is proven itself to be a contender for the industry standard Eckert method.
- This is the first slipstream correction method that accounts for the change in spanwise local angle of attack behind the propeller radius.
- There is evidence from the panel method solution that slipstream rotation induces asymmetrical angle of attack change. This phenomenon is usually disregarded in correction assumptions.
- The new correction method does not rely on empirical coefficients. It does not require preliminary propeller-off or isolated propeller tests for a meaningful solution.
- On a contrary note, it also showed that introducing a disregarded flow phenomenon does not guarantee a better correction. Slipstream effect was considerably simplified in the panel method, although it is a very complex flow region.

13.3 Future Work

- The accuracy and precision of the panel method can be tested using different aircraft models. It is currently not known if will the panel method correction will reach or exceed the accuracy presented in this thesis for other propeller-driven aircrafts.
- The effect of propeller rotation direction on the lift was contrary to Veldhuis' results. An investigation on why this was the case can be conducted. This would improve the overall panel method reliability.
- The correction method can be implemented in Reynolds Averaged Navier-Stokes solution for higher definition. Currently the model cannot be a consistent substitute for the Eckert correction. It should be determined how much the propeller slipstream can be simplified in order to reach higher accuracy.
- The swirl was implemented as a change in panel orientation. However there are other ways to implement swirl effect. Moreover, the wing is known to have a swirl recovery

effect, which diminishes the swirl by a large margin. For a better model, these effects can be further investigated for further research.

- The flow field is currently a two-dimensional construct with a time-stepping third dimension. Instead of having a 2D approximation, an entire 3D flow region can be created in the numerical solution. A turbulence model can be selected throughout many CFD models.

- A new method, which does not have presumed slipstream strength and shape can be implemented. This was the initial idea behind this thesis, but was abandoned due to convergence and time issues. There is strong evidence that propeller-wing interference is a non-linear effect.

- The panel method over simplifies the flow around the empennage for ease-of-use. There is clear evidence that propeller slipstream directly interferes with the tail. Unfortunately, this panel method is not able to solve for the flow wing trailing flow and empennage interference. The assumptions for the tail has to be better defined and documented.

REFERENCES

[1] S. P. Foster and H. S. Ribner, "Ideal Efficiency of Propellers Based on Theodorsen's Theory: A Review and Computer Study with Extended Plus Simplified Charts," *Toronto University, Institute for Aerospace Studies,* vol. UTIAS Technical Note No. 271, no. CN ISSN 0082-5263, February 1991.

[2] S. Goldstein, "On the Vortex Theory of Screw Propellers," *Proc. Roy. Soc.,* vol. 123, 1929.

[3] L. Prandtl, "Mutual Interfernce of Wings and Propeller," *NACA Technical Report No.74,* vol. Extract of the First Report in Gottingen Aerodynamic Facility, no. Chapter IV, Sec. 6, , 1921.

[4] L. L. M. Veldhuis, "Propeller Wing Aerodynamic Interference," *Ph. D. Thesis, Faculty of Aerospace Engineering, Delft University of Technology, Netherlands,* 2005.

[5] T. Sinnige, "Aerodynamic and Aeroacoustic Interaction Effects for Tip-Mounted Propellers," *Ph.D. thesis, Facultyof Aerospace Engineering, Delft University of Technology, Netherlands,* 2018.

[6] K. Richter and N. Witt, "Introduction: Supply Chain Integration Challenges in the Commercial Aviation Industry," *Supply Chain Integration Challenges in the Commercial Aviation Industry, Springer,* no. ISBN 978-3-319-46154-0, pp. 1-19, 2017.

[7] C. N. Reynolds, R. E. Riffel and S. Ludemann, "Propfan Propulsion Systems for the 1990's," *23rd Joint Propulsion Conference,* no. AIAA-87-1729, 1987.

[8] A. Schafer and D. Victor, "THE FUTURE MOBILITY OF THE WORLD POPULATION," *Transportation Research Part A: Policy and Practice,* vol. 34, no. 3, pp. 171-205, 2000.

[9] W. C. Strack, G. Knip, A. L. Weisbrich, J. Godston and E. Bradley, "Technology and Benefits of Aircraft Counter Rotation Propellers," *NASA Technical Memorandum ,* no. 82983, October 25-28,1982.

[10] L. Larsson, T. Groenstedt and K. G. Kyprianidis, " Conceptual Design and Mission Analysis for a Geared Turbofan and an Open Rotor Configuration," *ASME Turbo Expo,* no. GT2011-46451, June 6-10, 2011.

[11] Q. Li, X. Liu, E. G. and L. Veldhuis, "Numerical Investigation of Swirl Recovery Design for Propeller Propulsion Systems," *Applied Aerodynamics Conference, AIAA AVIATION Forum,* no. AIAA 2018-3648, 2018.

[12] P. van den Borne and J. van Hengst, "Investigation of Propeller Slipstream Effects on the Fokker 50 Through in-Flight Pressure Measurements," *AIAA,* no. 90-3084.

[13] L. J. Hess and M. O. Smith, "Calculation of Potential Flow About Arbitrary Bodies," *Douglas Aircraft Company, Aircraft Division,* 1967.

[14] G. M. van Beek, W. J. Piers and B. Oskam, "Aerodynamic Analysis of Slipstream/Wing/Nacelle Interference for Preliminary Design of Aircraft Configurations," *NASA Technical Report,* no. TP 91453, 1991.

[15] D.-Q. Li, "Investigation on Propeller-Rudder Interaction by Numerical Methods," *Chalmers University of Technology, PhD Thesis,* 1994.

[16] P. Loetstedt, "Propeller Slip-Stream Nodel in Subsonic Linerarized Potential Flow," *Journal of Aircraft,* vol. 29, no. 6, 1992.

[17] W. Phillips, "Propeller Momentum Theory with Slipstream Rotation," *Journal of Aircraft,* vol. 39, no. 1, 2002.

[18] H. Glauert, Wind Tunnel Interference on Wings, Bodies and Airscrews, R&M 1566, 1933.

[19] R. Clark and W. Valarezo, "Subsonic calculation of propeller/wing interference," *28th Aerospace Sciences Meeting,* no. DOI: 10.2514/6.1990-31 , 1990.

[20] T. C. A. Stokkermans, N. van Arnhem, T. Sinnige and L. L. M. Veldhuis, "Validation and Comparison of RANS Propeller Modeling Methods for Tip-Mounted Applications," *AIAA Journal,* vol. 57, no. 2, DOI: 10.2514/1.J057398, 2019.

[21] C. Lenfers, N. Beck and R. Radespiel, "Numerical and Experimental Investigation of Propeller Slipstream Interaction with Active High Lift Wing," *DLR,* 2018.

[22] J. E. Kerwin, S. A. Kinnas, J.-T. Lee and W.-Z. Shih, "A Surface Panel Method for the Hydrodynamic Analysis of Ducted Propellers," *THE SOCIETY OF NAVAL ARCHITECTS AND MARINE ENGINEERS Annual Meeting,* no. AD-A192 569, November 1987.

[23] D.-Q. Li, "A non-linear method for the propeller-rudder interaction with the slipstream deformation taken into account," *Computer methods in applied mechanics and engineering,* vol. 130, 1996.

[24] T. Bouquet and R. Vos, "Modeling the Propeller Slipstream Effect on Lift and Pitching Moment," *55th AIAA Aerospace Sciences Meeting: Grapevine, Texas,* no. AIAA 2017-0236, 2017.

[25] R. M. Howard, S. J. Miley and B. J. Holmes, "An Investigation of the Effects of the Propeller Slipstream on a Laminar Wing Boundary Layer," *Society of Automotive Engineers Technical Paper ,* no. 850859, 1985.

[26] H. Garner, E. Rogers, W. Acum and E. Maskell, "Subsonic Wind Tunnel Wall Corrections," *AGARDograph 109,* October 1966.

[27] D. Eckert, G. H. Hegen and W. Kuhn, "DNW's Method for Correct Support and Wall Interference Effects on Low Speed Measurements with a Large Propeller Powered Transport Aircraft Model," *ICAS,* 2006.

[28] R. E. Fitzgerald, "WIND TUNNEL BLOCKAGE CORRECTIONS FOR PROPELLERS," *Master of Science, Maryland University ,* 2007.

[29] R. Bass, "Small scale wind tunnel testing of model propellers," *24th Aerospace Sciences Meeting, Aerospace Sciences Meetings,* no. DOI: 10.2514/6.1986-392 , 1986.

[30] N. Ubrich and A. R. Boone, "Direct Validation of the Wall Interference Correction System of the Ames 11-Foot Transonic Wind Tunnel," *NASA Technical Report,* no. NASA/TM–2003-212268, May 2003.

[31] "AGARDograph 336: Wind Tunnel Wall Corrections," NATO, Neuilly-Sur-Seine Cedex, 1998.

[32] J. B. Barlow, W. H. Rae and A. Pope, "Low-Speed Wind Tunnel Testing," *JOHN WILEY & SONS, INC.,* vol. 3rd Edition, 1984.

[33] M. D. Patterson and B. J. German, "Simplified Aerodynamics Models to Predict the Effects of Upstream Propellers on Wing Lift," *53rd AIAA Aerospace Sciences Meeting,* no. 10.2514/6.2015-1673, 2015.

[34] G. Eitelberg, "AE 4115 Experimental Simulations Class Notes," 2018.

[35] J. Katz and A. Plotkin, "Low-Speed Aerodynamics, Second Edition," *Cambridge University Press,* pp. 206-433, 2010.

[36] N. Ulbrich, "The Real-Time Wall Interference Correction System of the NASA Ames 12-Foot Pressure Wind Tunnel," *NASA Technical Report,* no. NASA/CR-1998-208537.

[37] R. Mikkelsen and S. J.N., "MODELLING OF WIND TUNNEL BLOCKAGE," *Global Wind Tunnel Conference,* 2002.

[38] I. Phillipsen, "Analysis of Propeller/Wing Interference on a Straight Half Wing and Tractor Propeller," *TU Delft MSc Thesis,* August 1993.

[39] W. F. Durand, "Aerodynamic Theory," *Springer,* vol. IV, 1935.

[40] H. Multhopp, "Aerodynamics of the Fuselage," *NACA Technical Report,* no. NACA-TM-1942, 1942.

[41] M. A. Takalu and G. G., "Aerodynamic characteristics of a propeller powered high lift semispan wing," *NASA Technical Report,* no. DOI: 10.2514/6.1992-388, February 1992.

[42] E. W. M. Roosenboom, A. Heider and A. Schroeder, "Investigation of the Propeller Slipstream with Particle Image Velocimetry," *Journal of Aircraft,* Vols. 46, No: 2, no. DOI: 10.2514/1.33917, 2009.

[43] J. D. Anderson, in *Fundamentals of Aerodynamics*, McGraw-Hill, 1984, pp. 30-36.

[44] L. Ting, C. H. Liu and G. Kleinstein, "Interference of Wing and Multipropellers," *AIAA Journal,* vol. 10, no. 7, pp. 906-914, 1972.

[45] S. Gamme, G. De Oliveira Andrade, D. Ragni and F. Lau, "A Fast Panel Code for Complex Actuator Disk Flows," *55th AIAA Aerospace Sciences Meeting: Grapevine, USA,* no. AIAA 2017-0752.

[46] Y. Yang, "Aerodynamic Interaction between Propeller and Vortex," *PhD Thesis, Faculty of Aerospcae Engineering, TU Delft,* no. DOI: 10.4233/uuid:9efb571c-0441-4690-84ca-7c5d5e8bfea6, 2017.

[47] L. R. Miranda and E. B. James, "Aerodynamic Effects of Wingtip-Mounted Propellers and Turbines," *4th Applied Aerodynamics Conference,* no. AIAA-86-1802, July 1986.

[48] M. Metcalfe, "On the Modelling of a Fully-Relaxed Propeller Slipstream," *AIAA/SAE/ASME/ASEE 21st Joint Propulsion Conference,* no. AIAA-85-1262, July 1985.

[49] Hurst, Metheven and Owen, "Wind Tunnel Testing of Small Scale Pressure Tapped Model Propellers," *University of Southampton,* 1986.

[50] M. D. Patterson, J. M. Derlaga and N. K. Borer, "High-Lift Propeller System Configuration Selcection for NASA's SCEPTOR Distributed Electric Propulsion Flight Demonstrator," *16th AIAA Aviation Technology, Integration, and Operations Conference,* no. NF1676L-22882, June 13, 2016 - June 17, 2016.

[51] J. L. Hess, "Calculation of Potential Flow About Arbitrary Three-Dimensional Lifting Bodies," *Technical Report MDC,* no. J5679-01, 1972.

[52] J. L. Hess, "An Improved Higher Order Panel Method for Three-Dimenional Lifting Potential Flow," *NADC Technical Report,* no. 79277-60, 1981.

[53] F. T. Johnson, "A General Panel Method for the Analysis and Design of Arbitrary Configurations in Incompressible Flows," *NASA Contractor Report ,* no. 3079, 1980.

[54] H. Binkhorst, "Windtunnelonderzoek naar de toepassing van een gedeeld richtingsroer als luvhtrem voor de Fokker F27 "Friendship"," *TU Delft Memorandum,* no. M-177, October 1971.

[55] H. Lamb, "Hydrodynamics," *Cambridge University Press,* no. 6th Edition, 1932.

[56] M. J. T. Schroijen, "Propeller Slipstream Effects on on Lateral Stability and Control of Multi-Engine Propeller Aircraft," *TU Delft Faculty of Aerospace, MSc Thesis,* 2007.

[57] B. W. McCormick, "Chapter 4: Aerodynamics of Propellers," in *Aerodynamics of V/STOL Flight*, New York, Academic Press, 1967, pp. 73-93.

[58] B. W. McCormick, A. S. Aljabri, J. S. L. and Martinovic, "Tne Analysis of Propellers Inclduing Interaction Effects," *NASA Technical Report,* no. NASA-CR-158111, 1979.

[59] A. van Nispen, "Slipstream effects on the static lateral and directional control of a multi-engined propeller aircraft with one engine inoperative," *TU Delft MSc Thesis,* 2002.

[60] P. Rauhut, "Modelling of the slipstream effects on the static lateral and directional stability and control of a single engine propeller aircraf," *TU DELFT MSc Thesis,* 2002.

[61] M. Renooij, "Propeller slipstream effects and wing-fuselage lift carry-over effects on the stability of a single engine propeller airplane.," *TU Delft MSc Thesis,* 2005.

[62] P. Rauhut and R. Slingerland, "PROPELLER SLIPSTREAM EFFECTS ON LATERAL AND DIRECTIONAL STATIC STABILITY AND CONTROL OF A SINGLE ENGINE TRACTOR AIRPLANE," *41st Aerospace Sciences Meeting and Exhibit,* no. AIAA 2003-51, January 2003.

[63] M. Renooij and R. Slingerland, "Propeller Slipstream and Wing-Fuselage Interference Effects on Three-Axis Stability and Control," *42nd AIAA Aerospace Sciences Meeting and Exhibit,* no. AIAA 2004-214, January 2004.

[64] J. Giesing, "Lifting surface theory for wing-fuselage combinations," *Defence Technical Information Center,* vol. I, no. DAC-67212, 1968.

[65] A. W. Rogers, "Application of Two-Dimensional Vortex Theory to the Prediction of Flow Fields Behind Wings of Wing-Body Combinations at Subsonic and Supersonic Speeds," *NACA Technical Report,* no. NACA-TN-3227, 1954.

[66] TU Delft, "Low Turbulence Tunnel," [Online]. Available: https://www.tudelft.nl/en/ae/organisation/departments/aerodynamics-wind-energy-flight-performance-and-propulsion/facilities/low-speed-wind-tunnels/low-turbulence-tunnel/. [Accessed 17 05 2020].

[67] M. J. T. Schroijen and R. Slingerland, "PROPELLER INSTALLATION EFFECTS ON MULTI-ENGINE PROPELLER AIRCRAFT DIRECTIONAL STABILITY AND CONTROL," *25th INTERNATIONAL CONGRESS OF THE AERONAUTICAL SCIENCES,* 2006.

[68] M. Schroijen, V. L.L.M and S. R., "Propeller Slipstream Investiogation Using the Fokker F27 Wind Tunnel Model with Flaps Deflected," *ICAS 26th INTERNATIONAL CONGRESS OF THE AERONAUTICAL SCIENCES,* 2008.

[69] E. Obert, "Aerodynamic Design of Transport Aircraft," *Delft University Press,* 2009.

[70] S. Nebiolo, "CFD Analysis of a Basic Propeller/NAcelle/Wing Configuration Based on the Solution of the Navier-Stokes Equations," *MSc Thesis, Faculty of Aerospace Engineering, TU Delft,* 1990.

[71] J. D. Keller, "NUMERICAL CALCULATION OF BOUNDARY-INDUCED INTERFERENCE IN SLOTTED OR PERFORATED WIND TUNNELS INCLUDING VISCOUS EFFECTS IN SLOTS," *NASA Technical Note,* no. NASA-TN D-6871, 1972.

[72] R. G. Joppa, "WIND TUNNEL INTERFERENCE FACTORS FOR HIGH-LIFT WINGS IN CLOSED WIND TUNNELS," *NASA Technical Report,* no. NASA CR-2191, 1973.

[73] X. Vaucheret and J. C. Vayssaire, "Corrections de parois en ecoulement tridimensionnel ranssonique dans des veines a parois ventil6es"," *Wind Tunnel Design and TEsting Techniques,* no. AGARD CP-174,, 1976.

[74] N. Ulbrich, "Description of Panel Method Code ANTARES," *NASA,* no. CR-2000-209592, May 2000.

[75] J. D. Keller and R. H. Wright, "WIND-TUNNEL LIFT INTERFERENCE ON SWEPTBACK WINGS IN ,RECTANGULAR TEST SECTIONS WITH SLOTTED SIDE WALLS," *NASA Technical Report,* no. NASA TR R-344, 1970.

[76] J. D. Keller and R. H. Wright, "A NUMERICAL METHOD OF CALCULATING THE BOUNDARY-INDUCED INTERFERENCE IN SLOTTED OR PERFORATED WIND TUNNELS OF RECTANGULAR CROSS SECTION," *NASA Technical Report,* no. NASA TR R-379, 1972.

[77] "WIND-TUNNEL LIFT INTERFERENCE ON SWEPTBACK WINGS IN RECTANGULAR TEST SECTIONS WITH SLOTTED TOP AND BOTTOM WALLS," *NASA Technical Report,* no. NACA TR R-241, 1966.

[78] H. Ribner, "Propellers in Yaw," *NACA,* no. WR-L-219, 1943.

[79] J. de Young, "Propellers at High Incidence," *Journal of Aircraft,* vol. 2, no. 3, 1965.

[80] IHS, "Thrust and drag accounting for propeller/airframe interaction," *ESDU,* vol. 85017, no. ISBN: 978 0 85679 523 7, 1985.

[81] IHS, "Introduction to installation effects on thrust and drag for propeller-driven aircraft," *ESDU,* vol. 85015, no. ISBN: 978 0 85679 521 3, 2006.

[82] L. Mueller, D. Kozulovic and R. Radespiel, "Aerodynamic Performance of an Over-the-Wing Propeller Configuration at Increasing Mach Number," *CAES Aeronaut J,* no. 5:305-317, 2014.

[83] J. E. Hackett, D. J. Wilsden and W. A. Stevens, "A review of the wall pressure signature and other tunnel constraint correction methods for high angle of attack tests," *AGARD-R-692,* 1981.

[84] J. Hackett, "Tunnel Induced Gradients and Their Effect on Drag," *AIAA Journal,* pp. 2575-2581, 1996.

[85] H. NEUMANN, L. BOBER, J. SERAFINI and C. L.K., "An analytical and experimental comparison of the flow field of an advanced swept turboprop," *21st Aerospace Sciences Meeting, Aerospace Sciences Meetings.*

[86] T. Ikami, K. Kanou, K. Takahashi, K. Fujita and H. Nagai, "Flow Field on WIng Surface with Control Surface Propeller Slipstream at Low Reynolds Number," *AIAA SciTech Forum,* no. DOI: 10.2514/6.2019-2159 , 2019.

[87] C. Negulescu, "Airbus AI-PX7 CROR Design Features and Aerodynamics," *SAE International Journal of Aerospace,* vol. 6, no. 2, 2013.

[88] T. Sinnige, T. C. A. Stokkermans, D. Ragni, G. Eitelberg and L. L. M. Veldhuis, "Aerodynamic and Aeroacoustic Performance of a Propeller Propulsion System with Swirl-Recovery Vanes," *JOURNAL OF PROPULSION AND POWER,* vol. 34, no. 6, DOI: 10.2514/1.B36877, 2018.

[89] C. Spoon, "Windtunnelmetingen aan een model van de vleugel van de Fokker F-27 "Friendship" in de lage snelheidstunnel van de onderafdeling Vliegtuigbouwkunde," *TU Delft Memorandum,* no. M46, 1961.

[90] E. Garcia, A. van Nispen and R. Slingerland, "DOWNWASH AT THE TAIL OF SWEPT-WING TRANSPORTS WITH HIGH-LIFT DEVICES," *American Institute of Aeronautics & Astronautics,* no. AIAA 2001-5237 A01-43417 REVISED, 2001.

[91] M. Schroijen, L. Veldhuis and R. Slingerland, "Propeller Empennage Interaction Effects on Vertical Tail Design of Multiengine Aircraft," *JOURNAL OF AIRCRAFT,* vol. 47, no. DOI: 10.2514/1.46707, August 2010.

[92] H. Glauert, "The Elements of Aerofoil and Airscrew Theory," *Cambridge University Press,* 1948.

APPENDIX

A. Momentum and Energy Conservation in Fluid Mechanics (McCormick)

The momentum theory in fluid dynamics shows us that the sum of all forces (F) acting on a fluid is:

$$F = \iint_S \rho V(V.n)dS \ + \ \frac{\partial}{\partial t}\iiint_V \rho V \, d\tau$$

Where (ρ) is density of the fluid, (S) is the surface, (V) is the volume, (n) is the normal unit directed outward from the surface, ($d\tau$) is differential element of the volume. This equation can also be written for angular momentum, where Q is the sum of all the torques in the control surface.

$$Q = \iint_S \rho(V \times r)(V.n)dS \ + \ \frac{\partial}{\partial t}\iiint_V \rho(V \times r) \, d\tau$$

The distance where the forces acting from the fluid is denoted by (r). In words, these two formulas explain the relationship between the sum of external and internal forces (moments) on the fluid is equal to the change of momentum flux and the instantaneous rate of change of the momentum in the fluid.

The energy theorem presents us another conservation: the rate of heat input and work performed into a controlled surface (S) of a fluid has to be equal to the sum of energy flux and the instantaneous rate of change of energy out of the system.

$$\iint_S kn.\nabla T \, dS \ + \ \iint_S \tau.V \, dS + \dot{W} \ = \ \frac{\partial}{\partial t}\iiint_V \rho e \, d\tau \ + \ \iint_S \rho e(V.n)dS$$

In the equation above, (k) represents thermal conductivity and (τ) represent surface stress. ($\dot{W}$) is the power input. (e) is the specific energy in the system. (∇T) represents temperature, so it should not be confused with thrust. Assuming that viscous shear stress is neglected and the flow is steady. It is simplified into:

$$\dot{W} = \iint_S [(\rho e + p)(V.n) - \ kn.\nabla T] \, dS$$

B. Propeller Momentum Theory / Actuator Disk Model (McCormick)

Applying these two theorems on the axial propeller plane is called the Propeller Momentum Theory. Also named Actuator Disc Model, it assumes that the rotation axis of the propeller is at 0º angle of attack. The flow is defined at three locations: Upstream, actuator disc and downstream of the propeller; station 1,2 and 3 respectively. ADM is based on these assumptions:

1) The thrust produced by the propeller disk is uniform throughout. Therefore, it has infinite (continuous) blades.

2) Only axial flow is taken into account, no rotational flow comes out of the propellers.
3) The slipstream boundary is exactly at the tip of the propeller disc.
4) In the far upstream and downstream, the freestream static pressure is equal to static pressure in and out of the slipstream boundary.
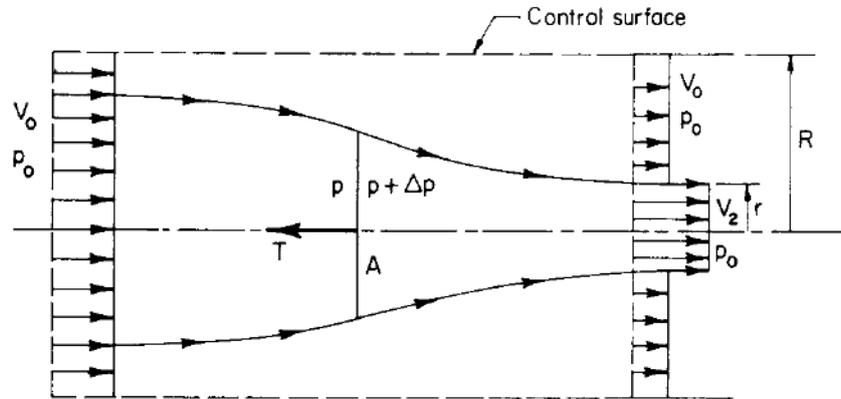
Figure 99: Streamtube and Control Surface for the Actuator Disk [57]

From the figure above, the pressure (p), velocity (V), radius (r) and area (A) can be identified at different locations. Since the flow should be continuous inside the walls (control surface), we can write the flux coming through the side walls as Q:

$$Q = V_2 \pi r^2 + V_0 \pi (R^2 - r^2) - V_0 \pi R^2$$

After simplifying:

$$Q = (V_2 - V_0) \pi r^2$$

The sum of momentum flux downstream is equal to sum of upstream momentum flux plus the thrust. Thrust is therefore equal to:

$$T + \pi R^2 \rho V_0^2 = \pi r^2 \rho V_2^2 + \pi (R^2 - r^2) \rho V_0^2 - \pi r^2 \rho (V_2 - V_0) V_0$$

Or:

$$T = \pi r^2 \rho (V_2 - V_0) V_2$$

According to this result, thrust is the mass flow rate going through the propeller times the increase in the velocity due to slipstream in the far upstream and behind the propeller. The thrust can be also approximated to the change in velocity at the instance where it crosses the disc.

$$T = A \Delta p$$

Using the Bernoulli's equation at the right before and after the pressure jump caused by the actuator, the velocity at the actuator and consequent induced velocity by the actuator disc can be found:

$$p_0 + \frac{1}{2} \rho V_0^2 = p + \frac{1}{2} \rho V_1^2$$

$$p_0 + \frac{1}{2}\rho V_2^2 = (p + \Delta p) + \frac{1}{2}\rho V_1^2$$

Two Bernoulli equations show the energy conservation in front and behind the propeller. Since we assumed that the slipstream boundary has the same area as the actuator disc area, the continuity of the fluid can be expressed as:

$$\pi r^2 V_2 = A V_1$$

From the equations above, the momentum theory states the velocity going through the propeller is equal to the average of the far upstream and downstream in the streamtube. Also it gives a solution for the thrust in terms of the induced velocity. This induced velocity is defined as the the difference between the velocity upstream and velocity behind the propeller: $V_i = V_1 - V_0$

$$V_1 = \frac{V_0 + V_2}{2}$$

$$T = \rho A (V_0 + V_i) 2 V_i$$

The mass flow rate through the propeller ($\rho A(V_0 + V_i)$) times two times the induced velocity ($2V_i$) is the thrust that is produced by an actuator disc. Another way of evaluating the actuator disc is to define the velocity change as a function of the freestream velocity ($V_{loc} = V_0 + cons.V_0$) at location 1 and 2. [46]

The velocity coefficients (a) and (b) are defined and the relationship between them is:

$$a = \frac{1}{2}b$$

Using the new term, the static pressure right in front and behind the propeller can be written in terms of the freestream velocity (V_0) and slipstream constant (b).

$$p_1 = p_0 - \frac{1}{2}\rho V_0^2 (\frac{1}{4}b^2 + b)$$

$$p_2 = p_0 + \frac{1}{2}\rho V_0^2 (\frac{3}{4}b^2 + b)$$
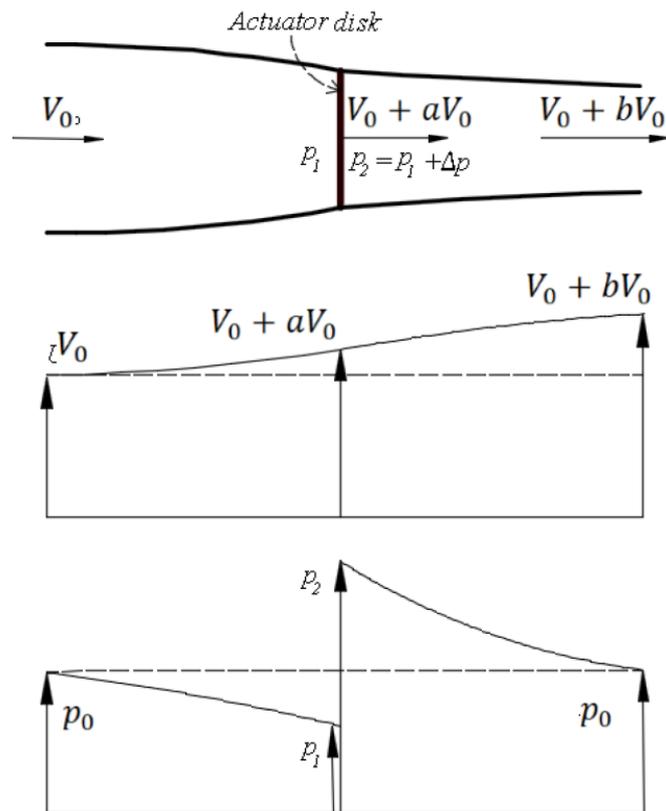
Figure 100: Velocity Increase and Pressure Jump along the Slipstream in ADM [46]

The static pressure jump at the actuator disc can be seen on. The velocity, unlike the static pressure, is continuously increasing while going from upstream to downstream. This trend can be observed until the windmilling condition where the produced thrust is 0. Wind turbines also work on the same principle however, the thrust is negative since the total momentum decreases because the energy is taken out of the system.

C. Blade Element Model (Yang)

The propeller momentum theory is a commonly used tool to measure the influence of the propeller; however, the physics of the actual blades are neglected in the actuator disk model. Blade Element Theory gives an insight on how the propeller should be designed and modeled in a qualitative way with the information from momentum theory. BEM is first used to explain the forces and moments on an airfoil by Drzewiecki. It introduces the torque and thrust created for a finite propeller blade, with the use of airfoil sections along the propeller.
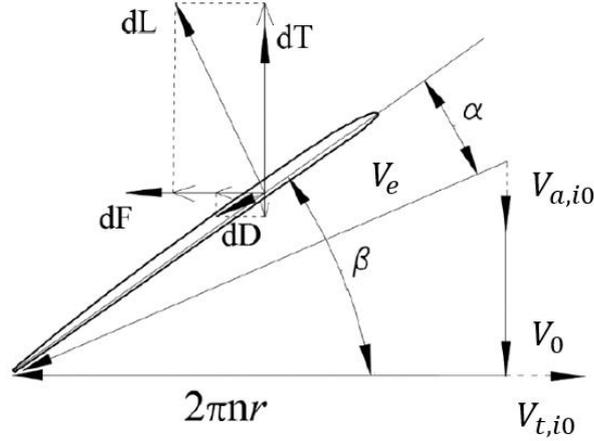
Figure 101: Forces on the Propeller Airfoil Section in BEM [46]

In the variables are defined as follows (n) is the rotational speed of the propeller. (V_0), ($V_{a,i0}$) and ($V_{t,i0}$) are the freestream velocity, induced tangential velocity and induced axial velocity. The blade is cut into airfoil elements in the radial direction. The geometrical properties of the blade are defined as (β) pitch angle, (c) chord length, (r) radius. In the diagram, the angle of attack (α) and (V_e) effective velocity can be also observed. The resultant forces on the blade section are thrust, lift and drag.

In Blade Element Method, axial velocity is determined using the momentum theory and the tangential velocity is determined by the vortex using Theodorsen's vortex theorem. The flow is assumed to be two dimensional with no radial flow and the flow going through the blade is assumed to be not affected by other blades. In other words, each blade is independent. Usually, Prandtl correction is used as a way to account for the tip losses that are absent in the 2D model.

The lift, drag and thrust forces can be written using the trigonometric relationship in the BEM diagram.

$$dL = C_l c \frac{1}{2} \rho V_0^2 \, dr$$

$$dD = C_d c \frac{1}{2} \rho V_0^2 \, dr$$

$$dT = \cos(\beta - \alpha)dL - \sin(\beta - \alpha)dD$$

The lift (C_l) and drag (C_d) coefficients can be extracted from an airfoil database for the calculation. Rest of the variables are known to find the lift and the drag. Then, the positive contribution of the lift and the negative contribution from the drag can be written. The torque can also be found since the distance (r) is known.

$$dQ = dF.r = r(\sin(\beta - \alpha)dL + \cos(\beta - \alpha)dD)$$

D. Propeller Axial and Tangential Vectors (Veldhuis)

The mutual interaction between propeller, wing and nacelle has to be well-defined because of the the complex flow, circulation structure inside the slipstream. The self-induced vortices and velocities in the propeller flow cause large gradients in both radial and axial direction. For a complete inspection of the BEM, there are seven important quantities that is required to comprehend the slipstream. These are: axial velocity profile, swirl velocity profile, total pressure distribution, static pressure distribution, vorticity, helicity and contraction.

Axial velocity profile is simply defined in the Cartesian coordinates in the streamwise (X-coordinate) direction, where (u) is the axial component of the velocity vector :

$$V = \begin{pmatrix} u \\ v \\ w \end{pmatrix}$$

The axial velocity (u) is defined as (V_a) in the former chapters. The axial velocity of the propeller blade is usually at a mazimum at ($\frac{r}{R} = \frac{3}{4}$). It can be observed that the location on the blade changes the resultant axial velocity substantially.
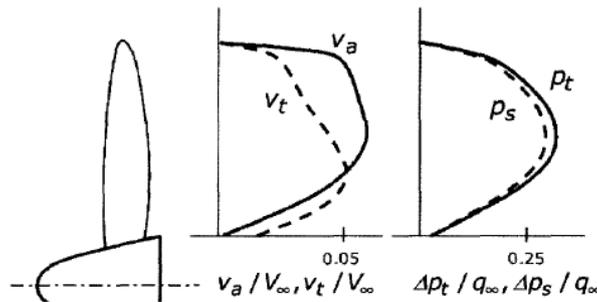
Figure 102: Axial and Tangential Velocity and Pressure Distribution on the Propeller [4]

The tangential velocity component is defined by a trigonometric relationship. It should not be forgotten that this model assumes infinite blades. $V_t = \sqrt{v^2 + w^2}$. This reationship is the result of the swirl of the tangential velocity vector on the advancing blade outside of the axial axis. Therefore, (V_t) is referred as the swirl velocity. The swirl can also change with the advance ratio. Therefore, swirl angle is defined as:

$$\theta_{sw} = \tan^{-1}(\frac{V_t}{V_a})$$

Since the swirl velocity is assumed to be constant in the axial direction, the angle of the swirl changes depending on the location of the wing behind the propeller. The static pressure changes have been discussed in the ADM on the axial plane. However, it should also be noted that the change in total pressure is directly related to the swirl velocity profile.

$$p_{t,slip} - p_{t,\infty} = \Delta p - \frac{1}{2}\rho V_t^2$$

Finally, vorticity has to be defined to convey the rotational flow in the slipstream. The vorticity is directly proportional to blade loading and it is also time-dependent and treated as unsteady.

Numerical vortex methods are usually used to determine the unsteady loads on the wing due to the vortex sheet with each blade pass.

$$\omega = \nabla \times V = \begin{pmatrix} \omega_x \\ \omega_y \\ \omega_z \end{pmatrix} = \begin{pmatrix} \xi \\ \eta \\ \zeta \end{pmatrix}$$

x-vorticity   y-vorticity   z-vorticity
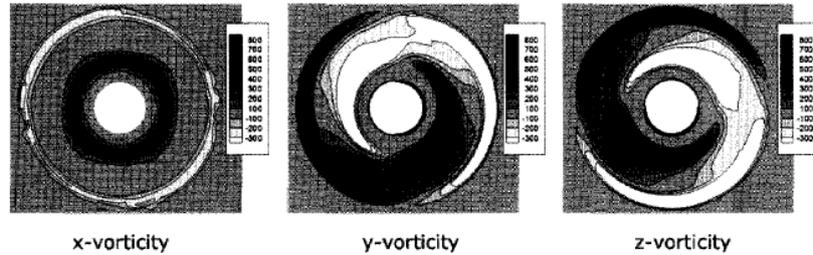
Figure 103: Visualization of The Vorticity Vectors Behind the Propeller [70]

To find the alignment of the vorticity vectors and the velocity vectors, the helicity of the flow is calculated.

$$h = \omega.V = u\xi + v\eta + w\zeta$$

E. Similarity and Scaling

For most engineering application, it is assumed that the laboratory conditions satisfy the real life implementation of the developed solution. However, this is usually not the case for transport vehicles. The characteristics of ever-moving ever-changing conditions require plethora of verification for its expected operation envelope. One of the requirements is to reduce the complexities in a system as it will be emphasized further in the report that contained experimental conditions already increase the complexity and distance from the actual resolution of a parameter. The dominant parameters are scaled using similarities between experiments and real life conditions.

The first scaling factor that is been widely used is the ratio which the fluid moves compared to the speed of sound in the same environment.

Mach number: The non-dimensional Mach number is the parameter that scales the advection velocity to speed of sound. This quantity shows if the fluid is (in)compressible. Also, the sonic envelope that the vehicle is going through is also determined by this factor.

$$Ma = \frac{advection}{speed\ of\ sound} = \frac{u}{\sqrt{\gamma RT}}$$

It is important to notice that Mach number is mainly affected by the temperature change. In fluid dynamics, there are 5 important forces: inertia, pressure, friction, gravity and capillary forces. Since all of the forces have the same units, their non-dimensional independent ratios could be identified by fractions of one and another.

Euler number: The non-dimensional Euler number is a way to represent the pressure forces to inertial forces. In aerospace, this connection is also identified in pressure coefficient. They are two quantities that can be directly related to each other.

$$Eu = \frac{pressure}{inertia} = \frac{p}{\rho u^2} = \frac{C_p}{2} \approx \frac{1}{\gamma M^2}$$

Reynolds Number: The non-dimensional Reynolds number is one of the most frequently used quantity that shows the relation between inertial forces to viscous (friction) forces.

$$Re = \frac{inertia}{friction} = \frac{\rho u L}{\mu}$$

F. Propeller Coefficients and Performance Parameters

An aircraft has many forces applied onto its surfaces, therefore it is a complex calculation to gather real thrust and drag data when propellers are installed. Even though isolated propeller shows the propeller stream in a constrained diameter, the addition of other surfaces like nacelles and wings create different results. As a result, replicating/scaling the conditions is not only necessary for the axial air stream produced by the wind tunnel, but also for the installed vortex air generators (in this case the propeller). Propeller scales are dependent in rotational speed, diameter, density and temperature or pressure or viscosity. For the low speed wind tunnel, compressibility and viscosity effects are minor (the last three properties have minor impact for scaling). Using the Buckingham Pi Theorem, the important non-dimensional parameters can be formulated to compare different aircraft. The remaining properties are non-dimensional performance criteria in thrust systems bookkeeping. These coefficient's were found using the Buckingham Pi theory. [43]

The three most commonly used coefficients are advance ratio (J), thrust coefficient (C_T) and power coefficient (C_P). These are defined as:

$$J = \frac{V}{nD}$$

$$C_T = \frac{T}{\rho n^2 D^4}$$

$$C_P = \frac{P}{\rho n^3 D^5}$$

Where (n) is the rotational speed, (D) is the diameter of the propeller, (ρ) is the ambient density, (T) is the propeller thrust and (P) is the input power. The efficiency of the propeller can also be calculated using these parameters.

$$\eta_P = \frac{Power_{out}}{Power_{in}} = \frac{T * V}{P} = \frac{C_T * J}{C_P}$$

The equations presented above are parameterized by the motion and geometry of the propeller. There is another parameter that is commonly used to relate the performance of the propeller on an aircraft. Instead of using the propeller velocity, the forward speed of the aircraft (V) is taken into account. This thrust coefficient (T_c) is often used by aircraft manufacturers to identify the overall aircraft propulsion performance.

$$T_c = \frac{T}{\rho V^2 D^2}$$

$$Q_c = \frac{Q}{\rho V^2 D^3}$$

The torque coefficient can be calculated to find the efficiency in terms of work done by the forward movement to the ratio of propeller shaft power. This results in:

$$\eta'_P = \frac{T_c * J}{2\pi Q_c}$$

In theory, to achieve similarity in the experimental setup thrust, power and advance ratio coefficients should be as close as possible. In practice, it is often not fully possible to operate these 3 parameters in the ideal conditions. The ideal facility to test the propeller is usually parallel with how much power it can provide to reach the desired power coefficient.

G. Derivation of Velocity Induced by a Single Panel (Johnson)

The method of Johnson's was used to obtain the velocities imposed by each panel. This method is used instead of Li's model because it allows for high order slipstream calculations. This means a higher order geometry and source strength distribution can be implemented, consequently leading to constant vorticity strength distribution.
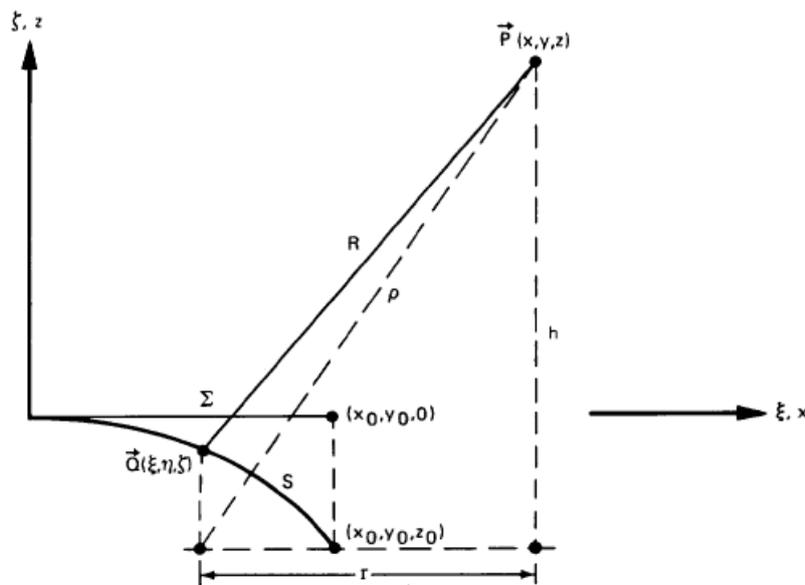
The mapping for the points can be seen above according to Johnson's usage of global and local coordinate system. For our model, some of the values like R and ρ can be the same. These relations will be specified as the content of equations are explained. According to Johnson, source potential and induced velocity can be calculated using $H(M,N,K)$ and $F(M,N,K)$ functions. These functions allows the utilization of algebraic recursive relations to solve differential equations.

$$H(M,N,K) = \iint\limits_{\Sigma} \frac{(\xi - x)^{M-1}(\eta - y)^{N-1}}{\left(\sqrt{(\xi - x)^2 + (\eta - y)^2 + z^2}\right)^K} d\xi d\eta$$

$$h = z - z_0 = z$$

$$\rho = \sqrt{(\xi - x)^2 + (\eta - y)^2 + h^2} = R$$

First of all the coordinate system on the panel has to be defined. It is portrayed in the figure below. The variable n and i is not portrayed. n is a number either 1 or 2 (the sides of a corner) and i is the corresponding corner between them.
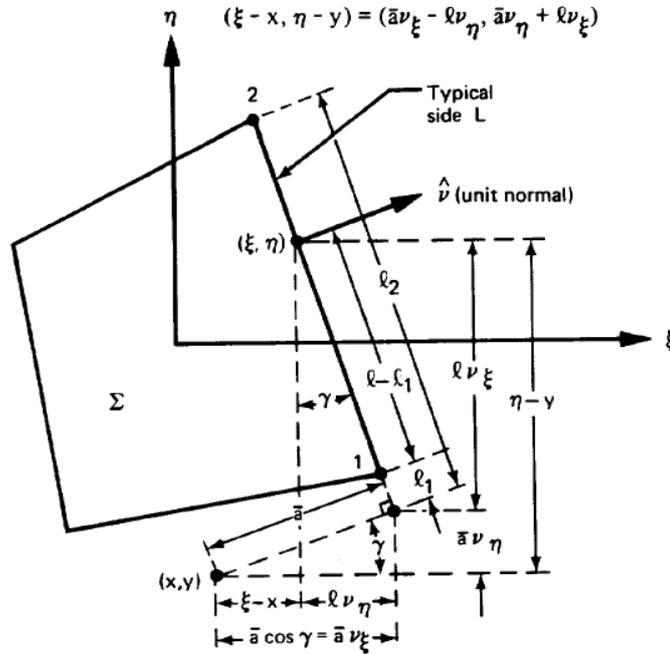
$$\vartheta_\xi = \frac{\eta_2 - \eta_1}{\sqrt{(\xi_2 - \xi_1)^2 + (\eta_2 - \eta_1)^2}}$$

$$\vartheta_\eta = -\frac{\xi_2 - \xi_1}{\sqrt{(\xi_2 - \xi_1)^2 + (\eta_2 - \eta_1)^2}}$$

In Appendix D of Johnson's paper, the velocity for a source panel is defined as below.

$$V_S = -\frac{1}{4\pi} \begin{bmatrix} H(2,1,3) \\ H(1,2,3) \\ -zH(1,1,3) \end{bmatrix}$$

There are 2 essential integrals that needs to be calculated to obtain H values. These are $H(1,1,3)$ integral and $F(1,1,1)$ integrals. When these initial values are known, the rest of H and F functions can computed by the recursing relations.

$$H(1,1,3) = \iint_\Sigma \frac{1}{\left(\sqrt{(\xi - x)^2 + (\eta - y)^2 + h^2}\right)^3} d\xi \, d\eta$$

$$F(1,1,1) = \iint_\Sigma \frac{1}{\left(\sqrt{(\xi - x)^2 + (\eta - y)^2 + h^2}\right)} dl$$

The extensive way to compute $H(1,1,3)$ is explained below. The equation for $H(1,1,3)$ can be expressed in polar coordinates where $r = \sqrt{(\xi - x)^2 + (\eta - y)^2}$.

$$H(1,1,3) = \sum_{i=1}^{4} \int_{\phi_i}^{\phi_{i+1}} \left(\int_0^r \frac{rdr}{\left(\sqrt{r^2 + h^2}\right)^3} \right) d\phi$$

Performing the inside integration yields the following equation.

$$H(1,1,3) = \sum_{i=1}^{4} \int_{\phi_i}^{\phi_{i+1}} \left(\frac{1}{|h|} - \frac{1}{\sqrt{r^2 + h^2}} \right) d\phi$$

This equation has to be converted into a line integral inside boundary of Σ. Also the point P lies outside of the boundary. $\bar{a}$ is the perpendicular distance from $(x, y, 0)$ to side L in the figure below.

$$r^2 = \bar{a}^2 + l^2$$

$$\cos(\phi) = \frac{\bar{a}}{\sqrt{l^2 + \bar{a}^2}}, \quad \sin(\phi) = l\frac{sgn(\bar{a})}{\sqrt{l^2 + \bar{a}^2}}, \quad \tan(\phi) = \frac{l}{\bar{a}}, \quad d\phi = \frac{\bar{a}dl}{l^2 + \bar{a}^2}$$

$$g^2 = \bar{a}^2 + h^2$$

$$H(1,1,3) = \sum_{i=1}^{4} \int_{l_i}^{l_{i+1}} \left(\frac{1}{|h|} - \frac{1}{\sqrt{l^2 + g^2}} \right) \frac{\bar{a}dl}{l^2 + \bar{a}^2}$$
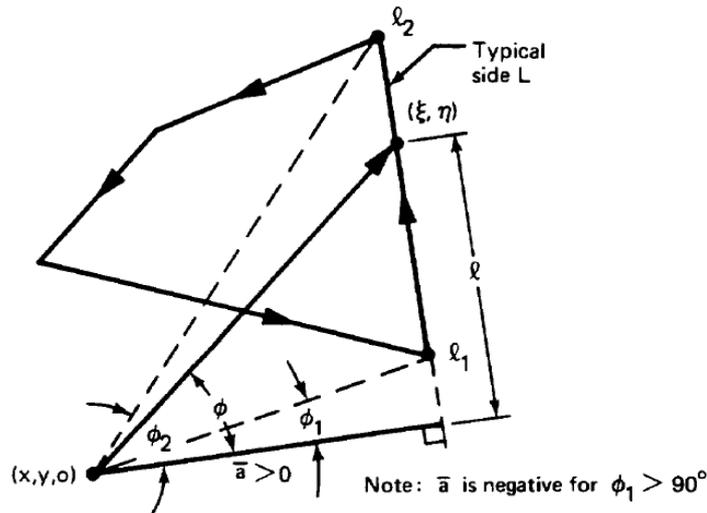
The resulting equation can be seperated into two sections: I_1 and I_2.

$$H(1,1,3) = \sum_{i=1}^{4} \left(\frac{\bar{a}}{|h|} I_1 - \bar{a}I_2 \right)$$

$$I_1 = \frac{1}{|\bar{a}|} \text{atan}\left(\frac{l}{|\bar{a}|} \right) \Big|_{l_i}^{l_i+1}, \quad I_2 = \frac{1}{|\bar{a}|.|h|} \text{atan}\left(\frac{|h|l}{|\bar{a}|\sqrt{l^2 + g^2}} \right) \Big|_{l_i}^{l_i+1}$$

Propeller Slipstream Correction for Wind Tunnel Applications   Ekin Orer

Finally the solution for $H(1,1,3)$ can be written in the algebraic form with and operator.

$$H(1,1,3) = \frac{1}{|h|} \sum_{i=1}^{4} \text{atan}[\, \bar{a}(l_2 c_1 - l_1 c_2), c_1 c_2 + \bar{a}^2 l_1 l_2]$$

Where:

$$\bar{a}_i = (\xi_i - x)(\vartheta_\xi)_i + (\eta_i - y)(\vartheta_\eta)_i$$

$$c_n = g^2 + |h|\sqrt{l_n^2 + g^2}$$

$$l_n = -(\xi_n - x)\vartheta_n + (\eta_n - y)\vartheta_\xi$$

The integral $F(1,1,1)$ is defined as below, however it results in many compuational errors.

$$F(1,1,1) = \int_{l_1}^{l_2} \frac{dl}{\sqrt{l^2 + g^2}}$$

So there needs to be 4 different conditions for function $F(1,1,1)$.

$$F(1,1,1) = \begin{cases} \ln\left(\dfrac{\left(\sqrt{l^2 + g^2} + l_2\right)}{\left(\sqrt{l^2 + g^2} + l_1\right)}\right), & l_1, l_2 \geq 0 \\[2ex] \ln\left(\dfrac{\left(\sqrt{l^2 + g^2} - l_1\right)}{\left(\sqrt{l^2 + g^2} - l_2\right)}\right), & l_1, l_2 < 0 \\[2ex] \ln\left(\dfrac{\left(\sqrt{l^2 + g^2} - l_1\right)\left(\sqrt{l^2 + g^2} + l_2\right)}{g^2}\right), & l_1 < 0, l_2 \geq 0 \\[2ex] \ln\left(\dfrac{g^2}{\left(\sqrt{l^2 + g^2} + l_1\right)\left(\sqrt{l^2 + g^2} - l_2\right)}\right), & l_1 \geq 0, l_2 < 0 \end{cases}$$

The second recursion is calculated from the relation below:

$$\iint_\Sigma \frac{\partial}{\partial \xi}\left[\frac{(\xi - x)^{M-2}(\eta - y)^{N-1}}{\rho^{K-2}}\right]\partial\xi\partial\eta = (M-2)H(M-2,N,K-2) - (K-2)H(M,N,K)$$

$$\xi - x = \bar{a}\vartheta_\xi - l\vartheta_\eta, \qquad \eta - y = \bar{a}\vartheta_\eta - l\vartheta_\xi, \qquad \partial\xi\partial\eta = \begin{vmatrix} \vartheta_\xi & -\vartheta_\eta \\ \vartheta_\eta & \vartheta_\xi \end{vmatrix}, \qquad \frac{\partial}{\partial\xi} = \vartheta_\xi\frac{\partial}{\partial\bar{a}}$$

It results in the following solutions:

$$H(2,1,3) = -\sum_{1}^{4} (\vartheta_\xi)_i F_i(1,1,1)$$

$$H(1,2,3) = -\sum_{1}^{4} (\vartheta_\eta)_i F_i(1,1,1)$$

Propeller Slipstream Correction for Wind Tunnel Applications

For more detailed information and thorough calculations, check Appendix D and G of Johnson's NASA report.

H. Vorticity Strength and Fluxes Extended (Li)

Define the following:

1) F_k Vorticity flux average on the side k
2) n_k Normal unit on the side k
3) $\vec{\omega}_k$ Vorticity vector average on the side k
4) S_k Geometric area on the side k, $S_k = \varepsilon l_k$
5) $\vec{\gamma}_k$ Vorticity strength density vector average on the side k, $\vec{\gamma}_k = \vec{\omega}_k(\varepsilon)$
6) l_k Length of the side k
7) $\vec{\gamma}_{ij}$ Vorticity strength density vector at the panel $C_{i,j}$
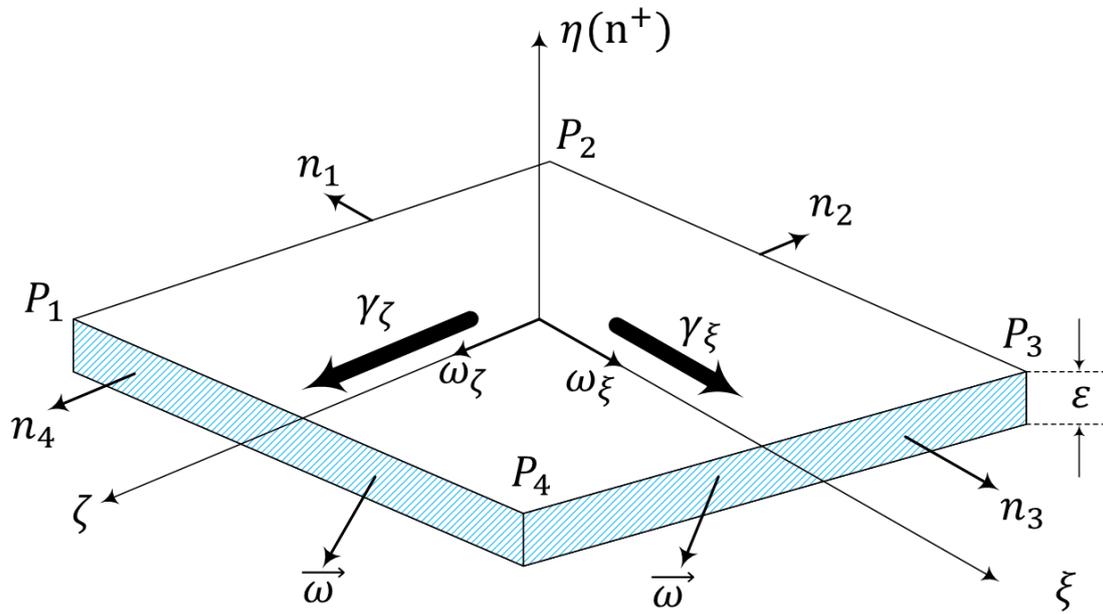
For each side S_k and vorticity flux F_k is defined by the formula below:

$$F_k = n_k.\vec{\omega}_k S_k = n_k.\vec{\omega}_k(\varepsilon l_k) = n_k.\vec{\gamma}_k l_k, \qquad k = 1 \dots 4$$

The slope and the angles of the slope of each panel can be calculated from the geometric parameters of the panels. For example, the slope of side 1 and 4, which is called S_{14} is defined by the angle that is associated by it (α_4). It goes the same for the side 2 and 3, which is called S_{23}. (The S_{14} here should not be confused with the area S_k)

$$S_{14} = \tan(\alpha_4), \qquad S_{23} = \tan(\alpha_2)$$

The width of the trapezoidal panel is the last geometric parameter to be calculated for the evaluation of SVPM.

$$w_{i,j} = \xi_4 - \xi_1 = l_4 \cos(\alpha_4) = l_2 \cos(\alpha_2)$$

The first quantities that can be obtained from the geometrical information is the normal vectors n_k in the local coordinate system (ξ, η, ζ).

$$\begin{bmatrix} n_1 = (-1,0,0) \\ n_2 = (\sin(\alpha_2),0,-\cos(\alpha_2)) \\ n_3 = (-1,0,0) \\ n_4 = (-\sin(\alpha_4),0,-\cos(\alpha_4)) \end{bmatrix}$$

For each side S_k there is a vorticity strength density average $\vec{\gamma}_k$. However, for a panel $C_{i,j}$ there is only a vorticity strength density $\vec{\gamma}_{ij}$. These two statements are normally not complimentary because there is only one $\vec{\gamma}_{ij}$ for each panel. The reason for defining two different terms is to satisfy the vorticity continuity equation between current panel and neighboring panels. The continuity equation cannot be fulfilled if the values for γ_ξ and γ_ζ are constant between panels because their derivatives will be 0. Therefore, the $\vec{\gamma}_k$ value on each side S_k can be separate from $\vec{\gamma}_{ij}$ but also be approximately calculated from the value of $\vec{\gamma}_{ij}$.
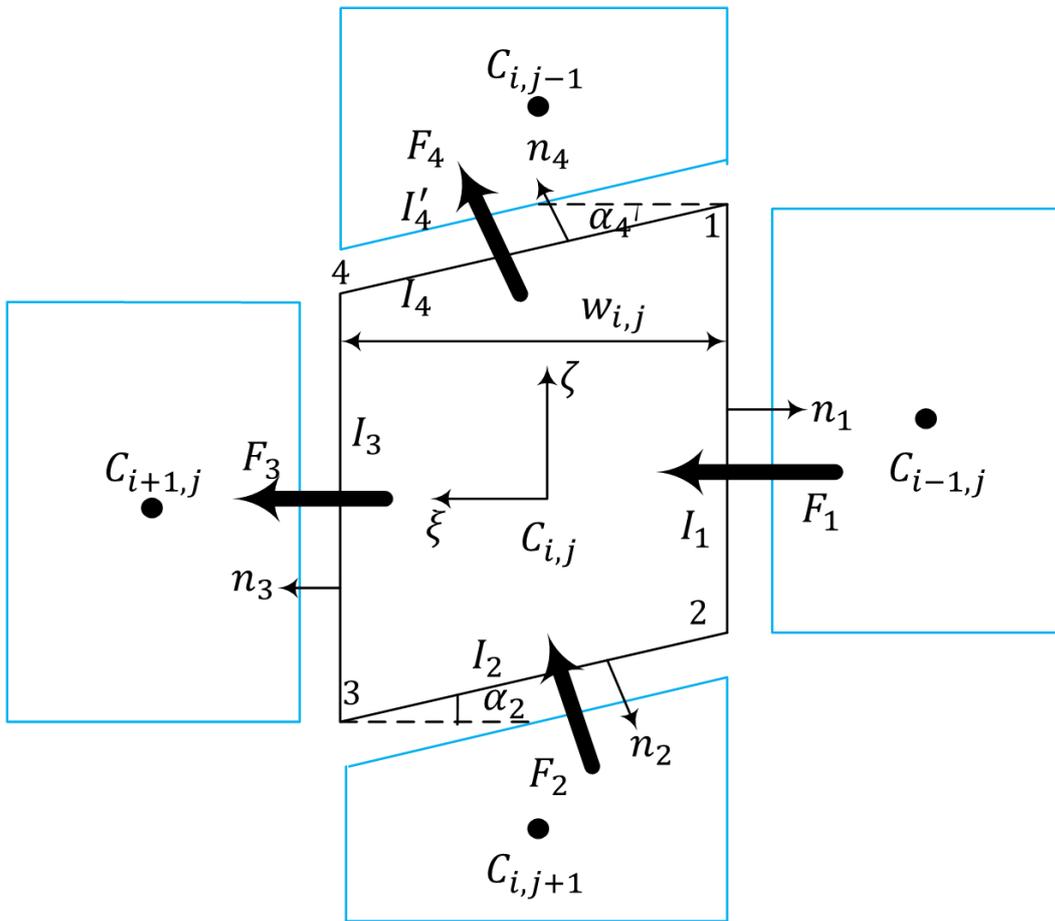
The approximate values for $\vec{\gamma}_k$ are evaluated as follows:

- For $\vec{\gamma}_1$, the vector is approximated by a straightforward manner on the panel $C_{i,j}$ in which the value for vorticity strength density is $\vec{\gamma}_{ij}$.

$$\vec{\gamma}_1 = (\gamma_{\xi_{ij}}, 0, \gamma_{\zeta_{ij}})$$

- For $\vec{\gamma}_3$, γ_ξ takes the value of the panel that is following the current panel, which is the value for $\vec{\gamma}_{i+1,j}$. Unlike γ_ξ value, γ_ζ takes the value of the panel that is the current panel, which is the value for $\vec{\gamma}_{ij}$.

$$\vec{\gamma}_3 = (\gamma_{\xi_{i+1j}}, 0, \gamma_{\zeta_{ij}})$$

-   For $\vec{\gamma}_2$, a central differencing scheme has been chosen to evaluate γ_ξ. The value is the mean between the current panel $C_{i,j}$ and the following panel $C_{i,j+1}$.

$$\vec{\gamma}_2 = \left(\frac{1}{2}\left(\gamma_{\xi_{ij}} + \gamma_{\xi_{ij+1}}\right), 0, \frac{1}{2}\left(\gamma_{\zeta_{ij}} + \gamma_{\zeta_{ij+1}}\right) \right)$$

-   For $\vec{\gamma}_4$, the same way was used with the preceding panel $C_{i,j-1}$, instead of the following panel.

$$\vec{\gamma}_4 = \left(\frac{1}{2}\left(\gamma_{\xi_{ij}} + \gamma_{\xi_{ij-1}}\right), 0, \frac{1}{2}\left(\gamma_{\zeta_{ij}} + \gamma_{\zeta_{ij-1}}\right) \right)$$

The reason why the central difference scheme is not used for $\vec{\gamma}_1$ and $\vec{\gamma}_3$ is that, for stable results of $\frac{\partial \gamma_\xi}{\partial \xi}$ in the partial differential equation a first order upwind scheme is needed.

For the γ_ζ components, only central differencing scheme is used in compliance with Finite Difference Method for the partial derivative of $\frac{\partial \gamma_\zeta}{\partial \zeta}$ value.

With the results of $\vec{\gamma}_k$ and n_k, the vorticity fluxes F_k become:

$$F_1 = n_1.\vec{\gamma}_1 l_1 = -\gamma_{\xi_{ij}} l_1$$

$$F_2 = n_2.\vec{\gamma}_2 l_2 = \frac{1}{2} w_{ij} \left[S_{23}\left(\gamma_{\xi_{ij}} + \gamma_{\xi_{ij+1}}\right) - \left(\gamma_{\zeta_{ij}} + \gamma_{\zeta_{ij+1}}\right) \right]$$

$$F_3 = n_3.\vec{\gamma}_3 l_3 = \gamma_{\xi_{i+1j}} l_3$$

$$F_4 = n_4.\vec{\gamma}_4 l_4 = \frac{1}{2} w_{ij} \left[S_{14}\left(\gamma_{\xi_{ij}} + \gamma_{\xi_{ij-1}}\right) - \left(\gamma_{\zeta_{ij}} + \gamma_{\zeta_{ij-1}}\right) \right]$$

It is known that the summation of these fluxes have to be zero. Therefore, substituting the geometric and strength density in the formula gives a relation between the current i-th station and $i + 1$-th station. The purpose of finding relation is to resolve the values for $\gamma_{\xi_{i+1,j}}$ by the values of $\gamma_{\xi_{i,j}}$. Then by the head jump formula the value for γ_ζ. In summary,

$$\gamma_{\xi_{i+1,j}} = \frac{I_1}{I_3}\gamma_{\xi_{i,j}} - \frac{w_{i,j}}{2 I_3}\left(\gamma_{\zeta_{i,j-1}} - \gamma_{\zeta_{i,j+1}}\right) + \frac{w_{ij}}{2 I_3}\left[S_{14}\left(\gamma_{\xi_{ij}} + \gamma_{\xi_{ij-1}}\right) - S_{23}\left(\gamma_{\xi_{ij}} + \gamma_{\xi_{ij+1}}\right) \right]$$

$$\gamma_\zeta^{(k)} = \frac{\frac{1}{\rho}\Delta H + \gamma_\xi^{(k)} V_{\zeta_m}^{(k-1)}}{V_{\zeta_m}^{(k-1)}}$$

The velocities for γ_ζ is obtained from the $k - 1$ iteration.

I. Step-by-step Modification of Panels to Resolve Unsatisfied Conditions (Li)

There are two apparent concerns that needs to be dealt with during the application of the SVPM. The first one is satisfying the kinematic boundary condition, when the mean velocity

$V_{\eta m}$ (the normal vector component of V_m) is not 0. The second one is the unique stagnation point where the wing-sliptream intersection takes place. In this case $V_{\xi m}$ and $V_{\zeta m}$ are 0, which fails the equations that are used to calculate $\vec{\gamma}$. A method of slipstream deformation will be introduced for the first problem. An exception to the vorticity flux calculation for the panels at the wind-slipstream intersection will be established as a second.

The idea behind the slipstream deformation is simple: the panels where $V_{\eta m} \neq 0$ has to be moved to a new position where the boundary condition is satisfied. Subsequently, all of the panels will be refreshed to their updated position. In summary:

- For every control point $C_{i,j+1}$, calculate the $V_{\eta m}$.
- For the panels that doesn't satisfy $V_{\eta m} = 0$, rotate the panel ϕ degrees in the 1-2 direction. (It can be observed in Figure)

$$\phi = \mathrm{atan}\left(\frac{V_{\eta m}}{V_{\xi m}}\right)$$

- Find new unit normal vector.

$$n' = \begin{bmatrix} -\sin(\phi) \\ \cos(\phi) \\ 0 \end{bmatrix}$$

- Calculate new plane of the panel by determining a point B on the 3-4 side of the previously deformed control point $C_{i-1,j+1}$ and n'.
- Find the corner points of the panel $C_{i-1,j+1}$, which are denoted by $P_3^{i-1,j+1}$ and $P_4^{i-1,j+1}$.
- The new corners are calculated by:

$$\Delta P_k = A^T \begin{bmatrix} \xi_k \\ \eta_k \\ \zeta_k \end{bmatrix}$$

- The value for the η_k can be calculated by the formula below, ξ_k is the width w. ζ_k is multiplied by 0, so the value is not needed for computation. From the formula, $n'.(r - r_0) = 0$ the η_k value can be singled out.

$$\eta_k = \frac{n'.r_0 + \sin(\phi)\,\xi_k}{\cos(\phi)}$$

- The definition of r_0 is the average distance between the R_2 and R_1.

$$r_0 = \frac{R_1 + R_2}{2}$$

- The corners are now ready to be updated by the new origin B and ΔP_k.

$$P_{k,new} = B + \Delta P_k$$

- The displacement of the slipstream is defined as Q, and it is the average of the two new corners of the adjacent panels.

$$Q = \frac{P_{3,new}^{i,j} + P_{4,new}^{i,j+1}}{2}$$
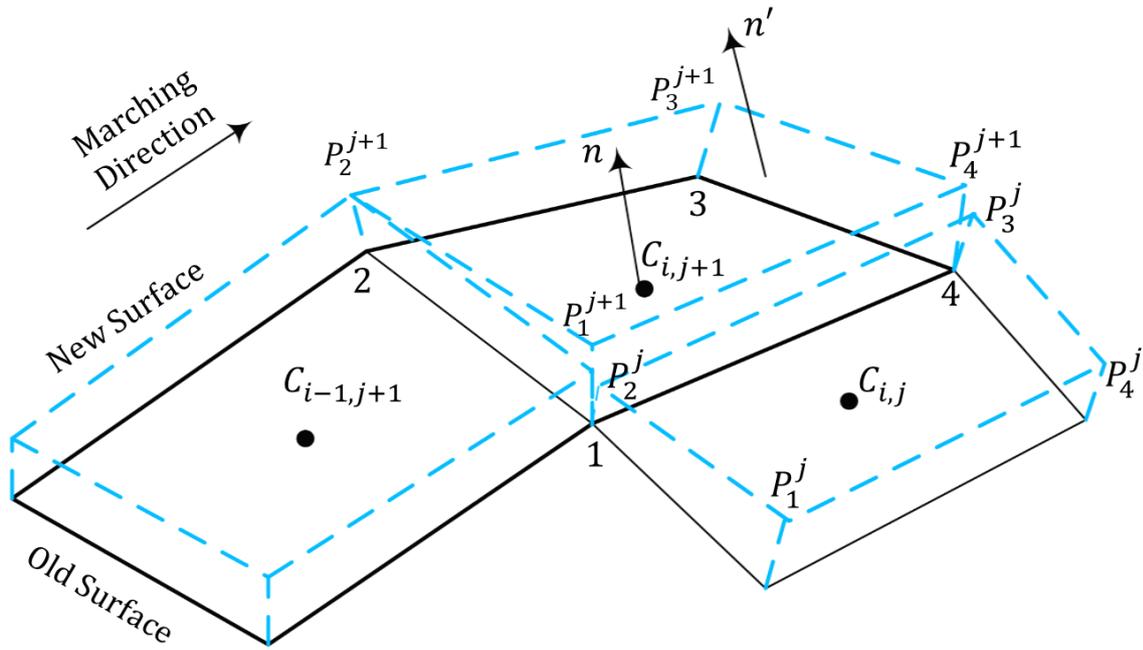
The computation of the γ_ξ and γ_ζ is different for the intersecting panels at the wing. Since it is assumed that the circulation of the propeller continues steady downstream, the shape of the helicoid has to be preserved. But, the wing is a solid boundary that doesn't allow information transfer between two panels where the slipstream and wing intercept. So the model assumes that these exceptional panels receive information only from the present panel instead of the mean strength value from $C_{i,j}$ and $C_{i,j-1}$. The panels in circumferential location $j = 1, \frac{NP}{2}, \frac{NP}{2} + 1, NP$ are the 4 intersecting panels. For $j = 1, \frac{NP}{2} + 1$ vorticity density strength $\vec{\gamma}_4$ and vorticity flux F_4 has to be recalculated, while for $j = \frac{NP}{2}, NP$ vorticity density strength $\vec{\gamma}_2$ and vorticity flux F_2 has to be recalculated.

For $j = 1, \frac{NP}{2} + 1$	$F_4 = -w_{i,j}(S_{14}\gamma_{\xi_{i,j}} - \gamma_{\zeta_{ij}})$
$\vec{\gamma}_4 = (\gamma_{\xi_{ij}}, 0, \gamma_{\zeta_{ij}})$	$\gamma_{\xi_{i+1,j}} = \frac{I_1}{I_3}\gamma_{\xi_{i,j}} + \frac{w_{i,j}}{2I_3}\left(\gamma_{\zeta_{i,j+1}} - \gamma_{\zeta_{i,j}}\right) + \frac{w_{ij}}{2I_3}\left[2S_{14}\left(\gamma_{\xi_{ij}}\right) - S_{23}\left(\gamma_{\xi_{ij}} + \gamma_{\xi_{ij+1}}\right)\right]$

For $j = \frac{NP}{2}, NP$	$F_2 = -w_{i,j}(S_{23}\gamma_{\xi_{i,j}} - \gamma_{\zeta_{ij}})$
$\vec{\gamma}_2 = (\gamma_{\xi_{ij}}, 0, \gamma_{\zeta_{ij}})$	$\gamma_{\xi_{i+1,j}} = \frac{I_1}{I_3}\gamma_{\xi_{i,j}} + \frac{w_{i,j}}{2I_3}\left(\gamma_{\zeta_{i,j}} - \gamma_{\zeta_{i,j-1}}\right) + \frac{w_{ij}}{2I_3}\left[S_{14}\left(\gamma_{\xi_{ij}} + \gamma_{\xi_{ij-1}}\right) - S_{23}\left(\gamma_{\xi_{ij}}\right)\right]$

J. Graphs for Estimation of Wind Tunnel Correction Coefficients (Barlow)
Solid Blockage Coefficients
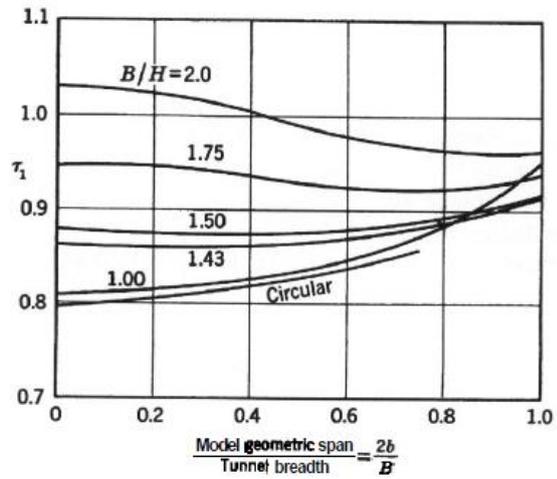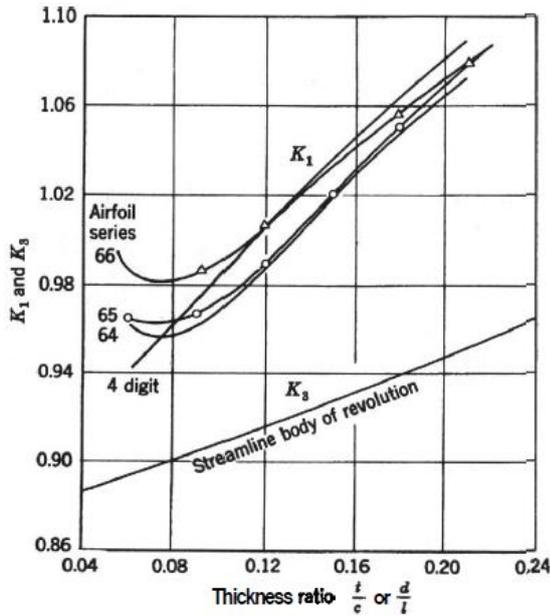
K. ANTARES Panel Method

The ANTARES model is developed by NASA Ames Wind Tunnel researchers to accompany their real-time transonic wind tunnel correction, in which the model is represented by singularities. However, there are some corrections that need to be implemented before the pressure data is processed. Therefore, a three-dimensional flow field solver was developed. It can calculate the blockage and lift interference for a given wind tunnel.

The model is based on Keller's model, in which the lift interference is calculated by Joppa's interpretation of lift interference. [71] In Joppa's method, the lifting body is represented as horseshoe vortices. [72] The model also assumes that the lift distribution on the wing is known. Then, the wing is divided into line doublets with different weights ($\Delta L/L$). This representation of the wing is proven to be used in AGARD 109 and Vaucheret. [26] [73]Lifting line theory is applicable to almost all high aspect ratio wings with low sweep, however point concentrations allows for a division of lift sections on the wing. The slipstream effect on the wing is local; the abrupt spanwise change in lift has to be rationed into sections for a better representation.
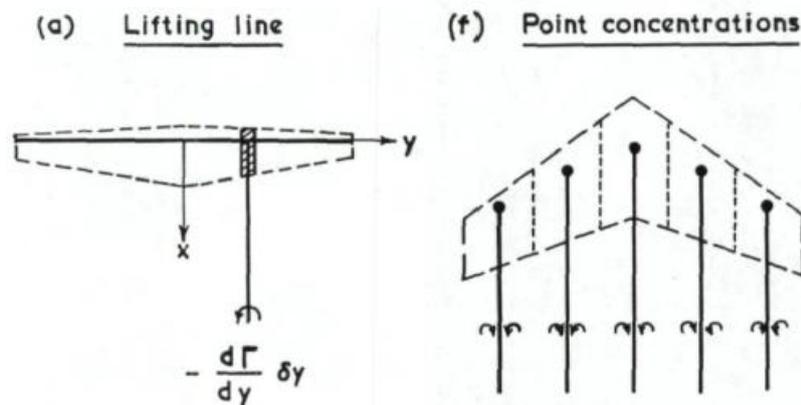
Figure 104: Two Different Ways of Modeling Wing in Potential Flow [26]

Vaucheret's study claims that for a wide range of span lengths and sweep angles, the wing can be represented as infinitesimally short horseshoe vortices. According to Keller, these horseshoe vortices become a vortex doublet (line doublet) starting at the center of the wing.
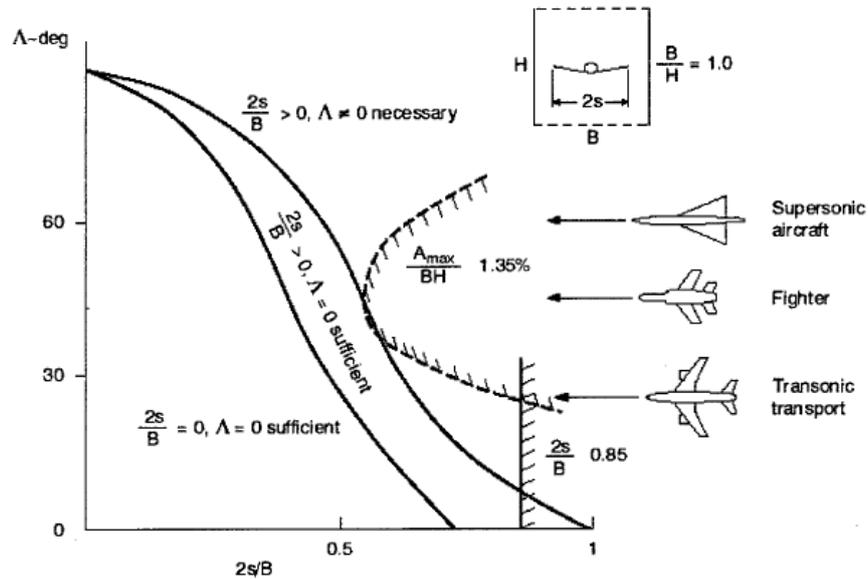
Figure 105: Modelling Requirements for Wings [73]

ANTARES method has the potential to be designed for very complex wind tunnel walls. [74] Even though the capabilities are coded inside the model, the closed test section model is quite straightforward. Therefore, only the closed section model will be represented in the explanation.

K-1 ANTARES Wall Representation and Boundary Conditions

The coordinate system is represented as Cartesian coordinates (x, y, z). x^+ is the freestream direction, z^+ points to the positive lift direction and y^+ is in line with the right-hand representation.

The wind tunnel walls are divided into rectangular panels and each boundary condition is satisfied in its centroid i. Every wall element j denotes a source distribution acting on the model.

The general wall boundary condition is represented to account for six different wind tunnel types. [75]

$$c_1\phi + c_2\frac{\partial \phi}{\partial x} + c_3\frac{\partial \phi}{\partial n} + c_4\frac{\partial^2 \phi}{\partial x \partial n} = 0 \tag{K.158}$$

The coefficients correspond to various wall types. For a closed test section:

Wall Type	c_1	c_2	c_3	c_4
Closed Wall	0	0	1	0

It is clear from the table that, the boundary condition for a closed section (provided in the previous chapter) is reached. The values for other wall types can be found in Keller's work. [76] The sum of perturbation velocity ϕ is the addition of the wall interference and model potentials.

$$\phi = \phi_m + \phi_w \tag{K.159}$$

The boundary conditions are satisfied at the centroid of each wall panel (i). The walls can have its own boundary characteristics depending on the placement towards the free-stream axis x and normal n. The closed wall wind tunnel perturbation velocity is only affected by the normal of each individual wall panel.

$$c_3(i)\left[\frac{\partial \phi_w}{\partial n}\right]_i = -c_3(i)\left[\frac{\partial \phi_m}{\partial n}\right]_i \tag{K.160}$$

The model potential ϕ_m can be represented by a line doublet (in Keller "vortex doublet") for the lifting surfaces and a point doublet for the blockage effects. The perturbation potential and its derivatives are rather long so it was covered in the Appendix L.

K-2 Setup Source Strength Matrix and Solution in ANTARES

Each panel's strength of the source distribution is denoted by σ and changes in linear trend with the slope $\mu = \frac{d\sigma}{dx}$. [74]For a total number of panels N, the relation between wall potential ϕ_w and source strength slope can be written as:

$$[\phi_w]_i = \sum_{j=1}^{N} [\phi^*]_{i,j} \cdot \mu_j \tag{K.161}$$

$[\phi^*]_i$ is the perturbation potential per unit source strength slope at the panel centroid i, caused by panel j. μ_j is the source strength slope of the panel. Furthermore, the relation can be improved for a closed test section:

$$\sum_{j=1}^{N} \left[\left[\frac{\partial \phi^*}{\partial n}\right]_{i,j}\right] \cdot \mu_j = -\left[\frac{\partial \phi_m}{\partial n}\right]_i \tag{K.162}$$

The system has to be solved for each centroid, which creates an equation of linear algebraic relation:

$$\begin{bmatrix} a_{11} & \cdots & a_{1N} \\ \vdots & \ddots & \vdots \\ a_{N1} & \cdots & a_{ij=NN} \end{bmatrix} \cdot \begin{bmatrix} \mu_1 \\ \vdots \\ \mu_{j=N} \end{bmatrix} = \begin{bmatrix} b_1 \\ \vdots \\ b_{j=N} \end{bmatrix} \tag{K.163}$$

$$a_{ij} = \left[\frac{\partial \phi^*}{\partial n}\right]_{i,j} \quad b_i = -\left[\frac{\partial \phi_m}{\partial n}\right]_i \tag{K.164}$$

Solving this linear relation in MATLAB allows for important parameters to be found. The axial perturbation velocity can be obtained by differentiating the total perturbation velocity in the x direction.

$$u(i) = \left[\frac{\partial \phi}{\partial x}\right]_i = \left[\frac{\partial \phi_m}{\partial x}\right]_i + \sum_{j=1}^{N} \left[\frac{\partial \phi^*}{\partial x}\right]_{i,j} \cdot \mu_j \tag{K.165}$$

The pressure coefficient at a specific centroid can be computed by:

$$c_p(i) = -\frac{2u(i)}{u_\infty} = -\frac{2}{u_\infty}\left(\left[\frac{\partial \phi_m}{\partial x}\right]_i + \sum_{j=1}^{N} \left[\frac{\partial \phi^*}{\partial x}\right]_{i,j} \cdot \mu_j\right) \tag{K.166}$$

For a given point k in the flow field, the perturbation velocity at that point can also be found:

$$u_w(k) = \sum_{j=1}^{N} \left[\frac{\partial \phi^*}{\partial x}\right]_{k,j} \cdot \mu_j \tag{K.167}$$

$$v_w(k) = \sum_{j=1}^{N} \left[\frac{\partial \phi^*}{\partial y}\right]_{k,j} \cdot \mu_j \tag{K.168}$$

$$w_w(k) = \sum_{j=1}^{N} \left[\frac{\partial \phi^*}{\partial z}\right]_{k,j} \cdot \mu_j \tag{K.169}$$

The blockage can be obtained by the computed perturbation velocity at point k in the flow field.:

$$\epsilon = \frac{u_w(k)}{u_\infty} = \frac{1}{u_\infty} \cdot \sum_{j=1}^{N} \left[\frac{\partial \phi^*}{\partial x}\right]_{k,j} \cdot \mu_j \tag{K.170}$$

The change in the angle of attack $\Delta \alpha$ is obtained using the perturbation velocity w_w.

$$\Delta \alpha(k) = \frac{180}{\pi} \cdot \frac{w_w(k)}{u_\infty} = \frac{180}{\pi} \cdot \frac{1}{u_\infty} \cdot \sum_{j=1}^{N} \left[\frac{\partial \phi^*}{\partial z}\right]_{k,j} \cdot \mu_j \tag{K.171}$$

The lift interference factor is calculated using Joppa's derivation for lift interference [72]:

$$\delta = \frac{1}{2}\frac{w_w}{\Gamma_m s} = \frac{1}{2}\frac{1}{\Gamma_m s} \cdot \sum_{j=1}^{N} \left[\frac{\partial \phi^*}{\partial z}\right]_{k,j} \cdot \mu_j \tag{K.172}$$

K-3 Performance of ANTARES Panel Code in MATLAB

The performance of the panel method has to be tested for assurance. There are two sources that can be used for a comperative test. The first one is Keller's swept wing experiment for lift interference in slotted tunnels. [76] This test was modified to a closed test section instead of a slotted one. The second compliance is with AGARDograph 336, in which the correlations between different lift interference values for different sizes of wind tunnel cross-sections. The values for AGARDograph 336 uses method of images solution. [31] Still, the values are expected to be very similar.
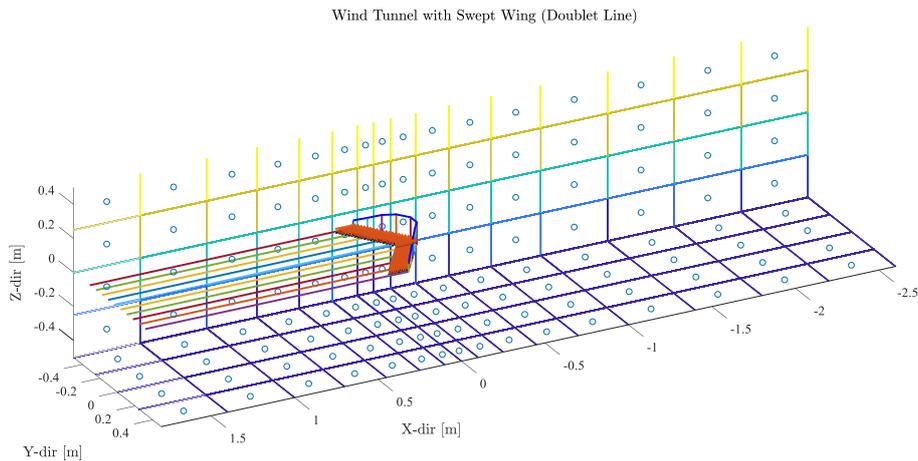
Figure 106: Cross-Section of the Wind Tunnel Panel Code

Tunnel walls are cut in 4 equal sections and each strip is divided in 16 pieces from $x = 2.6$ to $x = 1.8$. The sections concentrate towards the wing location. The constant strength portion of the downflow extends to $x_L = 10$. The source strength slopes μ_j are calculated at each wall panel centroid.
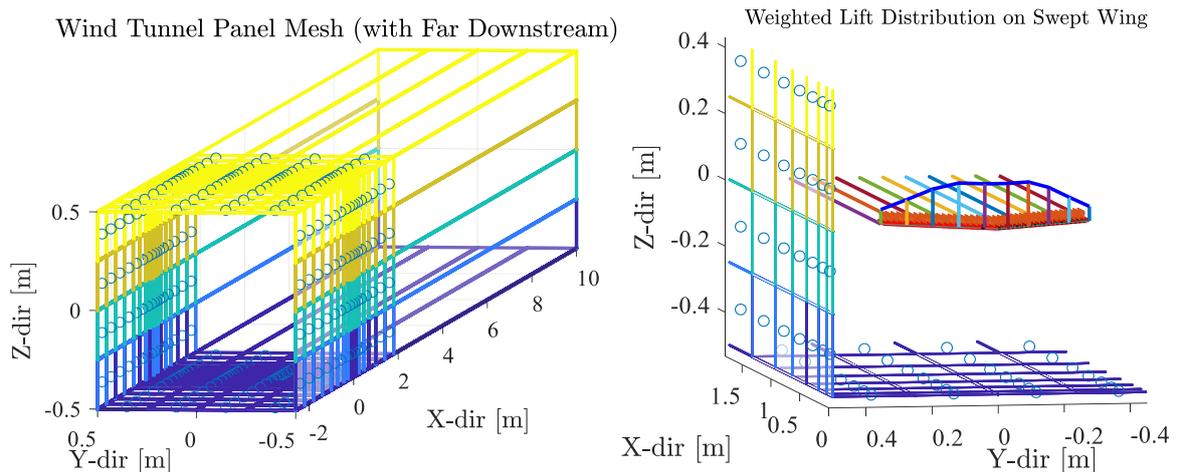
Figure 107: Layout of the Panels based on Keller's Parameters (Left), Visualized Swept Wing Lift Distribution (Right)

The test setup for Keller consists of a $35°$ swept wing. [71] The lift distribution of the wing was already approximated by Keller and was divided into 10 points $P_{1\dots10}$.

Table 10: The Relative Starting Position of The Swept Wing Doublet Lines

Point	$\dfrac{\xi_j}{h}$ or $\dfrac{x_i}{h}$	$\dfrac{\eta_j}{h}$ or $\dfrac{y_i}{h}$	$\dfrac{\zeta_j}{h}$ or $\dfrac{z_i}{h}$	$(\Delta L/L)_j$ or w_t
P_1	0.0246	0.0351	0.	0.1342
P_2	0.0738	0.1054	0.	0.1334
P_3	0.1229	0.1756	0.	0.1118
P_4	0.1721	0.2458	0.	0.0769
P_5	0.2212	0.3160	0.	0.0437
P_6	0.0246	-0.0351	0.	0.1342
P_7	0.0738	-0.1054	0.	0.1334
P_8	0.1229	-0.1756	0.	0.1118
P_9	0.1721	-0.2458	0.	0.0769
P_{10}	0.2212	-0.3160	0.	0.0437
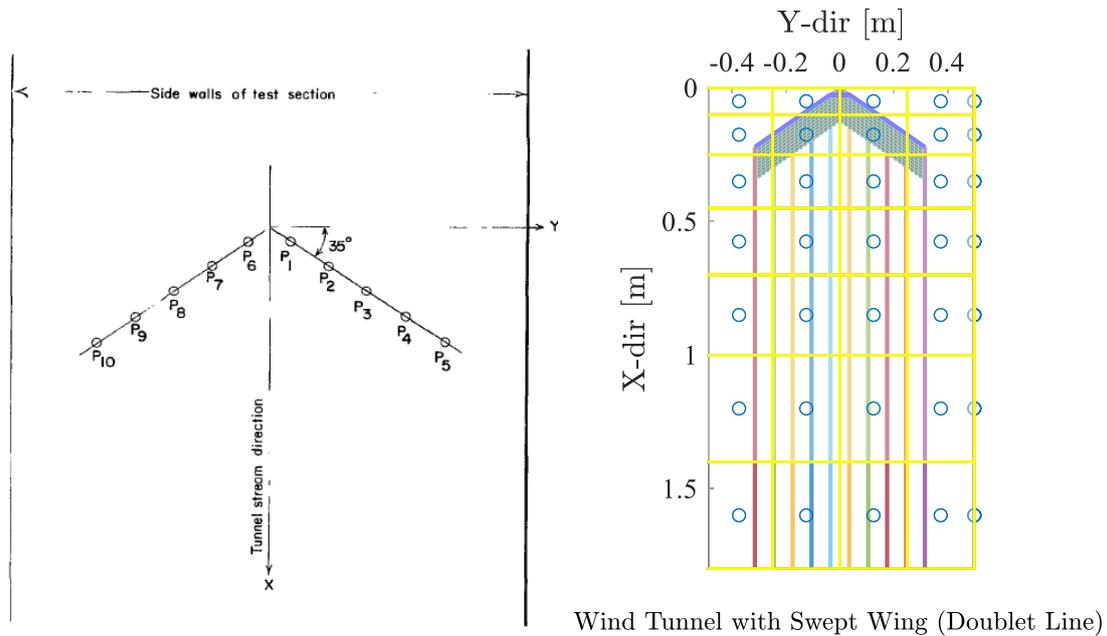
Figure 108: Swept Wing Used by Keller (from Wright) [77] (Left) and Swept Wing with Doublet Lines in Panel Code (Right)

Keller indicates that for a given control point, the upwash interference changes along the span. These can only be evaluated by computing each control point and adjusting $\Delta\alpha$ for each point along the span for a finite wing. For a single horseshoe vortex, the method of images solution was calculated for different height-to-width ratios in AGARDograph 109 by Garner. [26] However, the panel model chooses to divide the wing into sections of horseshoe vortices, albeit these are then assumed to have infinitesimal span. [71] As a result, they are compressed into doublet lines explained in the ANTARES and described in Appendix L-. [74]
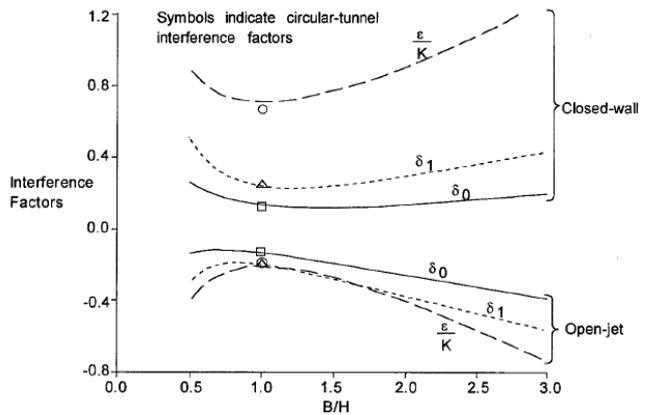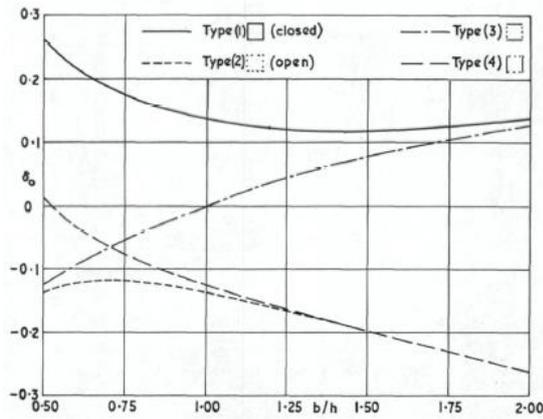
Figure 109: Change in Lift Interference Factor δ with Varying Breadth-to-Height Ratio (B/H) AGARD 109 (Left) AGARD 336 (Right)

With 256 total panels, execution of the file is less than 10 seconds for 10 control points. Therefore, time is not a real constraint as it was in SVPM code. One of the constraints were the division of panels chosen by Keller. (It is not specified in the reports, but it was assumed that the panels were divided so that the slotted sections correspond to one strip of panel each.) It was found that, using a concentrated distribution increases the smoothness of the graph. The new wind tunnel panel distribution is much more concentrated closer to the wing model.
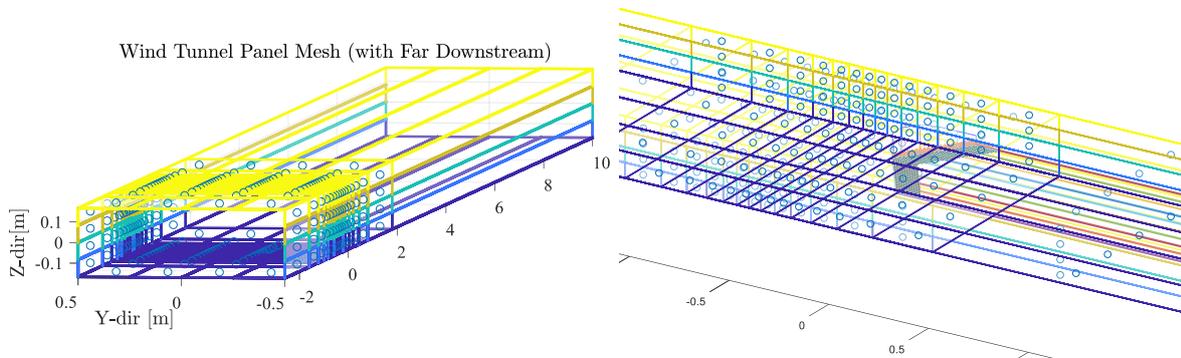
Figure 110: Example of A Wind Tunnel with $B/H = 3$ (Left) and Swept Wing Placed in a Higher Concentrated Panel Distribution to the Center Point/Wing Tip (Right)

Finally, the values for upwash interference factor for different control points were found. It should be noted that control point $P_0 = (0,0,0)$ and $P_{11} = (0.2451, 0.35, 0)$ are not singularity positions but extra control points. Also the values for $P_{6\ldots10}$ did not need to be calculated because of the model symmetry.
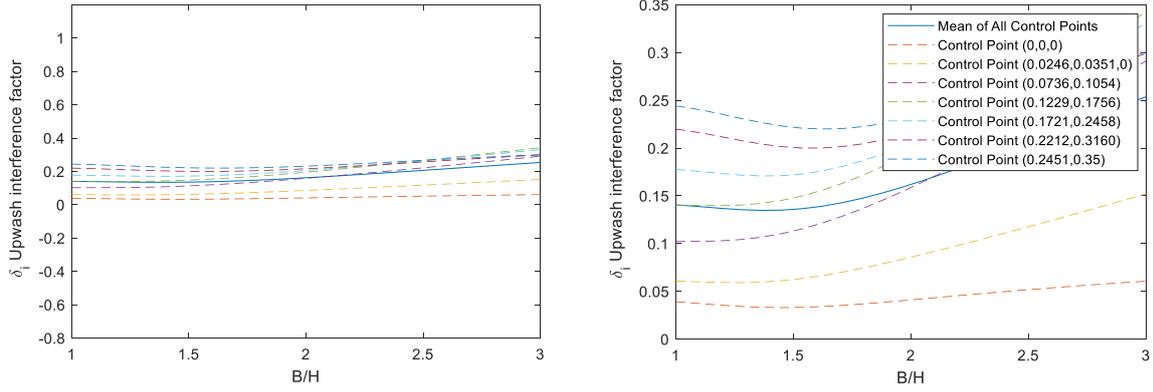
From the results, it can be observed that the values from AGRADograph 109 and 336 are very similar to panel method results. There does not seem a clear trade-off for the ANTARES panel method.

K-4 Example Line Doublet Potential Formula and Derivatives

In ANTARES panel method lifting effects on an aircraft is modeled as a line doublet in a 3D field for a rectangular wind tunnel. The values and derivations are gathered directly from Ulbrich's report. No changes have been made.

The coordinate transformation map for tunnel coordinates (x, y, z) to doublet orientation (ξ, η, ζ) is:

$$\xi = x$$

$$\eta(x, y, \Theta) = y * cos(\Theta) - z * sin(\Theta)$$

$$\zeta(x, y, \Theta) = y * sin(\Theta) + z * cos(\Theta)$$
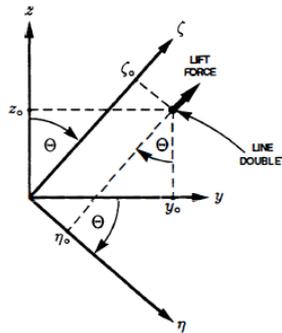
Similarly, coordinate transformation map for doublet starting point (x_0, y_0, z_0) to doublet orientation (ξ, η, ζ)

$$\xi_0 = x_0$$

$$\eta_0 = y_0 * cos(\Theta) - z_0 * sin(\Theta)$$

$$\zeta_0 = y_0 * sin(\Theta) + z_0 * cos(\Theta)$$

Potential in the doublet line local coordinates are:

$$\phi_m = \frac{\sigma}{4\pi} * \frac{\zeta - \zeta_0}{(\eta - \eta_0)^2 + (\zeta - \zeta_0)^2} * B$$

$$B = 1 + \frac{\xi - \xi_0}{[(\xi - \xi_0)^2 + (\eta - \eta_0)^2 + (\zeta - \zeta_0)^2]^{\frac{1}{2}}}$$

The first order derivatives are defined as:

$$\frac{\partial \phi_m}{\partial \xi} = \frac{\sigma}{4\pi} * \frac{\zeta - \zeta_0}{[(\xi - \xi_0)^2 + (\eta - \eta_0)^2 + (\zeta - \zeta_0)^2]^{\frac{3}{2}}}$$

$$\frac{\partial \phi_m}{\partial \eta} = \frac{-\sigma}{4\pi} * \frac{(\eta - \eta_0)(\zeta - \zeta_0)}{(\eta - \eta_0)^2 + (\zeta - \zeta_0)^2} * \left[\frac{2B}{(\eta - \eta_0)^2 + (\zeta - \zeta_0)^2} + C \right], where$$

$$C = \frac{\xi - \xi_0}{[(\xi - \xi_0)^2 + (\eta - \eta_0)^2 + (\zeta - \zeta_0)^2]^{\frac{3}{2}}}$$

$$\frac{\partial \phi_m}{\partial \zeta} = \frac{\sigma}{4\pi} * \frac{1}{(\eta - \eta_0)^2 + (\zeta - \zeta_0)^2} * \left[\frac{(\eta - \eta_0)^2 - (\zeta - \zeta_0)^2}{(\eta - \eta_0)^2 + (\zeta - \zeta_0)^2} * B + E \right], where$$

$$E = \frac{(-1)(\xi - \xi_0)(\zeta - \zeta_0)^2}{[(\xi - \xi_0)^2 + (\eta - \eta_0)^2 + (\zeta - \zeta_0)^2]^{\frac{3}{2}}}$$

The second order derivatives are defined as:

$$\frac{\partial^2 \phi_m}{\partial \xi \partial \eta} = -\frac{3\sigma}{4\pi} * \frac{(\eta - \eta_0)(\zeta - \zeta_0)}{[(\xi - \xi_0)^2 + (\eta - \eta_0)^2 + (\zeta - \zeta_0)^2]^{\frac{5}{2}}}$$

$$\frac{\partial^2 \phi_m}{\partial \xi \partial \zeta} = \frac{\sigma}{4\pi} * \frac{(\xi - \xi_0)^2 + (\eta - \eta_0)^2 - 2(\zeta - \zeta_0)^2}{[(\xi - \xi_0)^2 + (\eta - \eta_0)^2 + (\zeta - \zeta_0)^2]^{\frac{5}{2}}}$$

Since the line doublet is a scalar function and it uses the local coordinate system to resolve, the potential can be also defined as

$$\phi_m(x, y, z) = \phi_m\big(\xi(x), \eta(y, z, \Theta), \zeta(y, z, \Theta)\big)$$
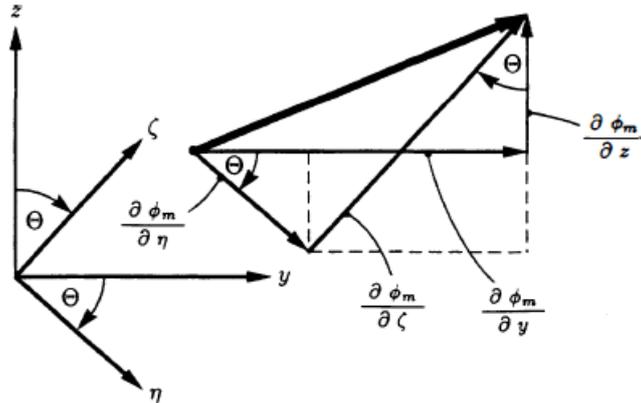
The derivatives for the global coordinate system is simply by reversing the coordinate transformation that was explained in the beginning of the Appendix.

$$\frac{\partial \phi_m}{\partial x} = \frac{\partial \phi_m}{\partial \xi}$$

$$\frac{\partial \phi_m}{\partial y} = \frac{\partial \phi_m}{\partial \eta} * cos(\Theta) + \frac{\partial \phi_m}{\partial \zeta} * sin(\Theta)$$

$$\frac{\partial \phi_m}{\partial z} = \frac{\partial \phi_m}{\partial \eta} * -sin(\Theta) + \frac{\partial \phi_m}{\partial \zeta} * cos(\Theta)$$

The second order derivatives are defined as:

$$\frac{\partial^2 \phi_m}{\partial x \partial y} = \frac{\partial^2 \phi_m}{\partial \xi \partial \eta} * cos(\Theta) + \frac{\partial^2 \phi_m}{\partial \xi \partial \zeta} * sin(\Theta)$$

$$\frac{\partial^2 \phi_m}{\partial x \partial z} = \frac{\partial^2 \phi_m}{\partial \xi \partial \eta} * -sin(\Theta) + \frac{\partial^2 \phi_m}{\partial \xi \partial \zeta} * cos(\Theta)$$

The normal derivatives for the wind tunnel walls are also required because it uses wall boundary conditions to satisfy the requirements of each wall panel.

Wall #	n	$\dfrac{\partial}{\partial n}$	$\dfrac{\partial \phi_m}{\partial n}$	$\dfrac{\partial^2 \phi_m}{\partial x \partial n}$
1	$\begin{pmatrix} 0 \\ 1 \\ 0 \end{pmatrix}$	$\dfrac{\partial}{\partial y}$	$\dfrac{\partial \phi_m}{\partial y}$	$\dfrac{\partial^2 \phi_m}{\partial x \partial y}$
2	$\begin{pmatrix} 0 \\ -1 \\ 0 \end{pmatrix}$	$-\dfrac{\partial}{\partial y}$	$-\dfrac{\partial \phi_m}{\partial y}$	$-\dfrac{\partial^2 \phi_m}{\partial x \partial y}$
3	$\begin{pmatrix} 0 \\ 0 \\ 1 \end{pmatrix}$	$\dfrac{\partial}{\partial z}$	$\dfrac{\partial \phi_m}{\partial z}$	$\dfrac{\partial^2 \phi_m}{\partial x \partial z}$
4	$\begin{pmatrix} 0 \\ 0 \\ -1 \end{pmatrix}$	$-\dfrac{\partial}{\partial z}$	$-\dfrac{\partial \phi_m}{\partial z}$	$-\dfrac{\partial^2 \phi_m}{\partial x \partial z}$

The solution for point doublet is simpler and can be found in the ANTARES Description

L. Fokker F27 Real and Model Parameters

The Fokker F27 model is tested in Delft Low Turbulence Tunnel (LTT) inside Low Speed Laboratory.
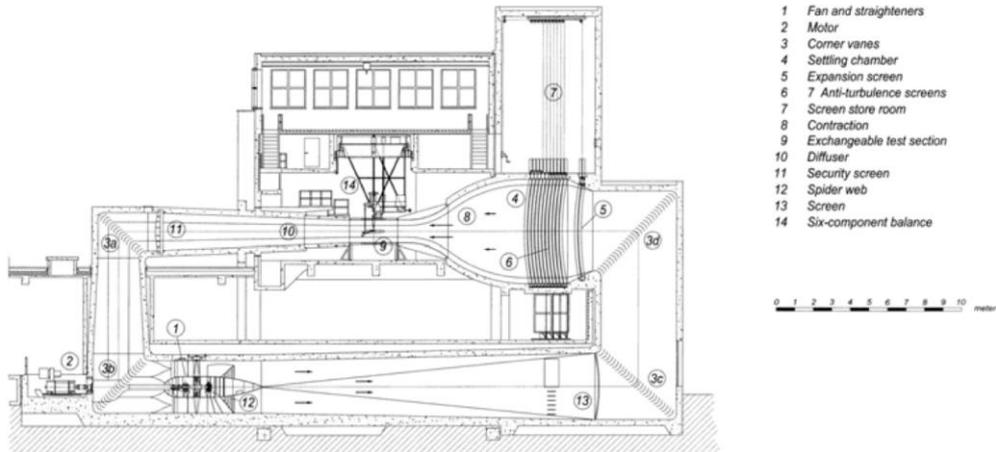
It is a closed return wind tunnel with a maximum achievable speed of approximately 120 m/s. It is driven by a 525 kW DC motor and is built on two floors. The maximum Reynolds number achievable is around $3.5 \cdot 10^6$. The test section area is given below:
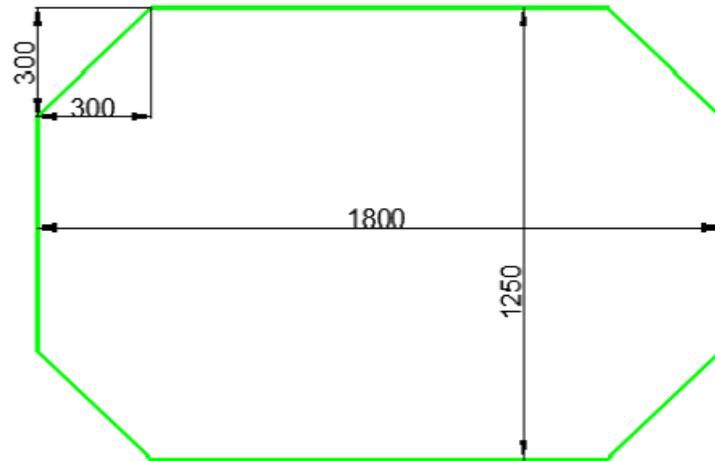
The contraction ratio of the wind tunnel is 1:17.8 and maximum turbulence is around 0.07%.

FOKKER F27 1:20 SCALE MODEL	
Wing	
SPAN	$1.450\ [m]$
AREA	$0.175\ [m^2]$
MEAN AERODYNAMIC CHORD	$0.1282\ [m]$
TAPER RATIO	0.4225
ASPECT RATIO	12
DIHEDRAL (0.4C) INNER WING	$0°$
(0.4C) OUTER WING	$2.5°$
SWEEP ANGLE (0.25C)	$1.15°$
INCIDENCE WITH RESPECT TO FUSELAGE CENTER LINE	$3.46°$
TWIST INNER WING	$0°$
TWIST OUTER WING	$-2°$

ROOT AIRFOIL	$NACA\ 642 - 421\ (adapted)$
TIP AIRFOIL	$NACA\ 642 - 415\ (adapted)$
POSITION OF WING PIVOT POINT	$X_0\ =\ 34.5\%\ MAC, Z_0\ =\ 60.8\%\ MAC$
Fuselage	
LENGTH	$1.155\ [m]$
HEIGHT (CYLINDRICAL PART)	$0.1385\ [m]$
WIDTH (CYLINDRICAL PART)	$0.135\ [m]$
FUSELAGE ATTACHMENT POINTS FRONT	$0.0442\ [m]$
FUSELAGE ATTACHMENT POINTS BACK	$0.4064\ [m]$
Horizontal tail	
SPAN	$0.490\ [m]$
AREA	$0.0402\ [m^2]$
MEAN AERODYNAMIC CHORD	$0.0877\ [m]$
ASPECT RATIO	5.95
NOMINAL INCIDENCE ANGLE	$0°$
TAIL LENGTH	$0.534\ [m]$
DIAMETER	$0.183\ [m]$
NUMBER OF BLADES	4
Engines	
MANUFACTURER	$TASK\ Corporation$
TYPE	$3 - phase\ induction$
POWER	$3.6\ kW\ +\ 3.6\ kW$
MAXIMUM RPM	$30000\ rpm$
NUMBER	2

FOKKER F27 CRUISE FLIGHT & ENGINE DATA	
CRUISE SPEED	$133.3\ [m/s]$
SERVICE CEILING	$8997\ [m]$
CRUISE ALTITUDE	$8475\ [m]$
AIR DENSITY AT CRUISE ALTITUDE	$0.497\ [kg/m^3]$
TEMPERATURE AT CRUISE ALTITUDE	$233\ [K]$
PRESSURE AT CRUISE ALTITUDE	$33220\ [Pa]$
SPEED OF SOUND AT CRUISE ALTITUDE	$306.042\ [m/s]$
DYNAMIC VISCOSITY OF AIR AT CRUISE ALTITUDE	$1.52377 \cdot 10^{-5}\ [Pa \cdot s]$
ENGINE - TURBOPROP (2X) ROLLS-ROYCE DART	$Rolls - Royce\ Dart\ Mk.356 - 7R$
PERMISSIBLE ROTATIONAL SPEED	$15000\ rpm$
MAXIMUM ROTATIONAL SPEED (20 SEC)	$17000\ rpm$
ENGINE POWER	$1.529\ MW$
PROPELLER DIAMETER	$0.96\ [m]$

M. Propeller and Wing Loading Simulation by BEM and VLM (Veldhuis)

One of the ways to compute high wing loading at high thrust conditions is to use a combination simplified analysis. The propeller can be modeled as a blade element while the wing loading due to slipstream can be modeled in the vortex lattice method. Since lift production on a surface is directly proportional to the circulation around it, the vortices can be modeled as multiple horseshoe vortices. In VLM, the lifting surface is divided into multiple lattices of quadrilateral panels. Then at the quarter chord of the wing, a horseshoe vortex is defined at the center of each panel in parallel with Prandtl lifting line theory. The advantage of using VLM is the straightforward solution for a complicated flow field behind the propeller-wetted wing. The control point is located at three quarter chord of each section and at the center of each panel span.
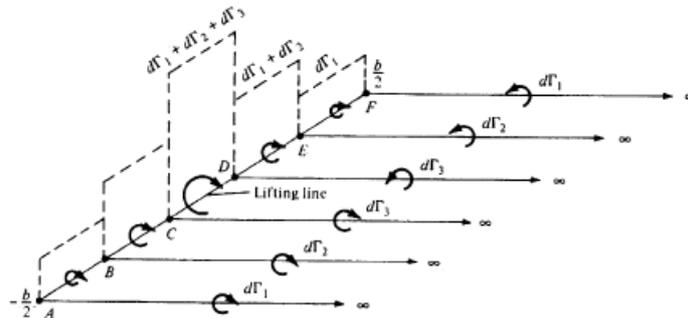
The advantages of the VLM method is the direct numerical solution and the accuracy of the lift coefficient that it predicts. However, for high angles-of-attack, the solution is not as reliable since the induced velocities increase the dynamic pressure and the lift coefficient is not in the linear range under slipstream. This will be assumed to be not the case to achieve a robust solution. Instead, a method of modified BEM will be included in the propeller simulation. Another problem with the vortex lattice is the absence of wing thickness, which doesn't account for leading edge effect where the thickness of the airfoil is significantly larger. Katz and Plotkin [35] has included couple of methods to overcome this issue, however the computation complexity increases with the alternative additions to simple vortex lattice solution.

In VLM, to obtain the aerodynamic characteristics, the strengths of finite number of vortices should be calculated. This gives a continuous distribution of vorticity leaving the wing surface. The sum of the vectors should satisfy the zero normal velocity boundary condition. The Biot-Savart Law can be used to give the induced velocity at a selected point, where a line vortex filament is adding momentum into the system.

For the propeller slipstream model, a propeller blade analysis is also included. The solution is taken as a time averaged solution, which is crude compared to the inclusion of azimuthal angles. However, the induced velocities can be calculated and added to the VLM method with ease. Each blade element is solved for a 2D airfoil and from propeller momentum theory iteratively. For a converged calculation, the axial and the tangential forces can be calculated to compute the swirl and axial velocity components around the blade element.
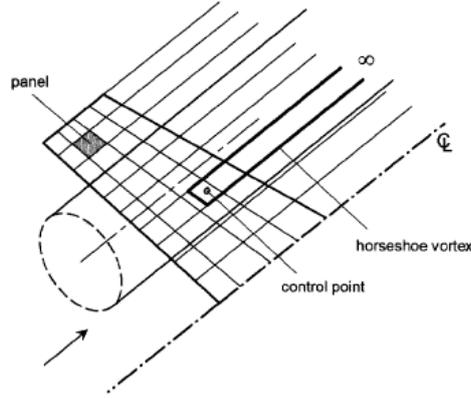
Figure 111: Panel Representation for VLM-BEM of Veldhuis [4]

For the propeller addition into VLM, the velocities in the horseshoe vortex system has to be defined. The total velocity is an addition of three velocities: V_∞, V_m, V_p free-stream, vortex model control point and propeller velocities respectively. The total velocity can be defined as:

$$\overline{V_{tot}} = \overline{V_\infty} + \overline{V_m} + \overline{V_p}$$

Applying the proper boundary conditions and approximations, the unknown circulation Γ_n can be calculated using the formula below. The in-between steps can be found in the Appendix.

$$\sum_{n=1}^{2N} \frac{(C_{m,n_k})\Gamma_n}{V_\infty} = \left(\frac{\partial g}{\partial x} - \alpha\right)_m + u_{m_p}\left(\frac{\partial g}{\partial x}\right)_m - w_{m_p}$$

When the circulation strength is known, the local forces on each panel can be found and therefore the total lift in the wake system.

$$C_{L_w} = \frac{\sum_{k=1}^{2N} 2\Gamma\left(U_\infty + u_{p_k}\right)\Delta y_k}{U_\infty^2 S}$$

The total lift produced by the VLM-BEM system can be represented as the sum of two lift forces.

$$C_{L_{tot}} = C_{L_w} + \Delta C_{L_p}$$

$$\Delta C_{L_p} = \frac{S_p}{S} T_c' \sin\left(\alpha_{p_{ref}}\right) + \frac{S_p}{S} C_{N_p} \cos(\alpha_{p_{ref}})$$

This method is proven to be useful at low angles of attack with a large range of T_c values (0.046 to 0.65). The biggest advantage of the VLM-BEM is that the swirl component is added into the analysis, which is essential for slipstream calculations.

M-1. Prandtl Lifting Line with Gauss-Sidel Solution (Anderson)

Prandtl's lifting line for high aspect ratio is formed as a linear system. The linear system is resolved by method of successive displacement in iterations(Gauss-Seidel method).

$$\bar{\bar{A}}\bar{x} = \bar{b}$$

The circulation is defined by the Kutta-Joukowski theorem.

$$L' = \rho V_\infty \Gamma, \qquad \text{where} \qquad \Gamma(y) = \frac{V_\infty}{2} c_l(y) c(y)$$

Since the wing is under the influence of different angles of attack, it is also need to be considered. Anderson gives the change in induced angle of attack:

$$\alpha_i(y_n) = \frac{1}{4\pi V_\infty} \int_{-b/2}^{b/2} \frac{\left(\frac{d\Gamma}{dy}\right) dy}{y_n - y}$$

Anderson also gives the formula for lift coefficient at a certain interval of vortices.

$$c_l = \alpha_0 \left[\alpha_{eff}(y_0) - \alpha_{L=0}\right], \qquad \text{where} \qquad \alpha_{eff} = \alpha - \alpha_i$$

The system of equations can be written as the sum of every circulation at collocation point j.

$$\alpha_i(y_i) = \sum_{j=1}^{N} A_{ij} \Gamma_i, \qquad \text{where} \qquad A_{ij} = \left(\frac{1}{y_i - y_{j-1}} - \frac{1}{y_i - y_j}\right)$$

All of the equations can be explicitly written for Γ_i.

$$\Gamma_i = C_i \left(\alpha_i - \sum_{j=1 \, (i \neq j)}^{N} A_{ij} \Gamma_j\right), \qquad where \qquad C_i = \frac{V_\infty}{2}(c\alpha_0)_i$$

The iteration scheme can be commenced at $\Gamma = 0$ and the values of Γ are calculated in a loop until the Γ_i values do not effectively change. In short, the notation can be written as

$$A\Gamma = b$$

M-2. BEM Propeller Integration into VLM (Veldhuis)

Each horseshoe vortex with index n has an induced velocity at control point m. If the model vorticity number is set as $2N$, then the total induced velocity at control point m becomes:

$$V_m = \sum_{n=1}^{2N} V_{m,n} = \sum_{n=1}^{2N} C_{m,n} \Gamma_n$$

C contains the influence coefficients in $m \, x \, n$ matrix. It is only affected by wing geometry and wake model. The circulation Γ_n is calculated using the flow tangency boundary condition. The total velocity vector is a sum of horseshoe vortex model and free stream velocity. For the slipstream condition, an additional propeller velocity vector is going to be added.

$$\overline{V_{tot}} = \overline{V_\infty} + \overline{V_m} + \overline{V_p}$$

$$\overline{V_\infty} = (V_\infty \cos(\alpha))\, \hat{\imath} + (V_\infty \sin(\alpha))\, \hat{k}$$

$$\overline{V_m} = (V_\infty \cos(\alpha) + u_{m_i} + u_{m_p})\, \hat{\imath} + (v_{m_i} + v_{m_p})\hat{\jmath} + (V_\infty \sin(\alpha) + w_{m_i} + w_{m_p})\, \hat{k}$$

$$\overline{V_p} = \begin{pmatrix} u_p \\ v_p \\ w_p \end{pmatrix}$$

The wing surface geometry G is described in the following form:

$$G(x, y, z) = 0$$

The boundary condition is implemented as follows:

$$\overline{V}.\frac{\overline{\nabla}G}{|\overline{\nabla}G|} = \overline{V}.\overline{\nabla}G = 0$$

Assuming the 2D blade element is on the $x - y$ plane, the unknown circulation can be solved.

$$G(x, y, z) = z - g(x, y) = 0$$

$$\sum_{n=1}^{2N} \left(C_{m,n_k} - \frac{\partial g}{\partial x} C_{m,n_i} - \frac{\partial g}{\partial y} C_{m,n_j} \right) \Gamma_n = V_\infty \left(\cos(\alpha) \frac{\partial g}{\partial x} - \sin(\alpha) \right) + u_{m_p} \frac{\partial g}{\partial x} + v_{m_p} \frac{\partial g}{\partial y} - w_{m_p}$$

Applying the small angle approximation and assuming a planar surface with no dihedral:

$$\sum_{n=1}^{2N} \frac{(C_{m,n_k})\Gamma_n}{V_\infty} = \left(\frac{\partial g}{\partial x} - \alpha \right)_m + u_{m_p} \left(\frac{\partial g}{\partial x} \right)_m - w_{m_p}$$

The local coefficient C_{l_k}, at spanwise location k, can be calculated once the circulation is obtained from previous equation.

$$C_{l_k} = \frac{2}{U_\infty c_k} \left(1 + \frac{u_{p_k}}{U_\infty} \right) \Gamma_k$$

The overall lift coefficient is written as:

$$C_{L_w} = \frac{\sum_{k=1}^{2N} 2\Gamma \left(U_\infty + u_{p_k} \right) \Delta y_k}{U_\infty^2 S}$$

The local induced angle is defined as:

$$\alpha_{ik} = \frac{-w_k - w_{p_k}}{U_\infty}$$

The upwash velocity due to trailing vortex system is found by Biot-Savart law.

$$w_k = -\sum_{n=1}^{2N} \frac{\frac{1}{4\pi}\Delta\Gamma}{y_k - y_j} \ for \ j = 1,2N$$

The wake model lift is defined above and using the thrust coefficient and normal coefficient, the blade element lift coefficient can be included to find the total lift coefficient.

$$C_{L_{tot}} = C_{L_w} + \Delta C_{L_p}$$

$$\Delta C_{L_p} = \frac{S_p}{S} T_c' \sin \left(\alpha_{p_{ref}} \right) + \frac{S_p}{S} C_{N_p} \cos(\alpha_{p_{ref}})$$

Finally, the effective angle of attack of the propeller can be calculated by the influence of fuselage angle of attack α_{fus}, propeller incidence angle α_{prop} and upflow angle produced by the wing α_{upflow}.

$$\alpha_{p_{eff}} = \alpha_{fus} + \alpha_{prop} + \alpha_{upflow}$$

N. Uncorrected Values Example

Alpha	CL	CD	Fx	Fy	Fz	Mx	My	Mz
degrees	/	/	N	N	N	Nm	Nm	Nm
-5.992	-0.2292	-0.05376	6.96	-3.86	-54.25	-0.3	6.21	-2.97
-5	-0.1164	-0.05667	6.31	-4.03	-26.41	0.08	5.85	-3.04
-4	0.0007	-0.05857	5.86	-3.84	2.16	0.3	5.5	-3.04
-3	0.1182	-0.05981	5.62	-3.84	30.94	0.66	5.22	-3.03
-2	0.2346	-0.05999	5.53	-3.95	59.62	0.83	5.01	-3.02
-1	0.3475	-0.05888	5.68	-4.06	88.2	0.98	5.03	-2.99
0	0.4609	-0.05668	5.92	-4.18	116.54	1.17	4.93	-2.99
1	0.5765	-0.05382	6.38	-4.18	145.04	1.27	4.72	-2.94
2	0.6924	-0.0506	6.99	-4.06	173.53	1.34	4.51	-2.87
3	0.808	-0.04585	7.8	-3.93	201.95	1.47	4.16	-2.71
4	0.921	-0.0402	8.99	-2.92	229.63	1.67	3.88	-2.45
5	1.0323	-0.03383	10.33	-1.89	256.56	1.75	3.61	-2.24
6	1.1231	-0.02529	12.07	-1.62	279.48	1.7	3.48	-2.13
7	1.1584	-0.01418	14.55	-1.78	287.29	2	3.78	-2.04

Rho	Q	V	Re	M
kg/m^3	Pa	m/s	/	/
1.176	1461.7	49.87	4.09E+05	0.144
1.175	1460.4	49.85	4.09E+05	0.144
1.175	1462	49.88	4.09E+05	0.144
1.175	1459.6	49.84	4.08E+05	0.144
1.175	1459.2	49.83	4.08E+05	0.144
1.175	1460.3	49.85	4.09E+05	0.144
1.175	1461.6	49.87	4.09E+05	0.144
1.175	1461.6	49.87	4.09E+05	0.144
1.175	1459.2	49.83	4.08E+05	0.144
1.176	1461.7	49.87	4.09E+05	0.144
1.176	1460.9	49.85	4.09E+05	0.144
1.176	1459.7	49.83	4.09E+05	0.144
1.176	1459	49.81	4.09E+05	0.144
1.176	1460	49.83	4.09E+05	0.144